The Q^p_{Weak} Experiment: "A Search for New Physics at the TeV Scale via a Measurement of the Proton's Weak Charge" Jlab E02-020 Technical Design Report

January 15, 2003

The Collaboration

D.S. Armstrong[1], T. Averett[1], J. Birchall[7], J.D. Bowman[5], R. Carlini[9] (Principal Investigator), S. Chattopadhyay[9], C.A. Davis[11] J. Dunne[14], J. Erler[3], R. Ent[9], W. Falk[7], J.M. Finn[1], T.A. Forest[6], D. Gaskell[9], C. Hagner[10], W. Hersman[12], M. Holtrop[12], K. Johnston[6], R. Jones[2], C. Keppel[18], E. Korkmaz[15], S. Kowalski[8], L. Lee[7], A. Lung[9], D. Mack[9], S. Majewski[9], H. Mkrtchyan[13], G.S. Mitchell[5], N. Morgan[10], A. Opper[17], S.A. Page[7], S. Penttila[5], M. Pitt[10], M. Poelker[9], T. Porcelli[15], W.D. Ramsay[7], M. Ramsey-Musolf[2,4], J. Roche[1,9], N. Simicevic[6], G. Smith[9] (Project Manager), R. Suleiman[8], S. Taylor[8], W.T.H. van Oers[7], S. Wells[6], W.S. Wilburn[5], S.A. Wood[9], C. Zorn[9]

The Institutions

[1]*College of William and Mary, Williamsburg, VA*, [2]*University of Connecticut, Storrs, Connecticut*, [3]*Instituto de Fisica, Universidad Nacional Autonoma de Mexico, Mexico*, [4]*Kellogg Radiation Laboratory, California Institute of Technology, Pasadena, California*, [5]*Los Alamos National Laboratory, Los Alamos, New Mexico*, [6]*Louisiana Tech University, Ruston, Louisiana*, [7]*University of Manitoba, Winnipeg, Manitoba, Canada*, [8]*Massachusetts Institute of Technology, Cambridge, Massachusetts*, [9]*TJNAF, Newport News, VA*, [10]*Virginia Polytechnic Institute, Blacksburg, Virginia*, [11]*TRIUMF, Vancouver, Canada*, [12]*University of New Hampshire*, [13]*Yerevan Physics Institute*, [14]*Mississippi State University*, [15]*University of Northern British Columbia*, [17]*Ohio University*, [18]*Hampton University*

Contents

1 Introduction

The Q^p_{Weak} experiment (E02-020) was approved at the 21st meeting of the Jefferson Laboratory Program Advisory Committee in January, 2002 and assigned an "A" scientific rating. This new experiment will provide the first precision measurement of the proton's weak charge $Q^p_{Weak}= 1 - 4\sin^2\theta_W$ by measuring the parity-violating asymmetry in electron-proton elastic scattering at very small momentum transfer. This in turn will constitute a precision measurement of the weak mixing angle $\sin^2\theta_W$ (to $\pm 0.3\%$) at low energy, which is uniquely sensitive to new physics beyond the Standard Model. The measurements will be performed at a scattering angle of 9° and a beam energy of 1 GeV, yielding $Q^2 = 0.03\ \ (GeV/c)^2$. A detailed description of the Q^p_{Weak} experiment can be found in the proposal "The Q^p_{Weak} Experiment: A Search for New Physics at the TeV Scale via a Measurement of the Proton's Weak Charge". The proposal is available at the home page of the Q^p_{Weak} Collaboration: http://www.jlab.org/Qweak/.

The Q^p_{Weak} experiment has great discovery potential and has become a major new thrust of the scientific program at Jefferson Lab. It is should be noted that the new NSAC Long Range Plan has identified the search for physics beyond the Standard Model as one of the five primary scientific goals for nuclear science during the coming decade. Like the parity violating deep inelastic scattering experiment performed at SLAC in the 1970's which had such a major impact on nuclear and particle physics, the Q^p_{Weak} measurement described here could become Jefferson Laboratory's signature contribution to the quest for physics beyond the Standard Model.

An aggressive schedule has been adopted for funding and construction with the aim of installing the experiment in Hall C at JLab in 2006. Cost and schedule estimates for the project have been made by the collaboration and have been steadily refined during the past year by technical working groups and endorsed at collaboration meetings. The cost of the project will be shared between the DOE, NSF, JLab, NSERC (Canada), and University matching contributions. The detailed management structure, cost and schedule are discussed in a separate Project Management document.

1.1 Physics Motivation

Precision tests have traditionally played a crucial role in elucidating the structure of the electroweak interaction. Measurements to date have provided an impressive array of constraints on the Standard Model as well as on proposed scenarios for extending it. Measurements at the Z^0 pole have constrained $\sin^2\theta_W$ to high precision at that energy scale. However, a precision experimental study of the evolution of the weak mixing angle to lower energies has not yet successfully been carried out. Similar tests have been crucial in establishing QCD as the correct theory of the strong interaction, and the renormalization group evolution (RGE) of the QED coupling has also been demonstrated experimentally.

The Standard Model evolution predicts a shift of $\Delta\sin^2\theta_W = +0.007$ at low Q^2 with respect to the Z^0 pole best fit value of 0.23113 ± 0.00015. (Figure 1). Testing this prediction requires

a set of precision measurements at a variety of energy scales with sufficiently small and well understood theoretical uncertainties that one can interpret the results with confidence. The expected evolution of $\sin^2\theta_W$ corresponds to a 10 standard deviation effect in our proposed measurement, including both experimental and theoretical systematic errors. Any significant deviation of $\sin^2\theta_W$ from the Standard Model prediction at low Q^2 would be a signal of new physics, whereas agreement would place new and significant constraints on possible Standard Model extensions.

Small but perceptible deviations of a handful of low energy observables from their Standard Model predicted values are already beginning to provide new clues about the nature of physics that lies beyond. Hints of a deviation from the Standard Model evolution of $\sin^2\theta_W$ may have been seen in atomic parity violation experiments which determine the weak charges of heavy nuclei, but a significant uncertainty in the theoretical interpretation severely limits the impact of the atomic physics results. In contrast, a precision measurement of the weak charge of the proton, $Q^p_{Weak} = 1 - 4\sin^2\theta_W$, addresses the same physics issues but is free of many-body theoretical uncertainties. The dominant hadronic effects that must be accounted for in extracting Q^p_{Weak} from the data are contained in form factor contributions which can be sufficiently constrained by the current program of parity violating electron scattering measurements without reliance on theoretical nucleon structure calculations.

In the absence of physics beyond the Standard Model, our experiment will provide a $\pm$ 0.3% measurement of $\sin^2\theta_W$, making this a very competitive stand alone measurement of the weak mixing angle. The complementarity between high energy studies at the Z^0 pole in e^+e^- collisions and precision low energy tests is essential: Q^p_{Weak} will be a key element of a program of very sensitive low energy tests of the Standard Model that is complementary to other efforts underway or planned world wide. One such effort is the SLAC experiment E158 which is carrying out parity violating asymmetry measurements in the purely leptonic sector at similar Q^2, but is currently not expected to reach a similar precision in $\sin^2\theta_W$.

The Q^p_{Weak} experiment builds on the world-leading parity violation program at Jefferson Lab. The current parity-violation experiments (SAMPLE, HAPPEX, HAPPEX II, HAPPEX ^{4}He, PVA4, and G^0) will provide high quality data on form factors that will be used to determine the contributions of hadronic structure to the proposed measurement. Unlike the other elements of this program, the Q^p_{Weak} experiment will constitute the first precision Standard Model test to be carried out at Jefferson Lab. Technical developments that are required for this experiment to proceed are relatively straightforward extensions of what has already been achieved with Jefferson Lab's world-leading polarized electron source or planned for future elements of the laboratory's parity program. The instrumentation design for the experiment is relatively simple, and we are confident that the stated precision goals can be met.

1.2 Theoretical Interpretability

An important consideration for the interpretability of the Q^p_{Weak} measurement is the degree to which hadronic contributions are under sufficient theoretical control. While in general one might

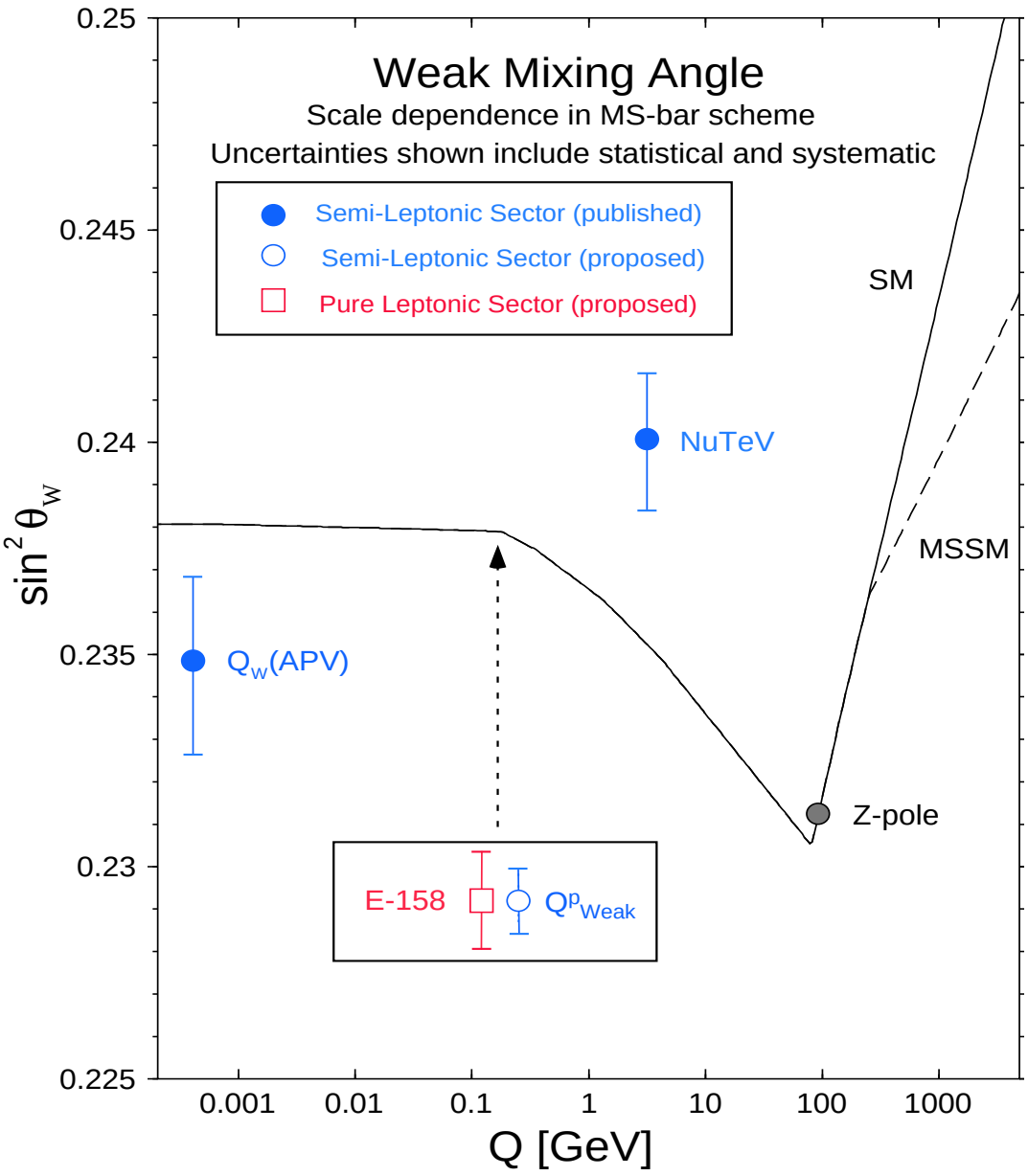

Figure 1: *Calculated running of the weak mixing angle in the Standard Model, defined in the modified minimal subtraction scheme (the dashed line indicates the reduced slope typical for the Minimal SuperSymmetric Standard Model). The solid error bars show the current situation, while the open symbols (with arbitrarily chosen vertical location) refer to the asymmetry measurements proposed here and for SLAC E-158. The previous measurements are determinations from atomic parity violation (APV), deep inelastic neutrino-nucleus scattering (NuTeV), and from Z^0 pole asymmetries (LEP+SLC).*

worry about incalculable, non-perturbative QCD effects for a hadronic target – especially in the case of an ultra-precise measurement - several factors conspire to minimize the hadronic uncertainties for Q^p_{Weak}. In order to understand these factors, it is useful to delineate two types of hadronic effects: those which depend on Q^2, and those which are Q^2 independent.

The Q^2-dependent effects include contributions from the Q^2 dependence of various nucleon electroweak form factors, such as the strange-quark form factors, as well as the 2 γ-exchange box graphs entering the QED radiative corrections. After dividing out the leading Q^2-dependence of the PV asymmetry, these residual Q^2-dependent effects vanish at $Q^2 = 0$. The present and future program of PV measurements at Jefferson Lab, MIT-Bates, and Mainz are designed to measure these contributions at somewhat larger values of Q^2 than will be employed for Q^p_{Weak} ($Q^2 = 0.03\mathrm{GeV}^2$). The extrapolation from these higher values of Q^2 to 0.03 GeV^2 will introduce some uncertainty into the extraction of Q^p_{Weak} from the measured asymmetry. This extrapolation can be carried out using chiral perturbation theory. The existing and future PV measurements, as well as the world data set for electromagnetic form factors, will constrain all of the relevant low-energy constants. An initial estimate of the uncertainty in Q^p_{Weak} due to these Q^2-dependent effects, performed using a simple linear regression, is about 2%. We anticipate further refinement of this uncertainty estimate using chiral perturbation theory once the existing program of PV measurements (SAMPLE, HAPPEX, G0, PVA4) is completed. No other theoretical nucleon structure computations will be needed in this case.

The second source of hadronic effects enter Q^p_{Weak} directly and do not vanish at $Q^2 = 0$. They include hadronic loops in the running of $\sin^2\theta_W$ and strong interaction corrections to the WW, ZZ, and $Z\gamma$ box graphs. Current conservation suppresses all other potential sources of hadronic effects, including isospin mixing in the proton wavefunction. A detailed analysis of these Q^2-independent effects are given in Ref. [1]. The QCD corrections to the WW and ZZ box graphs are perturbative and have been computed in that work through $\mathcal{O}(\alpha_s)$. Higher order corrections $[\mathcal{O}(\alpha_s^2)]$ contribute well below the one percent level. The leading, non-perturbative effects in the $Z\gamma$ box diagrams are suppressed by a $1 - 4\sin^2\theta_W$ prefactor. The associated uncertainty has also been estimated in Ref. [1] to be on the order of 0.7% , though this estimate could conservatively be inflated by a factor of five and still fall below the anticipated experimental error in Q^p_W. Finally, the hadronic loop contributions to the running of $\sin^2\theta_W$ are constrained by e^+e^- data and the running of α. The uncertainty associated with this effect is below one percent. In short, for the level of precision anticipated in the Q^p_{Weak} measurement, theoretical strong interaction uncertainties do not pose a barrier to interpretability.

1.3 Overview of the Experiment

The Q^p_{Weak}collaboration will carry out the first precision measurement of the proton's weak charge, $Q_{wp} = 1 - 4\ \sin^2(\theta_W)$. We will do this by measuring the parity violating asymmetry in elastic electron-proton scattering at very low momentum transfer, given by:

$$A = (\sigma_+ - \sigma_-)/(\sigma_+ + \sigma_-) = Q^2\ Q_{wp} + Q^4\ B(Q^2)$$

where σ_+ and σ_- are cross sections for positive and negative helicity incident electrons, and $B(Q^2)$ is a hadronic form factor contribution. The results of earlier experiments in parity violating electron-proton scattering will be used to constrain hadronic corrections to the data. A 2200 hour measurement of the parity violating asymmetry in elastic electron-proton scattering at a momentum transfer of $Q^2 = 0.03$ (GeV/c)^2 employing 180 μA of 80% polarized beam on a 35 cm liquid hydrogen target will determine the proton's weak charge with 4% combined statistical and systematic errors; this in turn implies a determination of $\sin^2(\theta_W)$ at the $\pm$0.3% level at low energy. As a standalone measurement of $\sin^2(\theta_W)$, the Q_{weak} experiment is competitive with any channel measured in the recently completed SLD and LEP programs at the Z resonance.

A sketch showing the layout of the experiment is given in Figure 2. A longitudinally polarized electron beam, a liquid hydrogen target, a room temperature toroidal magnetic spectrometer, and a set of detectors for the scattered electrons at forward angles are the key elements of the experimental apparatus. The toroidal magnetic field will focus elastically scattered electrons onto a set of 8, rectangular fused silica (synthetic quartz) detectors coupled to photomultiplier tubes, which will be read out in current mode to achieve the high statistical precision required for the measurements. Inelastically scattered electrons are bent out of the detector acceptance by the spectrometer and hence do not contribute to the signal. A new high power cryotarget will be developed and built at Jefferson lab for these measurements.

Basic parameters of the experiment are summarized in Table 1. The main technical challenges result from the small expected asymmetry of approximately -0.3 ppm, and we will measure this asymmetry to $\pm$1.9% statistical and $\pm$1.7% systematic errors. The optimum kinematics corresponds to an incident beam energy of $E_0 = 1.165$ GeV, scattered electron polar angles $\theta_e = 9.0 \pm 2.0$ degrees, and azimuthal detector acceptance as large as possible (8 electron detectors with acceptance $\Delta\phi_e = \pm 15$ degrees each, totalling $\frac{2}{3}$ of 2π).

Fixing $Q^2 = 0.03$ (GeV/c)^2 limits nucleon structure contributions which increase with Q^2 and avoids very small asymmetries where corrections from helicity correlated beam parameters begin to dominant the measurement uncertainty. The fixed Q^2 acceptance needs to be limited to $\pm$50% of the $Q^2_{central}$ to control the error associated with the determination of the average Q^2. With these constraints applied the figure-of-merit becomes relatively insensitive to the primary beam energy, as seen in Figure 3. Using a higher beam energy will result in a physically longer experiment with stronger magnetic field requirements, smaller scattering angles, and the possibility of opening new secondary production channels that might contribute to backgrounds.

The high statistical precision required implies high beam current (180 μA), a long liquid hydrogen target (35 cm) and a large-acceptance detector operated in current mode. We assume that

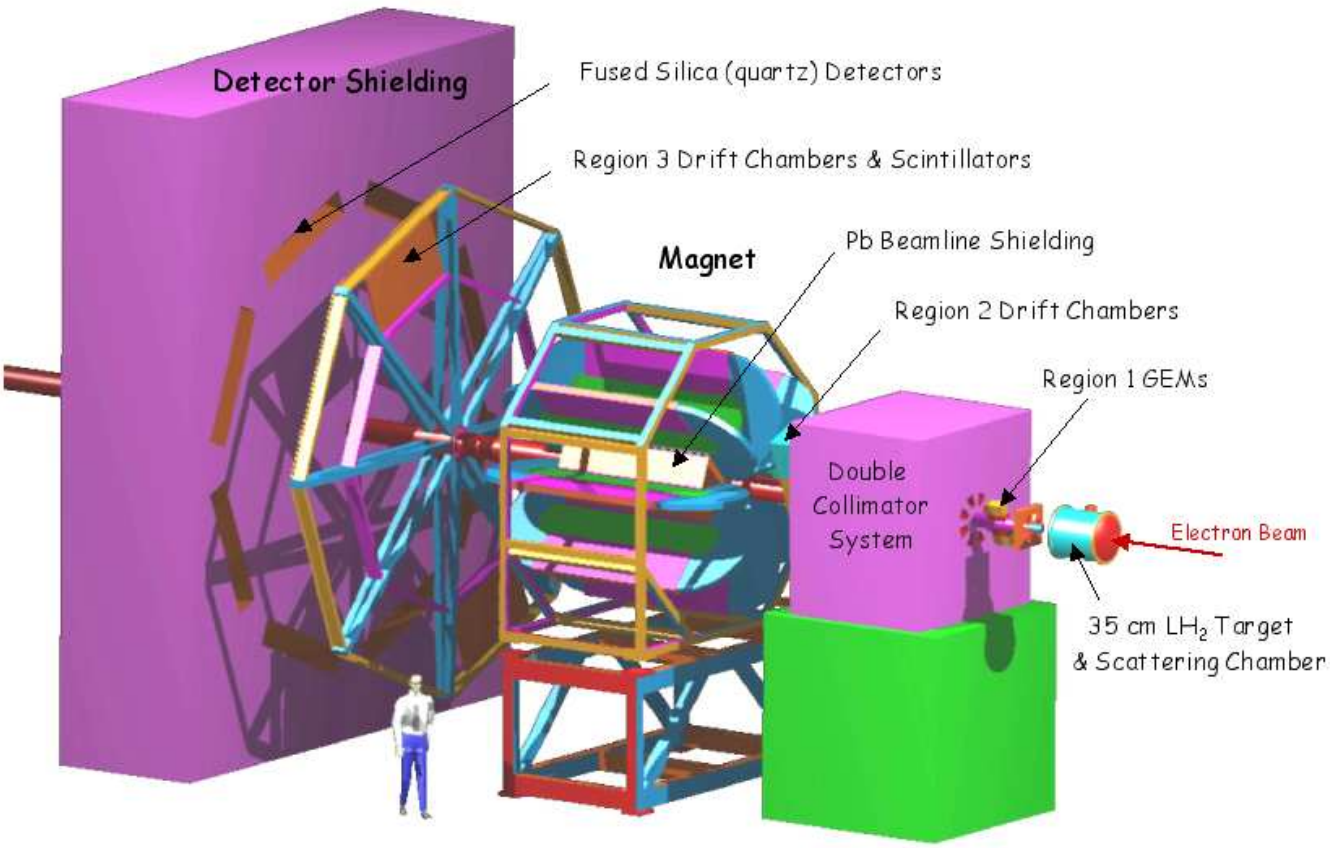

Figure 2: *CAD layout of the Q^p_{Weak} apparatus. The beam travels from right to left in this picture, through the target, the Region 1 GEM detectors, the first precision collimator, the mini-torus (not visible), the second precision collimator, the region 2 drift chambers, the toroidal magnet (shown cut-away on its stand), the region 3 drift chambers (shown supported in a ferris wheel structure), the trigger scintillator and finally through the re-entrant shielding (dark purple) in which the detectors are housed.*

Table 1: *Basic parameters of the Q^p_{weak} experiment.*

Parameter	Value
Incident Beam Energy	1.165 GeV
Beam Polarization	80%
Beam Current	180 μA
Target Thickness	35 cm ($0.04X_0$)
Running Time	2200 hours
Nominal Scattering Angle	9°
Scattering Angle Acceptance	$\pm 2°$
ϕ Acceptance	66.7% of 2π
Solid Angle	$\Delta\Omega$ = 45.7 msr
Acceptance Averaged Q^2	$< Q^2 >= 0.03\ (GeV/c)^2$
Acceptance Averaged Physics Asymmetry	$< A >$ = -0.28 ppm
Acceptance Averaged Expt'l Asymmetry	$< A >$ = -0.23 ppm
Integrated Cross Section	3.7 μb
Integrated Rate (all sectors)	6.1 GHz (or .76 GHz per sector)
Statistical Error on the Asymmetry	2.0%
Statistical Error on Q^p_W	2.8%

the source group will meet their stated goal of routine beam delivery at polarizations exceeding 80% by the time Q^p_{Weak} is ready to take data.

Radiation hardness, insensitivity to backgrounds, uniformity of response, and low intrinsic noise are criteria that are optimized by the choice of quartz bars for the main detectors. The combined beam current and target length requirements lead to a beam power of 2.1 kW, considerably over the present 1.2 kW capacity of the JLab End Station Refrigerator (ESR). This will require us to draw additional refrigeration capacity from the central helium liquefier (CHL) and CEBAF "standby" refrigerator, providing a cost effective solution for the required target cooling power. We note that the combination of high beam current and a long target flask will make the Q^p_{Weak}target the highest power cryotarget in the world by a factor of several; although the experiment could be run with a lower power cryotarget, the length of the run would have to be increased correspondingly.

It is essential to maximize the fraction of the detector signal (total light output in current mode) arising from the electrons of interest, and to calibrate both the dilution factor due to background and the detector-signal-weighted $< Q^2 >$ in order to be able to extract a precise value for $\sin^2(\theta_W)$ from the measured asymmetry. Q^2 definition will be optimized by ensuring that the first collimator will be the sole limiting aperture for elastically scattered events. Careful construction and precise surveying of the collimator geometry together with optics and GEANT Monte Carlo studies will be essential to understand the Q^2 acceptance of the system. This information will be extracted from ancillary measurements at low beam current, in which

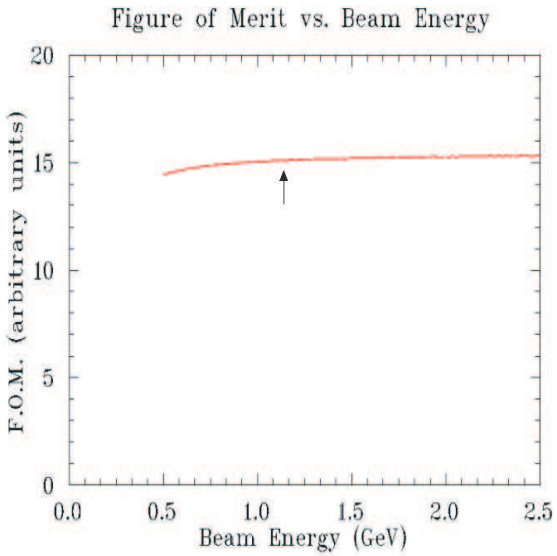

Figure 3: *Kinematics Optimization for* Q^p_{Weak}.

the quartz detectors are read out in pulse mode and individual particles are tracked through the spectrometer system using a set of wire chambers. The detector front end electronics are designed to operate in both current mode and pulse mode for compatibility with both the parity measurements and the ancillary $< Q^2 >$ calibration runs. The tracking system will be capable of mapping the $< Q^2 >$ acceptance to $\pm 1\%$ in two opposing octants simultaneously; the tracking chambers will be mounted on a rotating wheel assembly so that the entire system can be mapped in 4 sequential measurements. A small "mini-toroid" magnet will be installed downstream of the first collimator to sweep low energy Møller electrons out of the acceptance of the middle tracking chambers this will not significantly affect the optics for the elastic electrons of interest in the Q^p_{Weak} measurements). The front chambers are based on the CERN 'GEM' design, chosen for their fast time response and good position resolution. The chambers plus trigger scintillator system will be retracted during normal Q^p_{Weak} data taking at high current.

The experimental asymmetry must be corrected for inelastic and room background contributions as well as hadronic form factor effects. Initial simulations indicate that the former will be small, the main contribution coming from target walls, which can be measured and subtracted. The quadrature sum of the hadronic form factor errors is expected to be 2%, as noted earlier. Experimental systematic errors are minimized by construction of a symmetric apparatus, optimization of the target design and shielding, utilization of feedback loops in the electron source to null out helicity correlated beam excursions, careful attention to beam polarimetry, and by carrying out ancillary measurements to determine the system response to helicity correlated beam properties and background terms. The electron beam polarization must be measured with an absolute uncertainty in the 1-2% range; at present this can be achieved in Hall C using an existing Møller polarimeter, which can only be operated at currents below 8 μA. A major effort to

design and build a Compton polarimeter in Hall C at Jefferson Lab is underway as part of the laboratory's support of this and other experiments where precise beam polarimetry is an issue; the Compton polarimeter will provide a continuous on-line measurement of the beam polarization at full current (180 μA) which would otherwise not be achievable. Table 2 summarizes the statistical and systematic error contributions to the proton weak charge measurement that are anticipated for the experiment.

Table 2: *Anticipated Statistical and Systematic Errors on Q_{wp}. Run I assumes 12 days of production data and 11 days of systematic studies. Run II shows the cumulative error after completing both runs. The final experimental error of* $\pm$ 4% *translates to a* $\pm$0.3 % *uncertainty in* $sin^2(\theta_W)$.

Error Contribution	Run I (23 days) $\Delta Q_{wp}/Q_{wp}$	Run II (93 days) $\Delta Q_{wp}/Q_{wp}$
Total Statistical	8%	2.8 %
Systematic		
Helicity-correlated beam properties	0.6%	0.6 %
Inelastic contamination	0.6%	0.2%
Hadronic corrections	2.0%	2.0%
Average Q^2 determination	1.0%	1.0%
Beam polarization	1.4%	1.4%
Target window background	<2.0%	<1.0%
Total Systematic	3.4%	2.9%
Total	8.7%	4.0%

The Q^p_{Weak} apparatus includes a luminosity monitor consisting of an array of Čerenkov detectors located downstream of the Q^p_{Weak} experiment at a very small scattering angle. The detectors will be instrumented with radiation-hardened vacuum photodiodes with external current-to-voltage converters. The high rate (28 GHz/octant integrating mode) and the resulting small statistical error in the luminosity monitor signals will enable us to use this device for removing our sensitivity to target density fluctuations. In addition, the luminosity monitor will provide a valuable null asymmetry test, since it is expected to have a negligible physics asymmetry as compared to the main detector.

1.4 Conclusion

We have outlined a competitive measurement of Q^p_{Weak} with combined statistical and systematic errors of approximately 4% as given in Table 2. To put our experiment in perspective, the Q^p_{Weak} physics asymmetry is slightly smaller than the already approved JLab neutron radius measurement E00-003 (.3 ppm versus .5 ppm) with a slightly smaller statistical error (2% versus 3%). For more details on the experimental errors and their control refer to the Q^p_{Weak} physics proposal

and sections of this document pertaining to helicity correlated uncertainties and experimental backgrounds.

References

[1] J. Erler, A. Kurylov, and M.J. Ramsey-Musolf, Caltech preprint MAP-287 (2003).

2 The Magnetic Spectrometer

A key component of the Q^p_{Weak} apparatus is a magnetic spectrometer 'QTOR', whose toroidal field will focus elastically scattered electrons onto a set of eight rectangular quartz Čerenkov detectors. The main requirement for the spectrometer is to provide a clean separation between elastic and inelastic electrons so that a detector system of reasonable size can be mounted at the focal plane to measure the elastic asymmetry with negligible contamination from inelastic scattering and other background processes. The axially symmetric acceptance in this geometry is very important because it reduces the sensitivity to a number of systematic error contributions. A resistive toroidal spectrometer magnet is the preferred choice for Q^p_{Weak} because of the low cost and inherent reliability relative to a superconducting solution.

2.1 Basic Design Criteria

The QTOR magnet is required to bend the elastically scattered electrons at $\theta_e = 9.0°$ with momentum $p' \simeq 1.15$ GeV/c by approximately 10°. This implies a magnetic field integral $\int \vec{B}.d\vec{\ell}$ of approximately 0.67 T·m.[1] The focussing properties must provide clean separation of the elastic and inelastic channels, corresponding to a momentum resolution of about 10%. While the primary goal of the experiment is a measurement of the parity violating asymmetry in the elastic channel, it is desirable to be able to use the same apparatus to measure the asymmetry in the inelastic channel as well as the hall background, in order to limit their contribution to the systematic error.[2] The magnetic field also provides background reduction. The QTOR magnet design provides a field free region along the beam axis. It has an open geometry to allow for maximum detector solid angle and the magnet must be symmetric for systematic error reduction. The shortest distance between the coils and the outer edge of the beam pipe is set by the shielding requirements accounting for expansion of the beam in the 35 cm liquid hydrogen target. The magnet will use normal-conducting, water cooled copper coils to decrease the cost as compared to a superconducting design.

2.2 Geometry and Magnetic Properties

The coil geometry has been optimized in a series of simulation studies using GEANT plus numerical integration over the conductor's current distributions to determine the magnetic field. Several geometries were explored, including the use of circular coils, simple racetrack coils, tilted racetrack coils, and the BLAST modified racetrack coil shape. The simplest and least expensive

[1] This requirement is about one half the value for the G0 superconducting magnet (1.6 T·m) and is comparable to the maximum field integral for the BLAST design, which is 0.6 T·m.

[2] A measurement of the inelastic asymmetry, which is expected to be of order 10× larger than the elastic asymmetry but to contribute an upper limit of only 10^{-4} of the elastic signal, can be made in an ancillary experiment by reducing the magnetic field in QTOR to direct the inelastic electrons onto the quartz Čerenkov bars.

QTOR coil design that meets the needs of the Q^p_{Weak} experiment is a simple racetrack structure with a layout shown in Figure 4. Each coil package consists of a double pancake structure, with each layer consisting of two, 220 cm long straight sections, and two semicircular curved sections with inner radius 25 cm and outer radius 75 cm. The total DC current will be 6230 A at 160 V, implying a 1 MW power and cooling requirement. The shortest distance between a coil and the beamline will be 15 cm.

Figure 4: *Layout of the 8 magnetic field coils of the QTOR spectrometer. Design courtesy of MIT-Bates engineer S. Sobczynski.*

2.3 Field Calculations and Magnet Optics

The magnetic field was calculated using the Biot-Savart Law and performing numerical integration over the distribution of conductor current density. Each field coil was represented by a set of arcs and straight conductor segments. The field calculations were carried out assuming a nominal current density of 560 A/cm^2. Since the magnetic field scales in proportion to the current density, the calculated field map can be rescaled to any desired value.

A plot of the azimuthal magnetic field components B_ϕ is shown in Figure 5 as a 3d function of position along the beam axis (Z) and the radial distance (R) from the beam axis. The magnetic field on the beam axis is zero, and increases rapidly with distance from the beam axis, reaching a maximum at R=56 cm. From that point, the field falls off as $1/R$. For a target located upstream of the magnet, the field integral experienced by the scattered electrons depends on the scattering angle. Electrons with smaller polar angles θ_e will experience larger field integrals and will be deflected more strongly than electrons scattered at larger polar angles, which results in a focussing effect for the scattered electrons. In Figure 5, we also plot B_ϕ as a function of R and ϕ at the center of the magnet, which is defined as $Z = 0$ cm. The field profile in this plane indicates that there is an acceptably small variation in the toroidal field strength as a function of the azimuthal angle of the scattered electrons.

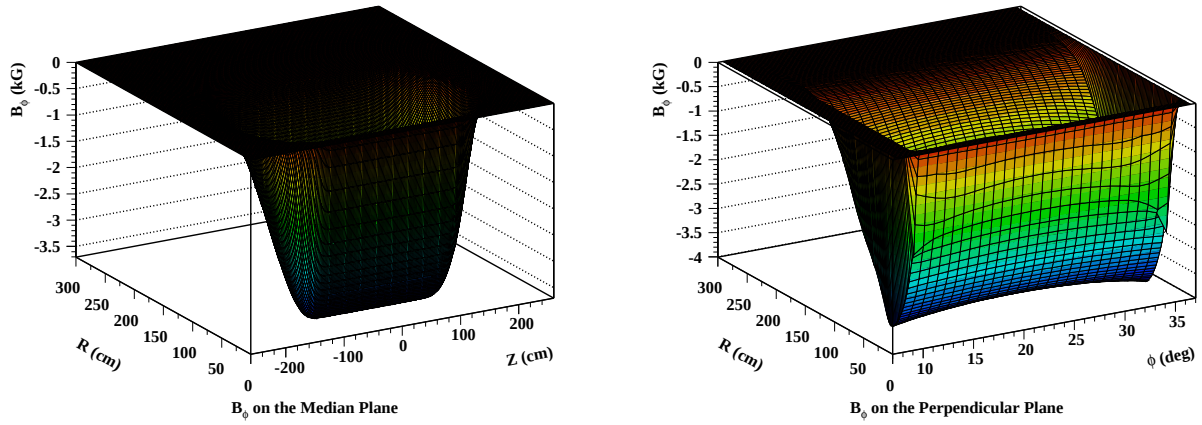

Figure 5: *Left: Three dimensional plot of the toroidal magnetic field component B_ϕ in the median plane between a pair of coils, as a function of position along the beam axis (Z) and the radial distance from the beam axis (R) . Right: A similar plot of B_ϕ as a function of ϕ and R in the midplane of the magnet, perpendicular to the beam axis at $Z = 0$ (magnet center).*

For an ideal toroid, the z component of the field is zero, while for a real toroidal magnet this component should be negligibly small compared to the B_ϕ component. The calculated B_z component for the QTOR design is shown in Figure 6 in the median plane between a pair of coils. As seen from this figure, the maximum strength of B_z is 1.5% of that of the main toroidal field B_ϕ; again, the small field imperfections are acceptably small for the purposes of the Q^p_{Weak} measurements.

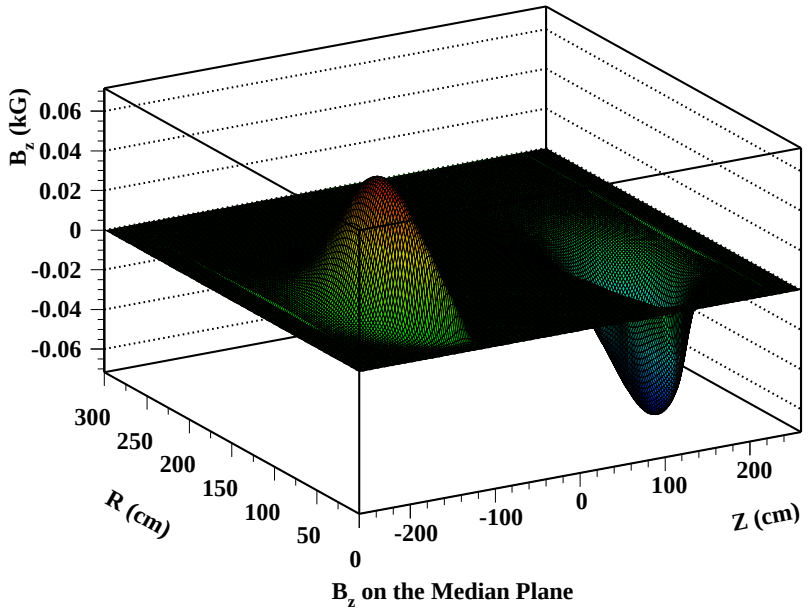

Figure 6: *Three dimensional plot of the z component of B on the median plane between two coils as a function of position along the beam axis Z and radial distance from the beam axis R. The maximum strength of this minor field component is about 1.5% of the main toroidal field* B_ϕ.

The kinematics of the Q^p_{Weak} experiment have been chosen to optimize the figure of merit for the extraction of Q_{wp} from the elastic asymmetry. This being done, the focussing properties of the magnet for the electrons of interest depend on the choice of target length and position. The target length has been fixed at 35 cm to achieve the highest practical luminosity, and the target assembly will be located outside and upstream of the magnet to allow for the detection of scattered electrons at angles from 7 to 11 degrees. By examining the scattered electron trajectories for various target locations, the optimum position of the target was found to be 650 cm upstream of the midpoint of the QTOR magnet.

The optical properties of the magnetic field were first verified by simulating the electron trajectories using GEANT, with initial scattering angles restricted to $\theta_e = 9.0 \pm 2.0$ degrees and azimuthal angles in the range $\Delta\phi_e = \pm\ 15.0$ degrees for both elastic scattering and pion production reactions ($ep \rightarrow en\pi^+$ and $ep \rightarrow ep\pi^0$). Figure 7 shows the distribution of elastic and inelastic electrons at the optimum detector location for each octant, which is 580 cm downstream from the center of the magnet, where a $220 \times 12 \times 2.5$ cm^3 quartz Čerenkov bar clearly intercepts the elastic scattering distribution with no contamination of inelastics. It is clear that for elastic scattering, the QTOR magnet has the required focussing property, which is essential for performing the Q^p_{Weak} measurements. This distribution was generated in the simplest possible configuration, with multiple scattering, radiative losses, collimator scattering and other background processes not included.

A more realistic simulation requires the kinematics of the experiment as defined by the collimators, as well as accounting for multiple scattering and all secondary reactions. Figure 8 shows

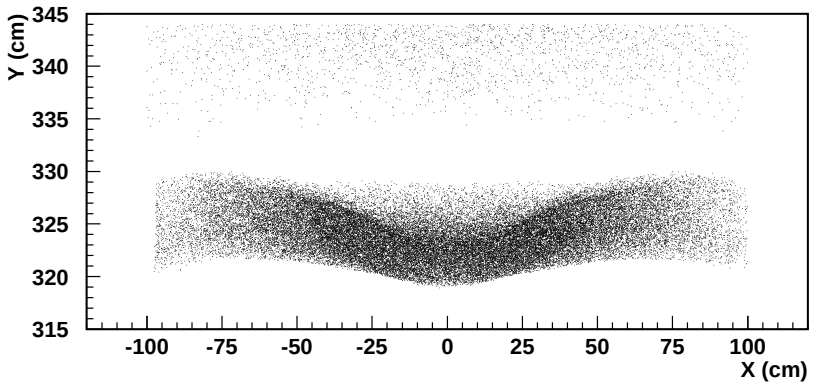

Figure 7: *Separation of elastically (lower distribution) and inelastically (upper distribution) scattered electrons at the detector location, 580 cm downstream of the magnet center. The kinematics sre restricted to* $\theta_e = 9.0 \pm 2.0$ *deg, and* $\phi_e = 0.0 \pm 15.0$ *deg.*

the results of a full GEANT simulation for elastically scattered electrons whose kinematics are selected by a conical input collimator. The secondary reactions consist mostly of bremsstrahlung radiation produced by electrons which strike the collimator walls. These events are well separated from the elastic electrons at the position of the focal plane, since the photons are not deflected in the magnetic field. The figure also shows a narrow band of elastic electrons sitting above the broad electromagnetic shower distribution. The projection of the collimator shape, which is clearly visible in the lower part of the figure, results from most of the showering occurring on the collimator walls. While the detailed collimator design has not yet been optimized, this simple initial choice is sufficient to demonstrate the general features of collimator showering effects; the contamination of the Čerenkov signal is already in this case acceptably small. The minimum design distance of 15 cm between the beam pipe and the inner coil windings is sufficient to accommodate the necessary beam pipe shielding taking into consideration the beam broadening that occurs in the 35 cm liquid hydrogen target.

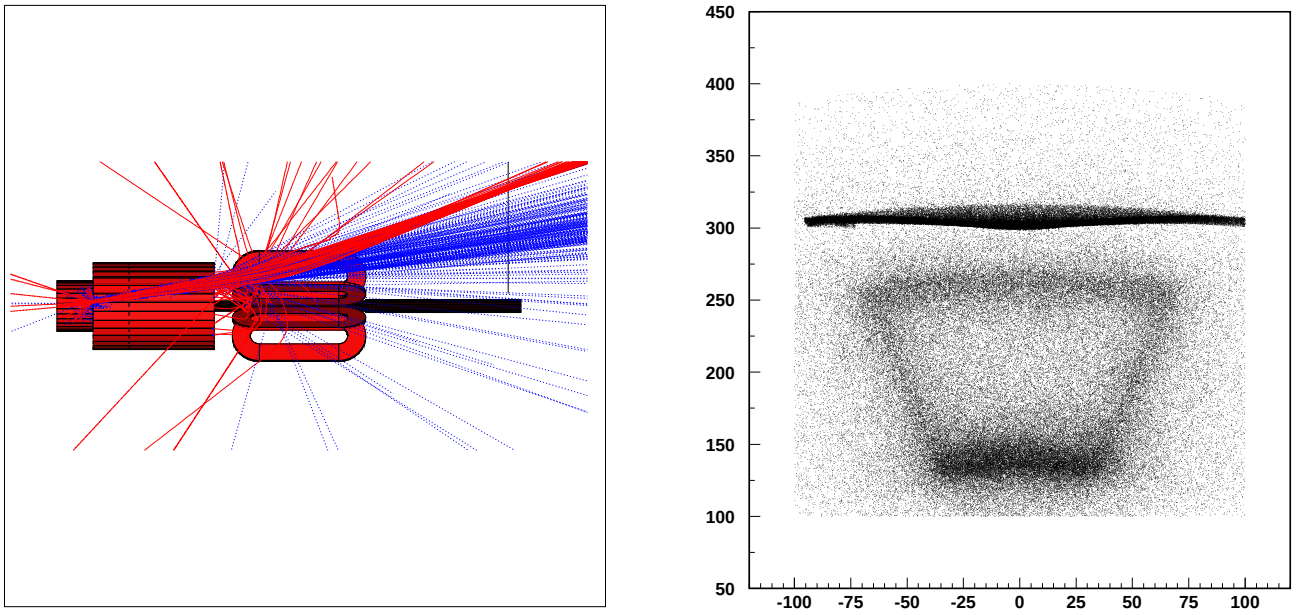

Figure 8: *Left panel: Side view of the experimental setup, consisting of a 35 cm liquid hydrogen target, conical collimator, QTOR spectrometer, and a focal plane detector. Electron kinematics are defined by the collimator, and all secondary reactions are included. The electron trajectories (red) are distinguished from photon trajectories (blue). Right panel: Separation of elastically scattered electrons (narrow dark band near y=300 cm) and electromagnetic shower events shadowing the collimator walls, projected onto the focal plane at 580 cm downstream of the QTOR magnet center. The 2 m long quartz Čerenkov bars will be placed to intercept the elastically scattered electrons shown in the figure.*

2.4 Detailed Coil Design

The Q^p_{Weak} collaboration has benefited greatly from experience acquired in design and construction of the BLAST toroidal spectrometer at MIT-Bates. The field integral requirements and basic geometry for QTOR are comparable, but fabrication and alignment tolerances are less stringent than for the BLAST design, which involved a modified racetrack coil shape to accommodate polarized internal targets in the Bates South Hall Ring. A simpler coil shape has been adopted for QTOR, but the methods of design, fabrication, water cooling and controls for the BLAST magnet, as well as the support structure and power supply requirements, are very easily adapted to meet the needs of the Q^p_{Weak} experiment. MIT-Bates engineers have adapted elements of the BLAST design to meet the specifications of QTOR, and their expertise has been invaluable in preparing a reliable preliminary technical design and cost estimate in an efficient and timely manner to meet the aggressive experiment schedule for Q^p_{Weak}.

The shape adopted for the QTOR coil design is shown in Figure 9. This is the simplest and least expensive coil design, and can be built with a very simple winding fixture. The coil consists of two, 220 cm long straight sections, and two semicircular curved sections with inner radius 25 cm and outer radius 75 cm. The total length of the coil is 370 cm. The coils will be built using the same procedure as the BLAST magnet coils, consisting of a two-layer pancake structure, each having 13 turns of OFHC copper (CDA 102) conductor material with square outer dimensions of 1.5×1.5 in^2 (3.81×3.81 cm^2) and an inner water cooling pipe diameter of 0.8 in (2.03 cm), as specified in Figure 10. Coil sections will be epoxy vacuum cast in a permanent mold. Reference points to locate the individual coils within the epoxy casing will be incorporated in the design and used in surveying and alignment of the coils when they are mounted on the frame, discussed further below. A total of nine coils will be ordered in order to have one spare available in case of failure.[3] Glass reinforced plastic (G10) sheets will be used on the sides of the coils for additional stiffness and thermal insulation. Taking into account the required fiberglass and epoxy insulating layers, the final cross-sectional dimension of the coil will be 9.1×54.0 cm^2. We will assemble eight such coils into a toroidal magnet configuration, which will be radially located and spaced at angles of $\pm$ 22.5°. The shortest distance between a coil and the beamline will be 15 cm.

As discussed below, there is a great advantage to incorporating individual trim coil windings as part of the magnetic coil package. Following the example of BLAST, each coil of the QTOR magnet will be constructed with an additional trim coil winding capable of making a 1% correction to the main magnetic field. While the geometrical requirements for the magnet, support structure, field mapping and alignment procedures are designed to meet the Q^p_{Weak} tolerances without requiring trim coil adjustments, the incorporation of this feature adds a highly desirable safety margin at negligible additional cost.

[3] One spare coil was also ordered for the BLAST magnet.

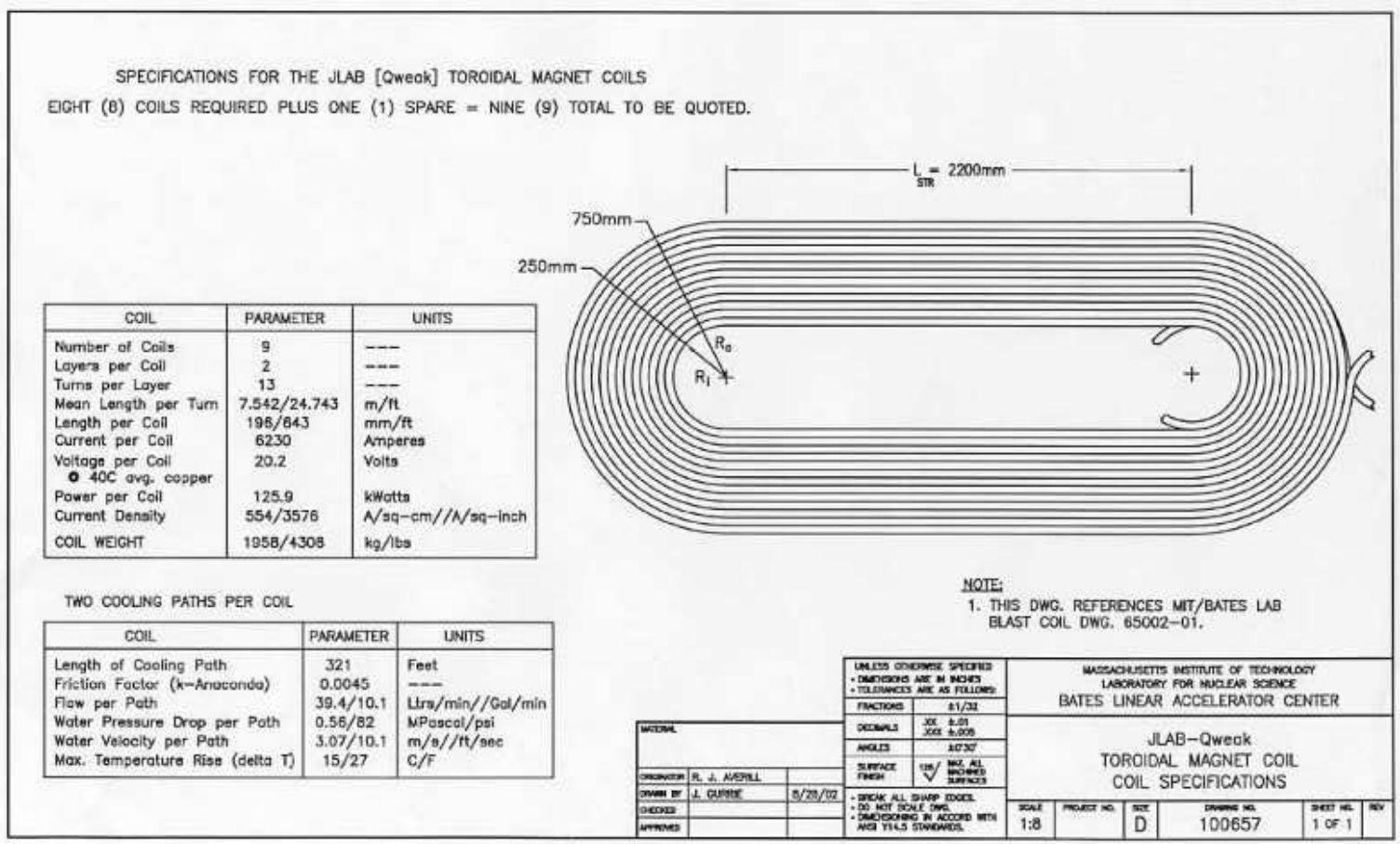

Figure 9: Q_{weak} *toroidal spectrometer coil specifications.*

Figure 10: *Conductor specifications for the Q_{weak} toroidal magnetic spectrometer.*

2.5 Fabrication and Alignment Tolerances

While the design of the spectrometer is essentially complete, some simulation work remains to be done to establish the final geometrical tolerances for coil fabrication and alignment. It is already established that the Q^p_{Weak} tolerances will be significantly less stringent than for the very similar BLAST spectrometer at MIT-Bates, which our technical design is largely based on. A GEANT Monte Carlo simulation is being used to study the effects of coil misalignments on the $< Q^2 >$ distribution at the focal plane as well as on the symmetry of the 8-octant system as required for systematic error reduction (see section on helicity correlated systematic errors). The most stringent requirement is for symmetry of the 8 octants to minimize sensitivity to helicity correlated beam motion; imperfections that affect all 8 coils in the same manner are much less of a concern for Q^p_{Weak}.

The sensitivity to an overall position offset of the magnet with respect to the symmetry axis of the collimator and beamline has been explored using GEANT. The effect of this type of misalignment is to shift the image of the elastically scattered events across the width of a Čerenkov bar. Figure 11 shows the effect of offsetting the magnet from the symmetry axis of the collimator and beamline. The plots show the profile of the scattered beam image across the width of a Čerenkov detector. The simulations which generated these plots are discussed in detail later in the Technical Design Report.

The effect of a global misalignment of the magnet can be largely compensated for by adjusting the currents in individual trim coils, which will be incorporated in the magnet design; in the simulations, a 1 cm global magnet offset, which is unrealistically large, required a 1.5% correction via the trim coils to bring the elastically scattered electron image back to the optimum position on the Čerenkov detector bars.

At smaller displacements of the magnet, effects are still seen when combined with position modulation of the beam on helicity flip. Tails of the distribution of electrons across the narrow dimension of the Čerenkov bars are cut by different amounts as the beam moves, resulting in a false parity asymmetry and a displacement of the position neutral axis of the apparatus. A 1 cm displacement of the magnet, for example, results in a shift of the neutral axis by approximately 0.4 mm, and a false parity asymmetry (if uncorrected) of about 30 $\times 10^{-9}$. To limit the uncorrected false asymmetry to be less than 6 $\times 10^{-9}$, which is our goal, the magnetic field should be centered on the beamline and collimators to within 3 mm.

Discussions with coil vendors have established that from a practical standpoint, the coils can be fabricated to within $\pm \simeq 3$ mm, which is consistent with our systematic error goals as modelled thus far. The effect of individual coil misalignments within the magnet package is currently under study; this is being modelled by generating a map of field displacements resulting from the coil misalignment and integrating the effect of the field displacements along the tracks of scattered electrons studied with GEANT. The effects of individual coil imperfections are expected to be on the order of what has already been explored for the misalignment of the magnet as a whole, but it is important to complete these studies prior to finalizing the tolerances for the magnet coil construction and alignment.

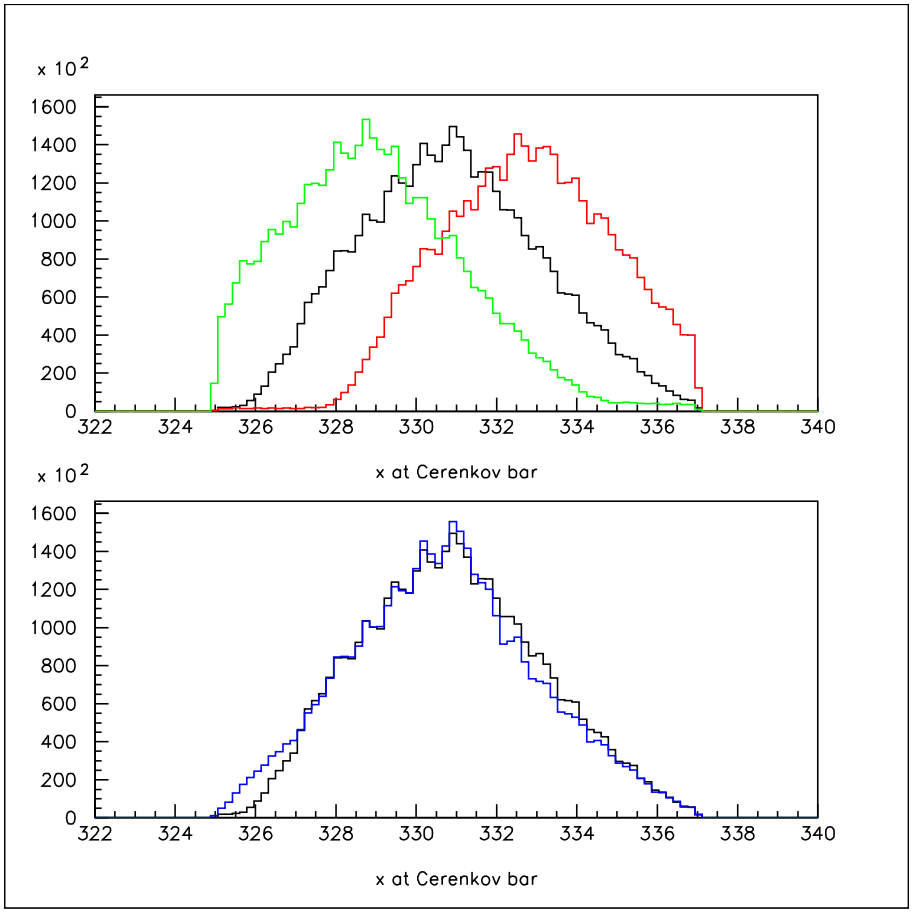

Figure 11: *The black histogram shows the beam profile across a Čerenkov bar when the magnet is correctly aligned. The green and red histograms show the effect on left and right detectors, respectively, when the magnet is moved 1 cm to the left (toward positive x). The blue histogram in the lower plot corresponds to the green peak that is brought back to the center of the detector by increasing the magnetic field by 1.5% through the use of a trim coil.*

2.6 Magnetic Field Verification

Acceptance tests of the assembled magnet of the QTOR spectrometer must guarantee that the desired Q^2 interval of the scattered electrons for each sector is properly focused on the quartz Čerenkov detectors. Sector to sector uniformity is important in order to keep systematic errors under tight control. The open structure of the Q^p_{Weak} magnet provides for easy access not only to the end regions but also to the strong field region between the coils. Optical alignment will locate the coils geometrically, in the first instance, to required tolerances.

A magnetic field mapping apparatus, built by the Canadian group for the G0 experiment, will be employed to map the QTOR spectrometer field. The field mapping system consists of a programmable gantry with full 3D motion within a (4 x 4 x 2) m^3 volume, and a set of high precision Hall probes, thermocouples and clinometers (which measure tilt angle) mounted on the end of a probe boom on the gantry. The field mapping device, on location at the University of Illinois for mapping the G0 magnet, is shown in Figure 12. The system is capable of providing an absolute position determination of ± 0.2 mm, and a field determination of ± 0.2 Gauss.

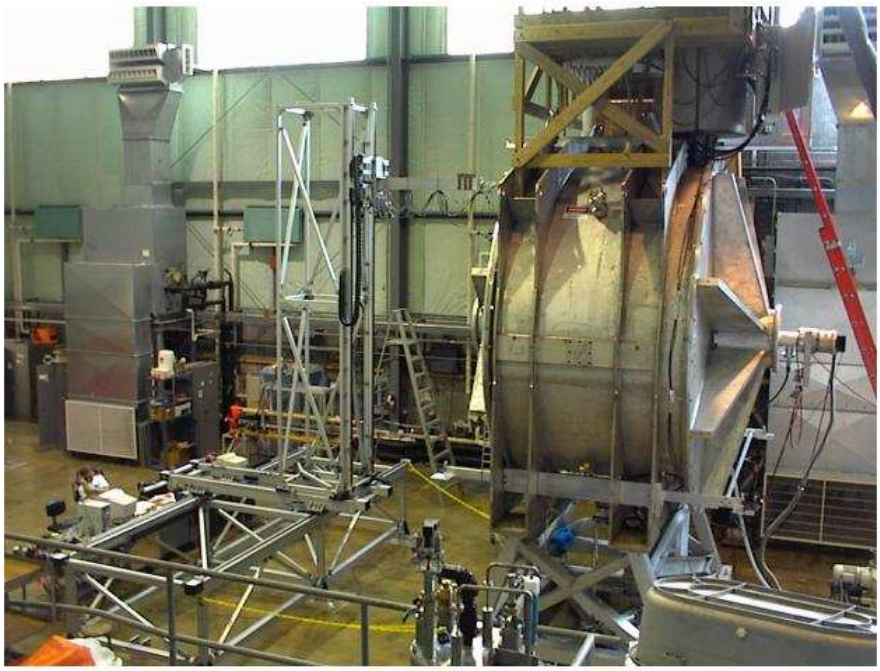

Figure 12: *Photograph of the magnetic verification device, on location at UIUC for mapping the G0 magnet.*

For the G0 experiment, the automated field measuring apparatus was used to determine the locations of a pre-specified set of magnetic reference points corresponding to the zero-crossing locations of specific field components at selected points of symmetry of the magnet. Determination of these zero-crossing points then allows the determinations of the actual coil locations

and hence, in principle, the complete specification of the magnetic field. In all, 30 zero-crossing points were scanned for each magnet sector, for a total of 240 zero-crossing values per data set. The analysis procedure used to extract the coil positions from the zero-crossing points was tested against computer simulations, where known coil displacements were used to generate simulated data. Not only were the 'displaced' coil positions correctly extracted, but the relative orientations and positions of the Hall probes themselves could also be extracted. Analysis of the experimental data also quickly revealed that the gantry frame was offset with respect to the toroid frame by about δX =6.2 mm (vertical) and δY=-3.3 mm (horizontal). Allowing the analysis procedure to correct for these offsets resulted in a full determination of the residual coil displacements for all 8 coils. Most of the angular displacements were about 0.1°, and the linear displacements less than 0.2 cm, well within the specification for the tolerances on the coil positions laid out in the original design. Finally, the behavior of δZ suggested that there was an offset in the axial (Z) direction between the gantry frame and the toroid frame, of about 1 cm, a fact later confirmed when the magnet was opened for inspection and repairs. The excellent performance of the magnetic verification device and the analysis procedure in extracting the coil positions for the G0 magnet provide confidence that the QTOR magnet coil positions can similarly be located to the required accuracy.

2.7 QTOR Support Structure

Meetings with Jefferson Laboratory engineers assigned to Hall C and MIT-Bates engineers have resulted in a design of the Toroidal Magnet Assembly support system consisting of two parts. One part is concerned with the Toroidal Magnet Assembly including the alignment and support of the eight racetrack coils. The other lower part or Base Support consists of the necessary supports required to allow support, alignment and safe-tracked rail motion to and from the beam line. This base supports the Toroidal Magnet Assembly of eight racetrack coils and its support members. MIT-Bates has produced concepts of support which are viewed as reasonable at this stage of the TDR, but which will need detailed design efforts in the next phases of the project. The array of racetrack coils have an axis which is horizontal and a radius of about 1.65 m (D = 3.30 m) with an axial length of just over 3.65 m. Notwithstanding the additional equipment needed for the experiment, it helps to see a large cylindrical object with horizontal axis of length of 3.66 m and a diameter of 3.35 m being supported by another lower frame of 3.66 x 3.66 m and 1.83 m high traveling over rails to and from the beam line. This two part frame and support scheme allows assembly and some testing of the Toroidal Magnet System in Hall C before being moved to the beam line in Hall C at JLab.

MIT-Bates has produced a number of drawings depicting the arrangement now envisaged. Detailed design is still needed to complete the support frame tasks. The QTOR Support Structure design represents the evolution of the MIT BLAST Frame to meet the specific requirements of the Q^p_{Weak} experiment. It retains many aspects of the BLAST Frame design that has proven itself to work well, and at the same time provides important, yet subtle improvements to specific design deficiencies which surfaced during the early stages of BLAST's commissioning run.

The Support Structure has to be non-magnetic. For this reason, both stainless steel and aluminum were considered as viable alternatives. In the end, aluminum was chosen for three reasons: ease of manufacturing, lower cost, and much greater availability of various standard structural shapes. Figure 13 shows a CAD drawing of the proposed QTOR support superstructure.

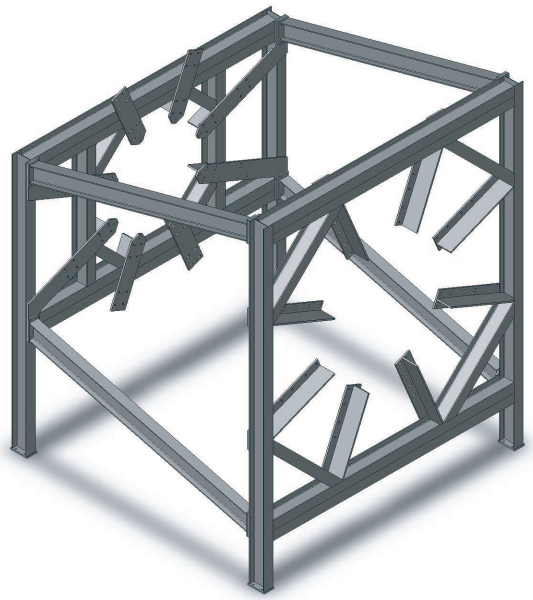

Figure 13: *Aluminum Support Structure Assembly.*

The proposed support structure is modular by design. It consists of two main weldments, upstream support frame and downstream support frame, and four longitudinal braces, which join the two support frames together. The design is based on readily available 6061-T6 aluminum I-beams, C-channels and flat plates. Individual weldments can be fabricated by any number of pre-qualified fabricators, and shipped to Jefferson Laboratory for final assembly and installation. At the time of assembly, no welding will be required. All the individual modules will simply be bolted together.

Preliminary stress and deflection calculations suggest that the proposed design is sound, and that the required coil position stability and repeatability can be achieved. Additional detailed finite element stress and deflection analysis are required to verify proper behavior of the proposed structure.

Each of the eight coils, spaced evenly every 45 degrees around the longitudinal axis of the toroid, is supported by a coil fixture as shown in Figure 14. The coil fixture is fabricated from a 10 cm thick aluminum plate, in order to achieve the necessary rigidity and positional stability

of each coil. The connection between the coil and the coil fixture is well understood, but the detailed design remains to be completed. It has to guarantee ± 1 mm positional reproducibility of each coil, while allowing unrestricted coil length expansion and contraction due to temperature changes.

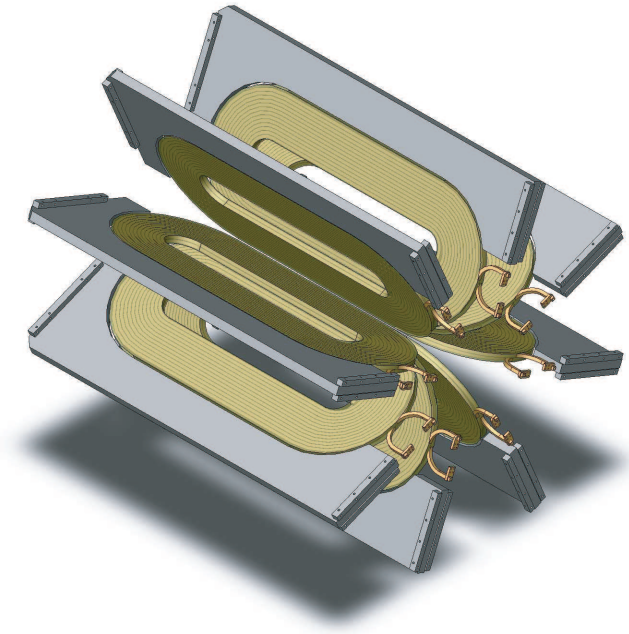

Figure 14: *QTOR coils and bracing fixtures.*

Coil fixtures are bolted to the support structure in such a way that the position of each coil can be independently adjusted to ±2.5 cm in any direction. The fully assembled QTOR is 523 cm wide, 645 cm tall, and 508 cm long. Its aperture centerline is 366 cm above the floor, which corresponds to the beam height in Hall C, at Jefferson Laboratory. The fully assembled and loaded structure is illustrated in Figure 15. The weights of the various components are summarized in Table 3.

Table 3: *Component weight breakdown.*

Subsystem	**Weight per unit**	**Weight of subsubassembly**
8 Coil Assemblies	8 x 2,041 kg =	16,328 kg
8 Coil Fixtures	8 x 794 kg =	6,352 kg
Support Structure		3,629 kg
TOTAL Weight		26,309 kg (29 Tons)

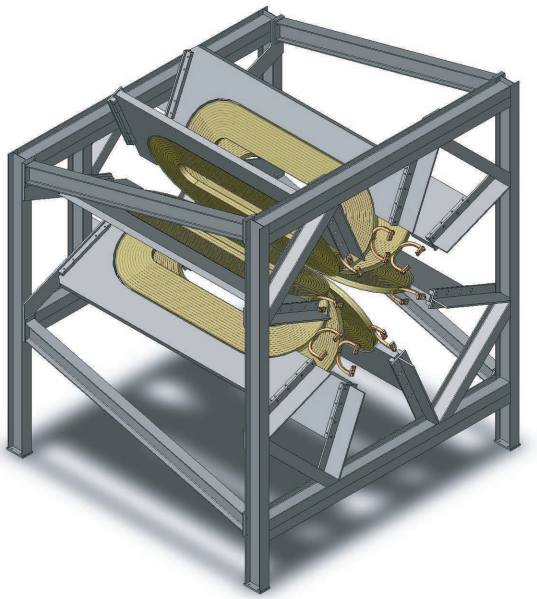

Figure 15: *Isometric view of the final QTOR Toroid Assembly.*

2.8 Electrical Specification of Magnet and Power Supply

The Toroidal Magnet System consists of the following subsystems, which are described as follows; conductor parameters, coil parameters, insulation scheme, toroidal assembly of eight coils, toroidal magnet coil alignment and support, moveable platform support for the magnet assembly, AC power distribution, DC power supply, DC feeds to magnet, instrumentation for local and/or remote control of the equipment and safety instrumentation for the protection of personnel, equipment and the building.

The conductor chosen for nine racetrack coils (eight coils required plus a spare) has been used for the MIT-Bates BLAST toroidal magnet. That profile is chosen again here because: the profile is available; a two layer design minimizes the cost of fabrication, simplifies the cooling (hosing/fitting) requirements, and satisfies the desire for relatively low voltage excitation with a relatively high current supply (170 Volts, 6230 Amperes, 0.027 Ohms). The 3.8 cm square conductor has a 2.0 cm round ID and is made of CDA 102 copper alloy with a soft temper, manufactured in 12.2 m lengths. Three suppliers have been located, which have given budgetary quotations for the supply of about 20,000 kg, equivalent to 2000 m of conductor. See Drawing No. A-100656 for the conductor specifications.

This racetrack coil is of simple design and should be easier to wind than the BLAST coil, because this design has no reverse bends allowing the coil to be wound in tension at all times during the winding. The coil is made up of two single layers of thirteen turns each such that the coil has a total of 26 turns per coil. The smallest inside radius is 250 mm and should not have any significant keystoning because the bending radius to conductor dimension ratio is greater than 6. The largest outside radius is 750 mm. The number of splices (joints) needed to make up a layer (97.8 m) is less than nine. Therefore the coil could require up to eighteen splices per coil. The total nine coils will require up to 162 splices to be made by the coil vendor. The advantage of a two layer design is finding the location of a very unlikely leak is facilitated and a repair in situ is possible should that unlikely event occur. A vendor QA program for making and testing splices is planned before any coils are wound as was successfully implemented for the BLAST coils.

The racetrack coil has been modeled using the magnetic program, TOSCA, to determine the magnetic fields, forces and energy storage of the toroidal magnet assembly when excited by the required number of ampere-turns, (8 x 26 turns x 6230 A) = 1.3 x 10^6 A-turns. Output from the TOSCA program is used to determine the necessary magnetic forces the frame structure must handle and to address the energy stored as it allows calculation of the effective inductance (L) of the toroidal magnet assembly. The electrical time constant of the toroidal magnet is the inductance divided by the resistance, which is 32 mHy/27 mOhms, or about 1.2 seconds. The coupling of a coil's flux to the adjacent coils in the assembly has been calculated to be rapidly diminishing to the coils on either sides at 0.3, then 0.18, and then 0.08 and finally to 0.07 for the coil opposite.

This magnetic coupling boosts the effective inductance of a single coil to twice its self inductance of about 2 mHy to 4 mHy. The stored energy was determined by TOSCA to be about 0.57

MJ when excited at the design current of 6230 A in the eight racetrack coils of 26 turns each. The coils weigh just over 1,814 kg each. The coil magnetic loads are both to the outside (38,400 N) and to the inside (99,200 N) resulting in a net centering force on each coil of about 62,000 N Mechanical design of the coil alignment and support will include these magnetic forces which are acting on the coil assembly. If the coils are positioned accurately and they are excited in series electrically as planned there are no net forces causing rotation of the coils as they are balanced to zero between the coils. If however a coil began to move towards another coil the forces would then become unbalanced with the coils approaching one another if not restrained by supports. The eight racetrack coils are positioned within the toroidal magnet assembly such that 4 pairs have a specific orientation with respect to the floor, which is 3.96 m below the long axis of the toroidal magnet assembly. Mechanical design is an important part of the alignment and support of the racetrack coils.

The insulation scheme designed for Q^p_{Weak} coils follows the BLAST coil design noting that the voltage stress on the insulation is low if operated in the balanced mode intended at ± 85 V to ground. The turn to turn insulation is a half lapped 0.19 mm thick treated fiber glass tape producing a 0.38 mm insulation turn to turn. The turn-to-turn and layer-to-layer voltage stress of a single coil is determined to be 0.82 Volts and 20 Volts respectively. The voltage stress to ground could be no higher than 85 Volts planned or 170 Volts if operated in a single ended mode with respect to ground. Ground wrap insulation of a 0.76 mm tape half lapped and applied provides sufficient insulation against inadvertent surface grounding. Each coil will have its insulation tested turn to turn and ground in a QA program designed to ensure the integrity of the coil insulation scheme.

The toroidal magnet assembly requires over 1300 kVA of power to supply the DC power supply which converts the AC to the required DC current and voltage. Discussions with Hall C engineers have determined that Jefferson Laboratory has begun planning for an upgrade to the AC power for Hall C which will be more than adequate to the needs of the Q^p_{Weak} project. The DC power supply will be designed to have a 12 pulse rectification scheme resulting in a harmonic ripple of 720 Hz in the output voltage and a reduced effect back on the supply mains. The Q^p_{Weak} project has yet to add up precisely the total AC power needs for the experiment, but it is prudent to allow for some growth in the supply to feed future AC power needs e.g. vacuum pumps, instrumentation and control elements. At this time we anticipate the AC 3-Phase power needed at 480V-60 Hz for the Q^p_{Weak} project at about 1500 kVA and recommend that Jefferson Laboratory plan on the installation of a 2500 kVA substation transformer to handle the future needs of Hall C including Q^p_{Weak}. Power panels, fused disconnect switches with local dry transformers and 480V/208V/120V power panels are expected to be part of Q^p_{Weak} needs when requirements are specified in detail.

The DC power supply AC input needs are 1360 kVA at 480 Volts 3-Phase, 60 Hz and AC rms line currents of 1636 A and are based an output of 170 Volts at 6500 Amperes with an efficiency of 0.9 and a power factor of 0.9 lagging. This feed from the sub station to the DC power supply shall be in conformance with Jefferson laboratory electrical distribution practices and installed and supervised by Hall C electricians.

Based on the budgetary RFQs for the DC power supply, which resulted in three responses, it is clear the unit will have delta-wye input transformers and combine on the secondary side as a twelve-pulse rectifier with a ripple frequency of 720 Hz and higher harmonics. This DC supply is designed to be current-regulated to one part in 10,000 over an eight hour period. Input voltage is designed for 480 Volts, 3 Phase, 60 Hz. Input AC power is specified at 1360 kVA. The DC power supply is designed to be locally and/or remotely controlled. The unit is designed to be nearby the toroidal magnet assembly and therefore will need some form of shielding hut or walls to protect the semi-conductors from the effects of harmful radiation. Cooling water is required for the unit with inlet temperature not greater than 30° C and inlet pressure of at least 100 psi and return pressure of 20 psi for a pressure difference of 80 psid and a flow rate of greater than 30 GPM. JLAB cooling water pressures are in the 200 psia range so a pressure regulator may be necessary to match Hall C water cooling with the DC power supply cooling needs.

The D. C. power supply required to power the Q^p_{Weak} toroidal magnet assembly to the required magnetic field is described below in general terms. This description and additional specifications will be used to complete a bid cycle when the purchase of the equipment is desired. Q^p_{Weak} engineers have obtained budgetary prices from three vendors. The DC power supply (DCPS) is rated at 170 Volts and 6500 Amperes for a maximum power of 1.1 MWatts. The supply current will be regulated to 1 part in 10,000 over an 8-hour period. The unit will include: a local control panel; AC input monitoring panel; TJNAF interlock module; RS232/RS422 interface; 8 bit current readback; AC input line filter (EMC); water flow and over temperature switches. In addition, other details are to be specified and included in the final RFQ. Delivery is approximately 8 to 12 months after receipt of an order (ARO) with payment terms consistent with TJNAF Purchasing Office.

The DC feeds to the toroidal magnet assembly have not been finalized to date. There are a number of approaches deemed acceptable namely: copper bussing of sufficient cross-section greater than 6 square inches of copper, so as to not need cooling water; heavy-walled copper tubing with internal water cooling sufficient to easily connect the current from the DC supply to the toroidal magnet; water cooled cable as is commercially available from a number of firms. The specification of the Hall C engineers in conjunction with the Q^p_{Weak} engineers will determine the approach selected from these three acceptable approaches.

Jefferson Laboratory Hall C engineers met recently with the Q^p_{Weak} engineers to discuss the water cooling needs of the Q^p_{Weak} toroidal magnet system. There is available in Hall C sufficient water to easily cool the toroidal magnet with the necessary inlet temperature of about 30° C and an inlet pressure of 200 psig with a back pressure of some 60-80 psig. The flows available exceed the needs of the toroidal magnet by at least a factor of two. The toroidal magnet design requires a flow of 30 GPM total in two parallel circuits per coil. For eight coils the requirement is 240 GPM in 16 parallel paths. Differential pressure across the cooling water inlet and outlet should be greater than 100 psid. A temperature rise of 15° C or less is desirable and should be easily achieved with the existing low conductivity cooling water available in Hall C. The DC power supply requires a cooling water supply of 30 GPM at a differential pressure of about 80 psid with maximum inlet pressure of 150 psig. In addition the DC current feeds from the DC power supply to the toroidal magnet may need a supply of cooling water to be determined in the detail

design stage. In summary, the cooling water requirements of the Q^p_{Weak} project toroidal magnet system is about 300 GPM. That total consists of 250 GPM for the toroidal magnet, 30 GPM for the DC power supply and perhaps another 20 GPM for the water cooled DC feeds between the DC power supply and the toroidal magnet if that approach is selected. Additional data about the DCPS is tabulated in Table 4.

Table 4: *High current magnet power supply for Q^p_{Weak} experiment.*

Parameter	**Requirements**
RECTIFIER FILTER	12 PULSE SCR BRIDGE WITH PASSIVE LCR
OUTPUT CURRENT	0-6500 AMPERES
OUTPUT RIPPLE	less than 0.5% OF Vout @ 720 Hz
CURRENT SETTING	18 bit DAC
CURRENT READBACK	8 bit ADC by DCCT supplied
STABILITY REQUIRED	0.0001 (8 hours standard)
AC INPUT MAINS	480, 3 Phase, 60 Hz
AC INPUT MAXIMUM	1500 kVA (soft start circuit required
COOLING WATER	less than 30 gpm @ 80 psid
Max. Dimensions (Est'd)	457 cm W x 122 cm D x 213 cm H

We are developing a list of possible instrumentation required for proper operation of the Q^p_{Weak} toroidal magnet system. The instrumentation is necessary to allow operation of the equipment in a safe reliable way consistent with the safety of personnel, equipment and the building. The list is fairly long with some redundancy to ensure safe and intended operation of the system. A list of the instrumentation includes; current sensor(s) AC and DC, magnetic field sensor(s), voltage sensor(s) AC and DC, water pressure sensors; inlet(s), outlet(s), and differential sensor(s), over temperature switches for coil cooling passages, temperature sensor(s) for critical components in the DC power supply, ambient temperature and humidity sensor(s). The DC power supply will have a complete set of instrumentation to monitor the state of the unit and to protect it from damage due to equipment failure within or without. Controls are anticipated to be computer controlled utilizing the EPICS type control system now operating at Jefferson Laboratory allowing turn on and off remotely as well as locally if desired. System crash circuits will ensure the toroidal magnet system can be turned off from any point, but only turned on from the desired selected location. It is anticipated that the Safety organization at Jefferson Laboratory will review all safety and operational issues the experiment presents to Hall C and its users.

2.9 QTOR Magnetic Spectrometer Collaboration

The magnetic spectrometer group for the Q^p_{Weak} experiment consists of scientists and engineers from the University of Manitoba, TRIUMF, MIT, Jefferson Laboratory, and Louisiana Technical University, led by W. van Oers (Manitoba) and S. Kowalski (MIT). Initial magnetic field studies and extensive GEANT simulations have been carried out by N. Simicevic of LaTech. The magnetic field calculations have been cross-checked using TOSCA by P. Brindza of JLab, and by comparing the simulations to results for the G0 and BLAST spectrometers. TRIUMF has provided consulting support for initial explorations of the magnetic spectrometer design. JLab has provided initial start-up funds in support of contract work to Bates engineer R. Averill, who, together with MIT-Bates engineer S. Sobcynski has prepared drawings and detailed specifications of a modified BLAST coil design for QTOR which have been sent to a selection of vendors for quotes on the copper conductor, coil fabrication, and DC power supply. NSERC funds have been used in support of travel to prepare a technical design for the QTOR magnet.

The division of responsibilities in the spectrometer collaboration is as follows. MIT-Bates collaborators are seeking US-DOE funding to purchase the copper conductor material, and to design and build the magnet support structure. The Canadian contribution via the University of Manitoba and TRIUMF are seeking NSERC funding for the coil construction. If the latter request is successful, TRIUMF will provide project management for the coil procurement, and the University of Manitoba will provide travel funds to manage the project. The DC power supply and installation costs will be covered by JLab, as well as support for controls and long term maintenance of the magnet and power supply systems.

2.10 Details of Budgetary Quotes for the Magnet System

Based on initial responses to a request for quotations solicited by R. Averill on behalf of the Q^p_{Weak} collaboration, plus experience with construction of a very similar magnet for the BLAST project at MIT-Bates (1998), we arrive at an estimated budget for the QTOR construction project that is shown in Table 2.10. Note that the requirements and tolerances for the BLAST magnet and support structure, which had to accommodate sensitive polarized targets and ensure precisely zero magnetic field along the beam axis, are much more stringent than for the QTOR case, and hence the estimated cost of engineering and design remaining to be done for QTOR is much lower than for BLAST. The engineering and design costs for QTOR shown in Table 2.10 refer only to the base support structure, since the coil engineering is essentially complete at this time. It is seen that the total estimated cost of the QTOR magnetic spectrometer is \$790k. It should be noted that the coil fabrication bids received thus far from the 3 vendors varied in price by a factor of three. The most reliable vendor from our standpoint is Everson Electric (US), who produced the coils for the BLAST magnet, costed at \$300k (1999), and Everson's initial bid on the QTOR coils was \$265k.

The schedule for construction of the BLAST coils by Everson Electric in 1998 covered 8 months from the date of the purchase order, with regular payments required upon completion

Table 5: *Cost estimates in US funds for the QTOR magnetic subsystems (2002,* **without contingency***) compared to actual costs incurred in building the BLAST magnet[7,8] at MIT-Bates (1999) Costs are based on 3 bids for the conductor and coil fabrication and 2 bids on the power supply.*

Magnet Subsystem	**QTOR Cost (k$US)**	**BLAST Cost (1999 k$US)**
Copper Conductor	160 (44.0 klb)	188 (54.0 klb)
Coil Fabrication	265	296
Power Supply	165	172
Stand	100	98
Engineering & Design	100	312
TOTAL	790	1066

of the tooling, and upon delivery of each batch of 3 coils. Assuming that a similar schedule could be worked out with the QTOR vendor, we would need to spend the bulk of the funds in one calendar year. To be consistent with the schedule that has been adopted for the experiment as a whole, we assume here that the copper conductor will be purchased in the second half of calendar year 2003, and that the QTOR coil fabrication would commence early in 2004. This would enable us to assemble, install, and map the field of the QTOR spectrometer during the fall and winter of 2005 and be ready for first data taking in 2006.

3 Detector System

The Q^p_{Weak} experiment will use eight large fused silica bars (synthetic quartz) as Čerenkov detectors to measure the asymmetry of the elastic polarized electron scattering from the proton target. Fused silica has the extremely stable mechanical and optical properties essential for this high precision asymmetry measurement. Due to the high rate, approaching 1 GHz per detector octant, the detectors will be operated primarily in current mode. On occasion a calibration pulse counting mode will be used as a method to determine both the average Q^2 acceptance and backgrounds (the dilution factor) in the quartz bars. This mode will include an additional tracking system consisting of drift chambers, a GEM detector and a scintillator which can be rotated to any octant or removed from the spectrometer. The combined ϕ acceptance for the eight octants will be $\frac{2}{3}$ of 2π.

Mounting and shielding of detectors as well as collimation of the scattered electrons have been studied. The detectors will be located 580 cm downstream of the center of the magnet. The eight quartz bars will be centered at 325 cm from the beam axis. A schematic picture of the detector arrangement is shown in Fig. 16. Each bar will be 220 cm long, 12 cm high, and 2.5 cm thick. A thickness of 2.5 cm was selected after extensive simulations were performed to determine both the optimum angle the quartz bars should be placed with respect to the nominal incidence of the particle trajectories and the thickness of the bar in order to be as close to counting statistics as possible. Basically, if the bars are too thin not enough light is produced while if the bars become too thick additional noise is generated from electromagnetic showering. This effect is shown clearly in Figure 17.

The front surface of each quartz bar is not normal to the center of the distribution of scattered electron trajectories, but instead is rotated along the long axis by 12.5° . This significantly increases uniformity of light response along the length of the bar. The effect is achieved by improving the light capturing efficiency of light from one side of the Čerenkov cone at the expense of some overall light loss. This selected collection enhancement of part of the Čerenkov cone phase space is illustrated in Figure 18. The total photoelectron yield for each electron event for the combined signal from both the PMTs is calculated to be 100. The response is predicted to be uniform to better than 10% over the length of the bar, as shown in Figure 19. Detailed Monte-Carlo modeling of this effect is discussed in Appendix C. The resulting uniformity in light collection as a function of position along the 2 meter length of the bar is impressive.

Polishing of the quartz is necessary to maintain total internal reflection of the Čerenkov photons and thus obtain a large signal per event, the surfaces of the quartz bars have to be polished to high degree. In addition a reasonably uniform thickness of the quartz is necessary to operate at counting statistics, since variation in path length for the electrons will lead to a variation in the number of Čerenkov photons. The variations have to be less than 2 mm out of the 2.5 cm thickness of the detectors. Polishing issues were the focus of significant development work for the BaBar DIRC detector, but this was required for the transmission of the photons to preserve the Čerenkov angle for individual events. Q^p_{Weak} has only the requirement to obtain as much light as possible (and uniformly across the area of the detector) for each event. Q^p_{Weak}

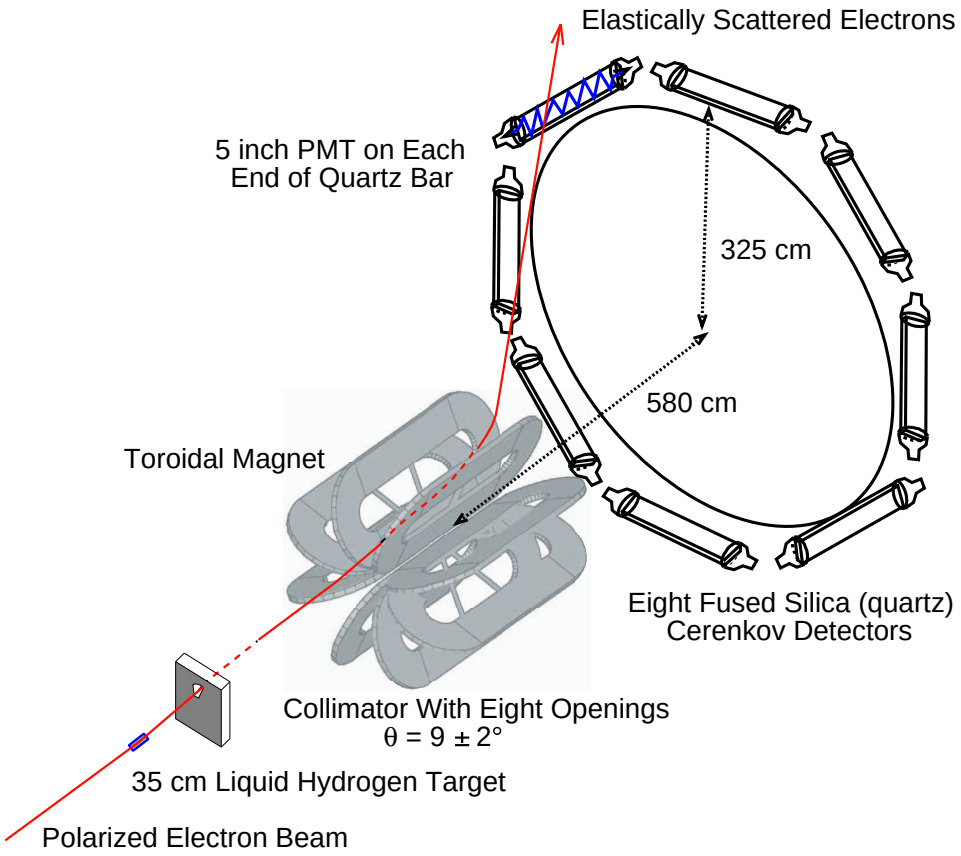

Figure 16: *A conceptual sketch of the Q^p_{Weak} detectors shown in relation to the target and the toroidal magnet. A representative electron trajectory and its Čerenkov light are shown. The detectors will be housed in a large concrete shielding assembly.*

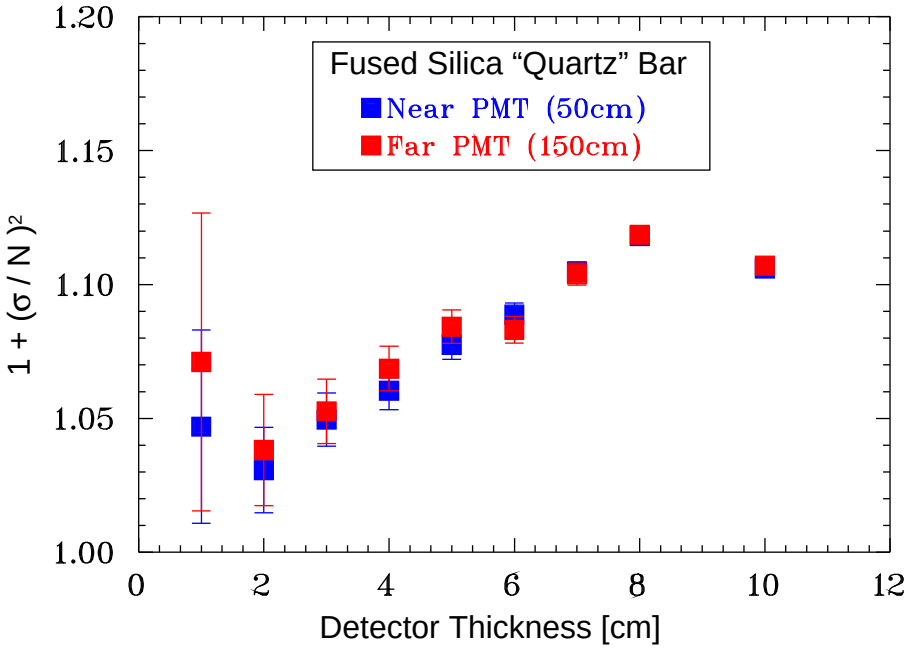

Figure 17: *Relative experiment running time versus quartz Čerenkov detector thickness.*

should not require polishing to better than 25 Å rms, a level easily commercially available.

The entire set of mechanical and optical properties of the single quartz bar were also studied. This includes the effects of the bar dimensions and orientations, the effects of the thickness, the quality of surface polishing, and the effects of the photocathode quantum efficiency. The conclusion is that there is a good working solution for the Čerenkov counter. Relevant parameters for this solution are summarized in Table 6. There is still a possibility for an improvement in the counter design, but this should be based on prototype testing rather than relying exclusively on simulations.

Q^2 acceptance needs to be known to better than 1% but will be determined through accurate survey, simulation studies, and the result of the pulse counting measurements with the auxiliary GEM, drift chambers, and scintillation detectors. The simulation work underway is discussed extensively in later chapters of this document.

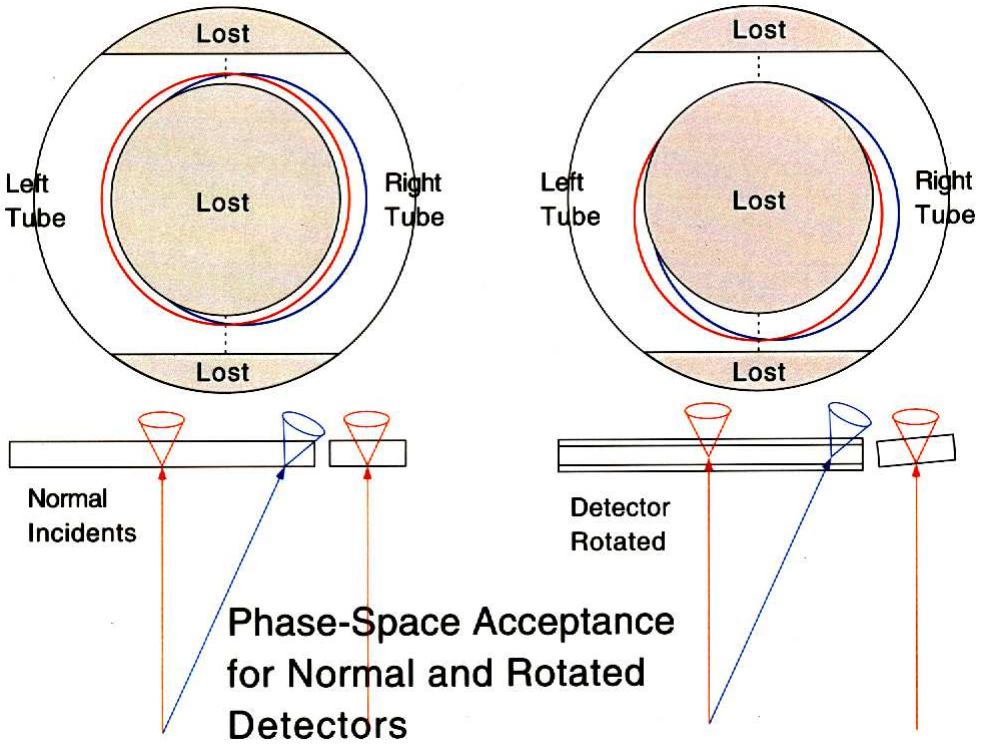

Figure 18: *Technique for selective collection of part of the phase space of the Čerenkov cone by rotating the quarts bars with respect to the incidence angle of the particles so as to optimize light collection uniformity along the length of the bars. The regions where light is not trapped by total internal reflection are denoted on the figure as "Lost".*

Table 6: *Optimized parameters of the Q^p_{Weak} Čerenkov detector.*

Parameter	Value
Detector Position	580 cm from the magnet center
Detector Height	319.5-331.5 cm from the beam axis
Bar Length	200-210 cm
Bar Width	11-12 cm
Bar Thickens	1.905-2.54 cm
Rotation Around Beam Axis	$12.5° \pm 2.5°$
Polishing Quality	Normal Polishing (25 A rms roughness)
Material	Quartz (Fused Silica)
Photocathode	S20 (high Q.E.)

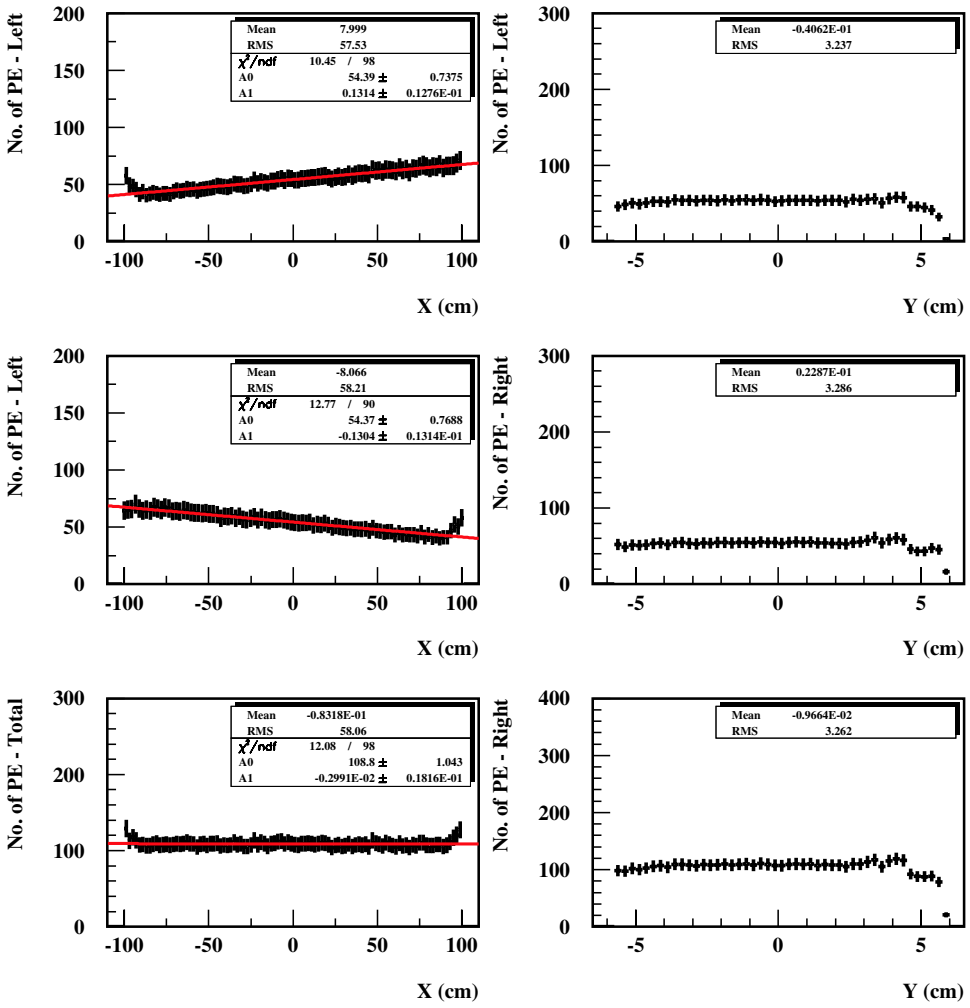

Figure 19: *The position dependence of number of photoelectrons on each of the phototubes and the total number along the length (left column) and the width (right column) of the 1 inch thick Čerenkov bar for a 12.5° rotated detector. This simulation includes the full weighted cross-section and optics of the spectrometer.*

3.1 The Dilution Factor Measurement and Non-Prompt Backgrounds

Generally backgrounds are anticipated to be small but must be understood. Backgrounds have to be measured in order to determine the dilution of the parity-violating asymmetry signal. Background contributions include inelastically scattered electrons, photons, pions, and neutrons. The dilution factor arising from background events will be measured using both the tracking system (drift chambers, GEM, scintillators, etc.) and the Čerenkov detectors operated in pulse counting mode at low beam current.

In addition to this technique we will take long calibration time-of-flight spectra out to 500 ns in order to verify that there are no long lived backgrounds or light from decays coming out of the quartz detectors that would require a correction in the central value of the measured asymmetry. We do not anticipate that this effect will be significant, but as careful experimentalists we will confirm this by measurement. For this we will briefly require a special low repetition rate pulsed diode mode from the injector at very low currents during the initial calibration of the apparatus as illustrated in Figure 20. More on this specific accelerator injector mode can be found in the polarized source requirements section of this report. It should be noted that from the GEANT simulation studies (Appendix C) we do not anticipate significant prompt electromagnetic backgrounds.

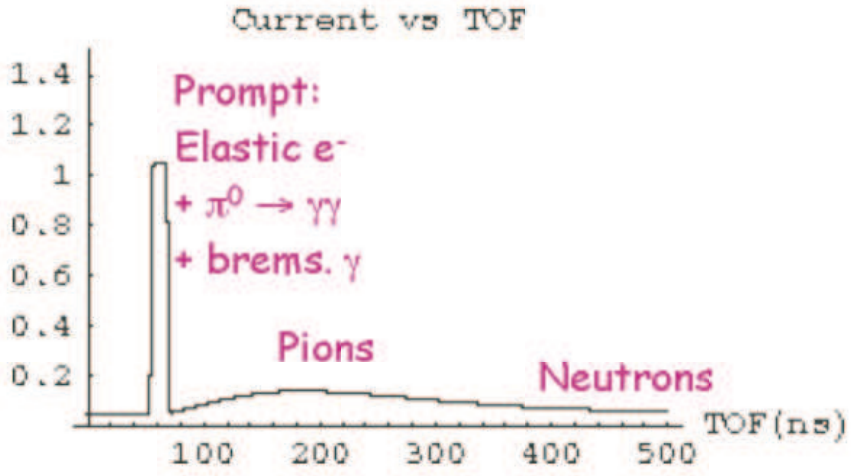

Figure 20: *Illustration of extended time-of-flight spectrum. This is just an illustration and not intended as a quantitative calculation.*

The lower rate will allow the quartz detectors to be read out in pulse mode. The readout will be to a fast transient digitizer (essentially a digital oscilloscope) per PMT, rather than the current mode FEE. The auxiliary detectors will provide tracking identification for elastically scattered electrons. The time of flight for an event and presence or absence of signal in the scintillator will provide particle identification information, for example: neutrons and many pions will have time of flight to the detectors of greater than 50 ns, and charged particles will produce a scintillator

signal, while neutral particles will not. Simulation work is underway to estimate the various contributions to background signals.

3.2 Technical Requirements of the Design

The Čerenkov detectors have to meet the following design specifications. The detectors must operate in an extremely linear current integrating mode. The geometric stability of the detectors must be well defined so that the average Q^2 can be determined to 1%. The actual dimensional tolerance of the quartz bars are not extreme as the focus of the elastic electrons lie well within the area of each bar. The detectors have to be capable of determining the background contributions to the current mode signals. The detectors have to be capable of operating in pulsed mode. The detectors have to be relatively insensitive to backgrounds, which is the case for Čerenkov counters. The detectors have to be stable. The Čerenkov material has to be radiation resistant. The Čerenkov material has to provide a large number of photoelectrons per detected electron so as not to increase the running time defined by the counting statistics.

The integrated high radiation dose during the lifetime of the experiment limits the possible detector types to shower detectors, or Čerenkov detectors. Several detector materials were considered. These included quartz, lucite, polycarbonate, polystyrene, and a lead/quartz sandwich. A design of $\sim$0.5 radiation length quartz Čerenkov detectors was selected because of radiation hardness, light transmission, and an ability to approach the counting statistics limit. Each end of the eight 2 m long quartz bars will be instrumented with a 130 mm (5 in.) diameter photo multiplier tube. Much research and development of quartz detector technology was done by the SLAC BaBar collaboration for their DIRC particle ID detector [1]. The quartz detectors are expected to receive of order 100 krad per detector of radiation in the course of the experiment. This high dose is a driving reason for the selection of quartz, since synthetic quartz has been measured to tolerate high doses [1]. Specifically, we want to insure that no optical "deadened zone" is imprinted on the bars as the experiment progresses. Aside from light loss this would result in time varying position sensitivity, something a good parity experiment must always avoid. The ends of the detectors where the PMTs and electronics are mounted are shielded and are expected to accumulate a total dose of about 10 krad.

The reference specifications for the PMTs include the following.

- S20 photocathode.
- 130 mm diameter flat face window made from radiation hard UVT glass, for mounting onto the detector.
- Eight dynode stages for 10^3 gain with reasonable voltage per stage.
- Acceptable performance with aging.
- Acceptable linearity.

Candidate PMTs satisfying the above criteria are commercially available [2]. For a rate of ~760 MHz per sector and 50 photoelectrons in each PMT per event, the PMT photocathode current will be about 5 nA. This leads to a 5 μA current from the last dynode of the PMT.

The detector front end electronics (FEE) have to meet the following design criteria. The FEE must be capable to operate in both current and pulse mode. The FEE must be linear to better than 10^{-4}. The FEE have to be low noise, with noise level significantly smaller than the counting statistics. The FEE cannot have any ground loops. The FEE cannot be sensitive to radiation damage.

The conceptual design of the front end detector electronics is shown in Fig. 21 and it includes the following.

- Low-noise, high gain I-to-V amplifier, AD745 from Analog Devices.
- 16-bit 1 MHz ADC, AD7671 from Analog Devices.
- Fiber optic converter, HFBR-1412T from Agilent, to send the ADC output to the DAQ.
- A remotely operable relay switch, CZX3500 from Tohtsu, for selecting current or pulse mode.

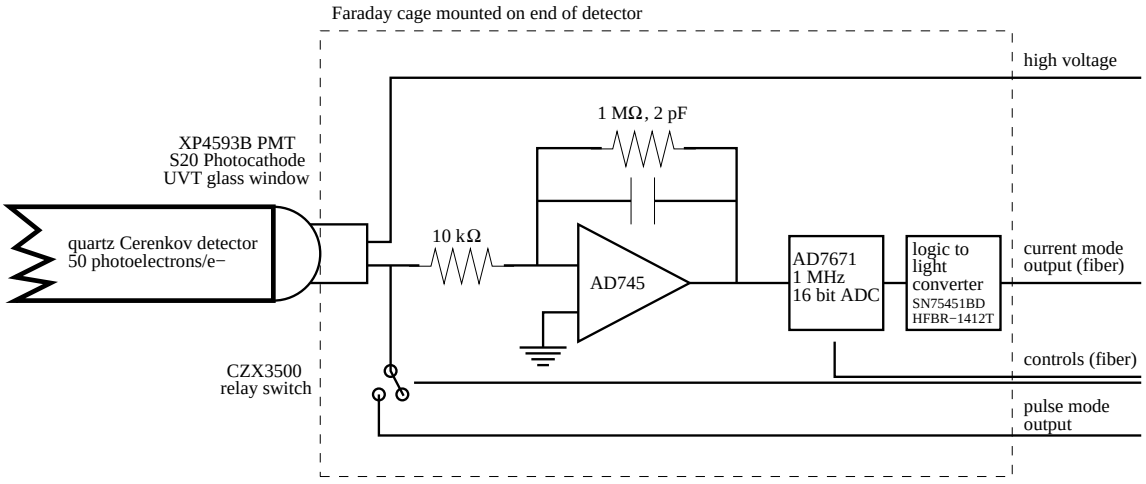

Figure 21: *The Q^p_{Weak} detector electronics scheme. In current mode running, the only non-isolated electrical connection to the detector will be the ground of the high voltage cable. Power for the chips and fiber optic components is not shown.*

These components will be mounted in a small Faraday cage, the FEE housing, with one housing for each end of each quartz bar. In production data taking current mode, the only non-isolated electrical connection from the detector to the outside will be the high voltage cable. Power for the chips in the circuit will be provided to the housing but will be isolated by filtering

and DC to DC converters. Fiber optic connections will be used to control the ADC operation and to output the ADC signal. LEDs mounted on the detectors will be used for calibration and gain monitoring purposes. The low-noise amplifier will allow beam-off measurements with no light and with LED light to quickly measure additive and multiplicative instrumental false asymmetries.

3.3 Progress to Date

The dimensions and parameters discussed above were determined in well-developed Monte Carlo work to study the magnet optics and detector geometry [3].

Four quartz bars (Spectrosil 2000) of dimension 100 cm by 12 cm by 2.5 cm have been ordered from Saint-Gobain. Delivery is anticipated January 2003. This vendor can produce 200 cm long bars. The four bars will be used for testing properties of the quartz for light collection and radiation damage, and to study options for reflective wrapping and optical coupling to PMTs.

Discussions with PMT vendors and individuals working on other experiments have led to a candidate of the 130 mm diameter PMT model. Six of these have been ordered from Photonis [2], along with sockets and voltage dividers for testing. The PMTs, XP4593B, have the following parameters: 130 mm diameter front window from UVT glass, 8-stages, and S20 photocathode. Delivery will be in January 2003. The tubes will be tested for linearity, radiation damage of the front window, and aging effects from running at high photocathode current. The lifetime of the photocathode is expected to be of order 500 C, which should not be an issue for the experiment. The nonlinearity of the tube gain is specified to be within 2% full scale at 200 mA photocathode current, so the expected nonlinearity at 5 μA photocathode current is 5×10^{-7}. The PMTs are produced with an internal getter to prevent or reduce photocathode poisoning. UVT glass front windows have been shown to retain 90% of their transmittance for light of $\lambda > 300$ nm for gamma radiation dose of up to 1.4×10^5 rad [4].

Electronics progress includes an identified candidate ADC, a chip by Analog Devices (the AD7671). Four of these low-cost ($\sim$\$35 each) chips have been ordered and obtained. The linearity of these chips is specified to be 4×10^{-3} of full scale, which is sufficient for linearity of better than 10^{-4} over the operating range of the detector signals. An PC-interface evaluation board for the chips has been ordered and obtained. Candidate digital signal processing VME modules for receiving the ADC signals and packaging them into a manageable data rate for the DAQ have been identified.

3.4 Items Remaining and Potential Issues

Once the pieces of sample quartz have been obtained, the material will be studied for: radiation hardness, light transmission, reflectivity, number of photoelectrons, uniformity of response, light output from showering/scintillation, and the existence of any long time tails. The PMTs will be studied for: radiation hardness of window, lifetime of anode/cathode, and linearity. Options for

wrapping quartz in reflective materials, for coupling to the PMTs will be investigated. Potential problems with the front end electronics include radiation damage of chips and components. The detector system and front end electronics for Q^p_{Weak} require continuing development, design, and testing of components but no issue known at present should prevent successful operation for the experiment.

3.5 Fabrication Schedule

Tables 7 and 8 provide the schedule for the detector and front end electronics development, construction, and testing. The listed items are the major milestones.

2003	obtain PMTs and sample quartz
	design tests for quartz and PMT performance
	build prototype PMT bases
2004	perform test measurements for: light collection efficiency, linearity,
	radiation damage and PMT aging, PMT/quartz coupling
2005	finalize design, select mounting and shielding scheme,
	test with final electronics and configuration
2006	install detectors, run experiment

Table 7: *Schedule for detector system.*

2003	obtain candidate ADCs, evaluation board, DSP
	develop design for pulse counting mode electronics
	build first generation prototype
2004	perform test measurements for noise levels, radiation damage
	build second generation prototype
2005	design finalized, assembly of final electronics
	test with final electronics and configuration
2006	install electronics, run experiment

Table 8: *Schedule for detector front end electronics (FEE) system.*

References

[1] 'Operational Experience with the DIRC Detector,' SLAC-PUB-9088, I. Adam, *et al.*, IEEE Trans. Nucl. Sci. 49:1071-1076, 2002.

'Optical Properties of the DIRC Fused Silica Čerenkov Radiator,' J. Cohen-Tanugi, *et al.*, ICFA Instrum. Bull. 21:20-44, 2001.

And references contained therein.

[2] Photonis, Avenue Roger Roncier, Z.I. Beauregard, B.P. 520, 19106 BRIVE Cedex, France.

United States distributor: Lanco International, Inc., Roswell, GA 30075.

[3] 'Design of a Čerenkov Counter for the Q^p_{Weak} Experiment II,' Simicevic, N., LATECH-CAPS-02-06a, 6/13/2002.

[4] Hamamatsu PMT Handbook, available from `http://usa.hamamatsu.com/`.
(Hamamatsu Corporation, 360 Foothill Rd, Bridgewater, NJ 08807.)

4 Liquid Hydrogen Target System

The design of the Q_W LH_2 target is based on the following parameters: safe and reliable operation for sustained periods of time with a beam current=180 μA, length=35 cm, location 4.75 m upstream of the magnet, raster size ~4x4 mm^2, 9° ± 2° acceptance for scattered electrons, thin windows, azimuthal symmetry, no local boiling, and minimal density fluctuations.

4.1 Beam Power

The combined beam current and target length requirements lead to a beam power of 2.1 kW, considerably over the present 1.2 kW capacity of the JLab End Station Refrigerator (ESR). To put our target coolant requirements in perspective, we show in Figure 22 a plot of beam current vs beam power for several relevant targets. We note that the beam current required for Q^p_{Weak} is only 30% higher than has already been employed in Hall A for physics production, and that the SAMPLE target at MIT Bates is 5 cm longer than the Q^p_{Weak} target. However, the combination of high beam current and a long target flask will make the Q^p_{Weak} target the highest power cryotarget in the world by a factor of several. Although the experiment could be run with a lower power cryotarget, the length of the run would have to be increased correspondingly.

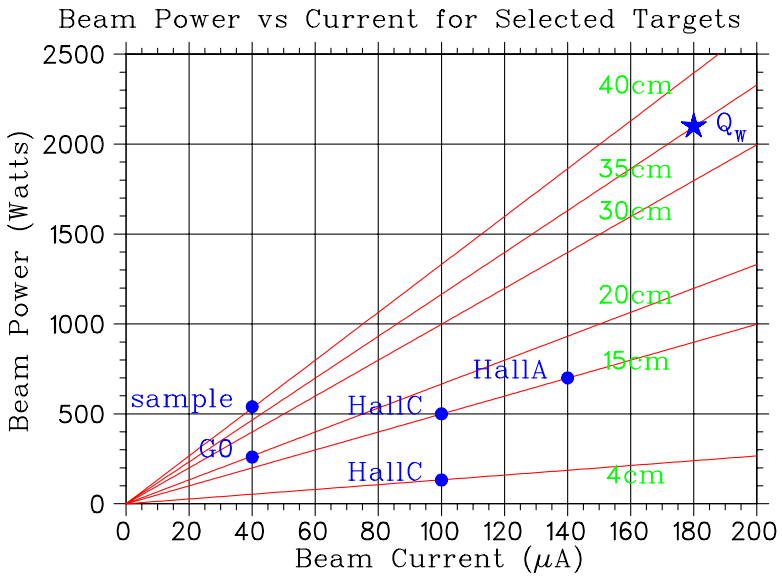

Figure 22: *Values of the beam power deposited in LH2 targets as a function of beam current, for target cells varying between 4 cm and 40 cm in length. The solid point indicates the expected* Q^p_{Weak} *configuration (35 cm target, 180 μA, 2.1 kW).*

4.2 Refrigeration

The cooling power available to the target is given by the change in enthalpy ΔH of the coolant. For LH2 targets, nominally 15 atm 15K coolant (H=81 J/g) is supplied by the JLab ESR, and returned at 19K and 3 atm (H=112 J/g). At maximum capacity the ESR can supply about 25 g/s, corresponding to a maximum cooling power of 775 W. Alternatively, the 3 atm 4K supply (H=9.5 J/g) from the ESR could be used. For sustained operation, the coolant must be returned cold at 1.2 atm and 5K (H=35 J/g). A flow of 25 g/s would only give 625 W of cooling power in this case. The mass flow required to achieve 2 kW of cooling power is plotted as a function of supply temperature in Figure 23.

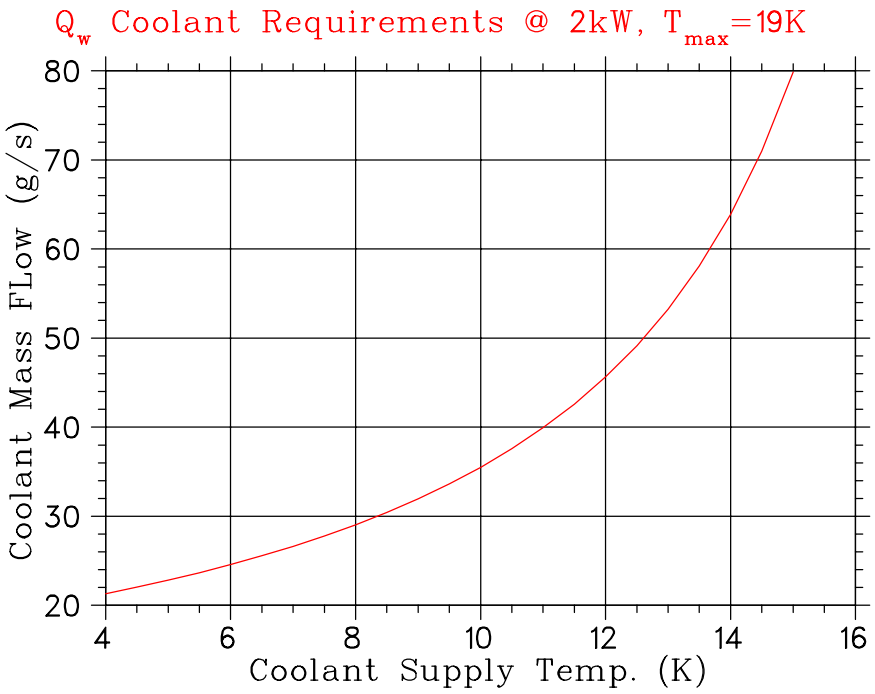

Figure 23: *The coolant supply temperature is plotted against the required mass flow to achieve 2 kW of cooling power for a 19 K target.*

The power deposited by the 180 μA, 1.165 GeV electron beam in the 35 cm long Q^p_{Weak} LH2 target (3.9% X_0) is that associated with ionization energy loss. At 19K and 25 psia, the density of liquid hydrogen is 0.0723 g/cm^3. The ionization energy loss (including the density effect) is then 4.65 MeV/g/cm^2, which corresponds to 2120 W of power (neglecting the windows). On top of the beam power of 2.1 kW, the Q^p_{Weak} target needs an additional several hundred Watts of cooling power to account for conductive heat losses, circulation fan heat load, reserve heat load for feedback control, etc. As a result, 2500 W is in fact the cooling power goal for Q^p_{Weak}.

Since this clearly exceeds the capacity of the ESR in its present configuration, an alternative solution has been developed in consultation with the JLab cryogenics group. The CHL backup refrigerator will be used to supply 4K helium at 3 atm. This coolant will be returned at 19K and

1.2 atm. The change in enthalpy is then 103 J/g, so the mass flow appropriate for 2500 W is a reasonable 24.2 g/s. This mass flow is routinely available on the conventional 4K/5K circuit in Hall C. In addition, LH2 targets have been run with 4K coolant at JLab before. Using a coolant temperature so far below the 13.8K freezing point of hydrogen is clearly more problematic, especially during the cool down. However, it can and has been done before. In fact, sending 4K coolant back to the ESR at temperatures near 19K has also been done at JLab before, during problem cool downs of, for example, the G0 magnet. This kind of ESR configuration can only be sustained for brief periods of time, however. To maintain this configuration for long periods of time, use of the CHL backup refrigerator is required.

This scheme will be tested with a dummy heat load in the spring or summer of 2003. Although we are confident that this scheme can be made to work, alternative ideas are being explored in parallel. In any case, by employing the backup CHL refrigerator it seems clear that the refrigeration demands of Q^p_{Weak} can be met, and the laboratory is committed to working out the details of providing this cooling power to the experiment. In fact, in the time since this solution to providing the cooling requirements for the high power Q^p_{Weak} target was worked out, other experiments have proposed to take advantage of it. The first of these will run in Hall A in 2003 or 2004. This means that by the time Q^p_{Weak} runs in 2006, a lot of experience with high power cooling will have accrued at JLab and be available for the benefit of Q^p_{Weak}.

4.3 Boiling and Density Fluctuations

In the past, two different approaches have been taken to the problem of target boiling and helicity correlated density fluctuations. On the one hand, targets have been designed to minimize these two effects, and luminosity monitors employed to measure and if necessary, correct for them. This was the approach taken by the SAMPLE experiment at MIT/Bates. The other approach is to completely ignore the two issues of boiling and density fluctuations, and use luminosity monitors as the primary normalization in the experiment. Then whatever boiling and helicity correlated density fluctuations are present in the primary measurement are also present in the normalization, and therefore cancel. This approach has been taken in the Mainz A4 experiment. For Q^p_{Weak}, we propose to use the SAMPLE approach and employ a target designed to minimize boiling and helicity correlated density fluctuations. Since it is difficult to predict in advance how well the target might behave, however, we intend to construct a luminosity monitor patterned after the Mainz design, and use it to measure the target boiling and helicity correlated density fluctuations. Then if the target performance in these two areas is unacceptable for some unforeseen reason, we could still fall back to the Mainz option and normalize the measurement with the luminosity monitors. This dual approach guarantees that the Q^p_{Weak} target will have target boiling and helicity correlated density fluctuations under control. Ultimately our goal is to obtain consistent results with both approaches. This would be the best way to prove to ourselves and everyone else that these problems have been licked in the Q^p_{Weak} experiment.

To understand the requirements that target boiling and helicity correlated density fluctuations place on the Q^p_{Weak} target, we look at each separately. Boiling is a bulk effect, and may be

estimated by recasting the basic definition of specific heat ($c_p = \frac{\Delta Q}{m\Delta T}$) as

$$\Delta T = \frac{\Delta E/\Delta x I_b}{c_p d_r v_s},$$

where ΔT is the temperature rise of the LH2 in K, $\Delta E/\Delta x$ is the energy loss in MeV/g/cm^2, I_b the beam current in μA, c_p the specific heat of H2 in J/gK, d_r the raster size in cm, and v_s the stream velocity of the LH2 in the target cell in cm/s. With $\Delta E/\Delta x = 4.7$ MeV/g/cm^2, $I_b = 180$ μA, $c_p = 10$ J/gK, $d_r = 0.4$ cm, and $v_s = 700$ cm/s, then $\Delta T = 0.3$ K. Since the target operating temperature of 19K is 3K below the boiling point, there is no bulk boiling. We point out that the 700 cm/s stream velocity is that appropriate for the G0 target at 30 Hz, half what we expect to employ for the Q^p_{Weak} target. So the 0.3K estimate is conservative. For the Q^p_{Weak} target it should be as little as $\Delta T = 0.15$ K.

To construct an estimate of the helicity correlated density fluctuations, we assume that the helicity correlated fluctuation in the beam current (I_A) is 500 ppm. This has been routinely achieved in G0, and should be relatively easy to achieve in Q^p_{Weak} since there is no unusual time structure. Then if the bulk temperature change is $\Delta T = 0.15$ K, the helicity correlated ΔT is only 75 μK. In the thermodynamic regime the target operates in, the density fluctuation can be approximated by $\Delta\rho/\rho \sim 1.5\%\Delta T$, so the expected helicity correlated density fluctuation for the Q^p_{Weak} target is only 1 ppm.

Is this good enough? It is if it's small compared to the expected width from counting statistics. The counting rate expected in the Q^p_{Weak} detectors is 800 MHz per octant. Therefore, with a 30 Hz helicity reversal frequency, we expect 2x10^8 counts in the whole detector, or a statistical width of about 70 ppm. The helicity correlated density fluctuations are expected to be only about 1.4% of this, so they should be a negligible contribution to the uncertainty in the experiment.

It's worthwhile to do a reality check at this point. The Q^p_{Weak} target design is based on that of the SAMPLE and G0 targets, so we should check to see what we might expect for the Q^p_{Weak} target density fluctuations based on what was actually observed for those two targets. In the case of the SAMPLE target, the results reported in the literature do not test their target to the level of sensitivity we require. They reported results based on only 4000 counts per detector, for an overall statistical width of 0.5%. They report their density fluctuations were no more than 0.1% based on these statistics, but clearly, more statistics would be required to obtain a more accurate result.

Although still quite preliminary, more statistically precise results were recently obtained for the G0 target in December, 2002. Tests were made with that target running in a 40 μA beam with a 2x2 mm^2 raster, and with the circulation pump running at 30 Hz. The width of the measured asymmetries was 360 ppm, of which no more than 41 ppm was attributed to density fluctuations. Again, better statistical precision would have made a more precise measurement possible. To extrapolate this result to the Q^p_{Weak} case, we have to account for the fact that the Q^p_{Weak} beam current is 4.5 times larger, and the Q^p_{Weak} target is 1.75 times longer. On the other hand, the raster area will be 4 times larger for Q^p_{Weak} and the Q^p_{Weak} pump will be run at 60 Hz rather than

30 Hz. Taken together, these factors cancel, and so the G0 target measurements taken under the conditions described above should correspond rather well to those expected for the Q^p_{Weak} target. In other words, the helicity correlated density fluctuations for the Q^p_{Weak} target should be less than about 40 ppm, based on what was observed for the G0 target. Although this is less than the expected 70 ppm Q^p_{Weak} statistical width, we would like it to be a little smaller still (below 10 ppm). It is very likely that better statistics would lower the 41 ppm density fluctuation measured with the G0 target, however until more statistics are acquired, this must remain a speculation. In the unlikely event it turned out to be a hard floor for Q^p_{Weak}, there are ways to improve the situation. For example, the helicity correlated charge asymmetry could be improved (a factor of two should be relatively easy to achieve here). The use of beryllium windows in the Q^p_{Weak} target should reduce boiling. The pump speed could be increased above the proposed 60 Hz. The raster area could be increased slightly. The beam current could be dropped a little. All together, the prospects of achieving a 10 ppm target for the Q^p_{Weak} experiment seem very promising, based not only on what should be possible, but on what has actually been observed with a target of similar design.

4.4 Basic Conceptual Design

We have studied several possible target concepts based on the above design parameters. The target concept of choice for the Q^p_{Weak} experiment is clearly the SAMPLE/G0 design. The density fluctuations experienced with these targets were studied extensively, and the results are extraordinarily good. Sketches of the G0 and SAMPLE target loops are shown in Figure 24 and 25. A high flow velocity is achieved in these targets by means of a perforated tapered cylindrical windsock concentric to an outer cylindrical cell. The flow area depends on the gap between the windsock and the target cell, as well as their respective radii, and the perforations. As a result the flow area can be made arbitrarily small and is almost independent of the length of the target cell. The small flow area inherent in this design contributes to the high flow velocity required by Q^p_{Weak}. A flow velocity of 500 cm/s (at 30 Hz) was achieved by the SAMPLE target, and as noted previously the G0 target flow velocity is designed to be 700 cm/s (also at 30 Hz). Although it would seem that these large flow velocities are moot since most of the flow appears to be longitudinal to the beam axis, in fact the high degree of turbulence (Reynold's number $\sim 10^7$) in these systems results in a significant transverse component.

The experience gained with the G0 target will carry over to Q^p_{Weak}, however, important changes need to be made. The target cell itself will need to be stretched from 20 to 35 cm. The SAMPLE target cell is 40 cm long. In addition the heat exchanger and high power heater capacity will need to be increased by a factor of 3 to 4. Whereas the SAMPLE and G0 targets share many common characteristics, they do have important differences. The SAMPLE impellers are powered by an external motor, the G0 impellers are powered by a submersible pump. The SAMPLE heat exchanger is an open design, in which the cryogen flows unobstructed through a large pipe. The helium refrigerant flows through copper piping wound around the outside of this large pipe. The G0 heat exchanger is modeled more upon what is in use here at JLab, with the cryogen flowing in direct contact with finned copper tubing which carries the refrigerant. The 25

liter SAMPLE loop is vertical, whereas the 6 liter G0 loop is horizontal. Finally, the diameter of the SAMPLE cell and associated windows is much larger than the corresponding diameters in the G0 target, which mitigates beam halo issues. From preliminary discussions with the JLab target group leader (M. Seely), we think that the Q^p_{Weak} target should be based more upon the SAMPLE design choices, with the exception of the heat exchanger. In addition, we are currently studying the possibility of fabricating the target cell or at least the windows from beryllium in order to reduce the background.

In the following sections, we provide some brief remarks about each of the Q^p_{Weak} target components.

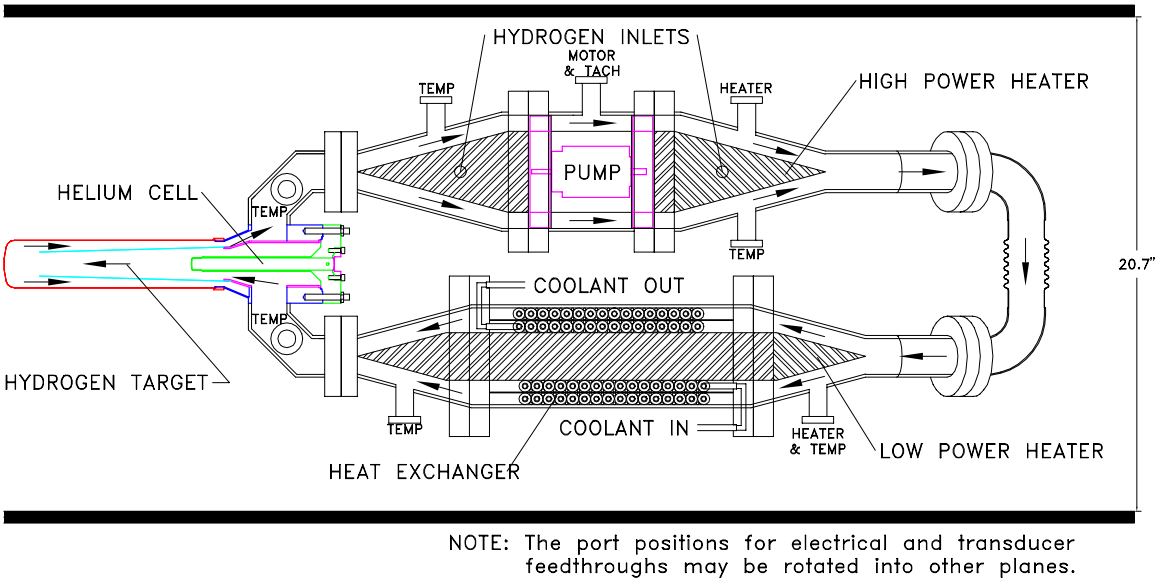

Figure 24: *A sketch of the G0 target configuration.*

4.4.1 Heat Exchanger

The proposed design for the 2500 W Q^p_{Weak} heat exchanger is basically a stretched version of the existing ∼1000 W design for G0. The 30 cm long G0 heat exchanger has been tested to 550 W. It consists of a tube with a plug (flow diverter) along the central axis. Finned copper tubing is wound in 2 helical layers between the plug and the tube. The copper tubing is 1/4" diameter, with 1/8" long fins (14 fins/inch). Based on scaling the Hall C or G0 heat exchangers, roughly 150' of finned copper tubing will be required for the Q^p_{Weak} heat exchanger. The liquid hydrogen is forced to flow past the finned tubing by the plug, where heat is exchanged with the refrigerant (counter-)flowing through the finned tubing. Beyond making the G0 heat exchanger longer and bigger in diameter, there are two more subtle differences imposed by Q^p_{Weak}. First, since the coolant is below the freezing point of hydrogen, care must be taken to avoid the buildup of hydrogen ice in the heat exchanger. To mitigate this potential problem, we propose to wind

nichrome wire between the finned copper tubing, which can be used as a defroster as well as to better restrict the flow along the fins of the copper tubing. Second, the pressure drop of the coolant across the heat exchanger has to be given careful consideration in the design, since the supply pressure is only 3 atm rather than the usual 15 atm.

4.4.2 Cryogenic Pump

Two solutions are being studied for the re-circulation pump. The first would follow the same general design as the G0 pump, ie a submersible vane-axial pump fabricated commercially. The G0 pump is powered by a 50 oz-in brushless DC motor, and has performed well so far for G0. A similar design could be engineered for Q^p_{Weak}. However, the company (Barber-Nichols) which was contracted for the G0 pump recommended that a radial pump would be better suited for our application. Such a pump could provide superior head and volume flow relative to the vane-axial design. This solution would be configured such that the pump motor would be exterior to the loop. One advantage to this design is that the heat dissipated by the motor would not contribute to the heat load of the target.

Either way, the pump must be able to provide a stream velocity of at least 7 m/s and a volume flow rate of at least 12 l/s at 30 Hz. The motor must have enough torque to push liquid neon through the loop (at 10 Hz) during commissioning. The motor should be capable of running 30–100 Hz with LH2 in the loop, without depositing more than 50 W into the system. Materials prone to radiation damage, like Teflon, should be avoided. The bearings must have a lifetime of at least 10,000 hours under load and in cryogenic conditions.

4.4.3 Target Heater

The heater is of standard design. Its function is to replace the power deposited in the target by the beam when the beam current drops, in order to maintain a stable temperature in the loop independent of beam current. It must be capable of providing at least 2500 W. Typically, resistive nichrome wire (0.19 Ω/ft) is wound around a conical standoff which is situated directly in the flow path. Although G10 has been used for this standoff in other applications, ceramic is the preferred material for the high power requirements of the Q^p_{Weak} target. The power supplied to the heater will be controlled in a feedback loop in a manner similar to that being used by G0. There, the heater power is adjusted automatically to keep the temperature in the loop constant by looking at a thermometer just upstream of the target cell. However, a signal from a beam current monitor is also used in the feedback logic to effect large and sudden changes in the heater power in response to sudden and dramatic changes in the beam current. This dual input PID logic should keep the temperature within 100 mK of the goal temperature even during repeated beam on and off cycles.

4.4.4 Target Cell

The target cell will be modelled after the SAMPLE design. In that target, LH2 flowed along the axis of a 0.13 mm thick (5 mils) perforated windsock. The windsock tapered to a diameter of 3 cm at its narrow end. The windsock was surrounded by a 7 cm diameter cylindrical tube 0.38 mm (15 mils) thick, and 40 cm long. The LH2 returned in the space between the windsock and the outer cylinder. The windsock was perforated to promote flow transverse to the (central) beam axis, and to counteract the Bernoulli effect which would otherwise crush the windsock. Both windsock and outer cell were fabricated of 6061-T6 aluminum. They were connected to a baffled manifold which directed the flow of hydrogen through the inside of the windsock and back along the outside of the windsock.

This hydrogen cell was backed by a helium gas cell which was maintained at the same pressure as the hydrogen cell. The purpose of the helium cell was to match the curvature of the window at the helium-hydrogen interface to that of the window at the other end of the hydrogen cell, which interfaced to vacuum. In this way the effective target length was constant as a function of beam position to first order. The other end of the helium cell interfaced to vacuum with a thin window.

For Q^p_{Weak} the target length would be reduced to 35 cm. The larger diameter cell associated with the SAMPLE target is preferred over the small diameter G0 cell in order to reduce effects associated with beam halo. Furthermore, larger windows mean less target length sensitivity to beam position differences. In order to minimize the background in the experiment, beryllium will be used for the windows. For the same thickness windows, the elastic rate from beryllium is about 5 times less than that from aluminum, and the energy loss is about 2/3 that of aluminum. At 20K the heat transfer capabilities of beryllium are only slightly better than that of certain aluminum alloys. The main advantage in beryllium for the target is lower background, and less heat deposited at the window due to the smaller energy loss there.

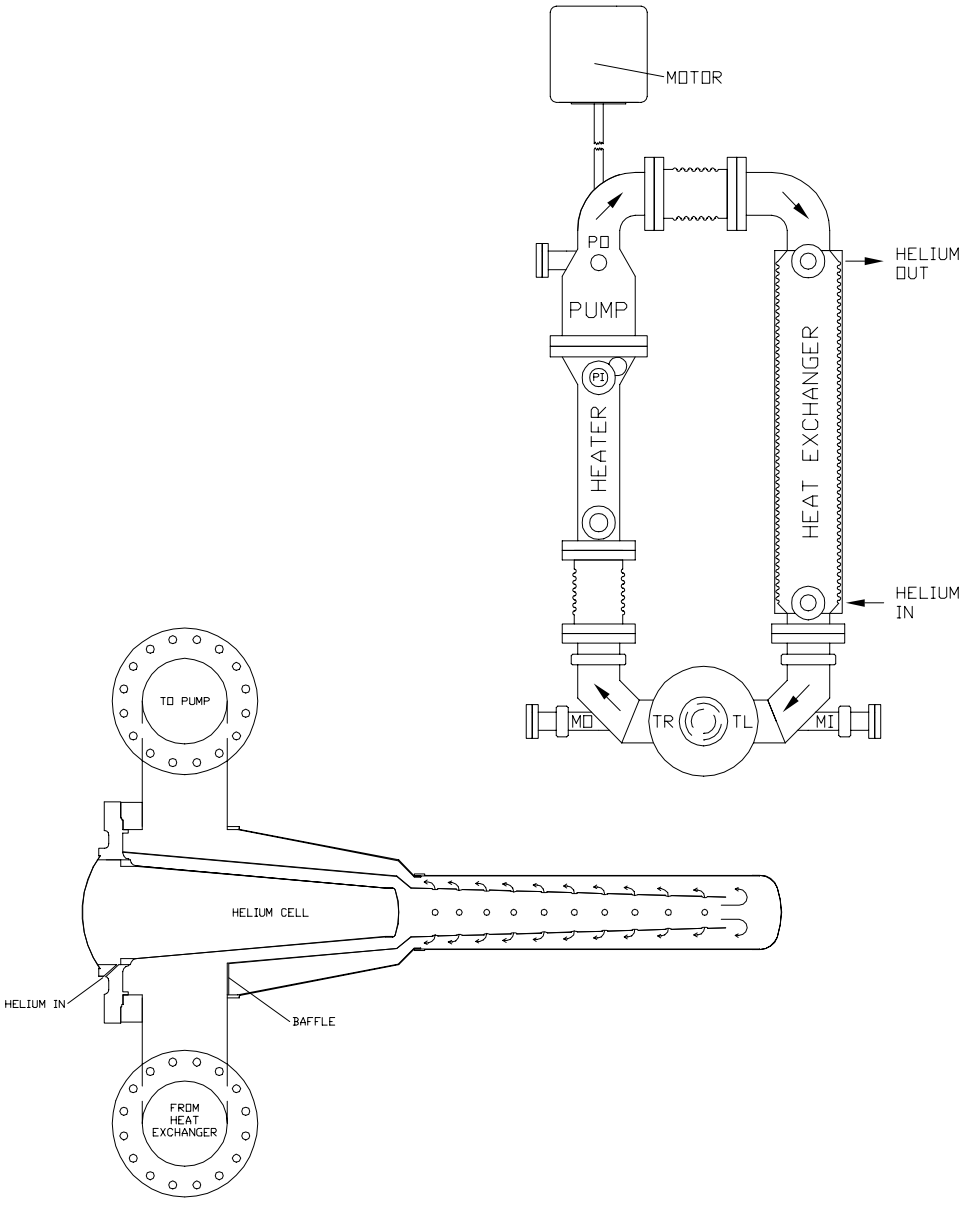

Figure II.1: Schematic view of the target loop and hydrogen flow manifold.

Figure 25: *A sketch of the SAMPLE target configuration.*

4.5 Luminosity Monitor

The luminosity monitor is a key normalization system as it has the potential to make the measurement essentially insensitive to target density variations and to first order helicity correlated beam size modulation effects. This device will consist of an array of Čerenkov detectors located downstream of the Q^p_{Weak} experiment at a small scattering angle. The monitors will be instrumented with very linear radiation hardened vacuum photo-diodes with external high gain linear current-to-voltage converters. This technology has been perfected at LANL and TRIUMF over the past 25 years. The high rate (28 GHz/octant integrating mode) and the resulting small statistical error make it useful for two major purposes. It can be used to do detailed studies of the possibility of target density fluctuations. Since it has a much smaller statistical error per measurement period than the main detector, it is much more sensitive to the onset of target density fluctuations. If these fluctuations are large enough to produce a problem, the results of the luminosity monitor can be used to regress out their effects. Secondly, the luminosity monitor can be used as a valuable "null asymmetry monitor" since it is expected to have a much smaller asymmetry than the main detector; thus if its asymmetry is non-zero it could indicate the presence of a false helicity-correlated effect in the experiment. Specifically, we will apply our standard corrections procedure for helicity-correlated beam properties to the luminosity monitor, as well. If we are properly accounting for all helicity-correlated beam properties we should be able to correct the luminosity monitor to zero asymmetry within errors.

The luminosity monitor will be located about 14.3 meters downstream of the Q^p_{Weak} target as shown in Figure 26. It will be an array of 8 Čerenkov detectors place symmetrically about the 60 cm diameter beampipe. The chosen location of the luminosity monitor corresponds to a mean scattering angle of about 1.2°. The two criteria for this detector are that it has an expected physics asymmetry much smaller than the main detector, and the statistical error on the asymmetry per measurement period is much smaller than the main detector. The cross section and asymmetry for the processes expected to dominate the luminosity monitor yield are shown in Figure 27. The processes considered in the figure are elastic e-p scattering, Møller scattering, and elastic scattering off of the aluminum nucleus. The latter process is explicitly considered because it has a roughly 10 times bigger asymmetry at a given scattering angle than the other two.

In addition to the primary processes considered in the plots in Figure 27, there are secondary scattering process that need to be looked into. In particular, elastically scattered electrons that pass through the aluminum beampipe of the experiment at upstream locations pass at small angles. They see a large effective number of radiation lengths and electromagnetic showers get initiated that can create signal in the luminosity monitor. This will also make the effective asymmetry larger, because the electrons that initiate these showers were scattered at large angles and therefore have bigger Q^2 and larger primary asymmetry. We considered this process in GEANT with a 3/8 inch thick aluminum beampipe upstream of the luminosity monitor. The results are shown in Figure 28. The background from the showering in the beampipe is low energy and significantly reduced in rate (10 MHz vs.] 238 Ghz) relative to the other processes. The relative contributions to the yield are summarized in Table 9.

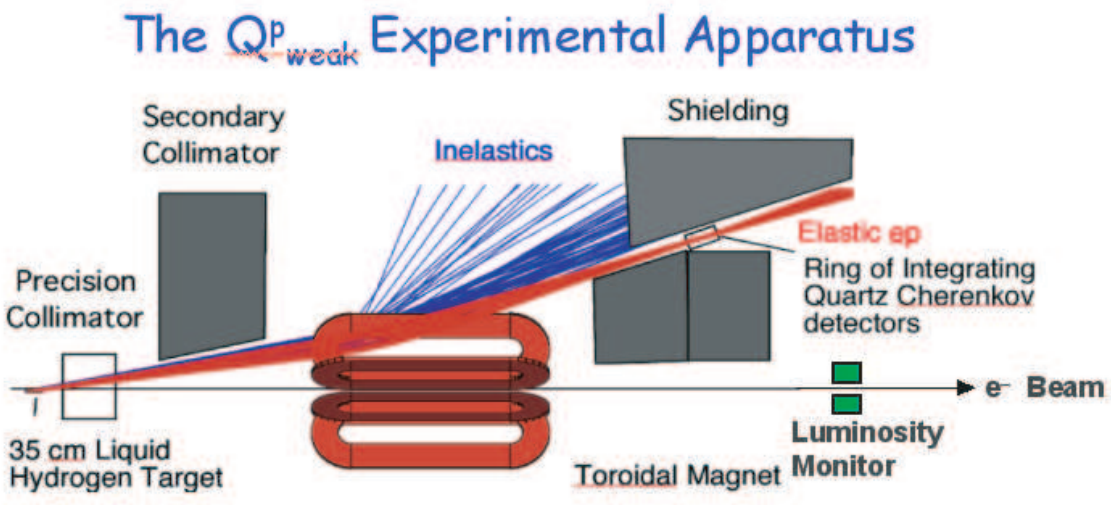

Figure 26: *Schematic of the location of the luminosity monitor array relative to the rest of the experiment.*

To minimize these secondary scattering effects, an inner collimator will be incorporated into the Q^p_{Weak} design, that will eliminate small angle scrape off along the beam pipe to the exit of the spectrometer. At the spectrometer exit, the pipe diameter will be increased and the luminosity monitors will be inset into this flared region. Therefore, these numbers represent a worst case estimate, since with proper design, scattering from the aluminum pipe can be minimized as was done for the Mainz luminosity monitor.)

Table 9: *Relative contributions to the Qweak luminosity monitor signal at the nominal scattering angle of 1.2°.*

Process	Relative contribution
e-e Møller	52%
e-p elastic	42%
e-^{27}Al elastic	5%
EM showers in beampipe	0.004%

A summary of the expected parameters for the luminosity monitor at a scattering angle of 1.2° relative to the main detector is presented in Table 10. The expected luminosity monitor physics asymmetry is 2% of the main detector asymmetry; it is comparable to the main detector's statistical error. The statistical error on the luminosity monitor asymmetry is about 1/6 that of the main detector. Also, Table 10 compares estimated sensitivities of the two detectors to beam energy, angle, and position changes. They are mostly comparable, so the luminosity monitor can be used as a good "null check" on the helicity-correlated beam parameter corrections procedure.

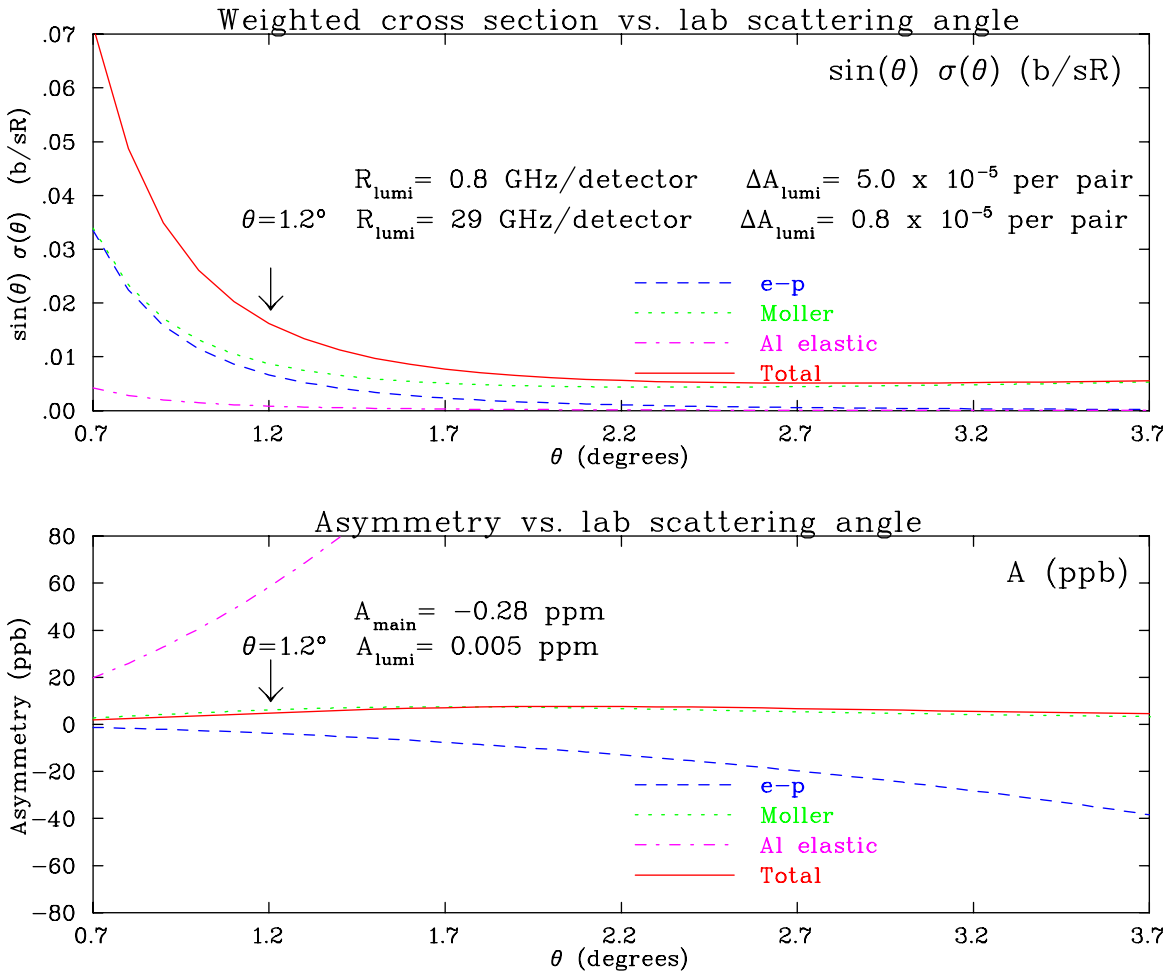

Figure 27: *Weighted cross section and asymmetry of the important processes in the luminosity monitor as a function of lab scattering angle.*

Table 10: *Luminosity monitor parameters at nominal 1.2° scattering angle compared to the main* Q^p_{Weak} *detector.*

Parameter	Luminosity monitor	Main detector
$\langle A \rangle$	0.005 ppm	-0.28 ppm
Count rate	29 GHz/det.	0.8 GHz/det.
δA_{stat}, complete experiment	0.0008 ppm	0.005 ppm
δA_{stat}, per pair	0.8×10^{-5}	5×10^{-5}
Energy sensitivity	-0.0015 MeV^{-1}	-0.0020 MeV^{-1}
Angle sensitivity	-168 rad^{-1}	-27 rad^{-1}
Position sensitivity	-12 m^{-1}	-18 m^{-1}

~ 238 GHz total

~ 10 MHz total

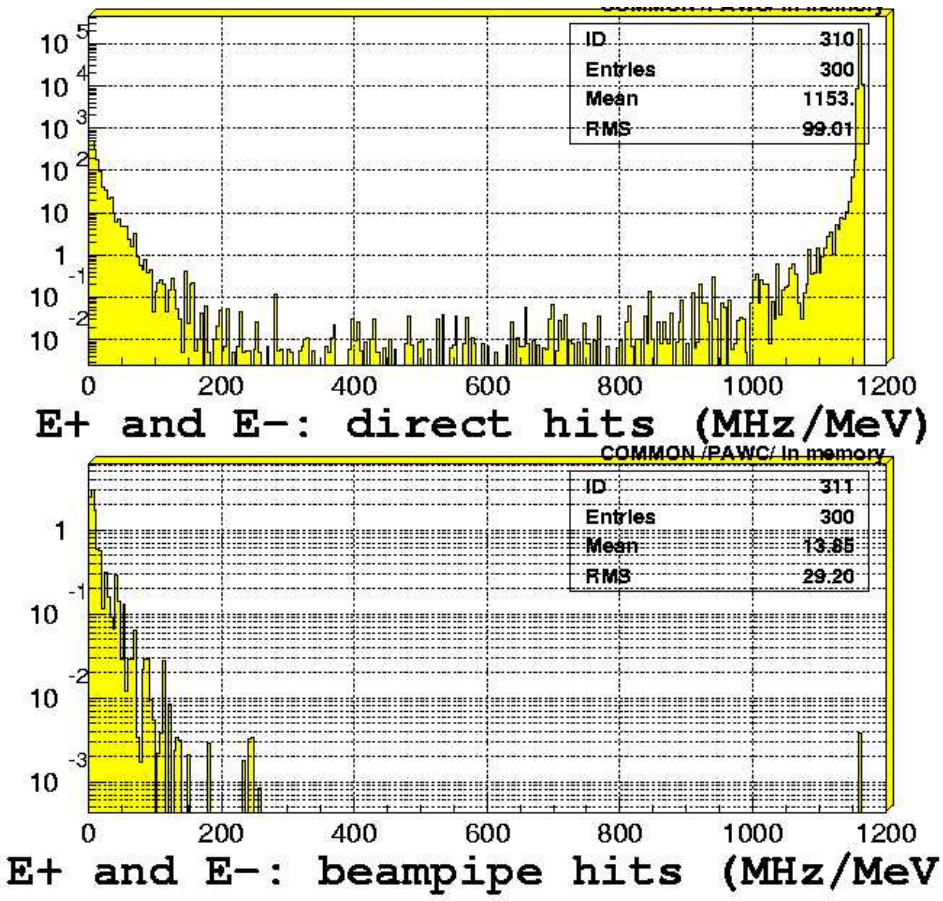

Figure 28: *Results of a GEANT Monte Carlo simulation of the contribution of electromagnetic showers in the beampipe to the luminosity monitor signal. The top panel shows the spectrum and integrated rate from the primary e-p and Møller events. The bottom panel shows the spectrum and integrated rate from the secondary particles due to showering in the upstream aluminum beampipe.*

The luminosity monitor will live in a harsh environment. The expected radiation dose over the course of the experiment will be about 150 MRad. Thus radiation hard materials are essential. For a Čerenkov radiator, the two good radiation hard material choices are water and quartz. A water based Cerenkov monitor has been used successfully in the A4 parity violation experiment at Mainz. A schematic of one of their modules is shown in Figure 29. We intend to use a similar design. Instead of a phototube for light detection, we will use a 3 inch Hammamatsu R2046PT vacuum photodiode. These are very linear devices, and we believe they will be more insensitive to events induced by charged particles passing through the photodetector than photomultiplier tubes. At our expected rates and likely Čerenkov photon yield, this device will have an anode current of about 0.6 μA. For electronics, we intend to use a low-noise, high gain I-to-V preamp design developed by our collaborators at Los Alamos. That will then feed into components that are the same as the main detector electronics chain.

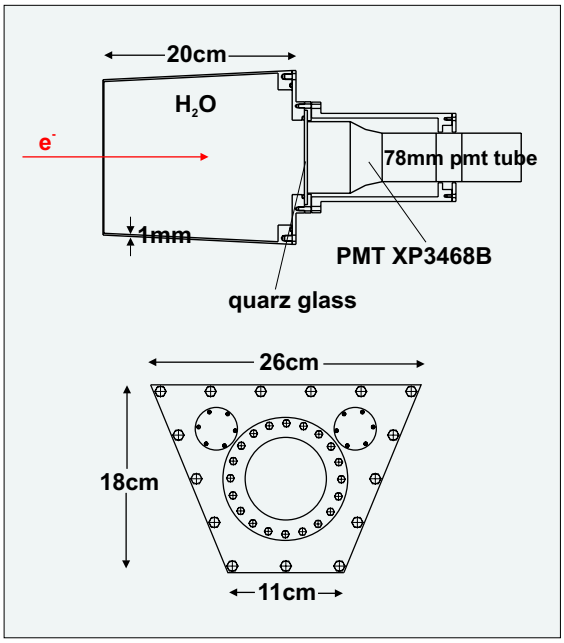

Figure 29: *A schematic of a water Čerenkov module used in the A4 parity violation experiment at Mainz. We intend to use a similar design, but with the PMT replaced by a vacuum photodiode.*

5 Precision Beam Polarimetry

The Q^p_{Weak} experiment requires that the beam polarization be measured with an absolute uncertainty in the 1% range. In principle, the technology to do this already exists in Hall C in the form of the University of Basel Møller polarimeter [1], which provides an accurate absolute polarization measurement but is limited to operation at low beam currents ($I_{beam} < 8\mu A$) and therefore cannot be run concurrently with parity data taking. While the Møller polarimeter will provide a very important capability for the Q^p_{Weak} experiment, the collaboration also plans to build a Compton polarimeter to provide a continuous, relative monitor of the beam polarization during the high current production running.

5.1 University of Basel Møller Polarimeter in Hall C

While the standard $e\vec{e} \rightarrow ee$ scattering process near $\theta_{CM} = 90°$ is used in the existing Hall C Møller polarimeter, its hardware configuration incorporates several significant improvements over previous devices of this type. A superconducting solenoid with a 3 Tesla, beam-axial field is used to drive a pure Fe target foil into saturation (See Figure 30), since the relationship between magnetization and electron polarization is best known for pure Fe. Coincidence detection eliminates most backgrounds, and the collimator design minimizes the effects of atomic Fermi motion in the target. A Monte Carlo program is used to determine the effective analyzing power of the apparatus, taking into account magnet and collimator positions and finite solid angles.

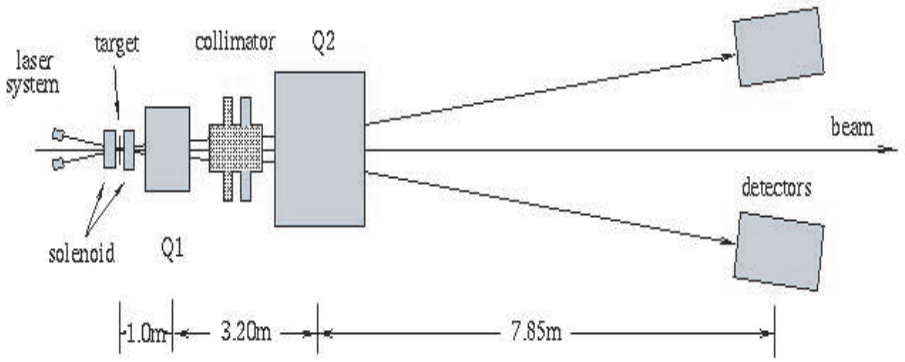

Figure 30: *Layout of the Hall C Møller polarimeter. Note especially the superconducting solenoid which is used to drive the pure iron target foil into saturation. The magnetic field and the foil are oriented perpendicular to the beam.*

The University of Basel Møller polarimeter was designed as an instrument to measure the beam polarization to an absolute accuracy of 1% up to about 8 μA of beam current. It is routinely used to measure the polarization of beam currents of several μA with an absolute accuracy of better than 1.5%. For measurements at the 1% level somewhat more time and care is required than for a routine turn key 1.5% measurement. Unfortunately, the low beam current restriction is presently unavoidable, since it is necessary to prevent significant heating and therefore depolarization of the iron foil. Experience from the last several years suggests that lowering the beam current for dedicated Møller runs can introduce systematic errors at the 1%-2% level if great care is not taken. For example, reducing the beam current by closing the chopper slit can change the average polarization since the beam has a polarization profile. This problem can be eliminated by using the laser light attenuator to adjust the beam current rather than the chopper slit. However, since the Q^p_{Weak} experiment will run at the elevated beam current of 180μA, we will need to better understand what happens to the beam polarization when the filter wheel attenuates the laser light by a factor of 30 [2].

Part of the Q^p_{Weak} collaboration's polarimetry effort will go into determining whether modifications to the Basel Møller polarimeter target can enable it to operate at higher currents while retaining high accuracy. For example, if the Møller polarimeter could be made to work accurately at 18.0 μA, this would "only" be a factor of 10 below the production current. Even higher operating current for the Møller polarimeter cannot yet be ruled out: methods such as actively cooling the target frame, employing quasi-CW beam with for example 10% duty factor, and using the thinnest possible free-standing Fe foils will be explored. Another Møller upgrade concept would be to replace the iron foil with two iron wires one above and one below the beam. If a true RF raster could be constructed and placed sufficiently upstream to create a fast vertical sweep of the beam such that even at the full Q^p_{Weak} beam current only a few percent would hit the iron wires, then in theory one could periodically measure (say every two hours) the polarization with full current by turning the RF sweeping field on for several minutes. This could achieve a pseudo continuous monitor of the beam polarization under the exact production running conditions.

5.2 Compton Polarimetry for Hall C

Clearly the Q^p_{Weak} experiment would prefer a continuous, relative monitor of the beam polarization during the high current production running. The absolute accuracy of this polarimeter need not be extremely high, as long an accurate calibration can be transferred from the Basel Møller polarimeter. Compton polarimetry is a technique for measuring the polarization of longitudinally-polarized electrons by scattering circularly-polarized photons off the electron beam. The cross section differential in the energy k of the scattered photon is given by

$$\frac{d\sigma}{dk} = \frac{d\sigma_0}{dk}\left(1 + P_\gamma P_e A_l(k)\right), \tag{1}$$

where $d\sigma_0/dk$ is the Compton cross section for unpolarized photons and unpolarized electrons, P_e is the (longitudinal) polarization of the incident electron beam, P_γ is the degree of circular polarization of the laser light, and A_l is the longitudinal asymmetry. The asymmetry in the cross

section for the two different helicity states of the electron is proportional to the polarization of the beam:

$$A(k) = \frac{\sigma^+ - \sigma^-}{\sigma^+ + \sigma^-} = P_\gamma P_e A_l(k). \tag{2}$$

The longitudinal asymmetry A_l is given by

$$A_l = \frac{2\pi r_e^2 a}{k_{max}\frac{d\sigma_0}{dk}} (1 - \rho(1+a)) \left[1 - \frac{1}{(1-\rho(1-a))^2}\right], \tag{3}$$

where r_e is the classical radius of the electron, k_{max} is the maximum back-scattered photon energy and $\rho = k/k_{max}$. The parameter a depends on the incident electron beam energy E_0 and the energy k_0 of the incident photons according to

$$a = \frac{1}{1 + \frac{4E_0 k_0}{m_e^2}}, \tag{4}$$

where m_e is the mass of the electron. The maximum back-scattered photon energy also depends on k_0 and E_0:

$$k_{max} = k_0 \frac{E_0 + p_0}{E_0 - p_0 + 2k_0} \approx 4ak_0 \frac{E_0^2}{m_e^2}, \tag{5}$$

where p_0 is the momentum of the electron.

The Hall-C Compton Polarimeter will measure the asymmetry given in equation 2 to extract the electron beam polarization. It will consist of a magnetic chicane, laser system, photon and electron detectors and beam and laser monitoring systems, including feedback to maintain luminosity. It will be located in the beam tunnel upstream of the production target. To achieve the highest accuracy in the measurement of beam polarization requires the coincident detection of the scattered electron and the associated photon. Our goal is to obtain a systematic error on the level of 1%. Baylac, *et al* quote a 3% systematic error at a beam energy of 3.3 GeV for the Hall A Compton Polarimeter[3], so a few percent measurement of the polarization should be fairly readily achievable. We will also cross-calibrate the Compton polarimeter to the Hall C Møller polarimeter, which can measure the polarization to 1%[4].

5.2.1 Chicane

The backscattered photons are emitted in a narrow cone about the incident electron's direction. Therefore the photon detector must be placed on axis with the electron beam. The electron beam must be deflected temporarily from the standard beam direction so that the photons can be detected. A magnetic chicane consisting of a symmetric arrangement of four deflecting dipoles accomplishes this with no net precession of the electron's spin. Each dipole has a length of 1.0 m and an air gap of 25.4 mm. The chicane optics is designed to produce a totally achromatic beam at the exit. Each dipole deflects the beam through the same angle θ. The dipoles are rectangular so that the effective entrance and exit pole edge angles are $\theta/2$. This ensures achromaticity.

The layout of the chicane involves several constraints. The most important parameter is the offset distance, D, between the laser line and the undeflected beamline. This distance determines the separation between the scattered electron and the unscattered beam after dipole D4. For D=30 cm the separation is close to marginal for a beam energy of 1 GeV and a green laser (512 nm). A UV laser could improve the separation by a factor of two.

To maximize the separation, D, requires deflection angles, θ, and dipole separations as large as practical. However, space in the beam tunnel is limited and deflection angles are limited by the maximum field (~15 kG) at the highest beam energies. Figure 31 shows a layout of the proposed beam deflection system. The insertion length of the polarimeter is 9.5 m.

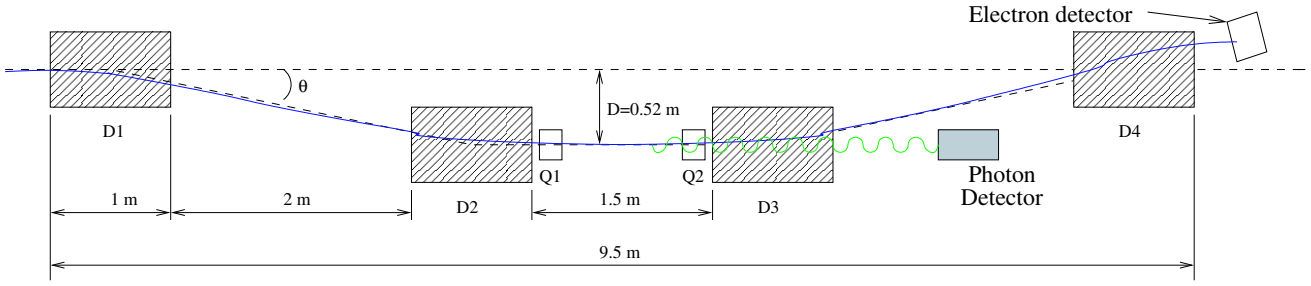

Figure 31: *Schematic diagram of the chicane.*

The beam deflection angle for each dipole is $\theta = 10.0°$. Entrance and exit pole edge angles are $\theta/2 = 5.0°$. The separation between dipoles D1 and D2 as well as between dipoles D3 and D4 is 2.0 m. The separation between D2 and D3 is 1.5 m and the beam offset, D=0.52 m. The dispersion following D4 is 5.2 mm/%, so for a 1 GeV incident beam, the separation of the scattered electron corresponding to the maximum energy of the back-scattered photons is 18.3 mm for a green laser. The separation is quite small but should be usable.

The B-Field in the dipoles for E = 1.0 GeV is 5.8 kG. This allows the polarimeter to be used up to a maximum beam energy of approximately 2.5 GeV. For operation at energies up to 6 or even 10 GeV the dipoles would have to be physically repositioned slightly. At 10 GeV, for example, the bend angle would be changed to $\theta = 2.5°$. In this configuration operating at an energy of 3.0 GeV the separation of the scattered electron is 14.3 mm which should be adequate.

A pair of very weak correction quadrupoles will be placed between D2 and D3. They will be used to dial out any residual chromaticity arising from physical misalignment or misadjustment of the dipoles. The drift space between D2 and D3 will be fully instrumented. A pair of beam position monitors will be used to adjust and control the electron beam to maximize the luminosity. A harp at the laser photon/electron beam interaction point will be used to monitor the electron beam profile.

The dipole magnets are similar to many which are currently in use at JLAB. They will be constructed of very soft iron; the amount of carbon will be less than 0.06%. Dipoles D1 and D4 will be constructed as H-magnets to keep the transverse dimensions small. The central dipoles,

D2 and D3, will be built as C-magnets to allow clearance for the undeflected beam. The magnet coils will be water cooled. The power supply current stability will be 1×10^{-4}.

5.2.2 Laser options

The relatively low intensity of the CEBAF beam ($\sim 100\ \mu$A) creates some difficulty in designing a Compton polarimeter. With existing standard visible and IR lasers, a 1% (statistics) measurement of the electron beam polarization would take on the order of days. This would be sufficient for Q^p_{Weak} given the planned several–month run time. However, in order to probe the systematics of the polarimeter itself and track the polarization of the electron beam over time, it is highly desirable to be able to make a measurement in several hours.

Table 11 lists the maximum scattered photon energy k_{max}, the maximum asymmetry A_{max}, and the average asymmetry $\langle A \rangle$ (integrating over all photon energies) for various electron energies. The table compares the results for three potential wavelengths of laser light, namely ultra-violet light at 248 nm, green light at 514.5 nm and infra-red light at 1064 nm. The total cross section σ_{TOT} goes down with decreasing wavelength but the asymmetry and the maximum backscattered photon energy increase. If we integrate over all the back-scattered Compton photon energies, the time required for a measurement of the polarization with precision δP_e depends on the inverse square of the average asymmetry $\langle A_l \rangle$ and the luminosity $\mathcal{L}$ according to

$$\Delta t = \frac{1}{\langle A_l \rangle^2 \, \delta P_e^2 \sigma_{TOT} \mathcal{L}}. \tag{6}$$

Clearly, we benefit from going to lower wavelengths for a given luminosity; however, it will still be necessary to maximize the luminosity. The maximum attainable luminosity occurs for non-crossing electron and photon beams; if the Rayleigh ranges of the two beams are matched,

$$\mathcal{L}_{max} = \frac{I_e P_\gamma}{e k_0 c} \frac{1}{\varepsilon_e + \varepsilon_\gamma}, \tag{7}$$

where I_e is the electron beam current, k_0 is the laser photon energy, and ε_e (ε_γ) is the emittance of the electron (photon) beam. The emittance is related to the Rayleigh range Z_e (Z_γ) and the beam spot size (characterized by the Gaussian standard deviation σ_e (σ_γ) at its narrowest point) according to $\varepsilon_{e,\gamma} = \sigma^2_{e,\gamma}/Z_{e,\gamma}$. If there is a small crossing angle α between the electron and photon beams, the luminosity is reduced to

$$\mathcal{L} \approx \frac{1 + \cos\alpha}{\sqrt{2\pi}} \frac{I_e P_\gamma}{e k_0 c} \frac{1}{\sqrt{\sigma_e^2 + \sigma_\gamma^2}} \frac{1}{\sin\alpha}. \tag{8}$$

To maximize the luminosity we need to maximize the laser power P_γ and/or minimize the crossing angle α.

There are several alternatives that one may pursue in order to reduce the needed measurement time. The solution chosen in JLab Hall A was to use a low–power IR laser in conjunction

Table 11: *Comparison of asymmetries, cross sections, and maximum back-scattered photon energies for three different wavelengths of laser light for some representative electron energies.*

E_e (GeV)	λ (nm)	k_{max} (MeV)	σ_{TOT} (b)	A_{max}	$\langle A \rangle$
0.85	248	51.9	0.625	0.0630	0.0148
	514.5	25.9	0.645	0.0309	0.0075
	1064	12.7	0.655	0.0151	0.0037
1.2	248	101.0	0.610	0.0877	0.0200
	514.5	50.9	0.637	0.0433	0.0104
	1064	25.2	0.651	0.0212	0.0052
2.5	248	401.7	0.563	0.1734	0.036
	514.5	211.2	0.610	0.0880	0.0201
	1064	106.8	0.637	0.0436	0.0104
5.0	248	1384.5	0.495	0.3133	0.0549
	514.5	779.1	0.566	0.1678	0.0351
	1064	409.7	0.612	0.0853	0.0195
7.5	248	2736.2	0.446	0.4251	0.0629
	514.5	1626.2	0.530	0.2397	0.0461
	1064	885.5	0.589	0.1250	0.0274
10.0	248	4336.9	0.409	0.5143	0.0644
	514.5	2696.2	0.499	0.3042	0.0539
	1064	1514.7	0.569	0.1628	0.0343

with a high gain Fabry–Perot cavity [3]. This provides an effective laser power of about 2100 W and enables a relatively fast measurement of the beam polarization. However, the Fabry–Perot cavity requires a complicated feedback system that significantly increases the cost and difficulty of building such a system.

Rather than using an external cavity to build up the (low) laser power, an alternative involves sending the electron beam through the laser cavity itself. This idea was originally conceived by Michael Dueren of the HERMES collaboration [5] and is shown schematically in Figure 32. Here, the output coupler is removed from the frame of the laser assembly and moved some distance from the nominal head of the laser. The polarization of the intra–cavity laser light is converted from linear to circular polarization via 1/4–wave plates. Ideally, one would like to focus the laser beam at the interaction point with the electron beam. This can be achieved using either a curved output coupler or a lens, although the latter requires careful design to ensure that the lens placement and focusing allows a stable solution to the cavity eigenmode equations.

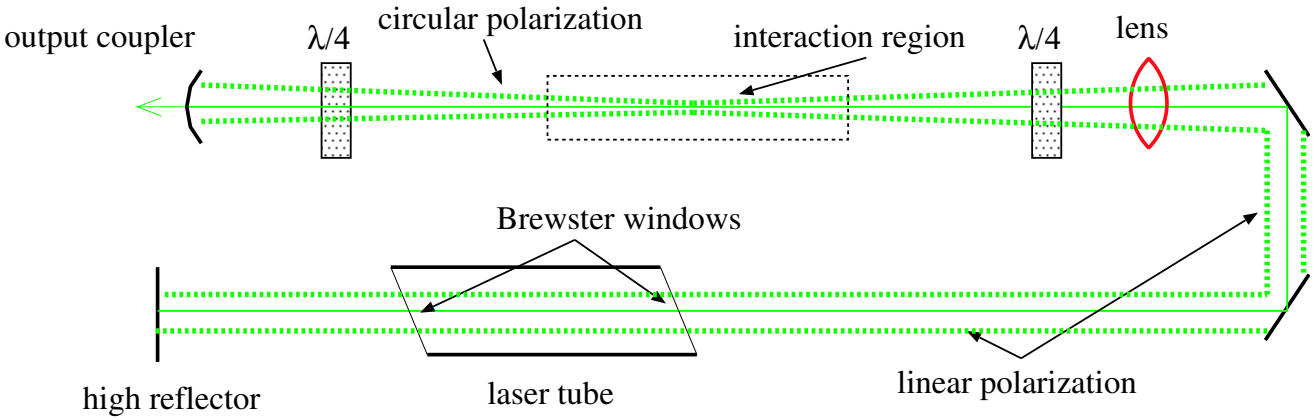

Figure 32: *Schematic of intra–cavity laser system for the Hall C Compton polarimeter. Laser light inside the cavity is usually linearly polarized due to the Brewster windows on the laser (gas) tube. The addition of 1/4–wave plates convert the linearly polarized photons to circularly polarized photons. An additional lens may be necessary to create a focus at the electron interaction point while keeping a fairly uniform beam size in the gain medium (laser tube).*

As an example, a typical Argon–ion laser with an output coupler reflectivity of 95% implies a power density $\approx$ 20 times larger inside the laser cavity. Hence, a 10 W laser has 200 W of power inside the laser cavity. The introduction of extra optical elements will increase absorption and reduce the intra–cavity power, however the power can in turn be increased by increasing the reflectivity of the output coupler.[4] One benefit of this intra–cavity design is that the complicated feedback mechanism that was necessary for the high gain external cavity design is no longer needed. The gain profile of the lasing medium ensures that several longitudinal modes will fulfill the resonance condition.

[4]Typically, one is interested in optimizing the power coming out of the laser and output couplers are usually chosen with this in mind. A higher reflectivity output coupler reduces the power coming out of the laser, but increases the intra–cavity power.

Such an intra–cavity design is being built and tested for the A4 experiment at Mainz. This system will use an Argon–ion laser and has been operated with 80 W of intra–cavity power [6]. For the Hall C Compton polarimeter, we are considering using a similar Argon–ion design. Commercial Argon–ion lasers that provide 10 W of power at 514 nm (green) are available [7]. Assuming that any intra–cavity losses created by introducing extra optical elements (1/4–wave plates and lens) can be offset by increasing the reflectivity of the output coupler, intra–cavity powers of 200 W should be accessible.

A second option under investigation is to use the intra–cavity design with a table–top, medium power UV excimer laser. Excimer lasers have become increasingly reliable to the point where extended periods (i.e. a few months) of remote operation now seem feasible. The benefits of UV lasers are clear: larger asymmetries and larger separation between the scattered electron and primary electron beam (although this latter benefit may not be useful, as will be discussed later). Two UV lasers are currently under consideration; an ArF laser at 193 nm providing 32 W nominal output and a KrF laser at 248 nm and nominal output power of $\approx$ 60 W. As with the Argon–ion option, the intra–cavity configuration should increase the effective laser power by about a factor of 20.

It should be noted that the emittance of the UV beam in the cavity for excimer lasers is much larger than the Rayleigh limit. The transverse size of the beam in the gain medium is typically several millimeters with a divergence angle of order 1 mrad. Using curved mirrors, such a beam can be brought to a focus at the interaction region with a spot size of order 200 μm r.m.s. and a divergence angle less than a degree. Such mirrors are available commercially with reflectivities in excess of 97% at 193nm. Apart from these details, the geometry for the UV laser cavity is similar to the one shown in Figure 32. Because of the high gain in the excimer medium, it is likely that the use of Brewster windows will not be sufficient to guarantee sufficiently pure polarization, in which case an additional polarizer must be added to absorb the unwanted mode.

For the Argon–ion option, one must use electron–photon coincidences to eliminate the rate in the photon counter not coming from Compton events. Another way to subtract this background is to operate the laser in pulsed mode and measure the background by monitoring the photon counter during the intervals between the pulses. In fact, this is the only option in the case of a UV laser because, at a typical pulse repetition rate of 1 kHz and pulse duration of 10-15 ns, the coincidence method is ruled out. Moreover several backscatter events will appear in the photon counter during each pulse, and only the total energy will be measured. This kind of energy–weighted counting has the advantage that it improves the average asymmetry by giving a larger weight to the part of the Compton spectrum where the asymmetry is largest, close to 180 degrees. The effect is that the run time required to reach a given level of statistical precision is reduced by more than a factor of 2 relative to a simple unweighted counting procedure. A similar weighting may also be applied to data collected in coincidence mode, if the pulse height is recorded.

In Table 12, we compare the options described above. As a baseline, we list the Hall A Compton polarimeter which is proven to give adequate rates at CEBAF currents and energies. To facilitate the comparison of each method, we define a simple figure–of–merit which is the

Table 12: *Figure–of–merit comparison of proposed laser options for the Hall C Compton polarimeter, for comparison, the Hall A configuration is also shown. The figure–of–merit is simply the time needed for a 1% (statistical) measurement of the electron beam polarization assuming an 80% polarized beam at 180 μA. Further assumptions include $\sigma_e = 100$ μm, $\sigma_\gamma = 100$ μm (200) μm for the Argon–ion (UV) laser, $E_{e,beam} = 1.165$ GeV and a crossing angle of 2 degrees between the electron and laser beams.*

Method	λ (nm)	Power (Watts)	E_γ^{max} (MeV)	$\int dE\sigma$ (mb)	Rate (KHz)	$\langle A \rangle$ (%)	t (1%) (min)
Hall A	1064	2100	23.7	514	350.4	0.68	16
Ar–Ion	514	10	48.1	501	0.8	1.37	1762
–intra–cavity		200			15.7		88
UV ArF	193	32	119.8	463	0.6	5.26	193
–intra–cavity		640			11.6		10
UV KrF	248	60	95.4	476	1.4	4.30	122
–intra–cavity		1200			28.5		6

time needed to make a 1% statistical measurement of the electron beam polarization assuming $P_e = 80\%$, and a perfect photon detector with 1 mrad angular acceptance. We further assume Q^p_{Weak} running conditions, $E_{beam} = 1.165$ GeV and $I_e = 180$ μA. The beam size at the interaction point for the electron beam is assumed to 100 μm (r.m.s.), the laser beam size 100 μm (200 μm) for the Argon–ion (UV) laser, and the crossing angle between the two beams is assumed to be 2 degrees. For the Hall A IR and Argon–ion option, the rates and measurement time are calculated assuming a pure "photon–counting" method, while the UV alternatives are calculated assuming energy–weighted counting.

From Table 12, we see that, even without the luminosity increase that comes from scattering the electrons from the laser light inside the laser cavity, the UV laser options are already comparable to the Argon–ion intra–cavity option (although the Argon–ion option would take about a factor of two less time if one used the energy–weighted counting method). The increase in flux that comes from intra–cavity scattering then puts the UV options on the same footing as the Hall A external cavity option.

The collaboration has extensive experience with Argon–ion lasers and can additionally draw on the expertise and experience of the Mainz A4 polarimeter collaboration. The intra–cavity Argon–ion laser option should be relatively straightforward to implement from a technical point of view and provides adequate rates to perform a polarization measurement on the several hour time scale. The UV option, on the other hand may prove to be slightly more challenging, but the benefits of this option merit further exploration. Over the short term, the Hall C Compton

polarimeter group plans to build a prototype of the Argon–ion intra–cavity system while further investigating the possibility of doing so with a moderate power UV system. It should also be noted that if the UV option proves workable, this would allow more flexibility in the design of the magnet chicane since coincident electron detection would no longer be necessary.

We are currently considering a couple of laser cavity geometries. The first idea is to fire the laser through the third dipole and out of the second dipole, thereby minimizing the crossing angle α. A concern for this design is synchrotron radiation damage of optical elements. The second idea is to place the laser cavity in between D2 and D3 at a $\sim 2-3^{\circ}$ angle with respect to the primary electron beam direction.

5.2.3 Photon Detector

In order to construct a compact, fast photon detector, we require a material with a small decay time and high density. We also require it to be radiation-hard. Since the asymmetry is strongly dependent on the back-scattered photon energy, some benefit can be gained from measuring the energy accurately. We would need good energy resolution and a procedure to calibrate the energy response of the detector. The resolution depends on photon statistics and how well the energy is contained within the active volume (i.e., we need to minimize shower leakage out of the sides of the detector). We would like the energy resolution to be less than ~10-20% at 50 MeV.

Various inorganic crystals are available for calorimetry; table 13 lists the properties of some of the crystals we are considering. NaI(Tl) has the highest light output of the crystals we are considering but must be hermetically sealed because it is hygroscopic. It is somewhat slow (230 ns decay constant) and suffers from radiation damage for an absorbed dose above about 1 Gray (100 rad)[8]. Undoped CsI has faster timing characteristics and is more radiation-hard than NaI(Tl) but the light output is poor compared to NaI(Tl) and is strongly dependent on temperature[9]. BGO ($Bi_4Ge_3O_{12}$) is very dense but it is also relatively slow and the light output also drops with increasing temperature[10]. $PbWO_4$ has the highest density and smallest radiation length of the materials we are considering; unfortunately, it also has the smallest light output. Furthermore, the material exhibits a $\sim 2\%/^{\circ}C$ variation in light output[11]. Nevertheless, we are currently leaning toward using $PbWO_4$ because of its small radiation length, fast timing characteristics, and radiation hardness. This material is currently being used in the Hall A Compton setup.

Preliminary GEANT simulations done for the Mainz polarimeter design (E_e=0.855 GeV, λ=514.5 nm) suggest that the optimum size for the photon detector (if space considerations are critical) is about $4R_M \times 4R_M \times 10X_0$, where X_0 is the radiation length of the detector material and R_M is the Moliere radius. Smaller crystals would lead to an unacceptable amount of leakage.

There are a couple of alternatives for calibrating the response of the crystals. They can be studied using tagged photon beams at Mainz or Hall B at JLAB. Alternatively, the Compton edge (corresponding to the maximum photon energy) provides a point of known energy for a given electron beam energy and laser wavelength.

Table 13: *Physical characteristics of potential calorimeter materials (at or near room temperature). Here λ_{max} is the wavelength of maximum emission of scintillation light, τ is the decay constant, X_0 is the radiation length, ρ is the density, and R_M is the Moliere radius of the material.*

Material	λ_{max}(nm)	τ(ns)	$\rho(g/cm^3)$	N_γ/MeV	X_0(cm)	R_M(cm)
NaI(Tl)	415	230	3.67	38000	2.6	4.5
CsI(undoped)	315	16,35?	4.51	2300	1.9	3.8
$Bi_4Ge_3O_{12}$	480	300	7.13	8200	1.1	2.4
Lead Glass			3.5-3.9		2.3-2.6	3.0-5.0
$PbWO_4$	460	$\sim$5,$\sim$20, $\sim$100,$\sim$1000	8.28	$\sim$500	0.9	2.2

5.2.4 Electron detector

Because the scattered electron loses energy to the backscattered photon during the Compton interaction, it undergoes a larger deflection in the chicane magnets than the primary beam. Consequently, the scattered electrons are separated from the primary beam by a small amount as they exit the chicane. We plan to take advantage of this to detect the scattered electron for a range in back-scattered photon energies. The highest energy scattered electron we can detect is limited by how close the detector can be placed relative to the primary beam axis. One of the options we are considering is to use a ribbon of scintillating fibers oriented in a plane perpendicular to the electron beam's direction. One drawback of this design is the potential for radiation damage to render the fibers useless. To mitigate this problem, the position of the ribbon with respect to the primary beam would be remote-controllable. In particular the detector would be completely retracted while beam tuning is underway to minimize unnecessary radiation damage.

An alternative to using scintillating fibers is to use silicon micro-strips. An electron detector based on these strips has already been developed for the Hall A Compton polarimeter. We are currently considering the feasibility of both options.

References

[1] M. Hauger *et al.*, "A high-precision polarimeter", NIM A461, 382 (2001), and nucl-ex/9910013.

[2] Matt Poelker, injector group guru, private communication.

[3] M. Baylac *et al.*, Phys. Lett. B **539**, 8 (2002).

[4] M. Hauger *et al.*, Nucl. Instrum. Meth. A **462**, 382 (2001) [arXiv:nucl-ex/9910013].

[5] M. Dueren, HERMES Internal Report 00–005 (2000).

[6] Y. Imai, Institut für Kernphysik at Universität Mainz, private communication.

[7] "SPECTRA–PHYSICS Beamlok Argon Ion Laser Beam Specifications", available at http://www.spectra-physics.com/products/pdfs/BeamLokPowerSpecifications.pdf

[8] "NaI(Tl) and PolyScin NaI(Tl) Sodium Iodide Scintillation Material", available at http://www.detectors.saint-gobain.com/Media/Documents/sodium%20iodide_62502.pdf .

[9] The Product Data Sheet for CsI is available at http://www.detectors.saint-gobain.com/Media/Documents/cesium%20iodide_602.pdf .

[10] The Product Data Sheet for BGO is available at http://www.detectors.saint-gobain.com/Media/Documents/bgo_602.pdf .

[11] D. Neyret *et al.*, Nucl. Instrum. Meth. A **443**, 231 (2000).

6 Polarized Source Issues for the Q^p_{Weak} Experiment

The Q^p_{Weak} experiment requires high average current with high polarization. Beam polarization has consistently been greater than 70 percent for the past few years at Jlab. Recent modification of photocathode cleaning techniques have produced a modest increase in polarization. Users report beam polarization in the upper 70's. The Source Group will continue to work to improve polarization with the goal of routinely providing polarization greater than 80 percent. New photocathode samples from Bandwidth Semiconductor (formerly Spire Corporation) and from Prof. Mamaev's group at the State Technical University, St.Petersburg are being tested at the Injector Test Stand at Jlab. Over the next few years, the source group expects to meet their goal of routine delivery of beam with polarization greater than 80 percent. The source group recommends restricting the combined maximum current to other users during Q^p_{Weak} to less than 50 muA. This will keep the total extracted gun current for all users to approximately 350 μA, a level not drastically greater than what we have successfully demonstrated (we have extracted 250 μA for weeks during simultaneous delivery to the G_{en} experiment in Hall C and G_{ep} experiment in Hall A). It is worth noting that successful delivery of 200 μA to Hall C will necessitate a better understanding of beam optics at the injector and possibly, other portions of the accelerator. The most production current delivered to a single user during a physics experiment has been 140 μA.

The dominant Polarized Source issue associated with this requirement is photocathode lifetime. Based on past experience, JLab photo-guns should be able to deliver 200 μA average current with 499 MHz pulse repetition rate to Hall C for 1 week, at which point the photocathode QE will have degraded and the laser spot will need to be moved to a fresh location on the photocathode surface. The laser spot diameter is approximately 0.5 mm and the photocathode active area is 5mm. Past experience indicates this provides roughly 5 photocathode locations, therefore we can expect 5 weeks of uninterrupted beam time for Q^p_{Weak}. After delivering beam from all available photocathode locations, subsequent high current operation will require heating and reactivating the photocathode. This process takes 8 hours and completely restores the photocathode QE. This task can be accomplished during a scheduled accelerator shutdown. Following reactivation, one can expect another 5 weeks of beam delivery. The source group will use a mode locked Ti-Sapphire laser from the vendor TimeBandwidth Products to drive the photocathode. This laser has been ordered, they expect delivery January, 2003. The source group will commission this laser during the Hall A HAPPEX II experiment Spring, 2003. Should the commercial laser prove unacceptable for use at the photoinjector, a homebuilt modelocked Ti-Sapphire laser can be used for Q^p_{Weak}. A version of the homebuilt laser was used for the high current, high polarization Gen experiment at Hall C. It has since been improved and the source group expects to test it at the photo-injector winter, 2002.

Reduced Duty Factor Modes of Operation are required for calibration runs. Specifically, low average current with unpolarized beam. These setups fall into several general categories as discussed below.

6.1 G0 Beam Microstructure

The existing G0 laser can be made available to provide Q^p_{Weak} with reduced duty factor beam suitable for calibration runs with the following parameters; beam with rf micropulses spaced 32 nsec apart (16th subharmonic of the standard 499 MHz repetition rate, or 31.1875 MHz) and average current from nA's to a few μA's, no beam polarization required. If Q^p_{Weak} must routinely take beam with the G0 time structure, the Source Group may pursue a diode-laser based system in an effort to save space on the laser table. Diode lasers with 31 MHz pulse repetition rate are low power devices but they may provide nA beam current suitable for this application.

6.2 Short Macropulse Mode with rf Microstructure

Q^p_{Weak} will also require a macropulse beam that contains 499 MHz microstructure for routine calibration runs. The beam parameters are; a macropulse duration of approximately 50 to 100 ns with repetition rate variable between 100 kHz and 1 MHz, an average current of a few nA and no polarization requirement. This is a new beam time structure for Jlab and some development is required. The Source Group envisions a gain switched diode laser to create the 499 MHz microstructure and a pulsed DC bias to create this calibration macropulse structure. The Source Group is confident this can be accomplished.

6.3 Control of Helicity Correlated Beam Residuals

Control of helicity correlated residuals will be accomplished in a manner similar to that used for the G0 and HAPPEX2 parity violation experiments. Every effort will be made to minimize the free-running beam asymmetries (e.g., properly aligned Pockels cell, rotating half-wave plate downstream of the pockel cell oriented to provide small helicity correlated asymmetries for all Users). Hall C will own and control independent optical elements to provide feedback to minimize helicity correlated charge and position asymmetry (low voltage IA pockel cell for charge asymmetry control and pzt mirror for position asymmetry control).

7 Tracking System

Good Q^2 determination is critical to the Q^p_{Weak} experiment, since the asymmetry at low Q^2 is directly proportional to Q^2. Thus, an error in Q^2 directly translates to an error in the extraction of Q^p_{Weak}. We are interested in determining the acceptance weighted distribution of Q^2, averaged over the acceptance and weighted by the analog response of the Čerenkov detectors. We intend to minimize the problem by making the entrance collimator the sole limiting aperture for elastically scattered events. Therefore, good knowledge of the collimator geometry and spacial location with respect to the target and the neutral beam axis will be sufficient to reduce a number of potential systematic errors. Furthermore, we plan to optimize the Čerenkov detector geometry to make its response as independent of Q^2 as possible. The long axis of the detector is along the azimuthal coordinate ϕ and, although the rate will necessarily change over the two meter length of the detector, there should be little physics dependence along this axis. To first order, ignoring finite target length, the optics focuses the elastic peak to a point along the short axis and thereby maps all Q^2 to the similar detector regions, although with differing angles of incidence. Optics studies and detector calibration measurements will be performed to correct deviations from ideal behavior. Residual effects due to multiple scattering and radiation effects in the spectrometer transport will be measured, analyzed, and corrected. Corrections will be made, as well, for inelastic and room background contributions. Initial simulations indicate that these will be small, the main contribution coming from target walls, which can be measured and subtracted. All these issues have been successfully dealt will in the previous HAPPEX[1] experiments and we plan to build on this experience.

The Hall A Proton Parity Experiment (HAPPEX) demonstrated that the proper acceptance averaged value of Q^2 was the most difficult part of the experiment to extract from the data.[1] The basic detection scheme for Q^p_{Weak} is in fact quite similar in concept to that used for HAPPEX. That is, the primary Čerenkov detectors are located in a shielded hut encapsulating the focal plane of a focusing spectrometer. The Q^2 determination for HAPPEX was made by using the standard Vertical Drift Chambers (VDC) tracking chambers installed in the High Resolution Spectrometer (HRS) detector huts. Like HAPPEX, the beam currents will have to be substantially reduced to use the counting mode electronics need for the Q^2 measurements. Thus, we will be sampling the Q^2 distribution at low currents and will have to model (or otherwise determine) any changes in the target density profile due to target heating at higher currents. Unlike HAPPEX, the intrinsic resolution and focusing properties of the Q^p_{Weak} spectrometer will not be sufficient to adequately determine the acceptance weighted Q^2 solely by the use of rear tracking chambers. Front tracking chambers will be needed as well. However, the alignment issues that were the most problematic sources of error for HAPPEX will be much simpler for Q^p_{Weak}, where the spectrometer has no quad elements to steer the beam, and where the entire device can easily aligned along a single axis, with good line of sight.

7.1 Q^2 Determination Requirements

The PV asymmetry can be separated into a term linear in Q^2 involving Q^p_{Weak}, and additional terms entering at higher powers of Q^2 called the QCD correction[2]:

$$A = -a_0 \tau Q_{weak} + A_{QCD},$$

$$A_{QCD} = a_0 \tau \left\{ \frac{\varepsilon G_E^\gamma (G_E^n + G_E^s) + \tau G_M^\gamma (G_M^n + G_M^s) - \varepsilon' [1 - \sin^2 \theta_W] G_M^p G_A^Z}{\varepsilon (G_E^\gamma)^2 + \tau (G_M^\gamma)^2} \right\},$$

$$a_0 \approx 316.7 ppm.$$

The electric charges of the neutron and strange quark sea are zero, so the Electric terms are of the same leading order in $\tau = Q^2/4m^2$ as the Magnetic and Axial Vector contributions. The only direct dependence on beam energy E is through the longitudinal polarization ε, which can be written for the elastic scattering case as:

$$\varepsilon = \left[1 + \frac{2(1+\tau)\tau}{1 - 2\tau(m/E)} \left(\frac{m}{E} \right)^2 \right] \underset{\tau=0}{\longrightarrow} 1,$$

$$\varepsilon' = \sqrt{(1-\varepsilon^2)\,(1+\tau)\,\tau} \underset{\tau \to 0}{\longrightarrow} 2\,(m/E)\,\tau.$$

Therefore, for constant beam energy, the QCD correction can be expanded in a power series in τ:

$$A_{QCD} = a_0 \tau^2 \sum_{n=0} B_{V,n}(m/E) \tau^n + 2 \frac{m}{E} B_{A,n}(m/E) \tau^n.$$

The leading contributions have been calculated by Ramsey-Musolf[2] using the $\overline{\text{MS}}$ coupling scheme:

$$Q_{weak} = (1 + R_V^p) \left[1 - 4 \sin^2 \theta_W \right],$$

$$B_{V,0} = (1 + R_V^n) \left[\mu_p \mu_n + \rho_n \right] + (1 + R_V^s) \left[\mu_p \mu_s + \rho_s \right],$$

$$B_{A,0} = [1 - 4 \sin^2 \theta_W] \{ -2[1 + R_A^3] G_A^3(0) + \sqrt{3} R_A^3 G_A^8(0) + [1 + R_A^s] G_A^s(0) \},$$

$$G_A^3(0) = \frac{g_A}{2},\ G_A^8(0) = \frac{g_A}{2\sqrt{3}}\left(\frac{3f-1}{f+1}\right),$$

$$\rho_{n,s} = \left.\frac{dG_E^{n,s}}{d\tau}\right|_{\tau=0},\ g_A = 1.261,\ f = F/D \approx 0.64.$$

Here, $R_{V,A}$ denote weak vector and axial-vector radiative corrections, respectively. If we define the acceptance averaged measurement of the asymmetry as the average over the extended target and spectrometer acceptance and weighted by the analog response of the detector, *i.e.,* $\langle A_{\rm exp}\rangle$, then, Q^p_{Weak} can be extracted from the data as follows:

$$Q_{weak} = \frac{1}{a_0}\frac{\langle A_{\rm exp}\rangle - \langle A_{QCD}\rangle}{\langle\tau\rangle} \approx \frac{\langle A_{\rm exp}\rangle - B_V(0)\,\langle\tau^2\rangle - B_A(0)\,\langle(2m/E)\tau^2\rangle}{a_0\,\langle\tau\rangle}.$$

Of course, in a full Monte Carlo Analysis, all significant moments would be included, but since $\tau \approx 0.01$, the higher moments are hardly significant for Q^p_{Weak} kinematics. The moments $B_{V,n}$ and $B_{A,n}$ would be extracted from a combined analysis with the HAPPEX and G0 data. The incident energy E is a constant in the absence of straggling and Bremsstralung in the target.

Reconstruction of the Q^2 calibration data gives the important moments, $\langle\tau\rangle$, $\langle\tau^2\rangle$, and $\langle\tau^2 m/E\rangle$ with high accuracy; however, the Q^2 measurement algorithm does not know about internal and external Bremsstralung. There are different experimental prescriptions for measuring Q^2 on an event-by-event basis. The most unambiguous is to use the front chambers to reconstruct the scattering angle and to define the incident energy at the scattering vertex as the most probable energy at the scattering point. Then, using elastic scattering kinematics, we find

$$Q^2\big|_{measured} = \frac{4\bar{E}^2\sin^2\theta/2}{1+2\frac{\bar{E}}{m}\sin^2\theta/2}$$

where $\bar{E} = E - (dE/dX)\Delta X_{vertex}$. In the peaking approximation, the scattering angle is unchanged by radiation and the correct incident energy at the vertex is given by

$$E_{vertex} = \bar{E} - \nu_{before}$$

where ν_{before} is the energy radiated before scattering. Then we apply a small Monte Carlo correction to determine Q^2 at the radiative vertex:

$$\langle\tau_{true}\rangle = \left.\frac{\langle Q^2(E_{vertex},\theta_e\rangle_{rad}}{\langle Q^2(\bar{E},\theta_e\rangle_{measured}}\right|_{MC}\langle\tau_{measured}\rangle$$

The resulting correction resulted in a reduction in Q^2 of less than 1% for the HAPPEX experiment, with similar results expected for Q^p_{Weak} kinematics[3].

7.2 Anticipated Accuracy in the Determination of Average Q^2

Since the parity-violating asymmetry is proportional to Q^2, it is critical to determine the average Q^2 for the electrons from the *ep* elastic scattering events of interest with $\simeq 1\%$ accuracy. The absolute beam energy will be known to $\leq 0.1\%$ accuracy using the Hall C energy measurement system. The central scattering angle for each collimator will be determined by redundant survey techniques to ≤ 1 mrad. Over short baselines, the JLab alignment group routinely achieves this accuracy. As was the experience from the HAPPEX experiment, angle errors will dominate the error in Q^2. In particular, the error for our kinematics is approximately 1.4%/mrad. The carefully measured target and collimator geometries relative to the electron beamline will then define the Q^2 bite in a simulation which properly accounts for radiative and multiple-scattering effects.

This is an integrating experiment, so determination of the average Q^2 has further complications. The Q^2 dependence of the *ep* cross-section will bias the average detected Q^2. This and any position-dependent detector bias must be taken into account (since Q^2 may be correlated with position at the focal plane). Although in principle these matters can be simulated, it is essential to check the experiment Monte Carlo using an ancillary calibration measurement: to measure the shape of the focal plane distributions, and to measure the position-dependent detector bias. Careful thought needs to go into the choice of survey techniques. Furthermore, since survey and alignment are critical, it is important that the experiment be designed from the outset such that the beamline, cryotarget and collimators can be accurately and redundantly surveyed.

Figure 33 shows an estimate of effects due to random angle errors, whether due to multiple scattering or hit position uncertainties in the chambers used to track electron paths. The black histogram shows the nominal Q^2 distribution. The red and green histograms show the Q^2 distribution reconstructed from the measured angle of deflection of electrons in the magnetic field. The red histogram is the result without angle uncertainties. The green histogram shows the effect of a 0.5° smearing of deflection angle. Although the effects of the smearing are evident, the angle smearing changes the average measured Q^2 by only 0.2%.

7.3 Tracking System Design Concept

The Q^p_{Weak} toroidal spectrometer, QTOR, views most of the 2π azimuthal acceptance at small forward scattering angles and is segmented into 8 octants. Figure 34 shows the expected distribution of events in the focal plane. In the absence of radiative processes, the elastic peak is entirely contained within the detector volume, minimizing edge effects. The inelastic response begins at pion threshold and is outside of the volume of acceptance. The focal plane of each octant is large, with a perpendicular cross-sectional area just before the quartz Čerenkov detectors of about $10 \times 200 cm^2$. To cover this area, wire chambers would have to be somewhat wider: about 25 cm wide, by 2 m long. For comparison, the internal dimensions of the HRS VDCs are 28 cm by 2.4 m long.

Three regions of tracking chambers are envisioned: The Region 1 vertex chamber having

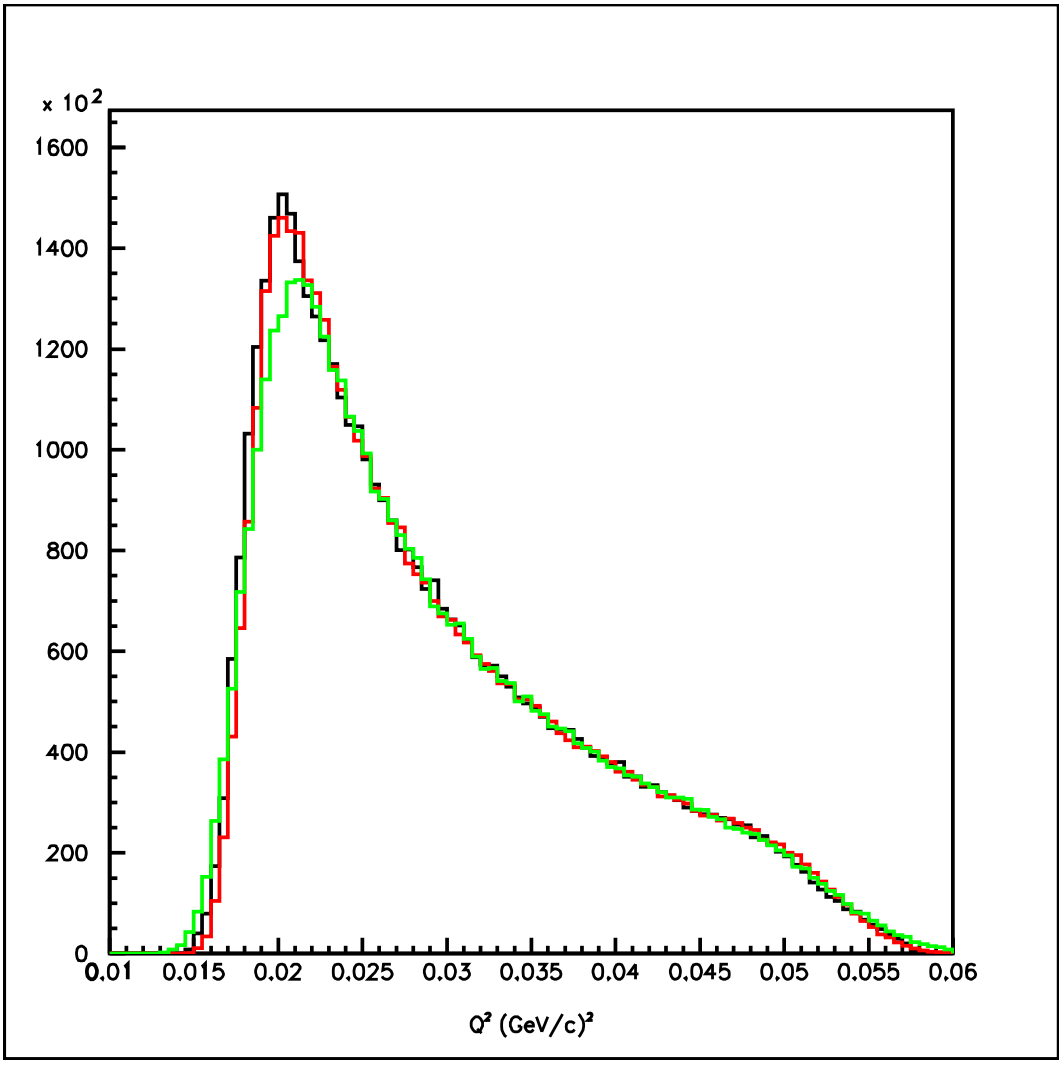

Figure 33: The black histogram shows the distribution of Q^2. The red histogram represents the Q^2 distribution as reconstructed from the measured angle of deflection of electrons in the magnetic field. The green histogram is the reconstructed Q^2 distribution when the deflection angle is smeared by 0.5°.

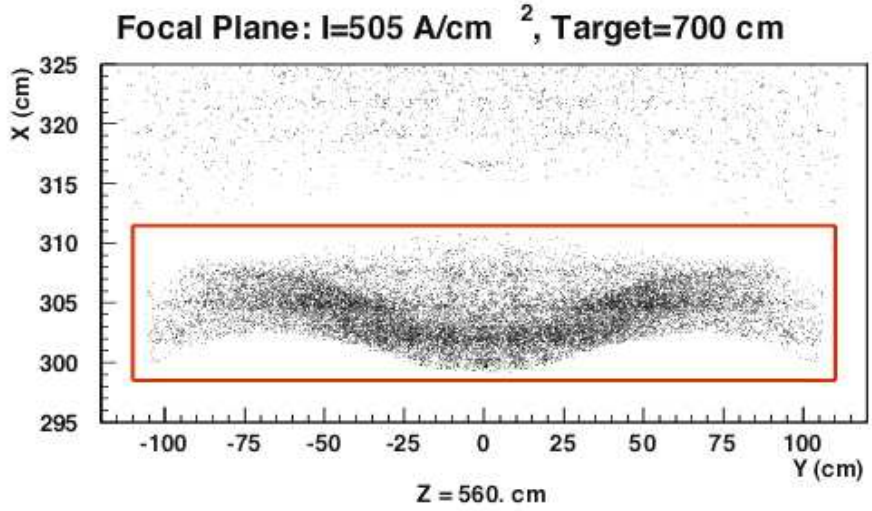

Figure 34: *Expected distribution of events in the focal plane. The box shows the area of coverage by the Čerenkov detectors. Inelastic electrons from pion production at threshold are well separated.*

excellent position resolution will be registered directly to the rear face of the collimator. Down stream from that, at the entrance of the spectrometer, magnet entrance chambers will be placed. The spatial separation between the two sets of chambers will define the scattering angle (and therefore Q^2) of elastically scattered events to high accuracy. To momentum analyze the events and for background analysis purposes, a third region of tracking chambers will be needed at the focal plane. These Region 3 chambers will provide a complete characterization of the particle trajectories entering the Čerenkov detector and of its response. The Q^p_{Weak} focal plane geometry, like that of HAPPEX, is well suited for use of VDCs. Fortuitously, we have an existing technical design of similar mechanical scale to draw upon as a reference design. This simplifies, somewhat, the cost and design analysis for these chambers. However, we retain the option to use a unified design approach for the Region 2 and Region 3 chambers if that proves to be of significant benefit in reducing cost and complexity. Figure 35 shows a cross section of the spectrometers indicating the positions of the three chamber packages. To contain costs, we plan to instrument only two complete sets of chambers on opposite sides of the beam line and rotate them to sample all other sectors sequentially as shown in Figure 35. The calibration runs are not time intensive and will not need to be repeated frequently, therefore the beam time overhead involved with this approach is acceptable.

7.4 Rate Considerations for Counting Mode Tracking Chambers

The instantaneous counting rate per octant at the focal plane is high, about 800 MHz. Fortunately, the beam current can be reduced from 200μA to 10nA for sampling purposes. This results in instantaneous counting mode rate of about 40 kHz/Octant at the focal plane. This could be further down sampled by a factor of 40 resulting in a data acquisition rate of about one

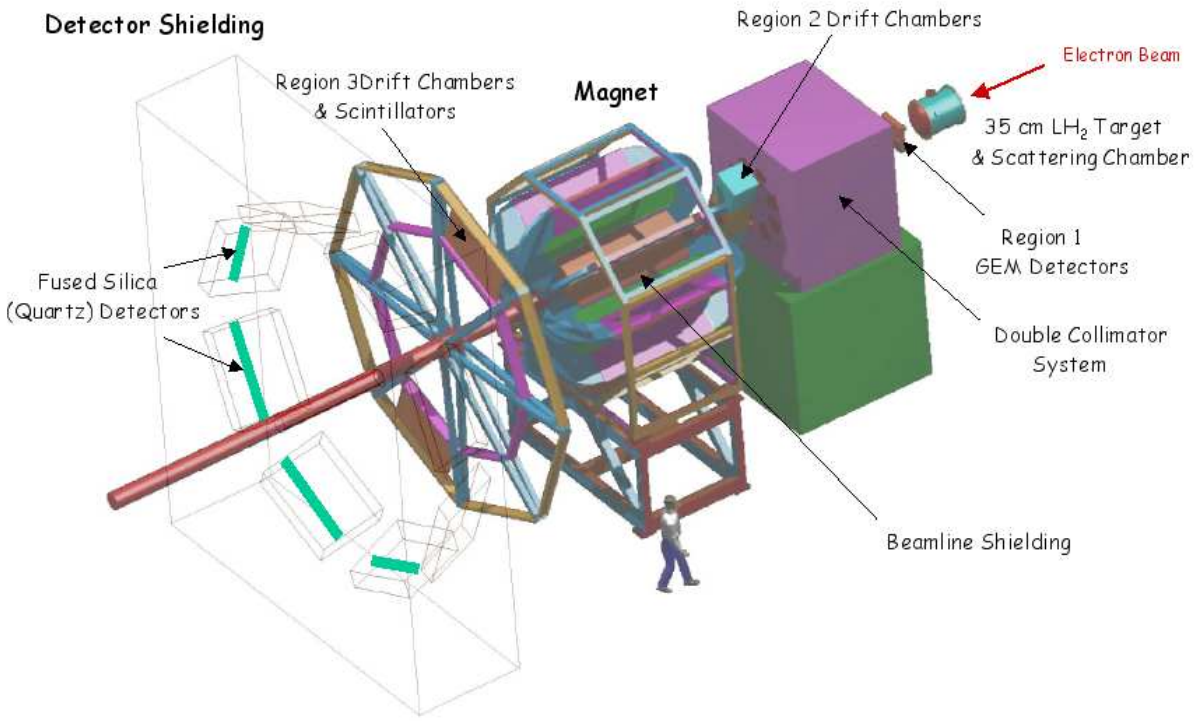

Figure 35: *CAD Illustration of the Q^p_{Weak} spectrometer showing the locations of the Regions 2 and 3 tracking chambers in relation to the overall apparatus. The region 1 GEM detectors are downstream of the target assembly, but not visible in the perspective of this drawing.*

kHz per octant. At the entrance to the spectrometer, rates are 2 orders of magnitude higher, and are dominated by low energy Møller electrons that fall within the collimator acceptance. To compensate, the Region 1 chambers will be GEM detectors, which are radiation hard and can work at the anticipated rates.

7.5 Mini-Toroid Møller Electron Sweeping Magnet

A low field mini-toroid sweeping magnet will be installed between the two collimator assemblies separating the Region 1 GEMs and Region 2 drift chambers to prevent Møller events from reaching the Region 2 chambers during low current calibration studies. The field polarity of this mini-torus would sweep Møller electrons into the inner radius of the second collimator. To reduce radiation damage when running under high-current parity production mode, the Region 2 tracking chambers will be moved out of direct line of sight of the electron trajectories and the chamber high voltages turned off. In the case of the Region 3 chambers in front of the detectors it should be sufficient to turn the high voltage off while leaving the chambers in place.

The min-toroid will need to have a field integral of 0.015 T-m (2% of the QTOR field

integral) to sweep the Møller electrons into the secondary collimator. It will pre-bend the elastic e-p electrons by about 3.5 mrad. The mini-torus will remain on during production running to maintain the same conditions between production running and Q^2 calibration runs. To study the effects of the sweeping magnet, we can run at very low beam currents (1 nA) to get a tolerable rate of about 420 kHz in the chambers. The mini-torus provides no significant shielding of the primary detectors during production running as any low energy Møllers that approach the QTOR magnet are deflected 180 degrees.

7.6 Region 1 Front Vertex Detectors

A front tracking system for Q^p_{Weak} needs to be more resistive to radiation than the remaining downstream elements because of its close proximity to the target. Even though the elastic rates at a beam current of 10 nA would approach 40 kHz, a large low electron momentum (50 MeV) background due to Møller scattering will be present which is at least a factor of 100 larger than the elastic rate. This large signal from Møller scattering will prevent the use of traditional drift chambers in the forward region. A tracking system in the forward region would need to survive for an extended period of time in a high radiation environment with doses of 1 Mrad/year and sustain a particle flux in excess of 1,000 particles per square millimeter of detector area every second.

The Gas Electron Multiplier (GEM) is one such high flux structure used to amplify the ionized charge within a gas chamber and thereby facilitate the detection of a charged particle trajectory. Micropattern gaseous detectors have matured substantially since the first introduction of the Micro-Strip gas chamber in 1988 [4]. Expensive and fragile Micro-Strip gas chambers with thin anode lines have been replaced by inexpensive and more robust structures. As shown in Figure 36, a GEM is basically a thin polymer (kapton) foil, metal-clad on both sides and perforated by holes having a radius on the order of 50 μm in a staggered grid pattern in which the distance between adjacent holes is on the order of 100 μm. The foil then acts as a pre-amplifier when immersed in the gas volume used by particle detectors which operate by ionization. Charge multiplication occurs when the electrons pass through the foil holes whose sides have had a electric potential difference applied to produce electric fields on the order of 40 kV/cm. The large amplification provided, beyond 10^4, facilitates single particle detection by charge collectors which may be as simple as a printed circuit board.

The design of the forward tracking system will be based on the tracking system which is used by COMPASS and has a well established performance record. In addition to adopting the triple GEM pre-amplification method employed by COMPASS, a similar multiplexing system will be used to minimize the amount of readout electronics by taking advantage of the small electron angle normal to the detector which limits the trajectory to a transverse distance of 5 mm across the face of the detector.

The ionization chamber is a lightweight structure built from Rohacell, aluminum, and kapton foils. The front entrance window to the detector is a sheet of 1mm thick Rohacell which supports a copper-cladded kapton sheet 50 μm thick. The walls of the ionization region are created

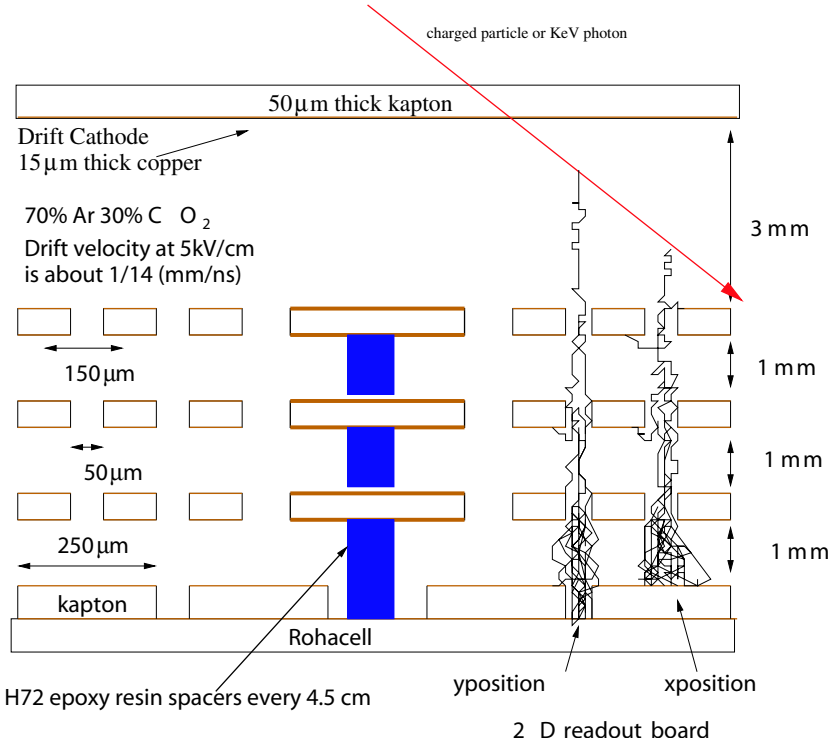

Figure 36: *The image is the side view of an ionization based tracking chamber with three GEM preamps and 2-D readout board.*

using a 3mm thick aluminum spacer. The first of three GEM foils is attached to the aluminum spacer. Each of the three foils is supported by a aluminum mesh (shown in purple in Figure 36 which is composed of several 8cm square regions that have H72 epoxy spacer spaced every 4.5 cm between the GEM foils and the aluminum mesh support. A charge detector, supported by Rohacell, is then attached to the rear of the chamber. The ionization chamber will be built using the students, faculty and staff at Louisiana Tech with substantial support from the Institute of Micromanufacturing (IfM) at Louisiana Tech.

Although the GEM foils will be purchased from CERN, the charge collector will be built at Louisiana Tech using a laser machining tool purchased from Trumpf Inc. [6] to mill kapton foils purchased from Boedeker Plastics [7]. This CO_2 laser has the ability to both cut and mill with a precision of 10 μm. The laser will be used to mill away material and construct a two dimensional charge collector to determine the position of the produced ions that will signal the position of a high energy electron responsible for the ionization. As shown in Figure 37, the charge collector will have 3 layers: 2 layers of conducting material with an insulator separating them. A charge collector pitch of 250 μm will provide sufficient resolution to facilitate a measurement of Q^2 with a relative error of 0.7%. Such charge collectors have been built with a pitch of 50 μm using photolithography techniques like those used for GEM foils.

Once charge is accumulated at the collector, pulse shaping and amplification electronics are needed which will convert a charge equivalent to 500 electrons to a mV signal. A multiplexing

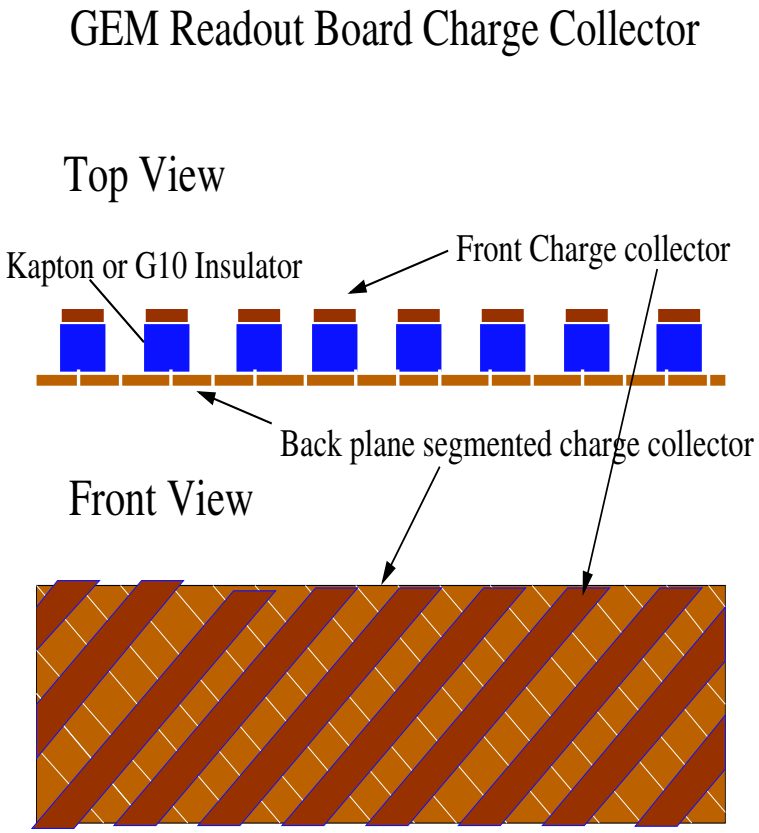

Figure 37: *2-D GEM Readout Board.*

circuit [8] was developed by ASIC laboratories and used by COMPASS to minimize the number of modules used to read out the charge collector signals. The pulse shaping and amplification electronics were incorporated into the multiplexing chip and wire-bonded to kapton leads that were connected to individual charge collector output channels. The resulting signal from a typical cosmic ray event is shown in Figure 38. An improved version of the HELIX chip, known as the BEETLE chip has been used to read out inner tracker Silicon prototype sensors which were tested in the X7 beam line of the SPS accelerator at CERN using a 120 GeV muon beam [9].

A majority of the performance information available on the use of a GEM based ionization chamber which is relevant for its application in the Q^p_{Weak} experiment comes from the use of such a device in the COMPASS experiment. Several studies have been conducted by members of the COMPASS group to evaluate the properties of a GEM equipped ionization chamber and establish a suitable operating point. The GEM based tracking system for Q_{weak} will be based on the COMPASS design and should possess similar performance attributes.

In December of 1999 at PSI, the LHCb Inner Tracker Collaboration tested a triple GEM chamber using 215 MeV/c π^- beam 6cm wide and at an intensity of 60 Hz/mm^2. High intensity studies indicated that the maximum achievable total rate was 60 MHz with a peak rate of 1×10^4 Hz/mm^2. For Q^p_{Weak} the design goal will be a maximum operating point of 10 MHz with

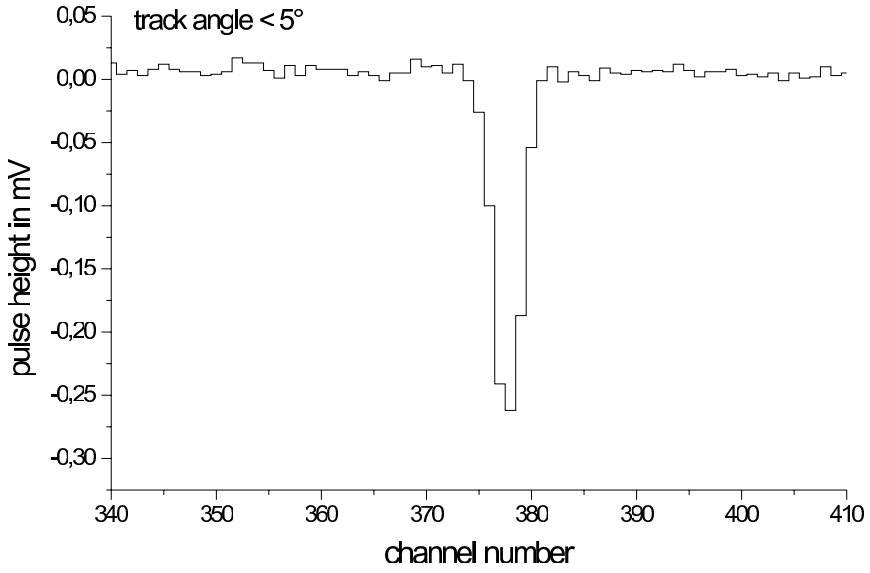

Figure 38: *The resulting signal from a typical cosmic ray observed in a triple GEM based tracking chamber.*

particle fluxes of 400 Hz/mm^2, substantially lower than those obtained in the tests at PSI.

The gain and tracking resolution for a GEM based tracking system are shown in Figure 39 and Figure 40, respectively. Spark discharges have the potential to damage ionization chamber detectors. The probability of a spark discharge for the GEM based ionization chambers was measured for several high voltage settings while operating at the high intensity rates of 60 MHz mentioned above. One would expect about 100 sparks every 12 hours of operation if a similar high rate of 60 MHz were used with each GEM preamplifier voltage set to 375 Volts. The operating point in Q^p_{Weak} will be at least a factor of 6 lower and the amplifiers will be segmented to minimize the impact in the event that one of the sparks actually caused damage.

Figure 41 illustrates the apparatus used to measure tracking efficiency of the GEM based tracking system in COMPASS [11]. A coincidence between the three scintillators was used as a trigger to identify events which originated from a test beam mixed with protons and pions. Since the divergence of the test beam was 20 mrad, at least three of the 50 μm wide charge collectors within the GEM tracking chamber would accumulate charge from particles which traverse a chamber approximately 7 mm thick. The tracking efficiency of the detector labeled TGEM10 was calculated by taking a ratio between the number of tracks found in TGEM10 to the number of tracks which went through the detector. The number of tracks which went through the detector was determined by observing a track in the TGEM11 and silicon micro-strip detectors. A prediction of the tracks location in TGEM10 was made based on the linear trajectory established by the TGEM11 and silicon detectors. A track in TGEM10 would be counted if a hit was observed within 400 μm of the predicted location.

Figure 42 shows the calculated efficiency for a 0.5mm $\times$ 0.5 mm cell size. The inefficient region located at x=235 is due to a $\sim$ 200 μm spacer used to support the GEM foils within the

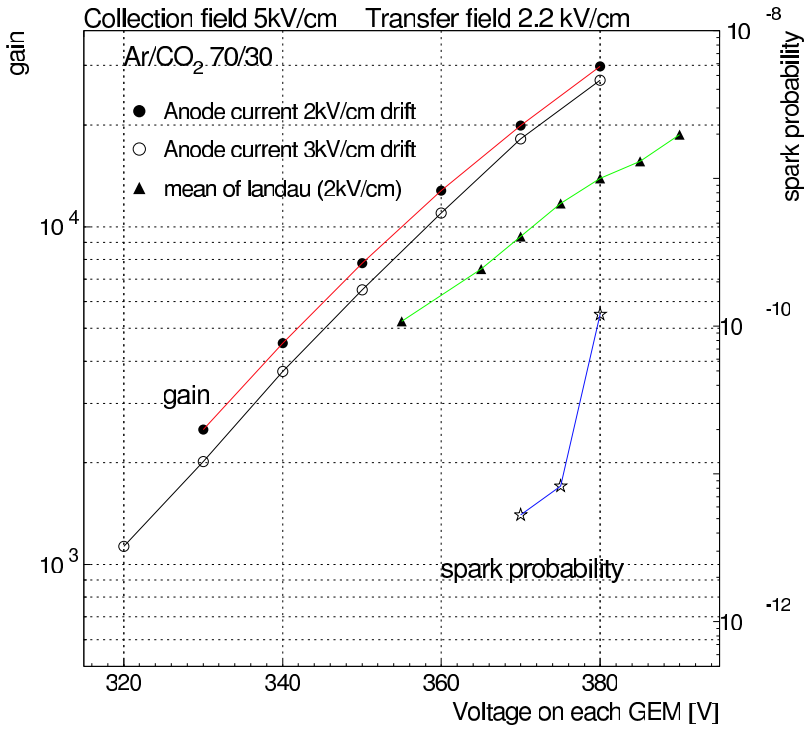

Figure 39: *The gain as a function of GEM voltage for an chamber with 3 GEM preamplification stages [10].*

tracking chamber. The inefficient region near x=209 is due to sector boundaries. An average tracking efficiency of 99.0 $\pm$ 0.1 % was measured in regions without spacers

The Region 1 GEM detector will have an area of at least 16 cm x 16 cm and a thickness of about 6 mm and be located just behind the first collimator. The entire detector will be mounted on a rail system to move radially so it may be used during low (nA) current measurements of Q^2 and then move out of the acceptance for the physics measurement at high currents of 180 μA or more. A rotation system as shown in Figure 43 will be used to move the detector between octants.

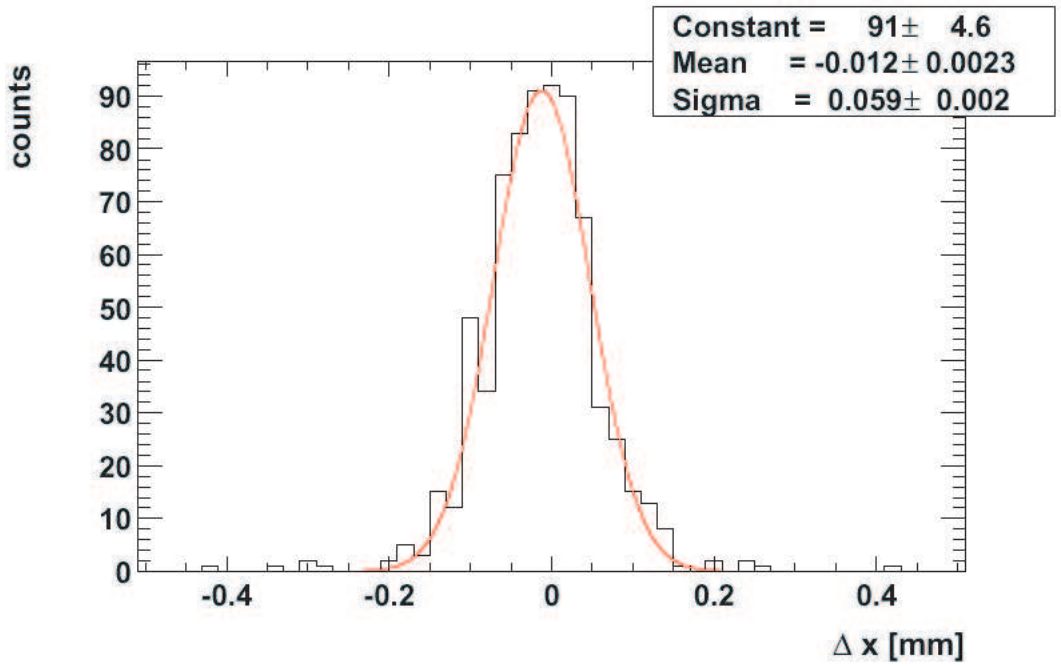

Figure 40: *The tracking resolution observed in COMPASS [11] from a a triple GEM based tracking chamber.*

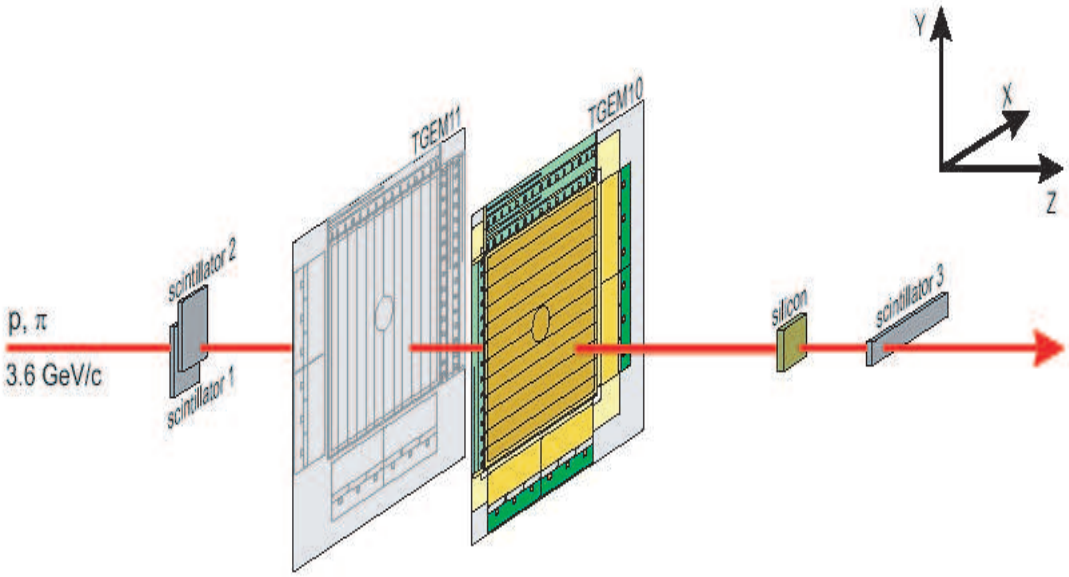

Figure 41: *Apparatus used to measure the tracking efficiency of GEM based tracking chamber TGEM10 for COMPASS. The scintillators are used in coincidence for a trigger. TGEM10 is placed between another GEM tracking chamber TGEM11 and a double sided silicon micro-strip detector in order to establish the presence of a track through GEM10 for the purpose of evaluating TGEM10's tracking efficiency.*

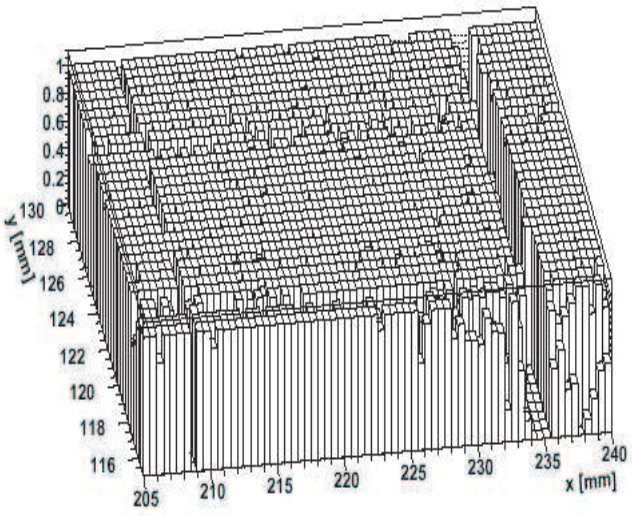

Figure 42: *The calculated tracking efficiency of 99.0 ± 0.1 % in TGEM10.*

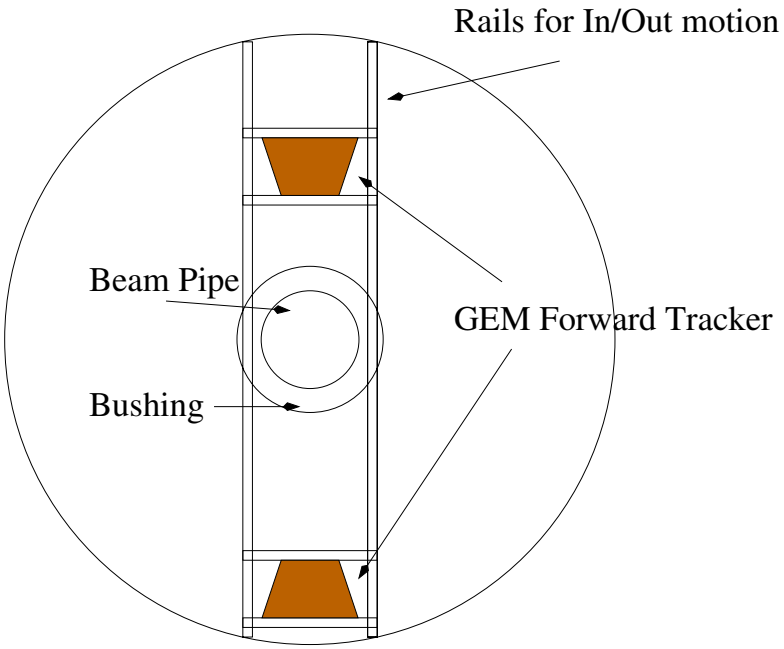

Figure 43: *Region 1 GEM in rotating mount.*

7.7 Region 2 Spectrometer Entrance Tracking Detectors

This middle set of chambers will be located just upstream of the QTOR magnet. Their purpose is to determine the position and direction cosines of the scattered electrons as they enter the magnet. The combination of these detectors and the Region I vertex detectors will provide an accurate measurement of the target vertex and scattering angle. They can also be used to reject events where the scattered particle originates from secondary scattering at one of the collimators between the Region 1 and 2 chambers. Finally, the region 2 chambers provide an accurate measurement of the entrance angle into the QTOR magnet. When combined with the exit angle determination from the Region 3 detectors and a QTOR field map, the scattered particle's momentum can be determined. With measurements of the scattered particle's momentum and scattering angle, we can properly tag elastically scattered electrons in the $< Q^2 >$ calibration process.

Given the desire to have substantial shielding after the target, these chambers should be located as close to the entrance of the QTOR magnet as possible. The region should be free enough of magnetic field that it does not affect the scattering angle determination, and so that it doesn't compromise the performance of the chambers. As shown in Figure 44, the field upstream of the magnet is down to 3 Gauss at the desired location, which is 250 cm upstream of the QTOR magnet center.

We would like to be able to determine the angle through these chambers with a precision of about 0.6 mrad. In the space we have we can make a self-contained unit with two chambers separated by 0.5 m. This implies that a 200 μm spatial resolution is necessary. We also desire a small amount of material to reduce multiple scattering. The rough area needed for these chambers is about 50 cm x 50 cm. These requirements and dimensions are very similar to those of chambers from other experiments that have operated reliably for years of running. In particular, the HERMES front chambers [12] and the Hall C SOS drift chambers are examples that we pattern our design after. Both of these sets of chambers have been operating for several years with typical resolutions of 200 μm.

For the Region 2 chambers, we propose to build two sets of 2 chambers each separated by 0.5 meters. The chambers will be located about 4.75 meters downstream of the Q^p_{Weak} target at a radial distance of about 70 cm from the beam centerline. A footprint for the detector frame of the downstream chamber is shown in Figure 45. The constraints are that the detector have active area over the full scattered electron envelope defined by the collimator for one octant. It must stay out of the scattered electron envelope of the neighboring octants; this constraint defines the trapezoidal shape. The drift chamber wires will be strung so that the electronic readout cards can all be mounted on the top of the drift chamber frame. This is desirable to keep them as far away from the high radiation near the beam centerline as possible. This is how the HERMES front chambers were constructed; see Figure 46.

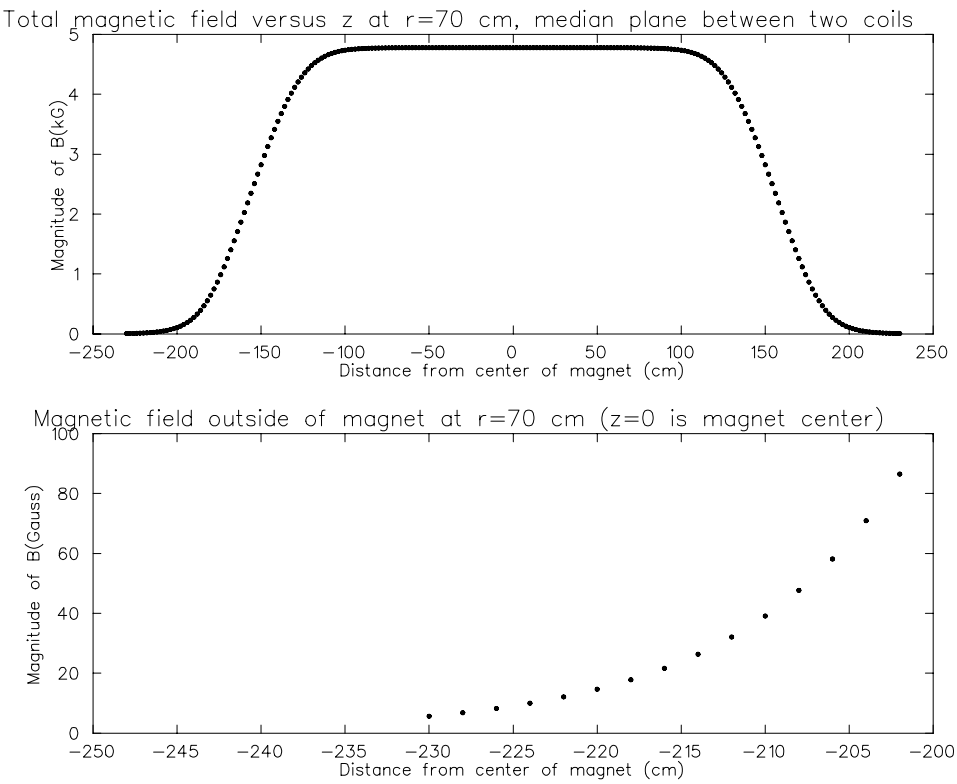

Figure 44: *Plots of the magnetic field at the radial (r = 70 cm) location of the middle chambers. We choose to sit at z=-250 cm upstream of the middle of the magnet where the magnetic field is about 3 Gauss.*

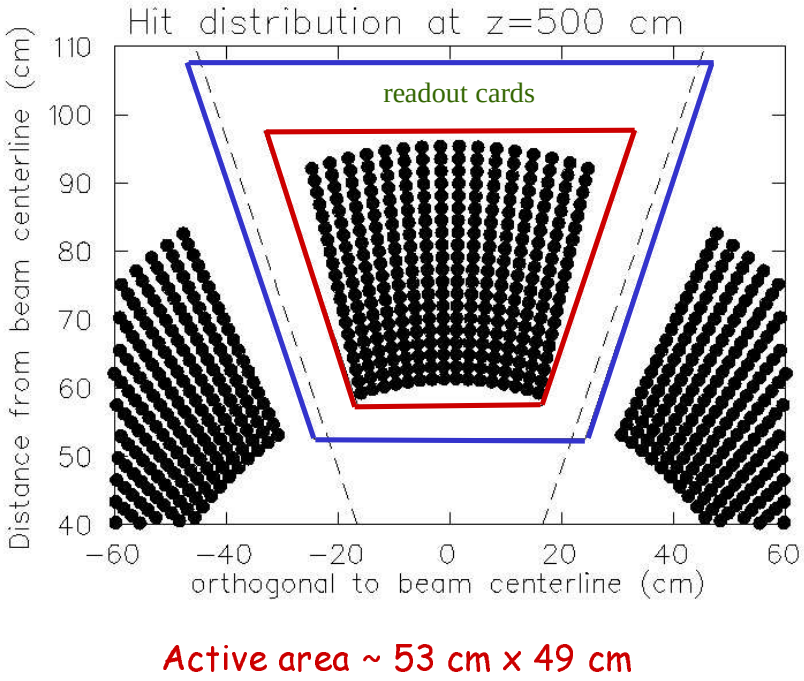

Figure 45: *This figure shows the scattered electron envelope defined by the primary collimator at 500 cm downstream of the target. An outline of the proposed drift chamber detector frame is shown. The electronic readout cards and cables will be mounted only on the top of the frame.*

A summary of the details of the chamber properties is shown in Table 14. The drift cell size will be 1 cm. Each chamber will have y, y', u, u', v, v' planes. The second plane of cells in each case will be offset by 1/2 cell to help resolve left-right ambiguities. The stereo u and v planes will be at an angle of $\pm 22.5°$. This is a convenient angle given the defining geometry of the octant. Each chamber will have an active area of approximately 53 cm x 49 cm. There will be 2x53 y wires, 2x67 u wires, and 2x67 v wires. Thus, we will need 374 electronic channels/chamber for a total of 1496 electronic channels for the four chambers. The cathode foils and anode and field shaping wires will be supported by G10 frames and the whole structure will be mounted to thicker outer aluminum frames. The anode wires will be attached to amplifier and discrimator cards mounted to the top of the chamber frames.

These chambers will be mounted in a similar (but appropriately scaled down) ferris wheel rotating hub structure like that used to mount the region 3 drift chambers. The chambers will have two pinned positions - "in beam" for the calibration runs and "parked" where they will sit with the protection of the shielding during the production running. This simple pinned scheme will make alignment more reliable and reproducible.

The rates in these chambers (per incident beam current) are expected to be about 4.2 kHz/nA of 1160 MeV elastically scattered electrons, and about 0.42 MHz/nA of low energy (about 40 MeV) Møller electrons. The expected radial distribution of these two classes of events in the chambers is shown in Figure 47. As discussed earlier, to deal with the high rate of Møller events,

Table 14: *Tentative properties of the Region 2 drift chambers.*

Distance from target	4.5, 5.0 m
Active area: horizontal	53 cm
Active area: vertical	49 cm
Cell design	horizontal drift
Cell size	1 cm
Anode wire material	Gold-plated tungsten
Anode wire diameter	20 μm
Field shaping wires	Gold-plated aluminum
Field shaping wire diameter	75 μm
Cathode material	Aluminized mylar
Cathode material thickness	6.4 μm
u, v stereo angle	$\pm$ 22.5 $^\circ$
Wires in each y plane	53
Wires in each u, v plane	67
configuration	y, y', u, u', v, v'
Radiation length per chamber	0.075 %
Total electronic channels	1496

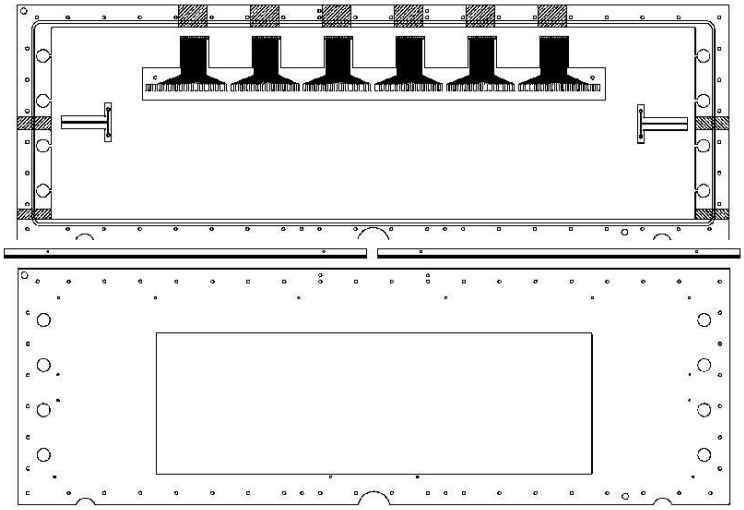

Figure 46: *A schematic of the HERMES front chamber sub-frame (lower) and sealing frame (upper) pieces that make up a plane. The region 2 chambers will have a different shape, but they will use similar mechanical construction techniques and materials and use the concept of having all electronic readout at the top of the chamber.*

we will install a sweeping magnet (mini-torus) to sweep away the low energy Møller background. As discussed previously we are exploring the possibility of a mini-torus located between the Region 1 and Region 2 drift chambers.

7.8 Region 3 Spectrometer Focal Plane Detectors

The baseline design for the Region 3 focal plane chambers call for use of vertical drift chambers (VDCs). A detail report of the Hall A VDC design, which is similar in size and geometry to the Region 3 chambers, can be found in the Hall A NIM article[13]. Figure 48 shows a schematic of the Jlab Hall A VDCs. Two sets of UV chambers are used to provide excellent position and angle reconstruction. Figure 49 shows a Garfield simulation of the electric field potential for the baseline design. The particle trajectory is defined by a set of 4 zero-crossing points, one per plane, for a two chamber system separated by 30cm. We plan to maintain existing cell dimensions, so that we can assume similar drift times and resolution properties for the same high voltages of the current chambers, but plan to reduce the electronics cost substantially by multiplexing the readout. Figure 50 shows how a particle crossing a VDC plane at a nominal angle of 45 degrees would typically strike 5 cells. A cell spacing of 0.5 cm would be maintained, giving the same intrinsic position resolution of the HRS chambers of about 100 nm. Measurement of drift times is used to determine the zero-crossing point of the geodesics. Unlike horizontal drift chambers (HDCs) where redundancy and thereby high efficiency is obtained by having multiple wire planes, the high number of wires hit per plane gives the same result in the VDC design. This further reduces the cost and complexity of the chambers.

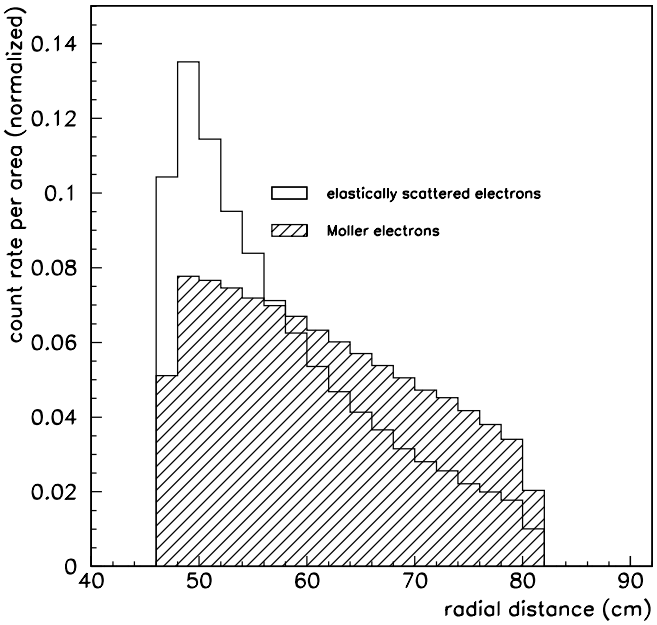

Figure 47: *The radial distribution of elastically scattered electrons compared to the radial distribution of Møller electrons at a chamber location 250cm upstream of the QTOR magnet center. The scaled distributions show the relative count rate per unit area as a function of the radial distance from the beam centerline.*

The VDC detector size requirements for Q^p_{Weak} are almost identical to that of the existing HRS detector. The chambers will be mounted on a Ferris Wheel, of 3 meters radius, which can be rotated about the beam line axis to provide coverage for all octants. Two sets of counterbalancing chambers will be attached to the Wheel as shown in Figure 35. As noted previously, sequential sampling of opposing pairs of octants is planned. The entire assembly would be placed immediately before the Q^p_{Weak} Čerenkov detectors, along with scintillator trigger counters. Angular resolution of a set of two UV chambers would be about 1-2mrad, sufficient to map out the analog response of the Čerenkov detectors. The chambers can be moved to avoid direct view of the beam by sliding them along the Ferris wheel axis to avoid damage in high luminosity production mode. Like the Region 2 design, there would be two positions "in" and "out" of direct view of the elastically scattered electrons. Other (minor) modifications include radiation-hardening the design and providing a higher gas flow rate for quick cycling of chamber gases.

Figure 51 shows the front end electronics used in the Hall A design, which we intend to copy. These consist of a preamp and discriminator for each sense wire and are mounted directly to the chambers on PC Boards. The Q^p_{Weak} design would differ in having every 8th wire multiplexed, with 40 wires per delay line. Assuming 2ns delay per wire, this would add 80ns to the readout time. Both ends of the delay line are read out, requiring 32 channels of TDC (1 VME module) per chamber. The time difference between the two ends of the readout can be decoded to yield the wire number, and the time sum provides the drift time spectra. The primary disadvantage of delay line readouts is increased dead time, but at $40kHz$ whole chamber event rates, this is

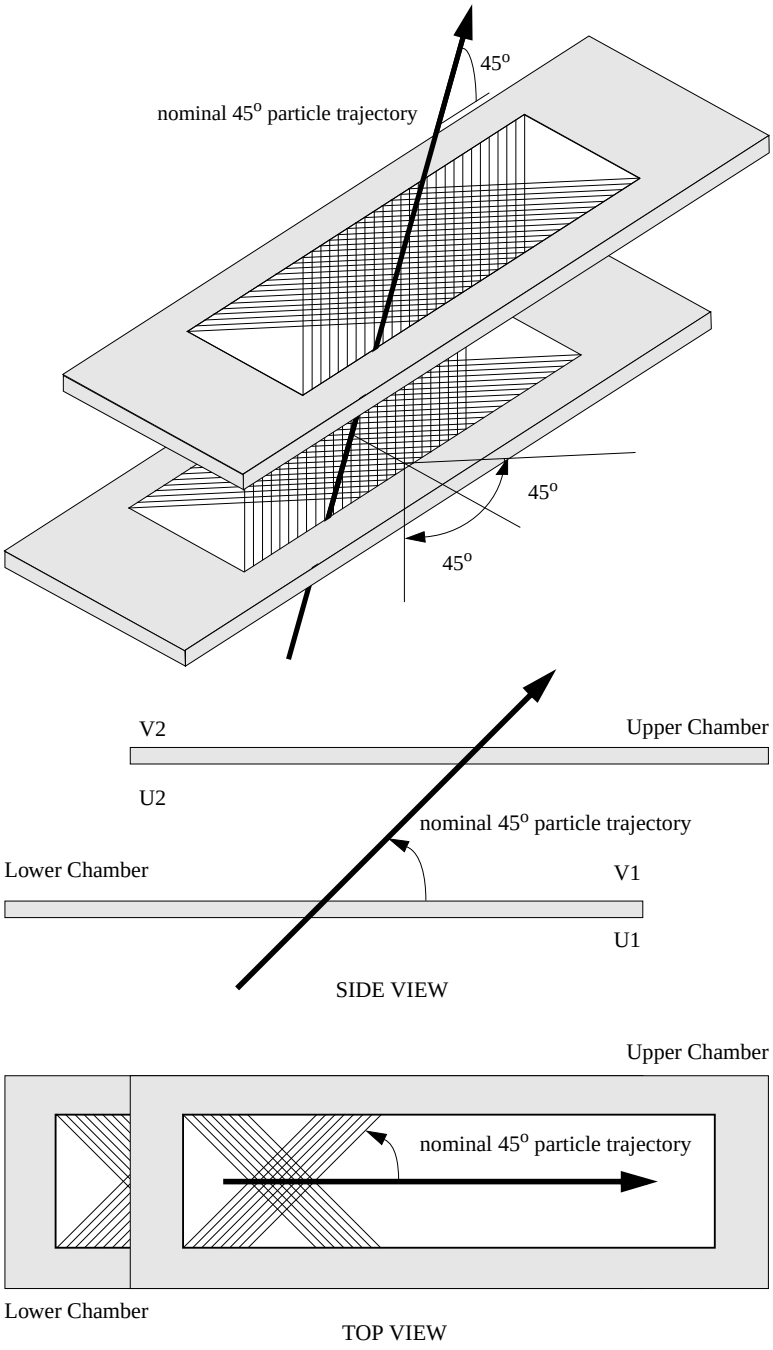

Figure 48: *Schematic of the Hall A VDC layout.[13] The orthogonal wire directions (UV) are rotated by 45 deg. relative to the (XY) coordinates of the chamber frame.*

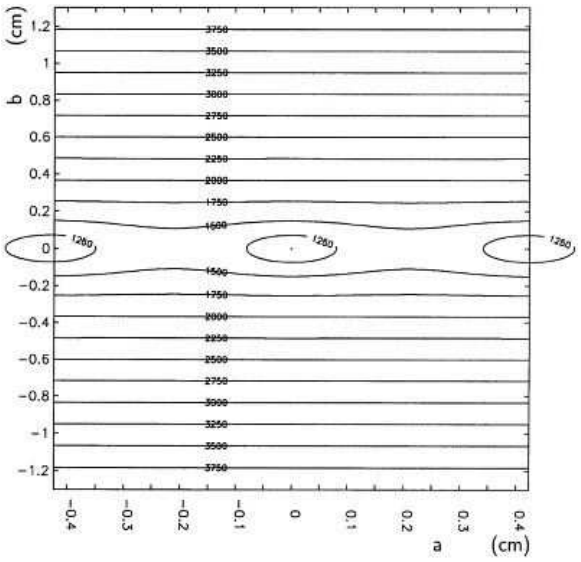

Figure 49: *A Garfield simulation of the electric potential for the HRS and* Q^p_{Weak} *cell geometries.[13]*

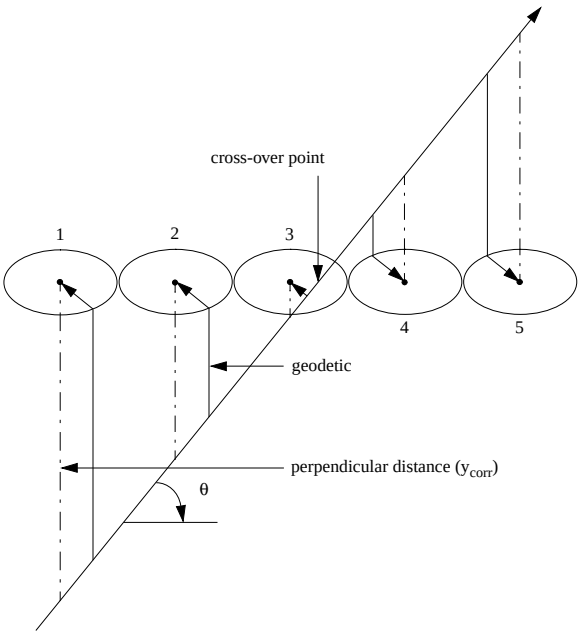

Figure 50: *Trajectory of electrons across a wire plane. Secondary electrons, produced by ionization, drift to the wires and cause an avalanche when they reach the high field near the wire.[13].*

hardly an issue. If the electronics were read out in common start mode, single-hit TDC's would be sufficient, however multi-hit TDCs are readily available and give more flexibility to the trigger design.

Figure 52 shows a schematic (not to scale) detailing the significant construction details of the existing Hall A chambers. The chambers are 10 cm deep and have 3 high voltage planes and two wire planes. In the HRS design, sense wires pass through precision-drilled holes and are spring mounted as shown in Figure 53. We plan to modify the design, using the simpler, and more traditional, method of soldering wires onto photo-etched frames. This is a trade-off in expensive machinist time for student labor, which is subsidized by W&M. As in the Hall A design, there will be no guard wires, unlike previously VDCs built for Bates. This requires a more sophisticated readout algorithm, but eliminates dead zones. Approximately 320 sense wires per plane would be required in the Q^p_{Weak} baseline design configuration (640 sense wires per chamber).

Figure 54a shows a typical drift time spectrum for the existing Hall A chambers. Because of nonlinearities in drift velocities, the drift times have to be mapped into drift distances, as shown in Figure 54b. The reconstructed drift distance spectrum for the white spectrum data of Figure 54a is shown in Figure 54c. Interpolation of the drift distance readouts yields about $100mu$m resolution for the cross over point of the geodesics shown in Figure 50. Chamber efficiency is nearly 100% as shown in Figure 54d. The HRS chambers have run for years with no significant problems in Hall A. Dead time, with the UV geometry and the delay line readout, should be nearly independent of position for the Q^p_{Weak} Region 3 chambers. The dead time in these chambers is small in any event, as we are limited by the higher rates seen by the Region 1 and 2 chambers.

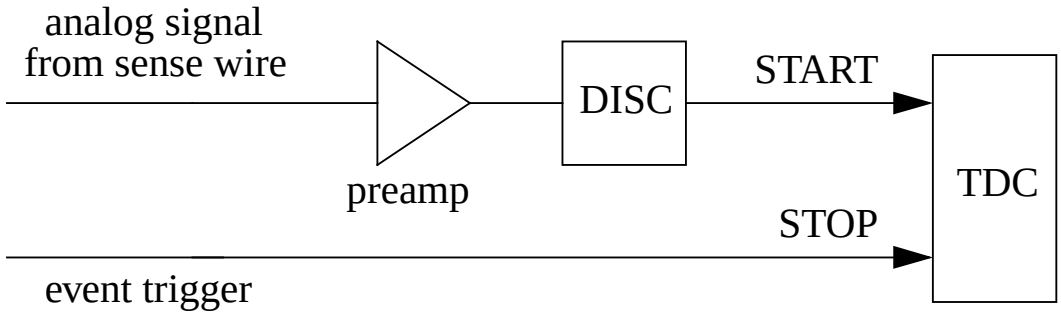

Figure 51: *Front-end electronics for the Hall A VDCs. Electronics for Q^p_{Weak} will differ mainly by multiplexing the readout using a delay line system. [13]*

The conceptual design concept for the Region 3 Ferris wheel is an aluminum wheel-like structure that rotates around a pair of 12 inch brass Garlock bushings. The axle is a 12 inch OD tube that is 3 feet long with an inverted Vee stand 13 feet high on center at each end. The wheel is made from 4 x 4 inch aluminum square tube. Due to the size the wheel must be partially assembled with some bolted joints in Hall C. The wheel could be welded into two half assemblies at a fabrication shop for ease of transport and a simple field bolted joint used for final assembly. The inverted Vee stands would be shimmed to height and positioned by survey to be on the Hall C beam line to +/- 1 mm. The wire chambers would use shims to facilitate mounting

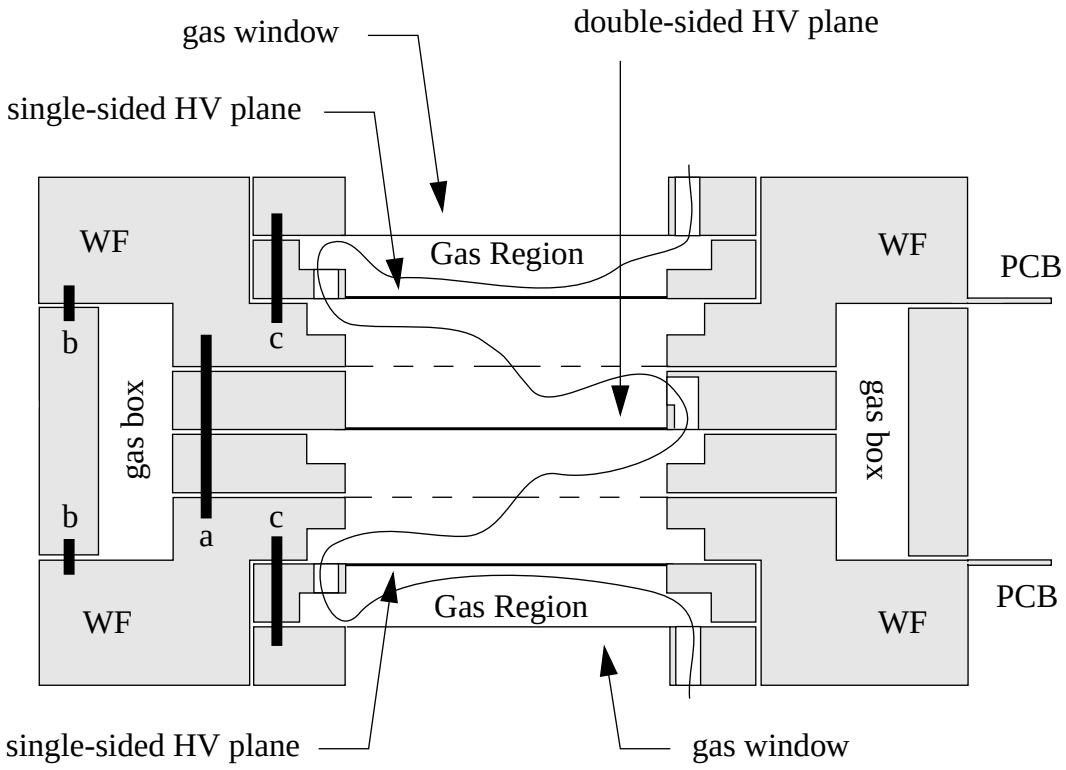

Figure 52: *Schematic of the Hall A VDCs (not to scale) The Q^p_{Weak} design will differ mainly in how the wires are mounted.[13]*

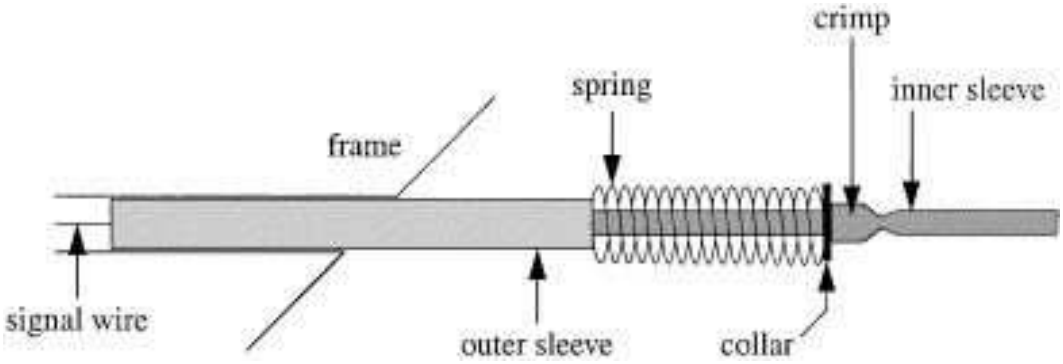

Figure 53: *Spring loaded technique for mounting wires to the chamber frame. This detail will change for the Q^p_{Weak} VDCs. We plan to solder wires unto photo-etched frames instead.[13]*

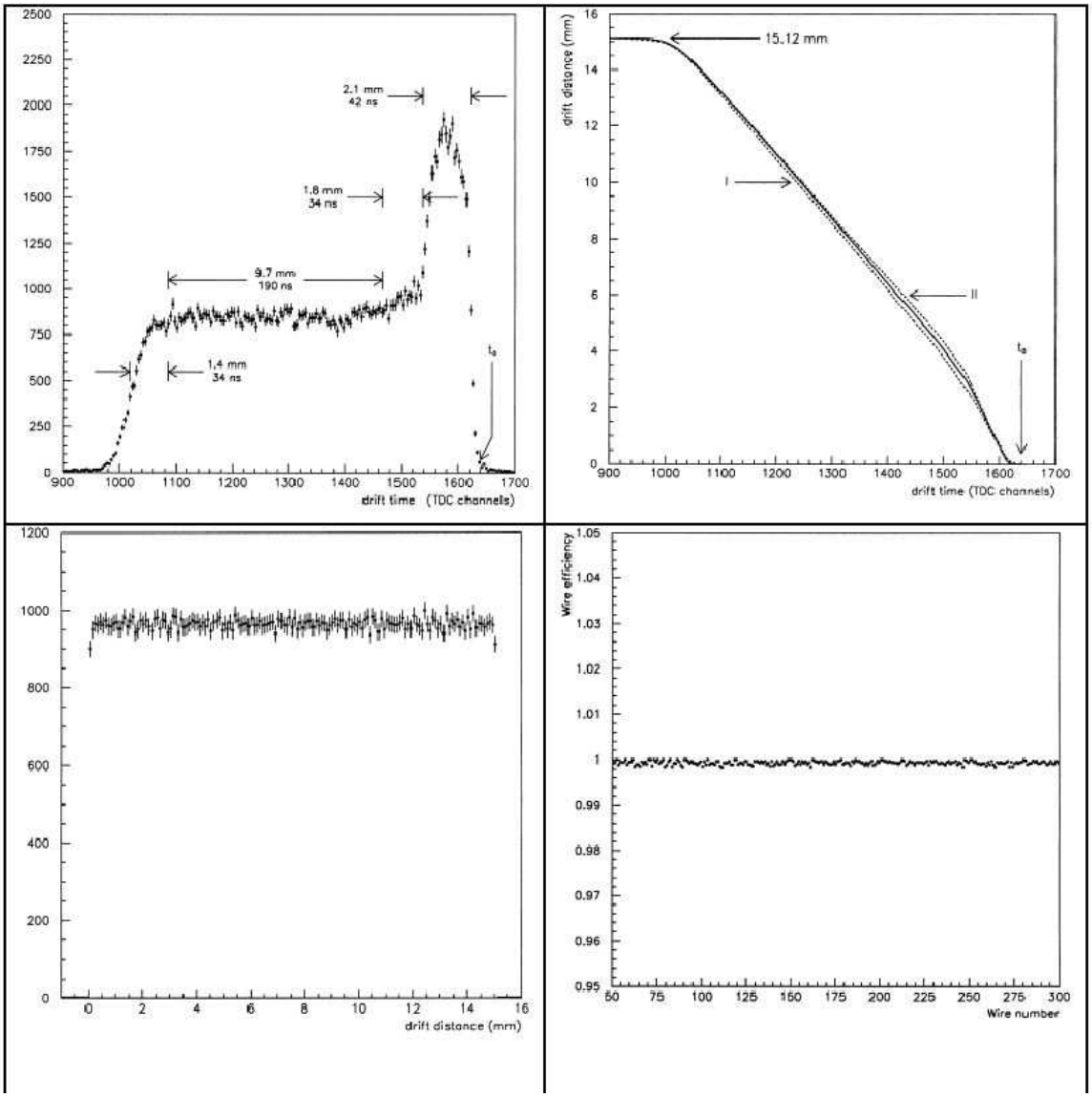

Figure 54: *a) Typical Drift time Spectrum for the HRS VDCs taken in a flat continuum region. b) Mapping of drift time to drift distance for different angles of incidence, c) Resulting Drift Distance Spectrum, d) Efficiency map for a single wire plane.[13]*

perpendicular to the Hall C beam line. No transverse to beam adjustment of the wire chambers is required. The wire chamber pair is mounted to the face of the wheel. An indexing collar is used to position the chambers in any of eight positions so, in principal, each chamber may be indexed to each gap of the Q^p_{Weak} magnet. The wheel would be moved by a circular worm gear. This device would require about 6 weeks for 3D modeling, drafting and engineering. The wheel could be fabricated at any of several local Tidewater Virginia fabrication shops in 3 months.

7.9 Scintillator Detectors

Scintillation counters will provide the trigger and time reference for the calibration system. These detectors must shadow the quartz Č bars and have sufficient energy resolution and timing capabilities so that a trigger which is defined as ($scint \cdot$ Č) is 99.9% clean with less than 0.1% of the triggers due to neutrals, non-elastic e^-, and other charged particles. The scintillators will be long bars, each with an area just slightly larger than the aperture it is covering in the re-entrant shielding and 1 cm thick. The scintillators will be mounted on the rear of the Region 3 chambers, just upstream of the apertures to the bars being calibrated. Each scintillator will have a photomultiplier tube at each end and have a mean time resolution of 250 ps or better. The scintillators will have sufficient energy resolution so as to help identify and reject multi-particle events from the analysis. Lightguide material will connect the scintillator and pmt's, and be of sufficient length ($\sim$ 1/3 the scintillator height) so that the corners of the scintillator are fully viewed by the pmts. Two scintillation bars and a spare will be made.

Each scintillator will be 225 cm $\times$ 16 cm $\times$ 1 cm and made from BC408 or its equivalent. The non-UVT lightguides at each end will be 5.6 cm $\times$ 16 cm $\times$ 5.08 cm with a 16 cm $\times$ 1 cm $\times$ 0.6 cm deep slot in the side facing the scintillator, which will provide a mechanically reliable optical coupling joint. UVT rods that are 5.08 cm in diameter and 5 cm long will couple the rectangular lightguide to the pmts. The long edges of the scintillators will be diamond milled and the ends finished to a 600 grit sanded finish. The 5.6 cm edges of the lightguide will also be diamond milled while the 16 cm $\times$ 5.08 cm faces will be painted a solid black, except where these faces couple to the scintillator and the UVT rods, to eliminate reflections. Given the extreme ratio of thickness to length, the scintillator counters must be supported by a frame which is then mountable to the rear chamber package. To reduce radiation damage, this package will be removed from direct view of the beam for the high current running mode.

References

[1] K.A. Aniol,*et al.,* Phys. Rev. Lett. **82**, 1096 (1999); Phys. Rev. Lett. B **509**, 211 (2001).

[2] M.J. Musolf, *et al.,* Physics Reports **239**, 1 (1994).

[3] J.M. Finn, *Monte Carlo Analysis of HAPPEX Systematic Errors*, HAPEX Collaboration internal report, Version 2, Aug. 22, 1998 (unpublished).

[4] A.Oed, NIM A 263 (1988) 351.

[5] http://gdd.web.cern.ch/GDD

[6] Model TCL 2530, TRUMPF Inc.,111 Hyde Rd , Farmington, CT 06032 ,Phone- (860) 255-6000, Fax- (860) 678-1704

[7] Boedeker Plastics Inc., 904 West 6th Street, Shiner, Texas 77984 USA , Phone: 1-800-444-3485, Fax:1-361-594-2349, http://www.boedeker.com/kapton_p.htm

[8] Helix 128 or beetle chip, ASIC laboratories, Heidelberg, http://wwwasic.kip.uni-heidelberg.de/~trunk/projects/Helix

[9] LHCb Note 2002-018, First Measurements on Inner Tracker Silicon Prototype Sensors Using The BEETLE v1.1 Readout C, T. Gleve *et. al.*, March 26,2002.

[10] hep-ex/0007007; LHCb Internal Note - inner tracking - LCHb 2000-056, M. Ziegler *et. al.*, June 29,2000.

[11] Frank Simon, Ph. D. Thesis, Physik-Department E18, Technische Universitat Munichen, Nov. 2001

[12] J.T. Brack, *et al.*, NIM A **469**, 47 2001.

[13] K. Fissum,*et al.,* NIM A **474**, 108 (2001).

8 Helicity-Correlated Systematic Uncertainties

8.1 Overview

Helicity correlations in the beam parameters can lead to false parity asymmetries. Parity violating scattering experiments generally have dealt with this by keeping helicity correlations as low as possible, by measuring residual correlations and by making corrections for them based on measured sensitivities. The measured parity asymmetry, A_{meas}, is written in terms of the physics asymmetry, A_{phys}, in the following way for sufficiently small helicity correlations:

$$A_{meas} = A_{phys} + \sum_{i=1}^{n} \Big(\frac{\partial A}{\partial P_i}\Big)\delta P_i,$$

where beam parameter P_i changes on helicity reversal to $P_i^{\pm} = P_i \pm \delta P_i$. The detector sensitivities $\partial A/\partial P_i$ can be determined preferably by deliberate modulation of the relevant beam parameter or from natural variation of beam parameters. The helicity-correlated beam parameter differences, δP_i, are measured continuously during data-taking. From estimates of the sensitivity of our apparatus to beam parameter variations, we can set requirements on how accurately beam parameters have to be measured and how small helicity correlations in these parameters must be. The goal is to constrain systematic uncertainties from each source to be no more than the statistical uncertainty on the measurement of the parity asymmetry, i.e., no more than 6×10^{-9}, and that corrections are accurate to 10%.

8.2 Sensitivity to Helicity-Correlated Beam Motion

A perfectly symmetric detector system, magnet and collimator aligned precisely with the beam should be insensitive to small modulations of beam position on helicity flip. If the beam is moved away from this "position neutral axis", however, symmetry is broken and false parity-violating effects are seen. These effects have been investigated with the help of the LaTech simulation package for Q^p_{Weak}. The Q^2-weighted event rate, $N(x, y)$, seen by a Čerenkov bar is mapped out as a function of the position of the beam on target and of displacement of the magnetic field. It is then possible to estimate the false parity asymmetry due to beam motion on helicity flip and to set tolerances on the positioning of the magnet. Tolerances break down into dc properties, that is, average values for beam parameters, and helicity-correlated changes. To see whether systematic errors can be kept under control for larger beam rasters which would decrease the chances of target bubbling, results are presented for a 4 mm $\times$ 4 mm raster, as well as for 2 mm $\times$ 2 mm.

From the map of event rates, the false parity asymmetry measured by a single detector is calculated:

$$\epsilon = \frac{N(x^+, y^+) - N(x^-, y^-)}{N(x^+, y^+) + N(x^-, y^-)},$$

where the beam position is $x^{\pm} = x_0 \pm \delta x$, $y^{\pm} = y_0 \pm \delta y$ for the two helicity states. The position neutral axis is nominally at $x = y = 0$. These asymmetries are averaged over diametrically opposite pairs of Čerenkov bars and then over all four pairs. Matching the acceptance and response of Čerenkov bars is not necessary with this method of calculating asymmetries. For motion of the beam in the x direction, false asymmetries for the left-right detector pair are reduced through cancellations, as a gain in acceptance for the left detector is compensated by a loss for the right. By symmetry, the up and down detectors measure the same quantity, so there is no cancellation, and there is reduced cancellation for diagonal pairs of detectors.

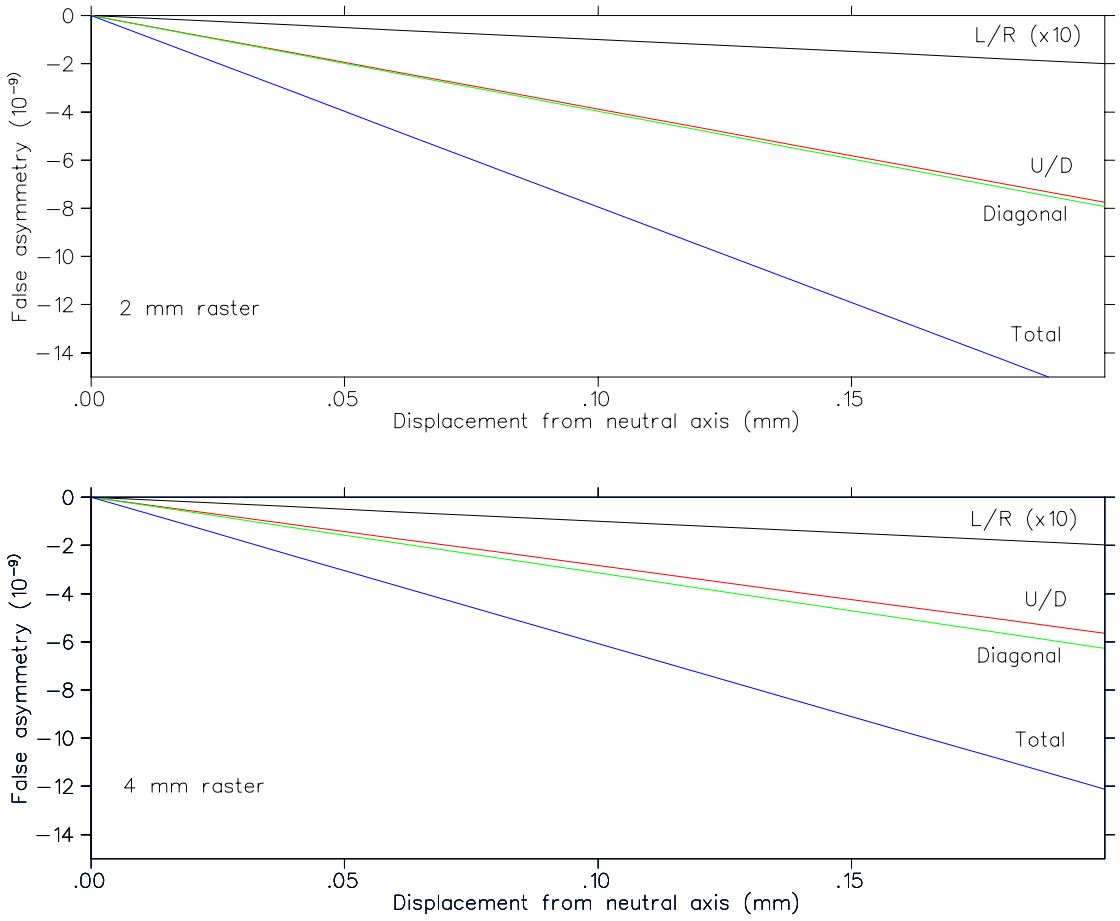

Figure 55: *Contributions to the false asymmetry due to beam motion for 2 and 4 mm raster sizes (upper and lower plots, respectively) for a 40 nm shift of beam position on helicity flip. The asymmetry is proportional to this shift. Curves are labelled 'L/R' for the left-right detector pair, 'U/D' for up-down, 'Diagonal' for the diagonal pairs and 'Total' for the sum. Note that the L/R curves have been multiplied by a factor of ten.*

Contributions to the false parity asymmetry for the left-right, up-down and the two diagonal pairs of detectors for $\delta x = 20$ nm (i.e. for a 40 nm shift of beam position on helicity flip) are shown in figure 55 as a function of displacement from the neutral axis for 2 mm and 4 mm raster

sizes. For the 2 mm and 4 mm rasters, the dc position of the beam should be set to within 75 and 100 μm respectively of the neutral axis to limit the false asymmetry to 6×10^{-9} for a 40 nm shift of beam position on helicity flip. The 1999 HAPPEX experiment was able to keep the run-averaged position difference below the 50 nm level. The G0 experiment, now at the engineering stage, should reduce this further so that, by the time Q^p_{Weak} runs, the helicity-correlated position feedback system should be in routine operation and the restriction on the dc position of the beam may be relaxed. Using the larger raster would decrease current density in the target by a factor of four, greatly decreasing the possibility of density fluctuations due to bubbling.

Note that it is assumed here that effects of varying target thickness, due for example to the windows of the hydrogen target being curved, are removed by normalizing the Čerenkov detectors to the luminosity monitors. Effects of target bubbling are removed in the same way.

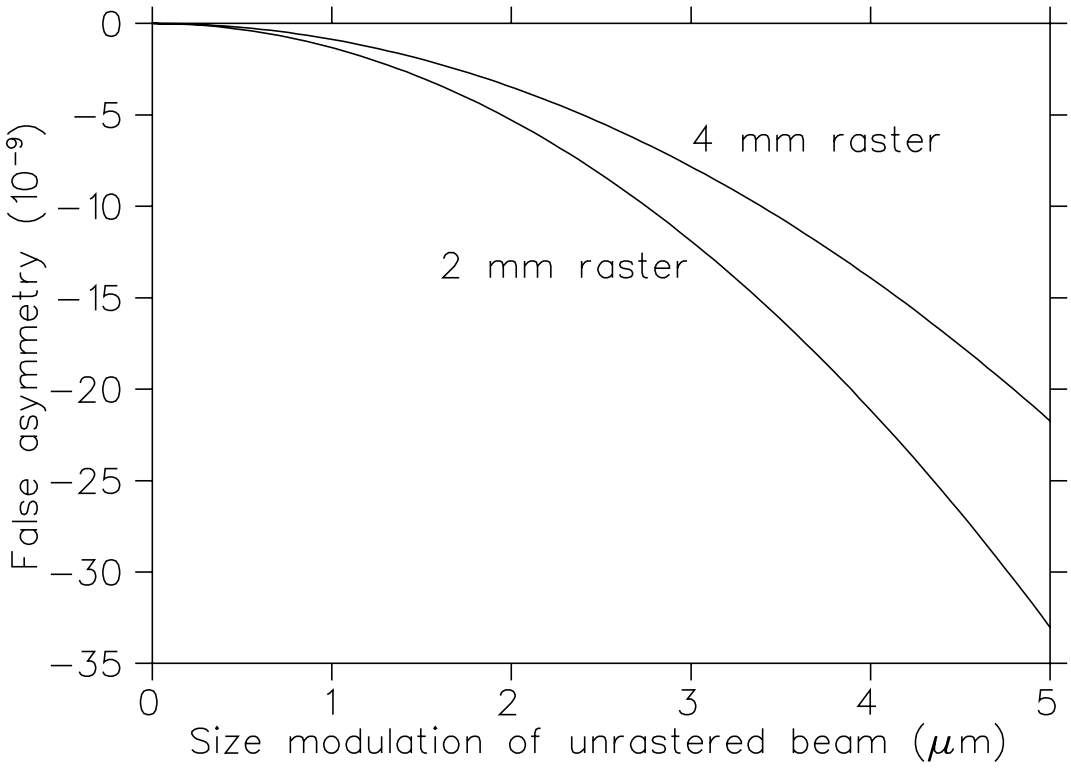

Figure 56: *Variation of false asymmetry with size modulation, δW, for 2 and 4 mm rasters. δW is for the raw, unrastered beam, its effect being diluted by a non helicity-correlated rastering which is taken into account in this figure.*

8.3 Sensitivity to Beam Size Modulation

Figure 56 shows the variation of false asymmetry as a function of the size modulation, δW, of the raw, unrastered beam which is then rastered to 2 and 4 mm full width. The effects of the size

modulation are diluted by the rastering if there is no correlation of the rastering with helicity. This dilution is taken into effect in the figure. For a false asymmetry of 6×10^{-9}, δW should be less than 2.1 or 2.6 μm when rastered to 2 and 4 mm, respectively, which is seen in the rastered beam as size modulations of about 2.2 and 1.7 nm.

8.4 Sensitivity to Variation of Angle of Beam on Target

As the angle of incidence of the beam on target is changed, so the range of Q^2 accepted by the collimators changes and with it the event rate. There is in addition a variation of effective thickness of the target, but the effect is small compared with the variation of cross-section and is, in any case, removed by normalization to the luminosity monitors. The contributions to the false asymmetry for the left-right, up-down and diagonal detector pairs are shown in Table 15. The results correspond to the beam being pivoted by $\pm\delta\theta$ about a vertical axis through the center of the target. There is then some cancellation for the left-right detector pair and none for the up-down detectors. θ_0 is the spin-averaged angle of the beam relative to the symmetry axis of detectors and collimators. The systematic error requirement becomes $|\theta_0 \delta\theta| \leq 6.3 \times 10^{-6}$ mrad^2.

Table 15: *Contributions to false asymmetry from angle modulation (angles in mrad).*

Detector Pair	False Asymmetry
Left-right	$0.5 \times 10^{-4}\theta_0\delta\theta$
Diagonal	$-4.7 \times 10^{-4}\theta_0\delta\theta$
Up-down	$-5.4 \times 10^{-4}\theta_0\delta\theta$
Total	$-9.6 \times 10^{-4}\theta_0\delta\theta$

Table 16 summarizes the requirements for the beam based on the correction for the associated systematic error being no greater than the expected Q^p_{Weak} statistical error, i.e. no greater than 6×10^{-9}.

Table 16: *Beam requirements.*

Parameter	Max. deviation from nominal (DC)	Run-averaged helicity correlation
Beam energy	$\Delta E/E \sim 0.6 \times 10^{-5}$	$\Delta E/E \sim 10^{-8}$
	$\rightarrow$ 21 μm at 35 mm/% dispersion	$\rightarrow$ 35 nm at 35 mm/% dispersion
Beam diameter	1 mm	2 μm
Beam position	75 – 100 μm	40 nm
Beam angle	60 μrad (1.2 mm at 20 m)	100 nrad (2.0 μm at 20 m)

8.5 Sensitivity to Magnet Misalignment

Figure 57 shows the effect of offsetting the magnet from the symmetry axis of the collimator and beamline. The plots show the profile of the scattered beam image across the width of a Čerenkov detector. The black curves in the upper and lower panes show the image for a correctly aligned magnet. The red and green plots show how the image is moved across the detector when the magnet is moved 1 cm to the left, to positive x. The deflection angle for electrons scattered to the left (red plot) is increased and is decreased for electrons scattered to the right (green plot). The lower pane shows that the effects of misaligning the magnet by such an unrealistically large amount can largely be compensated by the use of trim coils to increase the magnetic field to the right by 1.5% (blue plot) and decrease it to the left by the same amount. The trim coils will be capable of providing a 1% correction to the magnetic field over individual segments of the magnet.

At smaller displacements of the magnet, effects are still seen when combined with position modulation of the beam on helicity flip. Tails of the distribution of electrons across the narrow dimension of the Čerenkov bars are cut by different amounts as the beam moves, resulting in a false parity asymmetry and a displacement of the position neutral axis. A 1 cm displacement of the magnet, for example, results in a shift of the neutral axis by approximately 0.4 mm and a false parity asymmetry, if uncorrected, of about 30×10^{-9}. To limit the uncorrected false asymmetry to less than 6×10^{-9}, the magnetic field should be centered on the beamline and collimators to within 3 mm.

Procedure for tuning the magnet:

- Position the magnet within 3 mm of its correct location on the beamline.
- Conduct a magnetic field scan using the precision field-mapping apparatus built for the G0 experiment.
- Make small adjustments of coil positions to trim the field and to center it on the nominal beam path.
- Determine the position neutral axes in x and y by rastering the beam and imposing controlled modulations about each raster point to find the location of zero-crossing of false parity asymmetry. Steer the beam to the neutral axis.
- If necessary, adjust trim coils to bring the position neutral axes for the diagonal detector pairs into coincidence with the x and y neutral axes. Use the chambers close to the Čerenkov bars to aid in centering the image on the bars.

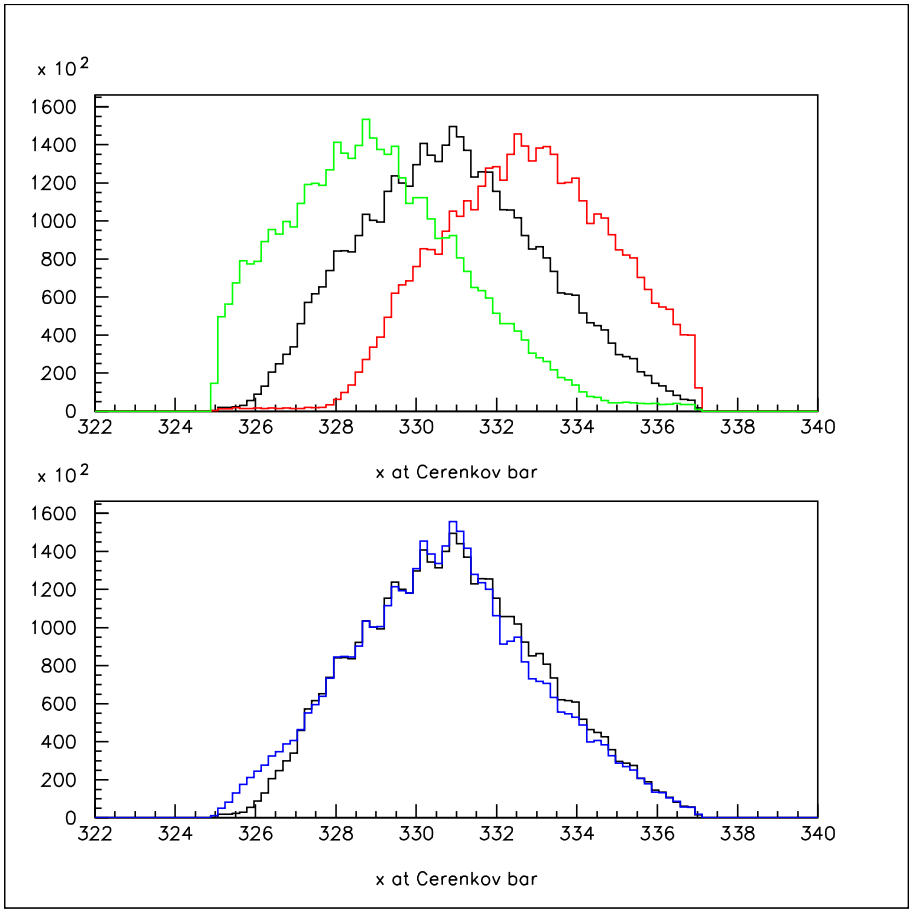

Figure 57: *The black histogram shows the beam profile across a Čerenkov bar when the magnet is correctly aligned. The green and red histograms show the effect on left and right detectors, respectively, when the magnet is moved 1 cm to the left (toward positive x). The blue histogram in the lower plot corresponds to the green peak that is brought back to the center of the detector by increasing the magnetic field by 1.5% through the use of a trim coil.*

9 Background Estimates

The challenges in the experimental design of the JLab Q^p_{Weak} Experiment (E02-020): "A Search for Physics at the TeV Scale Via a Measurement of the Proton's Weak Charge" [1] result from the small expected asymmetry of approximately 0.3 ppm and required accuracy of 4%, which will provide a $\simeq$0.2% accuracy in the measurement of $sin^2\theta_w$. The basic parameters of the experiment can be found in Table 17. Essentially the figure of merit of the experiment was optimized by selecting the incident beam energy at $E_0 = 1.165$ GeV, electron polar angle $\theta_e = 9.0^\circ \pm 2.0^\circ$ and azimuthal acceptance as large as possible, $\Delta\phi_e = \pm 15.0^\circ$ in each of 8 octants of the spectrometer. Also, large counting rates required high luminosity (1.77×10^{39} cm^{-2}s^{-1}), a long liquid hydrogen target (35 cm), and a large-acceptance detector system.

Table 17: *Basic parameters of the Q^p_{Weak} experiment.*

Parameter	Value
Incident Beam Energy	1.165 GeV
Beam Polarization	80%
Beam Current	180 μA
Target Thickness	35 cm ($0.04X_0$)
Running Time	2200 hours
Nominal Scattering Angle	9°
Scattering Angle Acceptance	$\pm 2^\circ$
ϕ Acceptance	66.7% of 2π
Solid Angle	$\Delta\Omega$ = 45.7 msr
Acceptance Averaged Q^2	$< Q^2 >= 0.03\ (GeV/c)^2$
Acceptance Averaged Physics Asymmetry	$< A >$ = -0.28 ppm
Acceptance Averaged Expt'l Asymmetry	$< A >$ = -0.23 ppm
Integrated Cross Section	3.7 μb
Integrated Rate (all sectors)	6.1 GHz (or .76 GHz per sector)
Statistical Error on the Asymmetry	2.0%
Statistical Error on Q^p_W	2.8%

The detector system, able to handle a counting rate of an order of 1 GHz per detector, able to maintain its properties through the entire run time, and be simple enough to reduce the systematic errors associated with the complex detector electronics, consists of one Čerenkov bar per magnet octant operating in the integration mode of data acquisition. Details of the design of this system are published in two reports [6,3].

In order for the detector system to operate, the experiment also requires a toroidal magnet which will generate a magnetic field that bends and focuses scattered charged particles into the detector position. The design of this large acceptance spectrometer evolved into a simple resistive toroidal magnet [8]. The magnet basically focuses elastically scattered electrons of the same

momentum and scattering angle from the 35 cm long target to a single point (zero magnification in the dispersion direction) covered by a set of eight rectangular quartz Čerenkov detectors. To reduce systematic uncertainties the spectrometer has an axially symmetric acceptance. The momentum resolution of the spectrometer is roughly $\leq 10\%$, which is sufficient to separate elastic and inelastic reaction channels.

The optical properties of the Q^p_{weak} spectrometer, coils of which are shown in Figure 58, are designed for the following kinematical inputs: $Q^2 = .03$ GeV^2, incident beam energy $E_0 = 1.165$ GeV, electron polar angle acceptance of $\theta_e = 9.0^\circ \pm 2.0^\circ$, and azimuthal angle acceptance of $\phi_e = \pm 15.0$ deg, as required in Table **??**.

The kinematical cuts on the scattered electrons are done by a collimating system [5] , shown in Figure 59, which allows the scattered electrons in the acceptance region of $\theta_e = 9.0 \pm 2.0$ deg for the polar angle and $\phi_e = \pm 14.5$ deg for the azimuthal angle to pass through, and, at the same time, block all other reaction products. The major components of the collimating system also provide an interface between the collimating system and the target chamber and shielding from beam line radiation. Additional detector shielding will be obtained from the toroidal magnet whose magnetic field focuses the elastically scattered electrons and disperses all the other charged particles.

In reality secondary particles do reach the detector system by having initial conditions such that the field bends them into the detector or by being neutral and therefore inert to the magnetic field. It is impossible to completely eliminate the effects of secondary particles, but it is possible to minimize their contribution to the final counting rate below the threshold of relevance. In the next section we will study the background of the "Q_{weak}" Experiment caused by electromagnetic processes since they are a major contribution to the background in any Jlab Hall C experiment. Contribution of nuclear processes, expected to be much smaller, will be studied in the next report.

9.1 Target Windows

The contamination of the elastic proton asymmetry from the scattering in 3.5 mil aluminum windows was estimated assuming nominal central kinematics. Here we are referring to the windows through which the primary beam enters and exits the target cell. It was also assumed that it will not be possible to reject these backgrounds in our focal plane detectors. Both elastic scattering on the aluminum nucleus and quasielastic scattering from the protons and neutrons in the aluminum were considered. (Transitions to excited states of aluminum, which may be important at $Q^2 \simeq 0.030$ $(GeV/c)^2$, have not yet been estimated.) The results are shown in Table 18. The relative contamination of the asymmetry of interest (elastic scattering from protons) is shown in the last column. Below, each of these processes is considered separately, and an estimate is made of the systematic error associated with these processes using our theoretical knowledge of their asymmetries. We find that, although we can make reasonable estimates of the window backgrounds, the resulting uncertainties are not comfortably below our other errors. Therefore a dedicated window background measurement will be performed. This measurement need not be nearly as precise as our primary measurement since the net target window contribution to

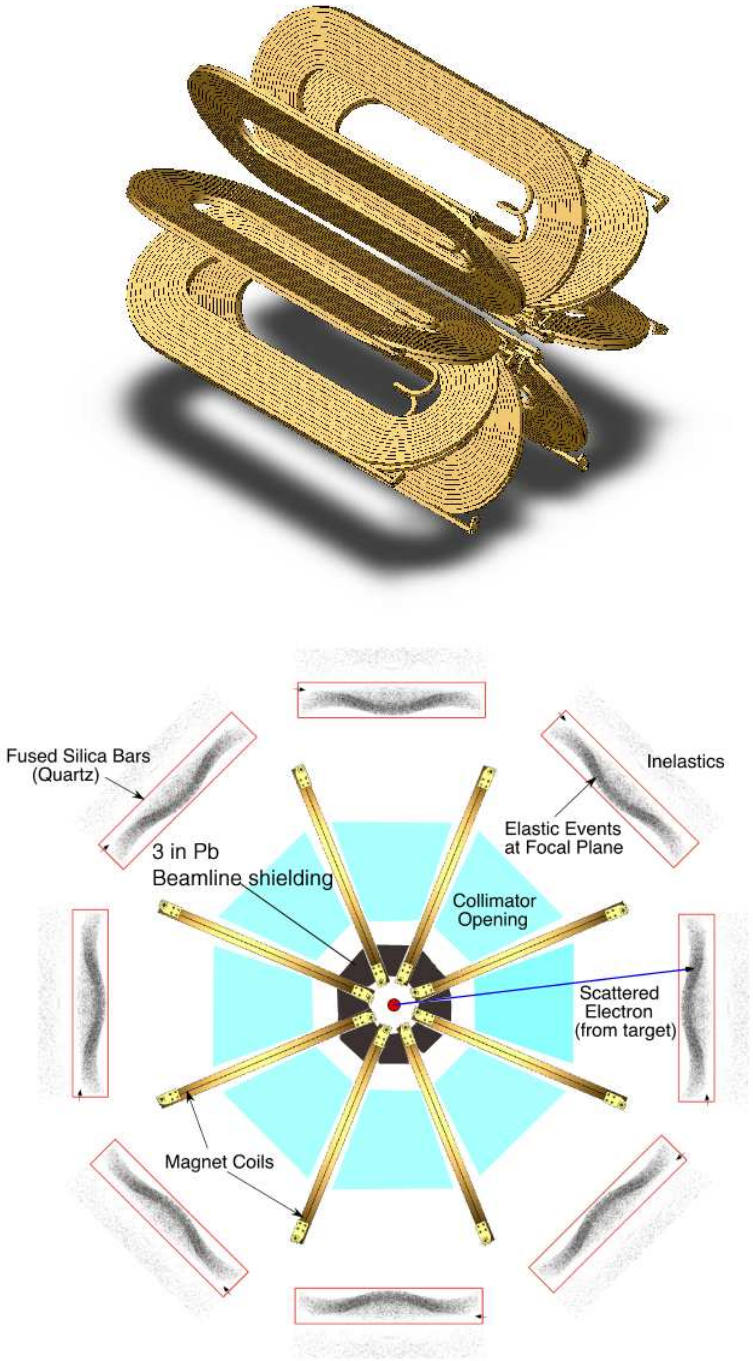

Figure 58: *The radial arrangement of the Q^p_{weak} Toroidal Magnet coils. The 3 inch thick wedge of lead filling the gap between coils at their inner radius provides additional shielding from the beam pipe. The top drawing is done by BATES engineer Stan Sobczynski.*

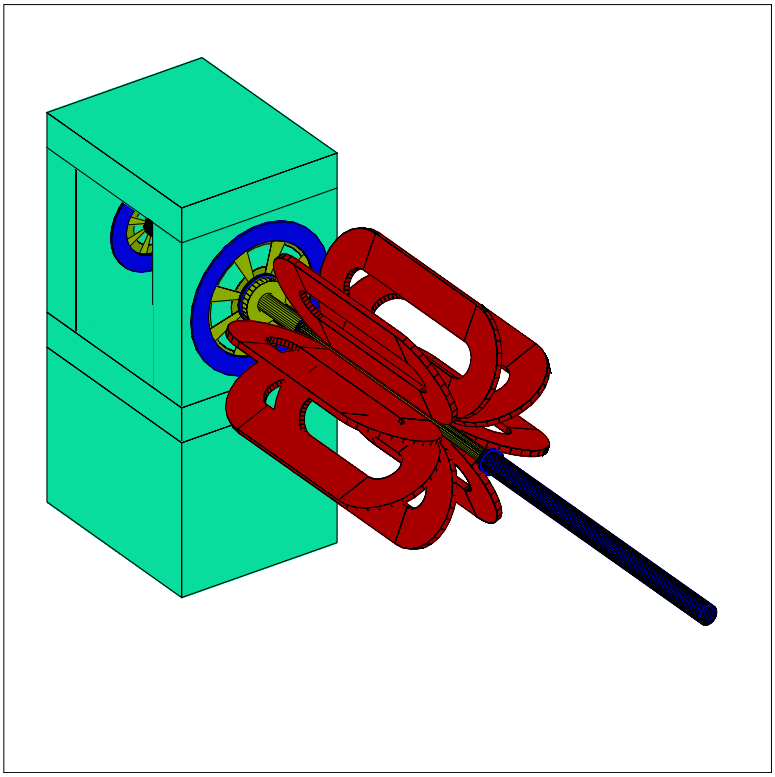

Figure 59: *3-D perspective of the collimating system in relation to the Q^p_{Weak} Spectrometer coils.*

the base parity measurement is relatively small. The use of Be entrance (trivial to implement) and exit window (more difficult to implement) is under investigation. If this prove feasible the contribution to our asymmetry from the windows should be significantly reduced.

Table 18: *Contributions of the various scattering processes in the Hydrogen target and the windows at the Q^p_{Weak} central kinematics. t is the target thickness in particles/cm^2, R_{cont} is the fractional contribution of the contamination to the rate in the detector, and A_{cont} is the contribution of the contamination to the overall asymmetry (=−0.27 ppm) from that process. The relative contamination of the elastic proton asymmetry from each process is shown in the last column.*

Process	σ (μb/sR)	A (ppm)	t (cm^{-2})	R_{cont} (%)	A_{cont} (ppm)	$\frac{A_{cont}}{(-.30)}$ (%)
Protons in LH_2 (elastic)	88	-0.31	1.3×10^{24}	97.8	-0.30	
Protons in Al (quasi-elastic)	88	-0.31	1.4×10^{22}	1.05	-0.0033	1.1
Neutrons in Al (quasi-elastic)	3	-3.1	1.5×10^{22}	0.04	-0.0012	0.4
^{27}Al nucleus (elastic)	1234	+3.0	1.05×10^{21}	1.1	+0.033	-11.0

The detailed calculations for target window backgrounds are found in the Appendix Section of the Q^p_{Weak} proposal. To summarize the discussion on window backgrounds, for aluminum end window thickness of 3.5 mil (front and back), quasi-elastic and especially elastic backgrounds must be taken into account. For our kinematics, the elastic contribution from the windows is dominant. In particular, the contributions to the asymmetry could be as large as 3.3% from the quasielastic and 11% from the elastic scattering. These estimates are based on what is currently available in the literature regarding these processes.

The aluminum background will be measured directly by using a special empty target cell with windows about 20 times thicker than the full target cell windows (to maintain the same radiation length). Assuming the rates in Table 1, and that the empty target cell can take full production beam current, it would take only 25 hours to determine the window asymmetry such that its contribution to the Hydrogen asymmetry error was at the 1% level.

In practice the indirectly cooled empty target cell windows are unlikely to withstand full production beam current, so we may have to allocate more time to the window background measurement. Clearly, we can do the experiment with aluminum target windows. However, we still plan to investigate whether beryllium would, for the same strength window, produce smaller backgrounds than aluminum.

9.2 Backgrounds from Other Reactions

In addition to elastic scattering on the proton, there are several other processes that can take place in our target. Our spectrometer and detector are designed to accept, in principle, only the elastic scattering peak. However, other reactions can reach the detectors by rescattering (*eg*, on the face of the collimators or in the Helium gas). It is useful to know which background processes are potentially important by determining what fractional contamination can be tolerated before a significant error results in the Q^p_{Weak} measurement.

In Table 19, we list the various potential background processes, their cross sections, and their parity violating asymmetries at our mean scattering angle of 9°. Only single pion inelasticities up to the Δ region have been considered. We also compute the maximum tolerable contamination of the elastic signal from each process such that they contribute $< 1\%$ to the elastic scattering asymmetry. The reactions are separated into those which produce positively and negatively charged particles. Positive particles are suppressed by an enormous factor by the bend direction of the magnetic field. Negative particles are suppressed by the elastic focus and the requirement to have sufficient rigidity to cross the magnetic field. Production of neutrals has not been examined yet because the detector is very insensitive to neutrons and because of the small large-angle rescattering probability for gammas. Assuming the electrons from Møller scattering have too low a rigidity to make it to the focal plane, the reaction of greatest concern is inclusive $p(e,e')X$ for which the allowable contamination is only 1.%. However, given the relatively small cross section for inclusive pion electroproduction ($\sigma_{el}/\sigma_\pi \simeq 10$) and the large separation between the elastic events and pion threshold at the detector plane, we expect the contamination from pion electroproduction will be negligible.

Table 19: *Cross sections and asymmetries for processes in the Hydrogen target at the mean scattering angle of 9°. The final column, F^{max}_{cont}, shows the maximum tolerable fractional contamination so that the given process will contribute less than 1% to the elastic scattering asymmetry.*

Process	Reaction	σ (μb/sr)	$\lvert A\rvert$ (ppm)	F^{max}_{cont} (%)
Negative products:				
Elastic e^-	$p(e,e)p$	88	0.31	
Møller e^-	$e(e,e)e$	80000	.0006	.6%
Inclusive e'	$p(e,e')X$	8.7	3.3	1%
Positive products:				
Recoil p	$p(e,p)e$	.0001	117	2300% (OK!)
π^+ Electroproduction	$p(e,\pi^+)en$	0.3	160 (max)	.6%
π^+ Photoproduction	$p(\gamma,\pi^+)n$	0.5	<1	50%

We have followed up on these estimates with a full GEANT simulation to examine the effects of rescattering of charged and neutral products. The results of these extensive simulations are discussed in the next section. This GEANT simulation includes the full target (with windows),

the complete collimator geometry, drift spaces (with air regions), the magnetic transport and integrating Čerenkov detectors.

9.3 Background from Electromagnetic Processes

In a completely designed experiment, estimation of the background rates is a straightforward computation. The experiment can be simulated using GEANT Simulation Package [12]. GEANT simulation includes tracking of the particles through the materials, complete physics processes involving photons and electron/positron interactions, and calculation of occurrence of the processes. Another parameter provided by the GEANT simulation tools is the energy threshold below which the particles are not tracked.

With all the experimental set-up in place, the simulation, as shown in Figure 60, consists of performing the experiment on the computer. This is particularly easy for the electromagnetic processes where the simulation consists of the exact mimicking of the real experiment without computational shortcuts. The only setback is the computational time since the useful statistics require large number of events. For the results in this report we scattered 100 milion electrons.

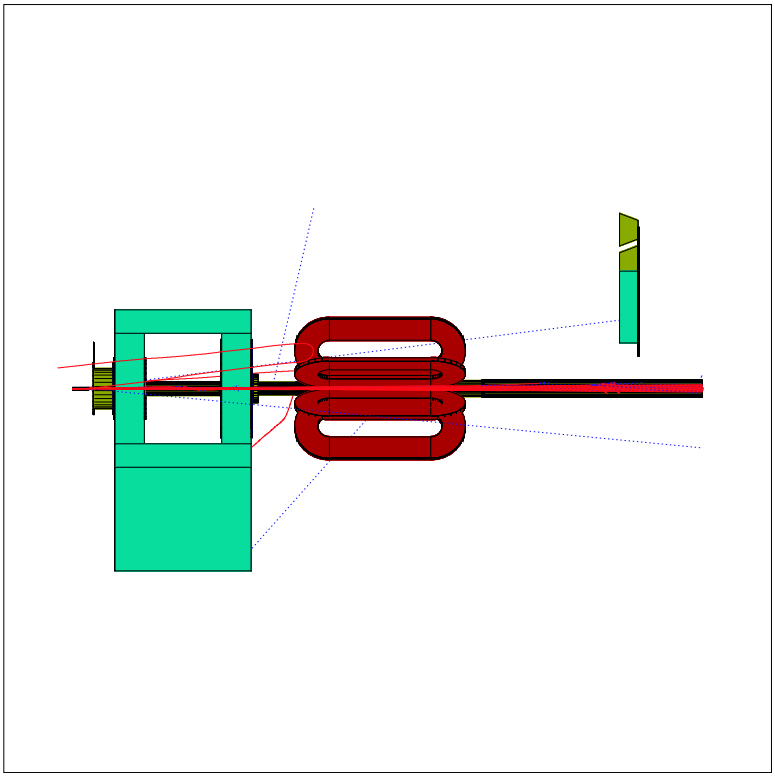

Figure 60: *Side view of the experimental setup and the secondary particles generated by the electron beam. The figure represents the events for about a 1000 primarily electrons.*

There are several questions one would like to answer about the electromagnetic background using the result of the simulation:

- Where are the secondary particles generated regardless of their direction of scattering? The answer to this question is shown in Figure 61 where the reaction points of the secondary particles are drawn as a function of the position along the beam line and the distance from the beam line.
- Where are the secondary particles which hit the Čerenkov detector generated? The answer to this question is shown in Figure 62. The reaction points of the secondary particles which hit the detector are drawn as a function of the position along the beam line and distance from the beam line.
- Which types of secondary particles generated by the collimating system hit the Čerenkov detector? As shown in Figure 62, there are only few charged particles among all the particles. The background consist mostly of photons.
- What is the energy distribution of the particles hitting the Čerenkov counter? As expected, and shown in Figure 63, most of the particles hitting the Čerenkov counter have very low energy.

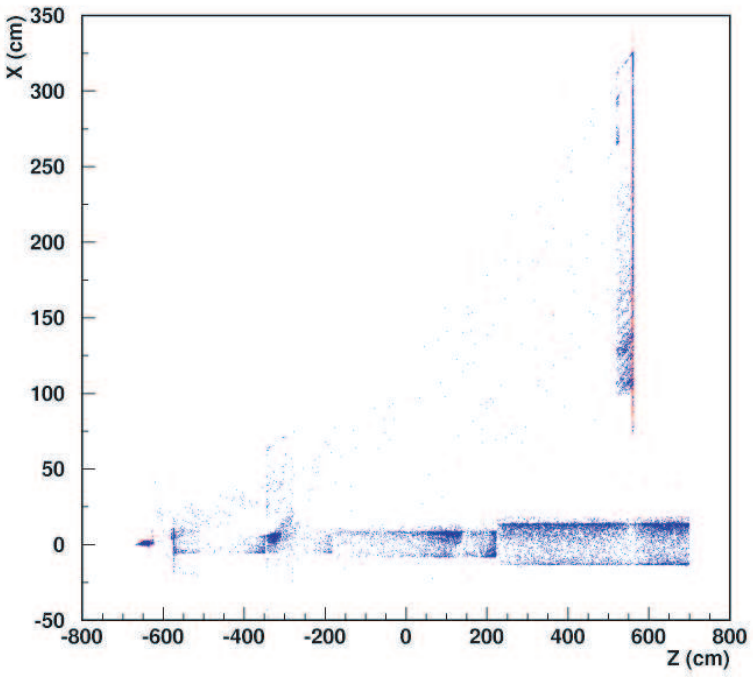

Figure 61: *Side view of the experimental setup generated by the vertexes of the positions where the primary and secondary particles are produced. Vertexes of photons are blue and electrons and positrons are red.*

The Čerenkov detector acceptance for the secondary particles is very low and even 100 million simulated scatterings produce a limited statistics for the background estimation. In the Table shown in Figure 64 we have separated the background rate normalized to the signal rate into

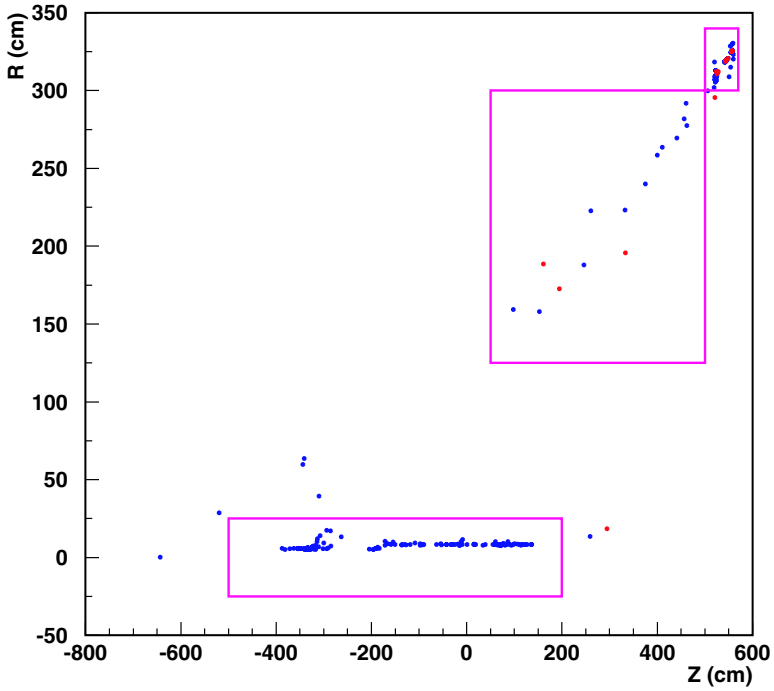

Figure 62: *Side view of the experimental setup generated by the vertexes of the positions where the primary and secondary particles which hit the Čerenkov detector are produced. Vertexes of photons are blue and electrons and positrons are red. One can separate the positions into three major regions: beam pipe, air, and the collimator window in front of the detector.*

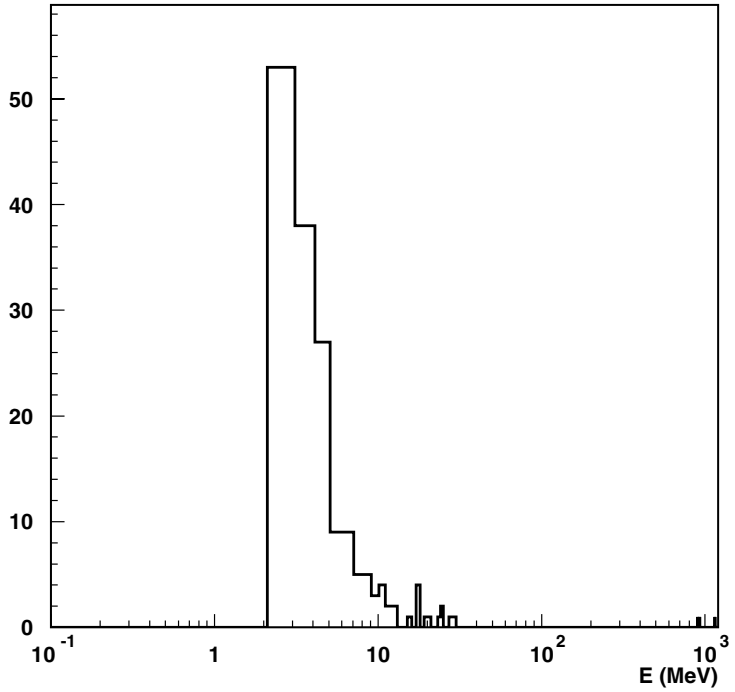

Figure 63: *Energy distribution of the secondary particles hitting the Čerenkov detector.*

contribution from neutral and charged particles, different experimental regions, and different detector response. The tabulated results in Figure 64 can be summarized as follows:

- Column 1 shows the separation of the background into particle types and the source of the background.
- Total number of background hits in the Čerenkov detector region, as seen in Column 2, is approximately equal to total number of elastic electrons hits ($Column/Signal \approx 1$). It consist mostly of photons ($\approx 95\%$), and most of them ($\approx 90\%$) come from the beam line.
- If Čerenkov signal is required, Column 3, the number of photons is reduced by a factor of ≈ 10). Under a signal we only assumed the photon produced a charged particle in the detector above the Čerenkov threshold. In Column 4 we normalized the signal to the average path of charged particles in the detector. This reduced contribution of photons to signal by another factor of 2.
- An estimation of asymmetry of the background was done in Column 5. Here we only assume that the false asymmetry signature is very small if the background is produced by very forward scattered electrons.
- Column 7 summarizes the results and estimates the total background contribution under the present experimental setup and under the assumption that the part of the air can be replaced by Helium bag, and there can be considerable improvement in the beam line shielding.

The final result in Figure 64 estimates the total background contribution to $\approx 4\%$. While this is already a low percentage, it can be easily reduced even further. The majority of this background consists of particles below 10 MeV energy. Theses can be stopped or greatly reduced by few millimeters of lead shielding placed in front of Čerenkov detector. Čerenkov detector studies have shown that such thin shielding would not compromise detector signal quality [6].

9.4 Signal-to-background Dilution Factor

The physics asymmetry in our experiment will be diluted by the signal-to-background dilution factor, $S/(S+B)$, where S is the signal due to elastic scattering on Hydrogen and B is the background due to other processes. This is a dilution factor just like the beam polarization, and it must be known with good relative precision (about 1%). Our detector is designed to be insensitive to everything except elastic scattering on Hydrogen. However, there is a direct measurement we can do to convince ourselves that we have adequately suppressed other background processes. The elastically scattered electrons will be the only reaction product that can make it through our collimation system with momentum near the beam energy. The typical elastically scattered electron will have a momentum of 1145 MeV. In our normal data-taking mode, we will integrate the detector signal, so we can't accumulate an energy spectrum. To determine the

	Hits (B/S)	Cerenkov Signal Required	Normalized Cerenkov Signal	Asymmetry Factor	Helium Bag Factor	Expected Background
All background	1.05	-	-	-	-	-
All $e^{+/-}$	0.054	0.054	0.054	-	-	<2.5% or with Helium bag <1.5%
Not from target	0.03	0.03	0.03	-	-	
From air	0.02	0.02	0.02	0.02	0.006	
From detector collimator	0.006	0.006	0.006	0.006	-	
From beamline	0.006	0.006	0.006	<0.006	-	
All γ	0.99	0.115	0.0575	-	-	<5.5% or with better beamline shielding <2.5%
From target	0.012	0.006	0.003	-	-	
From air	<0.006	<0.006	<0.003	-	-	
From beamline	0.896	0.066	0.033	<0.033	-	
From detector collimator	0.042	0.024	0.012	0.012	-	
From main collimator	0.042	0.024	0.012	0.012	-	
					Expected dilution	≤4%

Figure 64: *Separation of the electromagnetic background into different categories. See text for details*

energy spectrum, we can turn down the incident beam current low enough to allow the counting of individual pulses in our Čerenkov detector. If we then back part of this detector with a small electromagnetic calorimeter array with good (3-4%) resolution, we can make a measurement of the energy spectrum of the particles that deposit a signal in our Čerenkov detector. Combining this information with the photoelectron spectra from our Čerenkov detector will allow us to determine accurately the fraction of our "integration-mode" signal that is due to elastically scattered electrons.

In the previous section the background caused by electromagnetic processes for the Q^p_{Weak} experiment were estimated. In the worst case the contribution of background to the signal is of the order of 4%. Again note that if necessary this contribution can be reduced by a few millimeters of lead shielding in front of Čerenkov detectors without compromising the detector signal. While the contribution of the inelastic nuclear processes will also be studied in detail, the preliminary results estimate this contribution to be much smaller than the contribution from electromagnetic processes. The spectrometer and detector system are anticipated to be a very clean system with respect to backgrounds from rescattering processes. At this time we are GEANT modeling additional reaction channels, but these contribution are anticipated to be small. We are in the process of completing the experiment design so as to minimize the contamination from other reactions. It is also important to try to measure these effects during the experiment. This can be done by changing the QTOR field to put, in turn, the super-elastic and the pion threshold regions on the detector plane to measure their PV asymmetries.

References

[1] Jlab Proposal E02-020, "The Q^p_{Weak} Experiment: A Search for Physics at the TeV Scale Via a Measurement of the Proton's Weak Charge", D. Armstrong et al., 2002

[2] N. Simicevic, LaTech Technical Report LATECH-CAPS-01-03a, G0-01-007, 2001.
(at http://www.npl.uiuc.edu/exp/G0/docs/docs.html)

[3] N. Simicevic, LaTech Technical Report LATECH-CAPS-02-06a, 2002.
(at http://www.jlab.org/qweak)

[4] N. Simicevic, LaTech Technical Report LATECH-CAPS-02-08a, 2002.
(at http://www.jlab.org/qweak)

[5] N. Simicevic, LaTech Technical Report LATECH-CAPS-02-11a, 2002.
(at http://www.jlab.org/qweak)

[6] GEANT Detector Description and Simulation Tool, *CERN Program Library Long Writeup W5013*, CERN, Geneva, 1993

(at http://www.npl.uiuc.edu/exp/G0/docs/docs.html)

10 Infrastructure

The infrastructure hardware activities associated with Q^p_{Weak} consists primarily of the beamline instrumentation, detector shielding, collimators, beamline shielding, a possible Møller polarimeter current upgrade, cryo-target support systems, plus miscellaneous vacuum and electrical systems. The labor tasks associated with infrastructure include assembly of the experiment, survey/alignment of all sub-systems and in situ final checkout.

10.1 Detector Shielding

The detectors will be installed in recessed cavities within cast concrete structures. This is a very cost effective approach to the shielding of the detectors. The construction approach will be to build up the detector support/shielding structure from specialty cast concrete modules (blocks). By keeping the weight of each module under 20 Tons they can be assembled using the existing Hall C crane. The modules will be cast of normal density concrete with a fraction of a percent Boron Silicate to help absorb low energy neutrons. The fabrication technique will be to weld light weight aluminum plate into opened ended boxes designed to hold the detector assemblies and then cast them into the concrete modules. The result will be a ready to assembly set of modules with alcoves in place to receive the detector assemblies.

10.2 Collimators

The two collimators are the primary Q^2 defining apertures in the experiment. The spectrometer has a magnification of about unity and the GEANT simulations indicate that we need to control mechanical tolerances and assembly errors at around the 1 mm level. We will be taking a conservative approach and design to a somewhat tighter tolerance. The smaller front collimator will need to be constructed to somewhat higher tolerances than the second collimator which is the "clean up" collimator. Machinable Tungsten is a likely candidate for the first collimator, while sections of a cast Pb alloy will likely be the fabrication choice for the second collimator. Although, extensive simulations have been completed to determine the optimum shape for both collimator assemblies, detailed engineering of these devices remains to be done.

10.3 Beamline and Shielding

The Q^p_{Weak} apparatus will recycle most of the beamline systems constructed for the G0 experiment. These include the G0 downstream instrumentation girder plus associated electronics and all existing fixed installation parity related beamline instrumentation. This includes the extensive set of specially instrumented Hall C Arc beam position monitors (BPM's), the current measuring RF cavities, the beam raster system, the coil pulsing system (used for systematic studies), the precision Møller polarimeter, and a number of other specialized systems throughout the injector

and accelerator. The value of these existing systems in both capital hardware and invested labor is significant. If we had to reproduce all these system the cost would conservatively approach several million dollars.

Although, the QTOR magnet coils are very thick Cu when viewed radially, the small wedge gaps around the beam pipe need to be filled with 3" of Pb to insure the conservative shielding geometry we desire for the Q^p_{Weak} measurement. The scattering assembly will also be enclosed by existing concrete shielding blocks to reduce the ambient room radiation levels.

The vacuum system for Q^p_{Weak} includes the sections of beam transport pipe starting at the target chamber which pass through the magnet and hook up to a downstream transport line. There are also reuseable cryo-target support hardware, vacuum pumps, valves, cables, H.V. supplies and miscellaneous electrical systems available and reconfigured for each major installation class experiment that is performed in Hall C.

10.4 Installation

The philosophy of the Q^p_{Weak} collaboration is to keep the experiment physics goals aggressive while keeping the technology as simple as possible. This will ease both installation and commissioning while providing the experiment with maximum reliability. Large system such as the magnet and collimators will be assembled in the Hall from subassemblies each less than 20 Tons. Depending upon how the magnet assembly plan evolves there may be a final magnet lift onto its stand which will require an outside rigger with larger capacity equipment. These activities have occurred multiple times over the years for major installation class experiments mounted in Hall C. All smaller sub-systems will be installed and aligned by the Hall C and accelerator division technical staff. This is also true for electrical (other than high power), signal readout/control and cryogenic systems.

10.5 Survey and Alignment

The survey and alignment activities are critical for the Q^p_{Weak} experiment. Prudent alignment tolerances on critical components in this experiment appear to be on the order of 0.5 mm which is well within the capabilities of the Jlab survey group. We will be intelligent about designing systems which can be assembled, surveyed and aligned in a straightforward manner. The Q^p_{Weak} experiment yields itself well to this approach as it is intrinsicly a modular system. The critical alignments are the target-collimator-magnet assembly. The detectors are somewhat less critical as they are larger than the elastic focal plane. The target flask will be remotely movable in X,Y and pitch, while the beam can be moved to determine the experiment's neutral axis ("sweet spot" that provides the maximum suppression of unwanted helicity correlated position motion).

11 Summary

The Q^p_{Weak} collaboration, from the beginning, set out to undertake a best-possible measurement of the weak charge of the proton that could be undertaken at Jlab, given present limitations in experimental technology and practical limitations in beam availability and target power. When completed, the Q^p_{Weak} experiment will be the most precise measurement of the weak charge of the proton at low Q^2, and the results will either yield a smoking gun for new physics or put impressive constraints on new physics beyond the standard model at the TeV scale. Although, the Q^p_{Weak} experiment is quite innovative in concept and has lofty objectives, the approach taken to the experimental design is quite conservative, based on proven technology and modest extrapolations from existing devices. We expect, subject to funding and scheduling considerations, to be in a position to beginning take data by late 2006.

This technical design report summarizes the conceptual design and technical means for achieving the experimental goals of the Q^p_{Weak} experiment. As such it is intended to be a blueprint and a plan of action for the collaboration to follow. Costs and schedules can be found in the companion document, *The Q^p_{Weak} Experiment project management plan for experimental construction.* These are meant to be living documents that are expected to evolve as needed.

12 APPENDIX A: Optics Design Study of the Toroidal Magnet

The approved JLab Q_{weak} Experiment (E02-020): "A Search for Physics at the TeV Scale Via a Measurement of the Proton's Weak Charge" [1], proposed a test of the Standard Model by studying the evolution of the weak mixing angle $sin^2\theta_w$ to lower energies. It will be performed through a precision measurement of the proton's weak charge using the parity violating asymmetry in the elastic scattering of polarized electrons from unpolarized protons at $Q^2 = .03$ GeV^2. It is expected that any deviation of $sin^2\theta_w$, extracted from the proton's weak charge, $Q^p_{Weak} = 1 - 4sin^2\theta_w$, from the prediction of the Standard Model would be a signal of new physics, while the agreement would place significant constraints on possible Standard Model extensions.

In order for the Qweak detector system to operate, the experiment requires a toroidal magnet which will generate a magnetic field that bends/focuses scattered charged particles into the detector position. The design of this large acceptance spectrometer started with a possible modification of the existing superconducting G^0. The optimized accepted solution for the Q^p_{Weak} experiment ended up being a resistive toroidal magnet. The preference for a resistive toroidal magnet design is a result of the low cost and the inherent reliability relative to a superconducting solution. Construction of a resistive magnet would allow the execution of the Q^p_{Weak} experiment in a timely and independent manner. Recycling a toroidal magnet built originally for a different experiment (eg, the G^0 magnet), could not begin until the end of that experimental program. This section will summarize the design criteria and procedures related to the resistive Q^p_{Weak} Toroidal Magnet (QTOR) and finalize its design parameters.

12.1 Basic Design Criteria

As already stated, Q^p_{Weak} will be determined by measuring the parity violating asymmetry in elastic ep scattering at $Q^2 = 0.03\ \ (GeV/c)^2$. The expected acceptance averaged asymmetry of -0.28 ppm will be measured to $\pm 2\%$ statistical error. This requires a large counting rate which will be obtained by using a combination of high luminosities and a large acceptance detector system. The heart of the experiment is a spectrometer whose toroidal magnetic field will focus elastically scattered electrons onto a set of eight rectangular quartz Čerenkov detectors. The structure of this spectrometer should be similar to the structure of the G^0 spectrometer since the scope of the G^0 experiment is also measurement of small parity violating asymmetries [9,10] and the spectrometer is also designed to focus particles of the same momentum and scattering angle from the length of the extended target to a single point (zero magnification in the dispersion direction). For both experiments reduction in systematic uncertainties requires axially symmetric acceptance. As a result of those similarities, the Q^p_{Weak} Toroidal Magnet (QTOR) will have the same shape and same number of coils as the G^0 spectrometer arrangement of which is shown in Figure 65.

While the G^0 spectrometer might in principle be modifiable for the needs of the $in Figure$ 66.

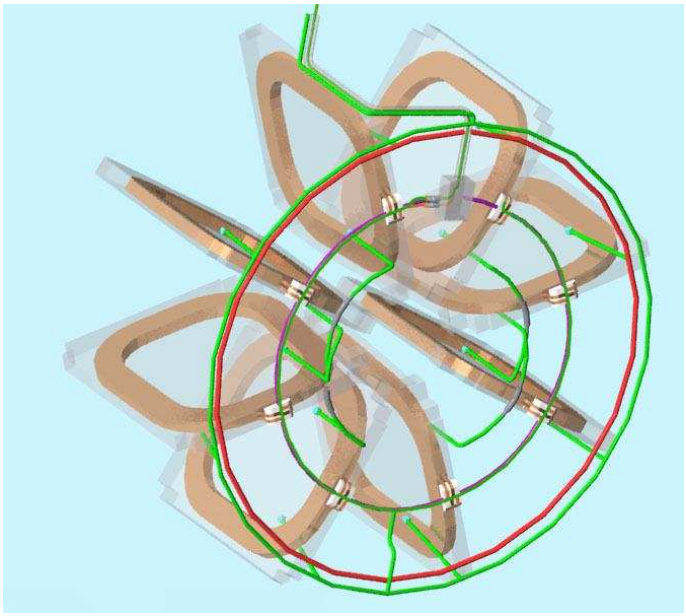

Figure 65: *Eight superconducting coils of the G^0 spectrometer and the liquid helium plumbing between them.*

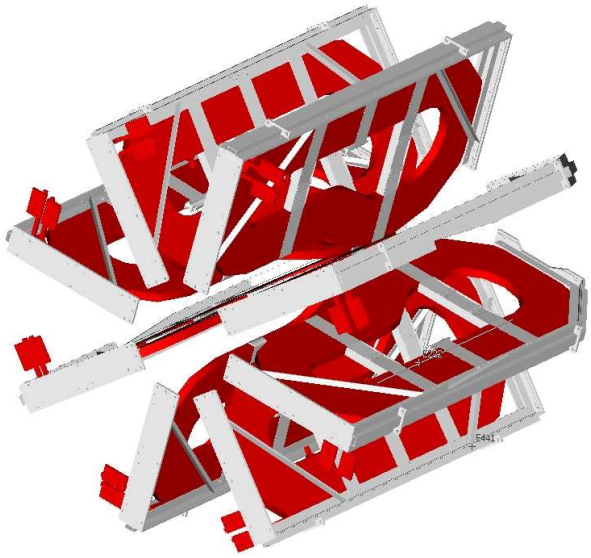

Figure 66: *Eight resistive coils and a support frame of the MIT-Bates BLAST toroidal magnet.*

A justification to make the Q^p_{Weak} Toroidal Magnet similar to the BLAST Magnet come from comparing the magnetic field requirements. The magnetic field has to have the strength to bend $\theta_e = 9.0$ deg scattered electrons with the momentum $P' \simeq 1.150$ GeV by approximately $\Delta\theta_e = 10.0$ deg. It is easy to calculate that such a requirement results in the $\int Bdl$ having a value of approximately 0.67 T·m. The value of this integral is about one half of the value for the G^0 Superconducting Magnet having $\int Bdl = 1.6$ T·m [2] and is comparable to the values of BLAST, designed for maximum field integral of 0.6 T·m [10]. Also, like for the BLAST design, the Q^p_{Weak} Toroidal Magnet will provide a magnetic field free region on the beam axis. On the other hand, the Q^p_{Weak} Experiment does not have to perform all the functions of the BLAST experiment which will result in the Q^p_{Weak} Toroidal Magnet being a simplified version of BLAST magnet.

In addition of the criteria already mentioned, the list of parameters which have an effect on the design of the Q^p_{Weak} Toroidal Magnet includes:

- Elastic and inelastic channel separation, corresponding to a momentum resolution of $\leq$ 10%.
- Background reduction.
- Systematic error control.
- Reliable operation and servicing.
- While the primary interest of the experiment is a measurement of the elastic channel, the experiment will benefit if the detector system would allow for a simultaneous measurement of the inelastic channel as well as the hall background.
- Normal-conducting water cooled copper coils in order to decrease cost.

12.2 Coil Geometry

As justified in the previous sections, the design of the Q^p_{weak} Toroidal Coil Magnet will be very similar to the design of the BLAST magnet. Every aspect of the original BLAST magnet design: the number and the shape of coils, the winding of copper conductor, the power supply and water cooling, parts of the support structure, experience, etc. will be used in the process of designing and constructing the Q^p_{Weak} spectrometer. The BLAST Magnet is described in detail in Ref. [10], while the later modifications can be found in the documents collected at http://mitbates.mit.edu/index2.stm web page. Some requirements imposed on the BLAST magnetic field, such as the magnetic field free region at the position of the target, do not apply to the Q^p_{Weak} measurement. Therefore, the tooling cost for the BLAST coil will be reduced by making the Q^p_{Weak} Magnet coils as simple as possible but still using the BLAST templates. We expect the coil performances to be similar to the performances of the BLAST coils and refer to Ref.[10] for further details.

To make sure that the design of coils similar to BLAST is the best solution for the Q^p_{Weak} experiment, several other coil arrangement and their optical properties have been studied. The shapes and the elastically scattered electron focusing properties have been collected in Figure 67, Figure 68 and Figure 69. While there was a potential for some of those solution to work, they were all abandoned in favor of modified BLAST magnet solution. The accepted solution is shown in Figure 70.

To study the optical properties of the coils, the cross section of a coil was set to 8 by 50 cm^2. It consists of two 220 cm long straight sectors and two bended sectors each covering half a circle with an inner radius of 25 cm, and an outer radius of 75 cm. Total length of the QTOR is 370 cm, shorter than the 434 cm length of the BLAST magnet. The coils will be built using the procedure for the Blast magnet coils [11] which consists of a two layer pancake, each having 13 turns of OFHC Copper (CDA 102) conductor material with the square dimensions of 3.81x3.81 cm^2 and inner water cooling pipe diameter of 2.03 cm. Taking into the account fiberglass and epoxy insulation the dimension of the coil will be 9.1 by 54.0 cm^2. The shape of the Q^p_{Weak} Toroidal Magnet coil is shown in Figure 71.

The eight coils of Q^p_{Weak} Toroidal Magnet will be radially located and spaced at angles of $\pm 22.5°$. The shortest distance between the coil and the beam line will be 15 cm. The arrangement of the coils from the preliminary drawings of BATES engineer Stan Sobczynski are shown in Figure 72.

Technical characteristics of the Q^p_{Weak} Toroidal Magnet are calculated and compared to the same characteristics of the BLAST magnet [12]. The result is shown in the Table below. Among other properties it includes: total length of the coil conductors, weight, current density and power requirements of the coils, and water cooling requirements.

12.3 Magnetic Field Calculations and Magnet Optics

The magnetic field was calculated using the Biot-Savart Law and performing numerical integration of the contribution of the conductors' current density. The coil was represented by the set of arcs and straight conductor segments. The BLAST magnet current density of 627 A/cm^2 which is reduced to an effective current density of 405 A/cm^2 as a result of the space of the coil used by the cooling system, would be barely acceptable for the Q^p_{Weak} Toroidal Magnet. The magnetic field of the Q^p_{weak} Magnet was calculated assuming a nominal current density of 560 A/cm^2. This value is considered reasonable for insulated water cooled copper windings [2]. Since the magnetic field scales proportionally to the current density, it is easy to scale any calculated field map to a desired value.

The plot of the azimuthal magnetic field components B_ϕ is shown in Figure 73 as a three-dimensional function of the position along the beam axis Z and the radial distance R from the beam axis. The field on the beam axis is zero, and increases rapidly reaching a maximum at a distance of 56 cm from the beam axis. From that point, the field falls off as $1/R$. For the target outside and upstream of the magnet, the value of the magnetic field integral depends on the

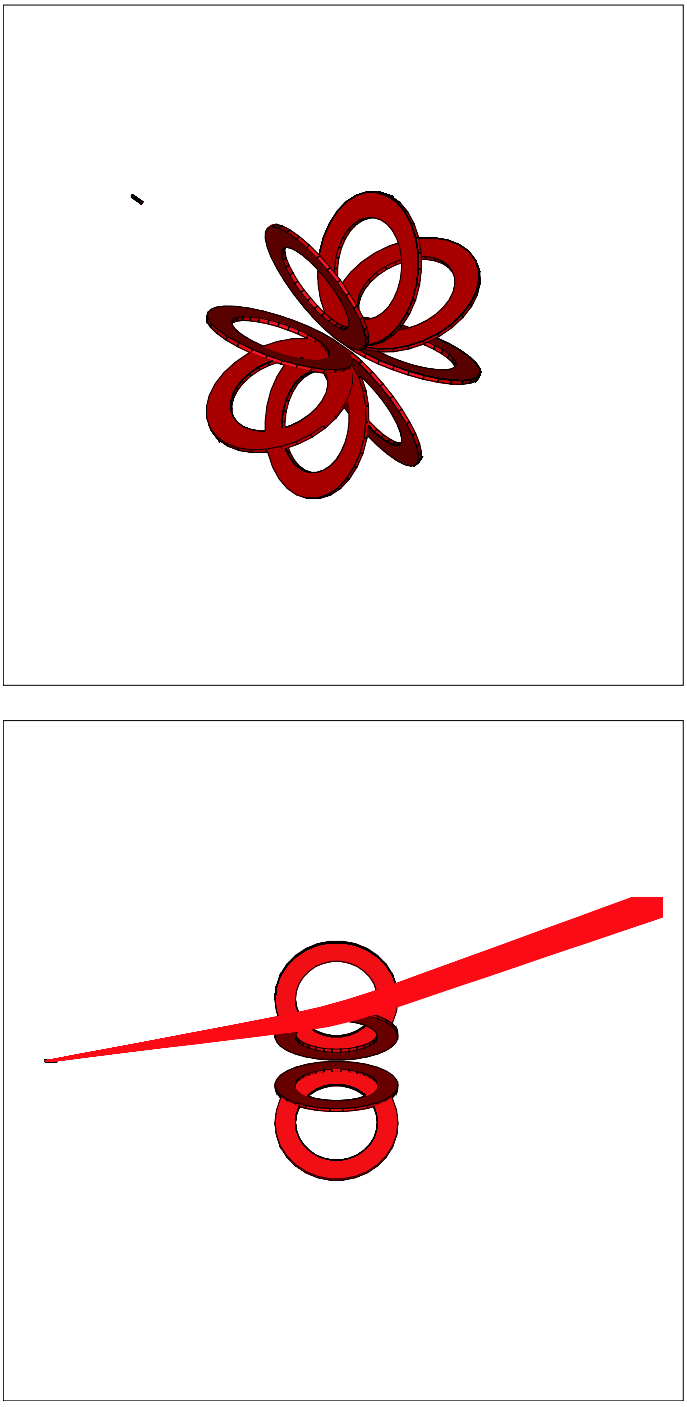

Figure 67: *The positions of one of the possible toroidal magnet design relative to the beam line and the position of the target (top). The coils are circular with the radius of 125 cm. The magnet does not focus elastically scattered electrons in the kinematics of the Q^p_{weak} measurement using acceptable current densities for water cooled copper (bottom). The kinematics is restricted to the electron scattering angles of $\theta_e = 9.0 \pm 2.0$ deg and $\phi_e = \pm 15.0$ deg.*

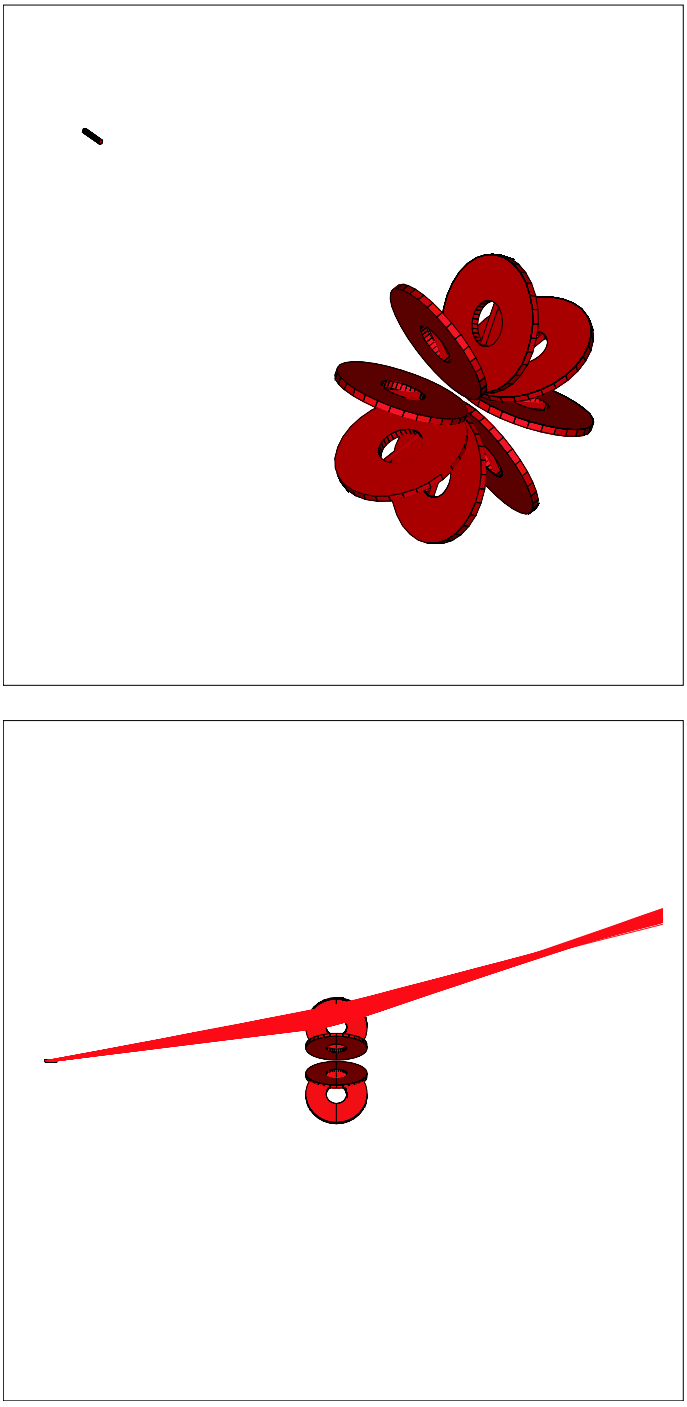

Figure 68: *The positions of one of the possible toroidal magnet design relative to the beam line and the position of the target (top). The coils are circular with the radius of 50 cm. The magnet focus elastically scattered electrons in the kinematics of the Q^p_{Weak} measurement using current densities approximately twice as high as normal for water cooled copper (bottom). The kinematics is restricted to the electron scattering angles of $\theta_e = 9.0 \pm 2.0$ deg and $\phi_e = \pm 15.0$ deg.*

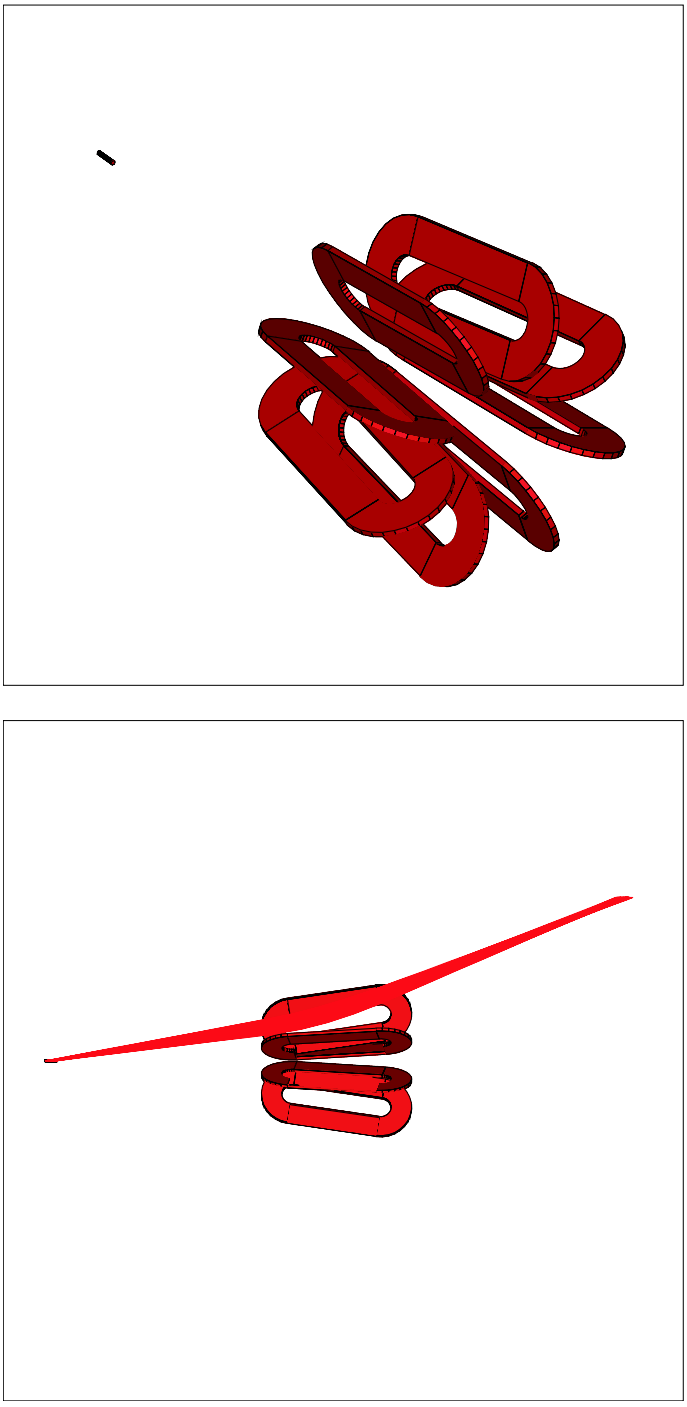

Figure 69: *The positions of one of the possible toroidal magnet design relative to the beam line and the position of the target (top). The coils are oval, but tilted relative to the beam axis by 9.0 deg The magnet focus elastically scattered electrons in the kinematics of the* Q^p_{weak} *measurement using acceptable current densities for water cooled copper (bottom). The kinematics is restricted to the electron scattering angles of* $\theta_e = 9.0 \pm 2.0$ *deg and* $\phi_e = \pm 15.0$ *deg.*

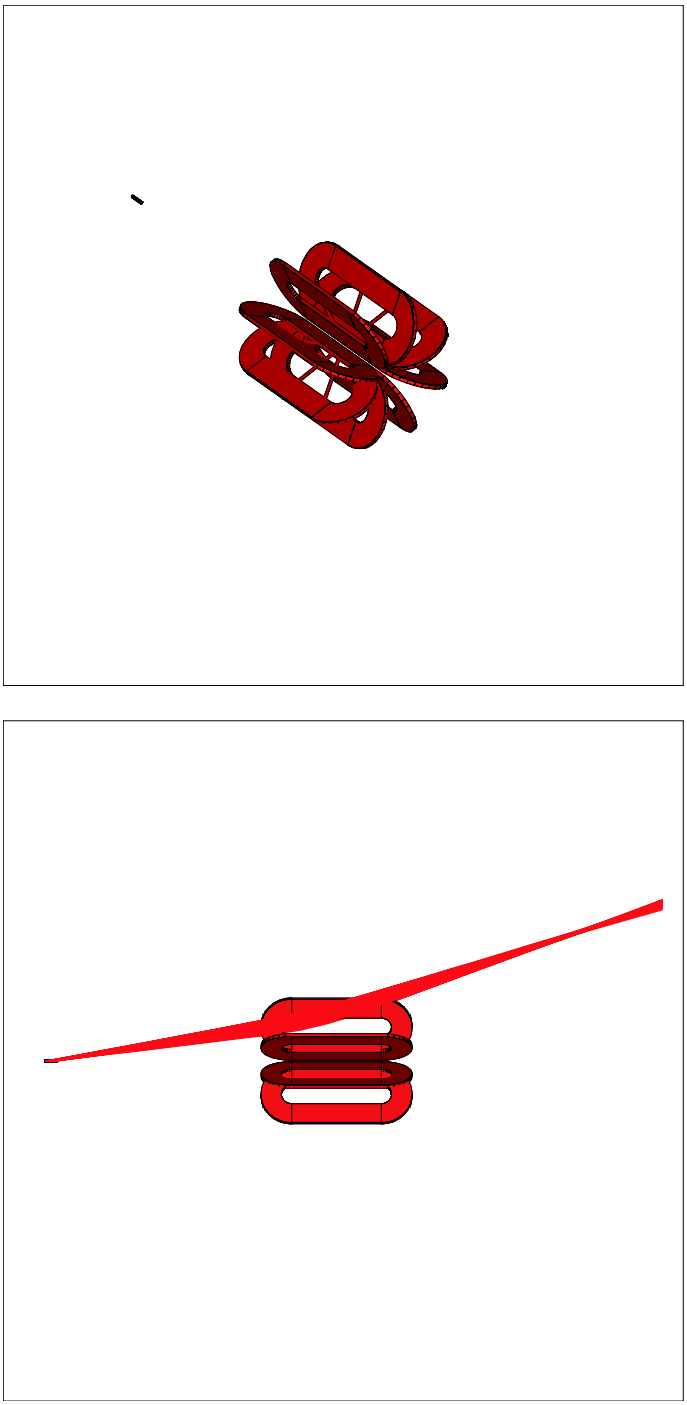

Figure 70: *The positions of modified BLAST magnet design relative to the beam line and the position of the target (top). The magnet focus elastically scattered electrons in the kinematics of the Q^p_{Weak} measurement using acceptable current densities for water cooled copper (bottom). The kinematics is restricted to the electron scattering angles of $\theta_e = 9.0 \pm 2.0$ deg and $\phi_e = \pm 15.0$ deg.*

Figure 71: *The simplest and least expensive Q^p_{Weak} Toroidal Magnet coil design built using two identical conductor layers, two independent water circuits, no reverse bends, and which requires very simple winding fixture. The drawing is done by BATES engineer Stan Sobczynski.*

scattering angle. The electrons with smaller polar angle θ_e will have more $\int Bdl$ and bend more than the electrons at larger polar angles. This will result in focusing of the scattered electrons. In Figure 9 we also plot B_ϕ in a plane perpendicular to both, the median plane and the beam line at the center of the magnet, $Z = 0$ cm. The profile of the field in this plane, as in the case of the BLAST magnet, indicates that there is a small field variation in the regions covered by the azimuthal distribution of the scattered electrons.

For an ideal toroid, the B_z component of the field is zero, while for the real toroidal magnet we expect this component to be negligibly small compared to the B_ϕ component. In the case of the Q^p_{weak} Toroidal Magnet this component on the median plane between two coils is shown in Figure 74. The strength of the B_z component at its maximum is about 1.5 % of the strength of the B_ϕ component.

Finally, the profile of the azimuthal magnetic field component B_ϕ as a function of radial distance R are shown in Figure 75. The field component B_ϕ is calculated in the median plane at $Z = 0$ cm, the center of the magnet.

Fixing the kinematics of the Q^p_{Weak} experiment by optimizing the figure of merit [1], the focusing properties of the magnet depend of the target length and position. To achieve high luminosity the length of the liquid hydrogen target was chosen to be 35 cm. The target assembly is located outside and upstream of the magnet to allow for the detection of electrons with a scattering angle of $\theta_e = 9.0 \pm 2.0$ deg. After several iterations, the optimal position of the target

Figure 72: *The radial arrangement of the Q^p_{Weak} Toroidal Magnet coils. The drawing is done by BATES engineer Stan Sobczynski.*

Magnets Technical Comparison		
Mean Turn Length (cm)	908.1	754.2
Number of Turns	2 X 13 = 26	2 X 13 = 26
Total Length (cm)	23618	19609
Volume of Copper (cm^3)	265435	220379
Weight/Coil (kg)	2380.4	1976.4
Total Weight (kg)	19043	15811
Current Density (A/cm^3)	600	555
Current in the Conductor (A)	6731	6230
Resistance (Ohm/Coil) @ 60 C	0.0042	0.0035
Power (kW/Coil)	190	136
Voltage (V)	28.2	21.8
Total Power (MW)	1.52	1.09
Cooling Water Flow (gal/min)	24.0	16.5
Water Velocity (m/s)	2.4	1.7

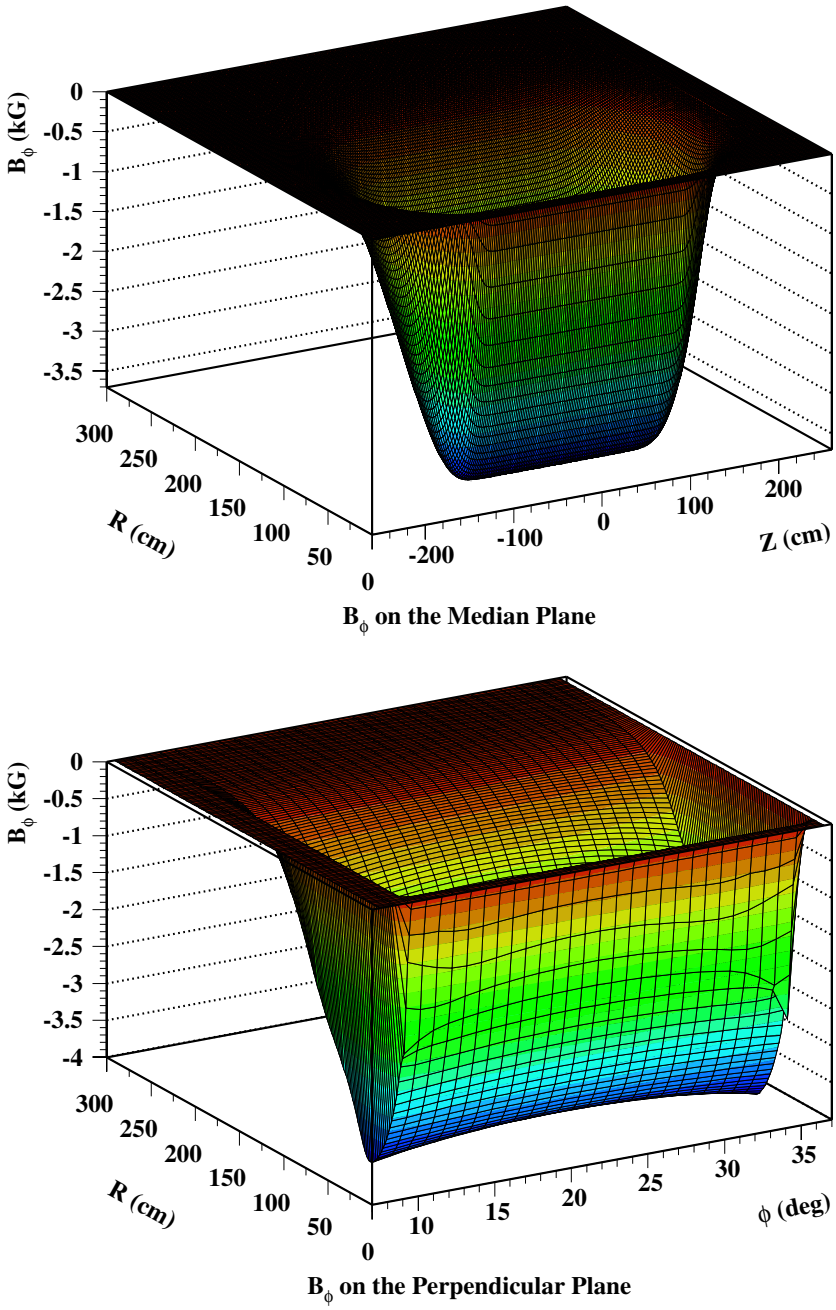

Figure 73: *The 3D plot of the azimuthal magnetic field components B_ϕ on the median plane between two coils as a function of the position along the beam axis and the radial distance from the beam axis (top), and the 3D plot of the azimuthal magnetic field components B_ϕ on the plane perpendicular to both, the median plane and the beam line at z=0 (bottom).*

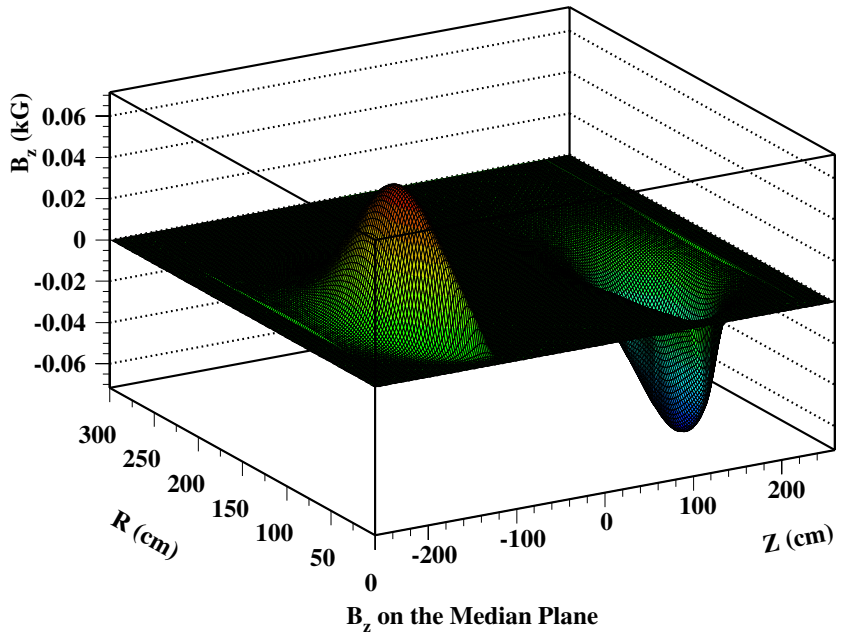

Figure 74: *The 3D plot of the magnetic field components B_z on the median plane between two coils as a function of the position along the beam axis and the radial distance from the beam axis.*

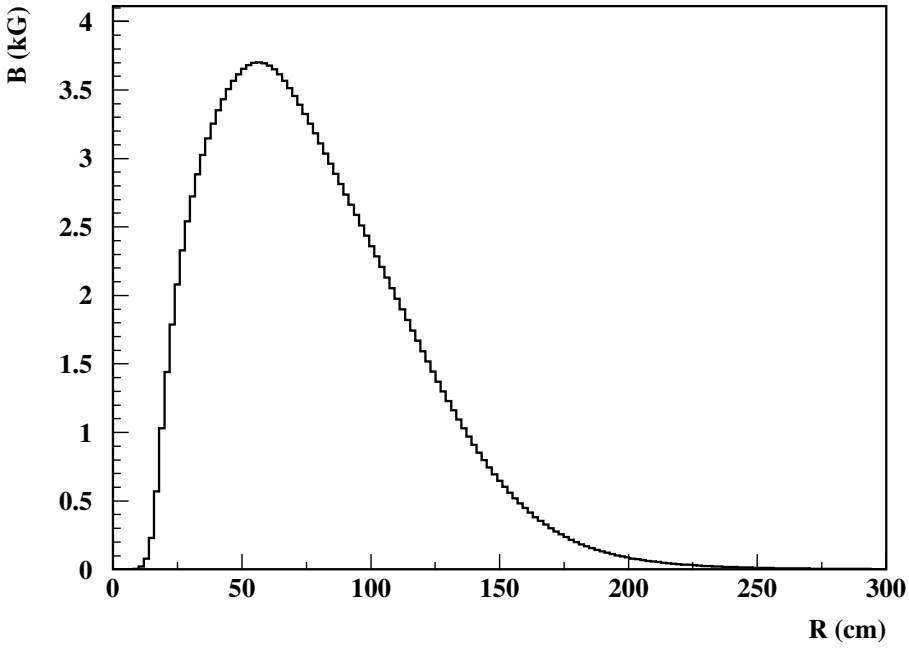

Figure 75: *The azimuthal magnetic field components B_ϕ on the median plane between two coils at for $Z = 0$ cm, corresponding to the center of the magnet. The value is calculated for 75% of nominal current density of 560 A/cm^2.*

was found to be 650 cm upstream from the mid point of the magnet.

The optical properties of the magnetic field were verified simulating the electron trajectories, restricted to initial polar angle $\theta_e = 9.0 \pm 2.0$ deg and azimuthal angle $\Delta\phi_e = \pm 15.0$ deg, for following reactions:

- elastic scattering, $ep \rightarrow ep$,
- and pion production reaction, $ep \rightarrow en\pi^+$ or $ep \rightarrow ep\pi^0$.

Elastic electron trajectories with those settings are shown in Figure 76. It is clear that for elastic scattering the magnet has the required property of focusing scattered electrons. This is essential to perform these measurements.

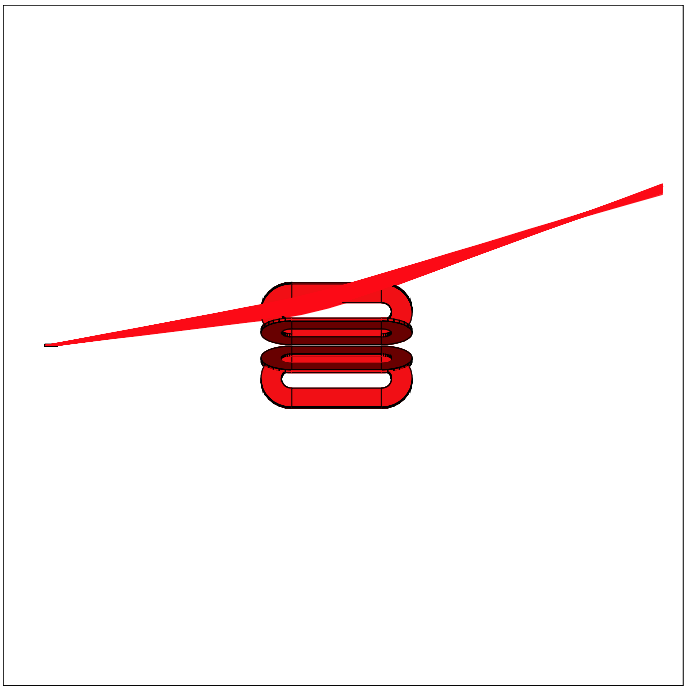

Figure 76: *The side view of the modeled setup with a sample of elastic trajectories restricted to* $\theta_e = 9.0 \pm 2.0$ *deg and* $\phi_e = 0.0 \pm 15.0$ *deg.*

As shown in Figure 77, the resolution of Q^p_{Weak} spectrometer is sufficient to separate elastic and inelastic electrons at the position of choice, allowing sufficient space to build a detector which will cover only the elastic electrons focal plane area. This area is approximately 12 cm wide and 2 m long.

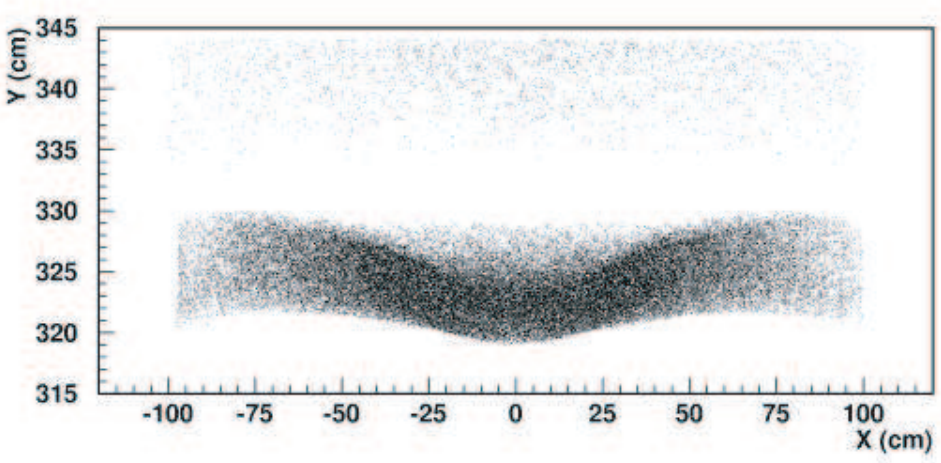

Figure 77: *Separation of elastically (lower distribution) and inelastically (upper distribution) scattered electrons at the position 580 cm downstream from the magnet mid point. The kinematics is restricted to* $\theta_e = 9.0 \pm 2.0$ *deg and* $\phi_e = 0.0 \pm 15.0$ *deg.*

12.4 Anticipated Magnet Performance

In the previous chapters the optical properties of the Q^p_{weak} spectrometer were studied using artificially restricted kinematical inputs: $Q^2 = .03$ GeV^2, incident beam energy $E_0 = 1.165$ GeV, electron polar angle $\theta_e = 9.0 \pm 2.0$ deg, and azimuthal angle $\phi_e = 0.0 \pm 15.0$ deg, using the GEANT simulation package [12] with all the secondary reactions turned off. A more realistic simulation requires the kinematics of the experiment defined by the collimators and all the secondary reactions turned on. Figure 78 shows the elastically scattered electrons whose kinematics is selected by the conical collimator. The secondary reactions consist mostly of bremsstrahlung shower from the fraction of the electrons hitting the collimator walls. This shower is well separated from the electrons at the position of the focal plane as a result of the electrons bending and the photons continuing in a straight path. Figure 79 shows a narrow band of electrons above the broad electromagnetic shower distribution. The projection of the collimator shape is a result of most of the showering happing on the collimator walls

To increase the field for the same current density, the magnet was positioned as close to the beam line as possible. The inner radius of the Q^p_{weak} spectrometer hub was designed to be 15 cm. As shown on Figure 80, this distance is sufficient to accommodate the beam pipe shielding taking into consideration the beam broadening in 35 cm of liquid hydrogen target.

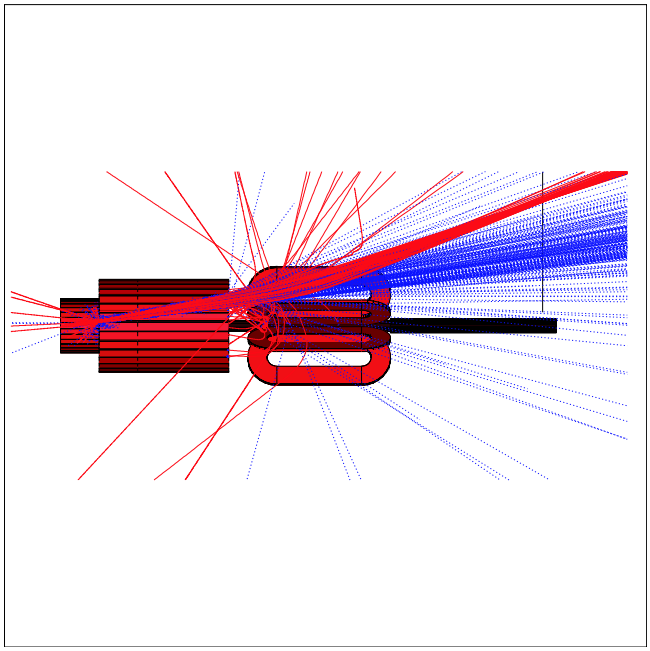

Figure 78: *The side view of the modeled experimental setup consisting of a 35 cm long liquid hydrogen target, conical collimator, Q^p_{Weak} spectrometer, and the focal plane detector. Electron kinematics is defined by the collimator, and all the secondary reactions were allowed. The electron trajectories (red lines) are distinguished from the photon trajectories (blue lines).*

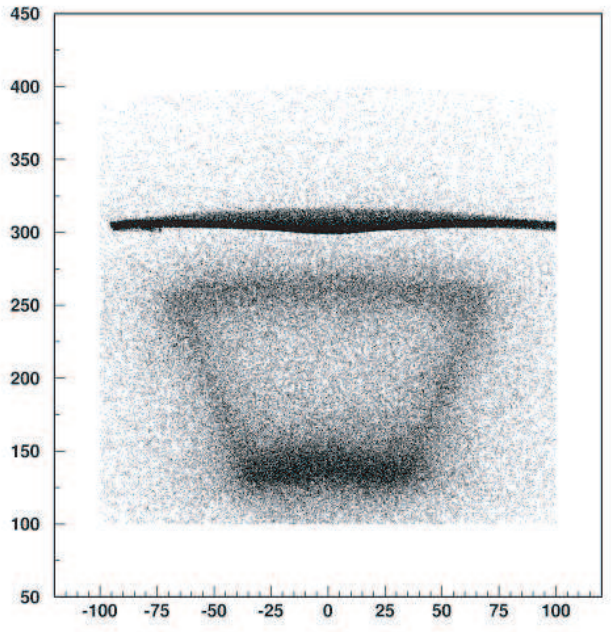

Figure 79: *Separation of elastically scattered electrons (narrow band) and electromagnetic shower depicting the collimator walls at the position 580 cm downstream from the magnet mid point.*

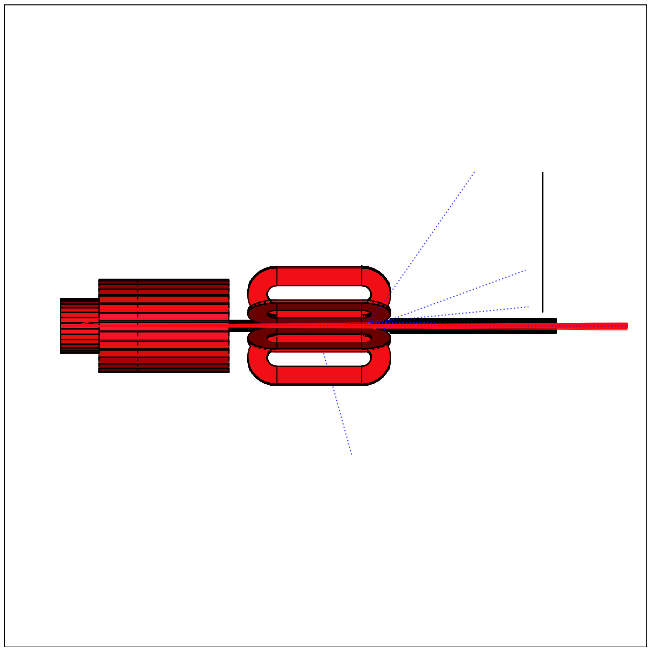

Figure 80: *The side view of the modeled experimental setup as in Figure 78, but including beam line shielding. Only the electron electromagnetic showering in liquid hydrogen was allowed. The electron trajectories (red lines) are distinguished from the photon trajectories (blue lines).*

12.5 Conclusion

This report contains the description of the Q^p_{Weak} spectrometer design, the essential magnet properties and the implication on the experimental kinematics, setup, and procedures. The design is based on kinematical constraints which optimize the figure of merit of the Q^p_{weak} Experiment, the incident beam energy of $E_0 = 1.165\ GeV$, electron polar angle $\theta_e = 9.0 \pm 2.0$ deg, and azimuthal angle $\phi_e = \pm 15.0$ deg for each sector. The similarity with the MIT Bates BLAST Toroidal Magnet was done on purpose to minimize the cost of engineering and construction of the Q^p_{Weak} Magnet.

References

[1] Jlab Proposal E02-020, "The Q_{weak} Experiment: A Search for Physics at the TeV Scale Via a Measurement of the Proton's Weak Charge", D. Armstrong et al., 2002

[2] N. Simicevic, LaTech Technical Report LATECH-CAPS-01-03a, G0-01-007, 2001. (at http://www.npl.uiuc.edu/exp/G0/docs/docs.html)

[3] N. Simicevic, LaTech Technical Report LATECH-CAPS-02-06a, 2002. (at http://www.jlab.org/qweak)

[4] G0 Technical Design Report, Nuclear Physics Laboratory, University of Illinois at Urbana-Champaign, 1993.

[5] Letter of Intent to TJNAF, R. Carlini, J. M. Finn and M. J. Ramsey-Musolf, spokespersons.

[6] N. Simicevic, LaTech Technical Report LATECH-CAPS-00-06a, G0-00-026, 2000. (at http://www.npl.uiuc.edu/exp/G0/docs/docs.html)

[7] N. Simicevic, LaTech Technical Report LATECH-CAPS-00-06b, G0-00-028, 2000. (at http://www.npl.uiuc.edu/exp/G0/docs/docs.html)

[8] TJNAF Experiment E91-017, D. Beck, spokesperson.

[9] TJNAF Experiment E97-104, S. P. Wells, N. Simicevic and K. Johnston, spokespersons.

[10] A Proposal for the Bates Large Acceptance Spectrometer Toroid, The BLAST Collaboration.

[11] Final Signoff Specifications for the BLAST Toroidal Spectrometer Coil(s), J. Kelsey, 1997.

[12] BLAST Coil Calculations, J. Kelsey, E. Ihloff, G. Dodson, S. Sobczynski, and R. Averill, BLAST Technical Note #2, 1997.

[13] GEANT Detector Description and Simulation Tool, *CERN Program Library Long Writeup W5013*, CERN, Geneva, 1993

13 APPENDIX B: Collimator Design Study

The kinematics of the Q^p_{Weak} experiment is fixed by optimizing the figure of merit [1]. The kinematical cuts on the electron scattering angles were chosen $\theta_e = 9.0 \pm 2.0$ deg for the polar angle, and $\phi_e = \pm 15.0$ deg for the azimuthal angle. The cut on polar angle defines the accepted Q^2, while the cut on the azimuthal angle defines overall counting rate and the statistical precision of the experiment. With those quantities fixed, the design of the collimating system depends on the target length and position relative to the position of the Q^p_{Weak} Toroidal Magnet. To achieve high luminosity the length of the liquid hydrogen target was chosen to be 35 cm, and the optimal position for the center of the target was found to be 650 cm upstream from the mid point of the magnet. Additional factors taken into consideration in the collimator system design are as follows:

- The collimator system should provide an exit from the target chamber. There should be a place for the windows through which the scattered electrons can transit from the scattering chamber's vacuum into the air.
- Most of the shielding should be positioned close to the target to reduce the volume and the weight of the shielding material.
- The kinematics of the experiment should be defined by a collimating wall placed further away from the target to minimize the effect of the target length on the kinematical quantities.
- There should be sufficient spacing between two collimating walls to accommodate instruments necessary to measure Q^2 (GEMs) as well as a miniature toroidal magnet which may be necessary to sweep away electrons resulting from Møller scattering out of the line of the Q^2 determining apparatus.
- There should be sufficient spacing between the last collimator wall and the Q^p_{Weak} Toroidal Magnet to accommodate two wire chambers which will be used in the Q^2 determination.
- The amount of the shielding material should be no more or less than necessary for adequate shielding.

All of the above criteria were taken into account in the process of designing the collimating system for the Q_{weak} Experiment. The schematic side view and the electron collimation by the collimator are shown in Figure 81. More detailed description of the parts of this collimating system, shown again in Figure 82 as the 3-D perspective in relation to the spectrometer coils, will be done in the next section.

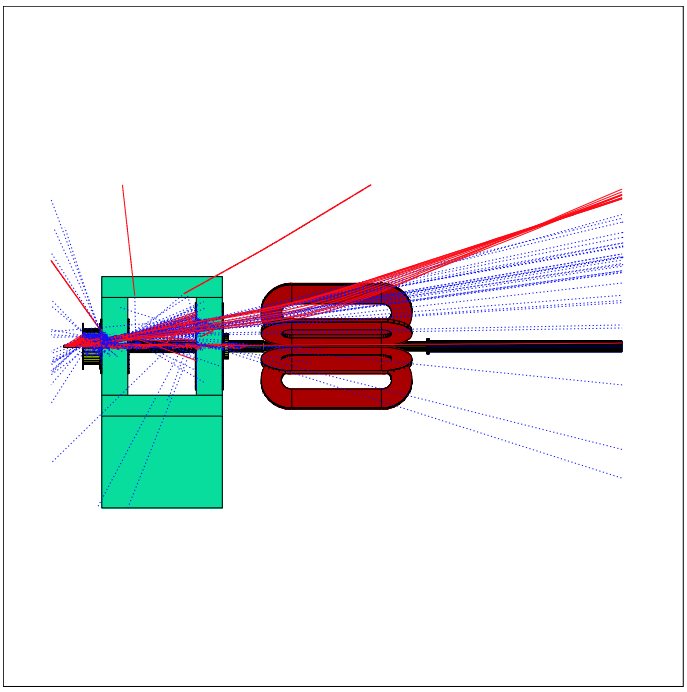

Figure 81: *Side view of the collimating system and its electron collimation.*

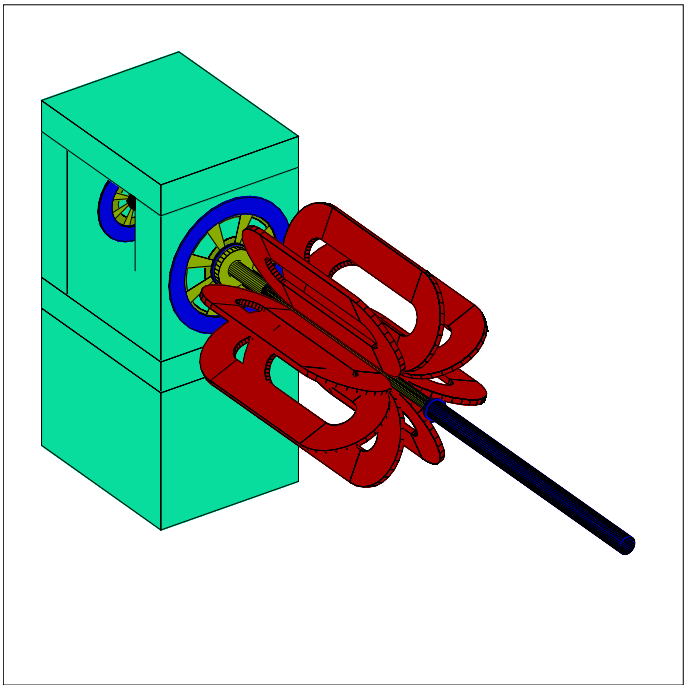

Figure 82: *3-D perspective of the collimating system in relation to the Q_{weak} Spectrometer coils.*

13.1 Components of the Q_{weak} Experiment's Collimating System

The major components of the collimating system perform all the functions required and described in the previous section. They can be separated into five major parts:

- The preshielding cylinder, shown in Figure 83, is positioned immediately after the target. Its center is 50 cm downstream from the target center. Its role is to be an interface between the collimating system and the target chamber, to provide close to the target shielding and to provide the exit windows for the scattered electrons from the target chamber vacuum.
- The precollimator, shown in Figure 84, is positioned 107 cm downstream of the target center. It consists of 25 inches thick concrete wall and a lead cylinder with conical windows positioned in that wall. The lead is supported by 1 inch thick aluminum tubes.
- The primary or kinematics defining collimator, shown in Figure 85, is positioned 338 cm downstream of the target center. It has the same structure as the precollimator, but with the dimensions appropriate for its distance from the target.
- The beam shielding, shown in Figure 86, consists of several lead elements around the aluminum beam pipe.
- There are also a concrete collimator support and the concrete roof, shown in Figure 82. Concrete side walls are not shown.

While the precise dimensions of the collimating system are known and are part of the input file for the simulation program, to avoid any confusion in further references, they will not be officially published in this report, but only in the engineering design report. This report will use the preliminary dimensions and concentrate on the collimating properties of the collimating system. The only relevant information at this point is that the azimuthal angle acceptance is reduced from $\phi_e = \pm 15.0$ deg to $\phi_e = \pm 14.5$ deg in order to avoid the magnetic field close to the coils as well as allow some more space for the coil support structures.

13.2 Collimating Properties

The collimating system for the Q^p_{Weak} experiment should, in an ideal case, allow the scattered electrons in the acceptance region of $\theta_e = 9.0 \pm 2.0$ deg for the polar angle and $\phi_e = \pm 14.5$ deg for the azimuthal angle to pass through, and, in the same time, block all other reaction products. Some help in this process the collimating system will get from Q^p_{Weak} spectrometer whose magnetic field optical property is such that it focuses the elastically scattered electrons in defined acceptance range, and disperses all the other charged particles.

In a real case, secondary particles, product of the reaction of elastically scattered electrons and parts of the collimating system, do reach the detector system by having initial conditions such that the field bends them into the detector or by being neutral and therefor inert to the

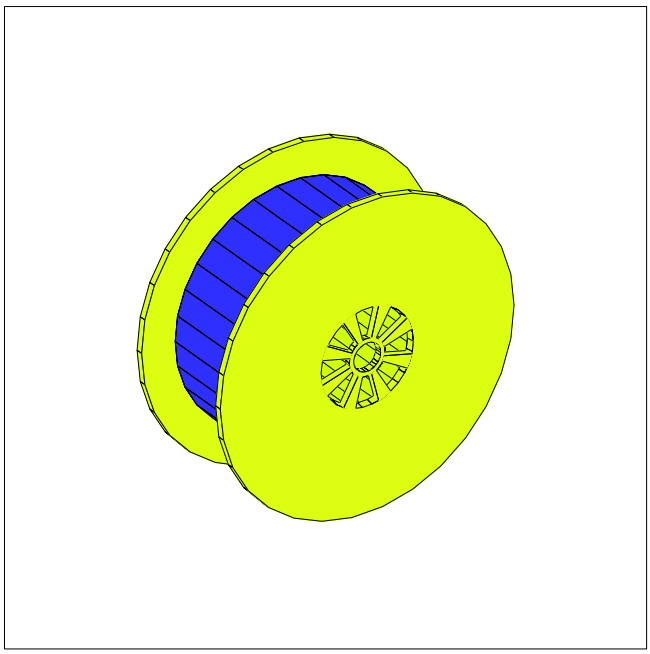

Figure 83: *The preshielding cylinder consist of two aluminum plates, one with the exit windows, aluminum tubes, and 8 inch thick lead cylinder. In addition to shielding it provides an exit for the scattered electrons from the target chamber vacuum.*

magnetic field. It is impossible to completely eliminate the effects of secondary particles, but it is possible to minimize their contribution to the final counting rate below the threshold of relevance.

Next several figures will help understand the properties of secondary particles. To generate those figures the kinematics of the experiment in the simulation program was defined by the collimators and all the secondary reactions were turned on. The secondary reactions consisted mostly of bremsstrahlung shower from the fraction of the electrons hitting the collimator walls. As shown in Figure 82, this shower is well separated from the electrons at the position of the focal plane as a result of the electrons bending and the photons continuing in a straight path.

There are several questions one could try to answer about the collimating system using the result of the simulation:

- Where are the secondary particles generated regardless of their direction of scattering? The answer to this question is shown in Figure 87 where the reaction points of the secondary particles are drawn as a function of the position along the beam line and radial distance from the beam line.
- Where are the secondary particles which hit the Čerenkov detector generated? The answer to this question is shown in Figure 88. The reaction points of the secondary particles which

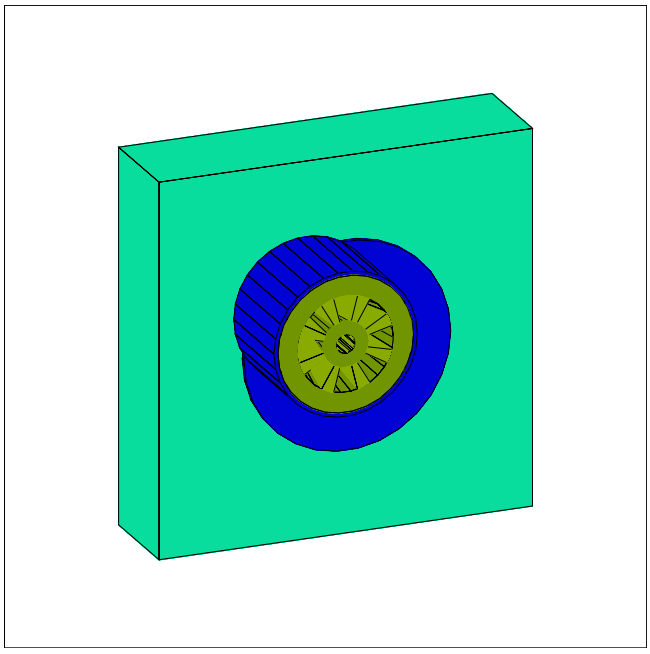

Figure 84: *The precollimator consists of 25 inches thick concrete wall and the lead cylinder with a conical windows positioned in that wall. The shape of the windows are calculated from the experimental requirements on the polar and azimuthal angles.*

hit the detector are drawn as a function of the position along the beam line and radial distance from the beam line.

- Which kind of secondary particles generated by the collimating system hits the Čerenkov detector? Overall distribution of the types of secondary particle is shown in Figure 89. One can see that only few per-mills are charged. While an extensive study of the Q_{weak} background will be performed in the near future, short simulations done for this report showed no secondary charged particles and only 1 photon hit the Čerenkov detector over 150 primary electrons.

- What is the energy distribution of the photons hitting Čerenkov counter? As shown in Figure 90, short simulation runs show only low energetic photons hitting the Čerenkov counter.

Realistic simulation can be performed only when the kinematics of the experiment is defined by the collimators and all the secondary reactions turned on. Since the Čerenkov detector acceptance for the secondary particles is very low, the simulation will require very high statistics. It will be performed for all the reactions in a near future. Short simulation runs on the properties of the collimators show that the secondary reactions consist mostly of bremsstrahlung shower from the fraction of the electrons hitting the collimator walls. This shower is well separated from the electrons at the position of the focal plane as a result of electrons bending and photons

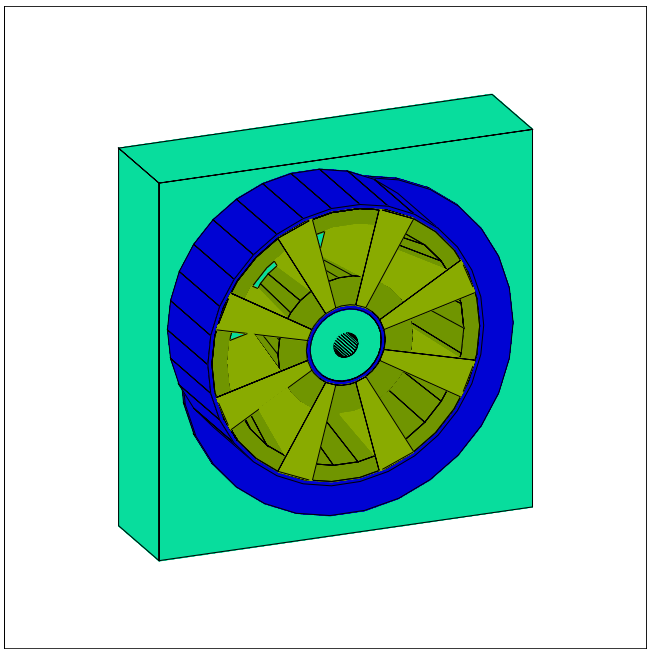

Figure 85: *The primary or kinematics defining collimator consists of 25 inches thick concrete wall and the lead cylinder with a conical windows positioned in that wall. The shape of the windows are calculated from the experimental requirements on the polar and azimuthal angles.*

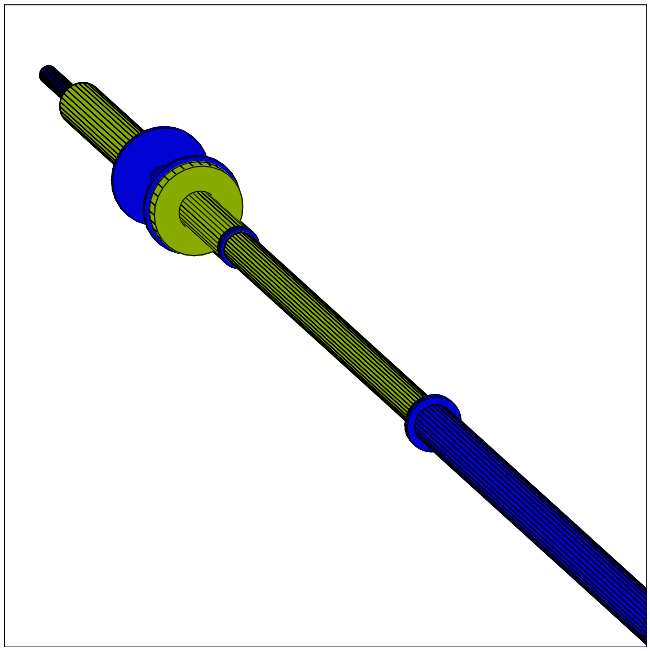

Figure 86: *The beam shielding consists of several lead elements around the aluminum beam pipes.*

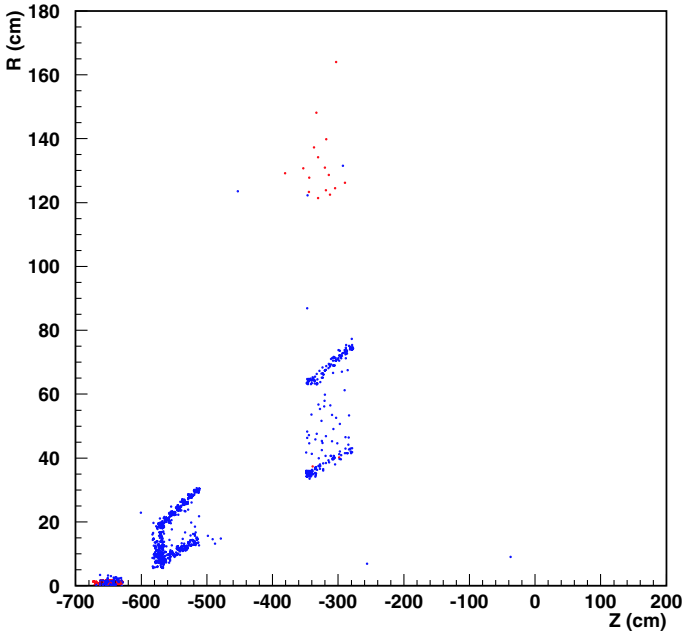

Figure 87: *Side view of the collimating system generated by the vertexes of the positions where the secondary particles are produced. Vertexes of photons are blue and electrons and positrons are red. It is clear that the sources of the secondary particles are in the target and the collimator walls.*

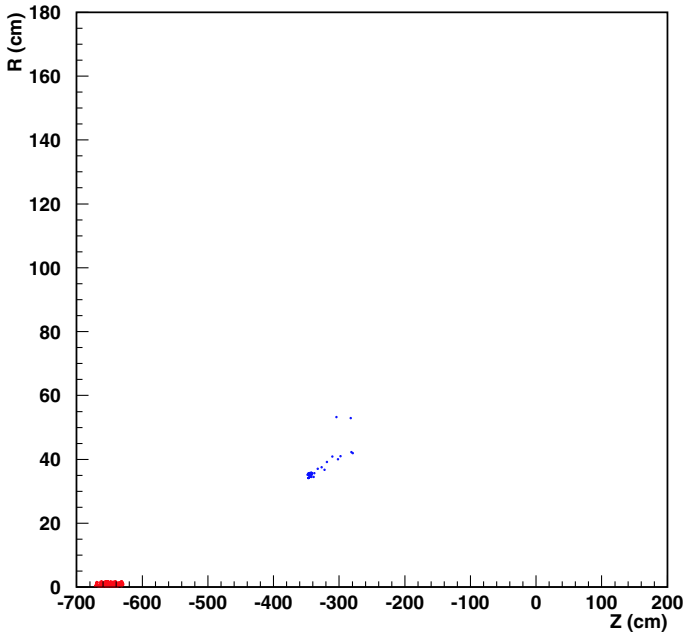

Figure 88: *Side view of the collimating system generated by the vertexes of the positions where the primary and secondary particles that hit the Čerenkov detector are produced. Vertexes of photons are blue and electrons and positrons are red. The sources of the secondary particles are at the collimator walls and consists almost entirely of photons.*

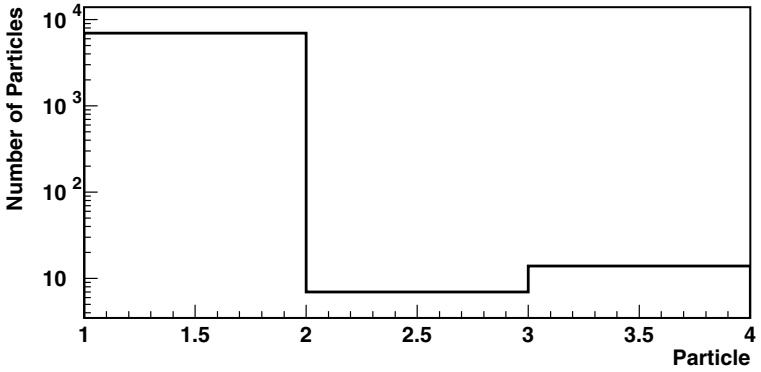

Figure 89: *Distribution of the types of secondary particle produced by the elasticly scattered electrons. 1-2 are photons, 2-3 positrons, and 3-4 electrons.*

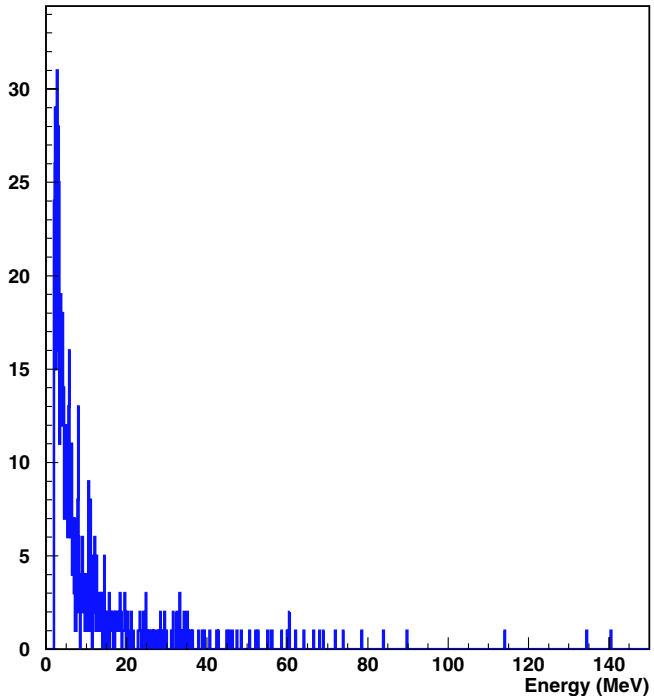

Figure 90: *Energy distribution of the secondary photons from the collimator hitting the detector.*

continuing in a straight path, shown in Figure 81. Figure 91 shows a narrow band of elastically scattered electrons above the broad electromagnetic shower distribution. The projection of the collimator shape is a result of most of the showering happing on the collimator walls.

But, there is an effect which has to be studied in more details; the effect of the air. Some results of very preliminary studies on the effect of the air are described in the next section.

13.3 The Background Produced by the Air

The study of the background produced by the air is very preliminary in this report. It assumes that the entire path of each scattered electron goes through the air. However, it is highly likely that we will take the more conservative approach and fill magnetic region with Helium. Also, this study does does not discriminate by the signal produced in the Čerenkov detector which will greatly suppress any low energy or non-relativistic residual backgrounds. The purpose of this study is to look at the position of sources of background in the air and the physical properties of the background, and compare it to the collimator as a source of the background. The number of secondary particles generated in the air outnumbers the secondary particles generated in the collimator by factor 16 to 1. Distribution of the vertexes of the positions where the secondary particles are produced is shown in Figure 92. Figure 93 is one dimensional projection of the Figure 92 along the beam axis and represents the number of secondary particles produced as a function of the position downstream of the target. Normalized to the number of primary

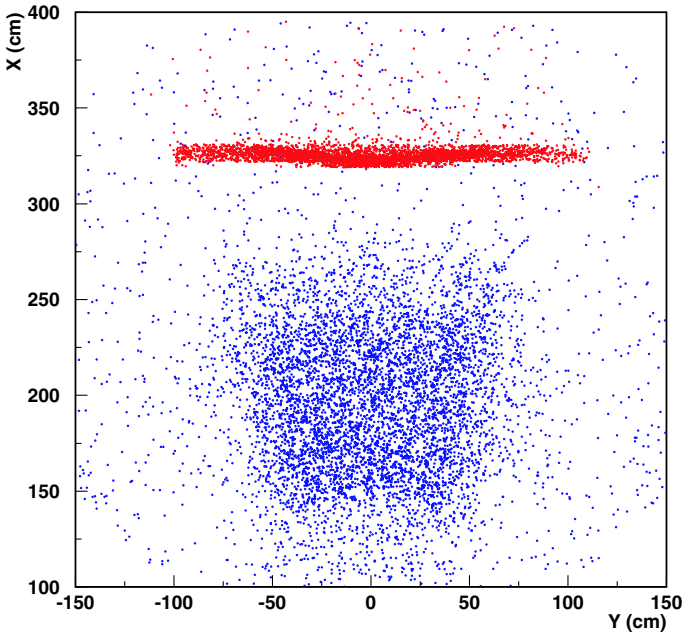

Figure 91: *Separation of elastically scattered electrons (narrow red band) and electromagnetic shower (blue dots) depicting the collimator walls at the vertical plane positioned 580 cm downstream from the magnet mid point.*

particles, the secondaries with the energy above 1.5 MeV make 12% of total number of hits. This does not mean that our background is 12% because one has to convolute the Čerenkov detector signal into the process of estimating the background.

As in the case of the background produced by the collimators, secondary particles produced in the air by the primary electrons consist mostly of low energetic photons, as shown in Figure 94.

13.4 Conclusion

This report contains a description of the Q^p_{Weak} collimator design. It contains only the essential collimator properties and the impact on the experimental kinematics, setup, and procedures. The design is based on kinematical constraints which optimize the figure of merit of the Q^p_{weak} Experiment, the incident beam energy of $E_0 = 1.165\ GeV$, electron polar angle $\theta_e = 9.0 \pm 2.0$ deg, and azimuthal angle $\phi_e = \pm 14.5$ deg for each sector. While the collimator described in this report satisfies the Q_{weak} experimental requirements, no final dimensions of the collimator are reported here. We expect that there will be some modification of the collimator design as a result of detailed simulation of the experimental background in the near future and the engineering requirements.

While not completed, we have shown in this report that the background produced by the collimator is much smaller than the background produced by the primary electrons in the air

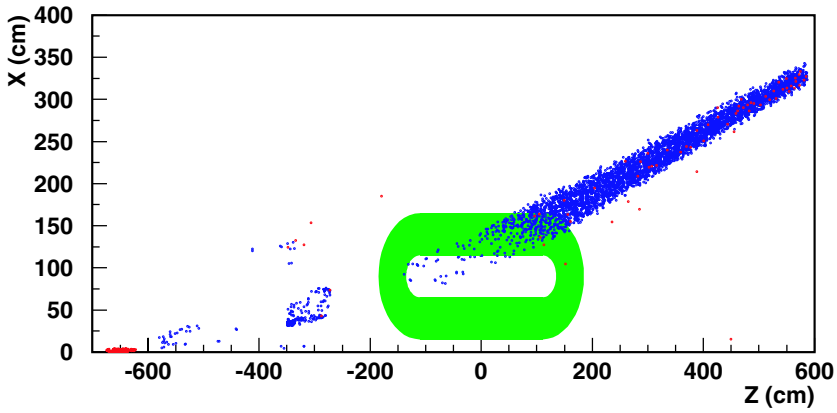

Figure 92: *Side view of the magnet coil and the vertexes of the positions where the primary and secondary particles that hit the Čerenkov detector are produced. Vertexes of photons are blue and electrons and positrons are red. The major sources of the secondary particles is the electron bremsstrahlung in the air after the bending in the magnet and consists almost entirely of photons.*

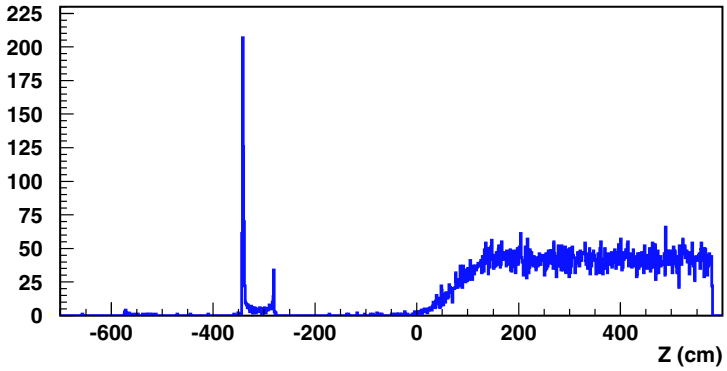

Figure 93: *Number of secondary particles hitting the Čerenkov detector as a function of the position downstream the target.*

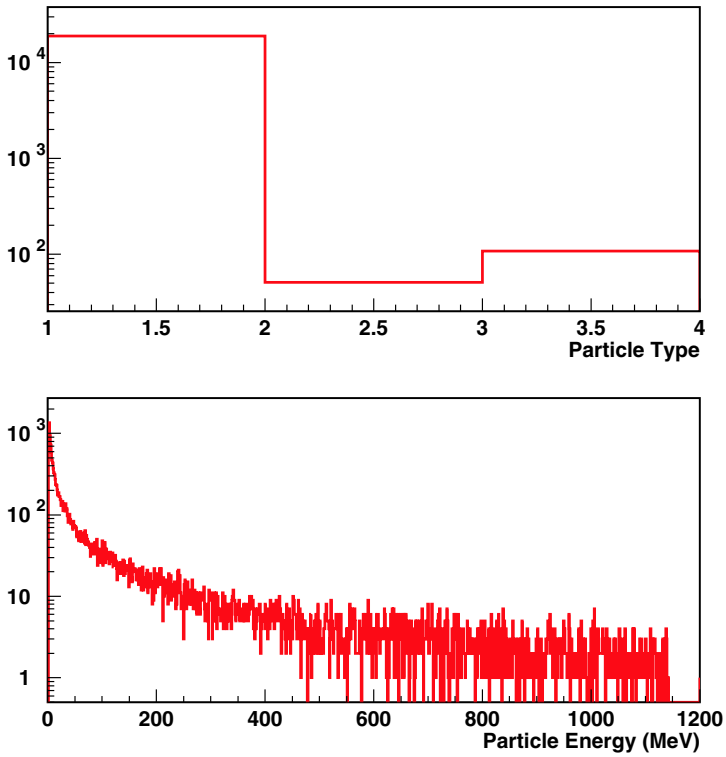

Figure 94: *Distribution of the types of secondary particle produced by the elastically scattered electrons in the collimator and air (top). 1-2 are photons, 2-3 positrons, and 3-4 electrons. Energy distribution of those particles (bottom).*

through the process of bremsstrahlung. This effect will be studied in more details as a part of an overall experimental simulation program. It is mentioned in this report as a motivation for possible planing to fill regions of the primary electron paths within the magnet region with helium.

References

[1] Jlab Proposal E02-020, "The Q_{weak} Experiment: "A Search for Physics at the TeV Scale Via a Measurement of the Proton's Weak Charge", D. Armstrong et al., 2002

[2] N. Simicevic, LaTech Technical Report LATECH-CAPS-01-03a, G0-01-007, 2001. (at http://www.npl.uiuc.edu/exp/G0/docs/docs.html)

[3] N. Simicevic, LaTech Technical Report LATECH-CAPS-02-06a, 2002. (at http://www.jlab.org/qweak)

[4] G0 Technical Design Report, Nuclear Physics Laboratory, University of Illinois at Urbana-Champaign, 1993.

[5] Letter of Intent to TJNAF, R. Carlini, J. M. Finn and M. J. Ramsey-Musolf, spokespersons.

[6] N. Simicevic, LaTech Technical Report LATECH-CAPS-00-06a, G0-00-026, 2000. (at http://www.npl.uiuc.edu/exp/G0/docs/docs.html)

[7] N. Simicevic, LaTech Technical Report LATECH-CAPS-00-06b, G0-00-028, 2000. (at http://www.npl.uiuc.edu/exp/G0/docs/docs.html)

[8] N. Simicevic, LaTech Technical Report LATECH-CAPS-02-08a, 2002. (at http://www.jlab.org/qweak)

[9] TJNAF Experiment E91-017, D. Beck, spokesperson.

[10] TJNAF Experiment E97-104, S. P. Wells, N. Simicevic and K. Johnston, spokespersons.

[11] GEANT Detector Description and Simulation Tool, *CERN Program Library Long Writeup W5013*, CERN, Geneva, 1993

14 APPENDIX C: Čerenkov Detector Design Study

While the design of the large acceptance spectrometer started with a possible modification of the existing superconducting G0 magnet the optimized solution for the Q^p_{Weak} experiment is a new resistive toroidal magnet, the coil shapes and arrangement of which are shown in Figure **??**. The advantage of this magnet is low cost and better reliability relative to a superconducting solution. A new resistive magnet would also allow execution of the Q^p_{Weak} experiment in a timely and independent manner.

The detector system for the Q^p_{Weak} experiment must be able to handle counting rate of the order of 1 GHz per detector and must maintain its properties through the entire run time. It also has to be simple to reduce the systematic errors associated with the complex detector electronics. This leads to a choice of integration mode of data acquisition, and the detection of the elastically scattered electrons using only one Čerenkov bar per magnet octant.

The position and shape of such a Čerenkov bar is defined by the physical simulation using the optical properties of the Q^p_{Weak} magnet, as shown in Figure 95. Some preliminary studies of the detector [6] found that rough experimental requirements are a length of 200 cm and width of 12 cm to cover the entire elastically scattered electron region at the focal plane. The elastically scattered electron envelope at the focal plane shown in Figure 96 is such that the inelastic channel is clearly separated from the elastic region. Because the properties of the magnetic field also depend on the scattered electrons' azimuthal angles, the minimal area of the detector is slightly shifted from the focal plain at the point which minimizes the difference between the midpoint and the endpoint electron distributions. The optimal position for the detectors was found to be 580 cm downstream of the center of the magnet.

14.1 Criteria for Čerenkov Counter Design

The factors that drive the design of the Čerenkov detectors have been slightly modified since the original design [6]. They can be summarized as follows:

- the radiation hardness requires the material for the detector to be quartz (fused silica),
- the area of the detectors should cover the entire "focal" plane of the elastically scattered electrons uncorrected for the radiation losses,
- the number of photoelectrons should be independent of the position on the detector as defined by the position dependent "false" asymmetry limits,
- the photocathode diameter should cover the entire edge of the Čerenkov bar with a high quantum efficiency photo cathode, and
- a minimum of about 50 photoelectrons per phototube with a small variance in the number of photoelectrons should be required.

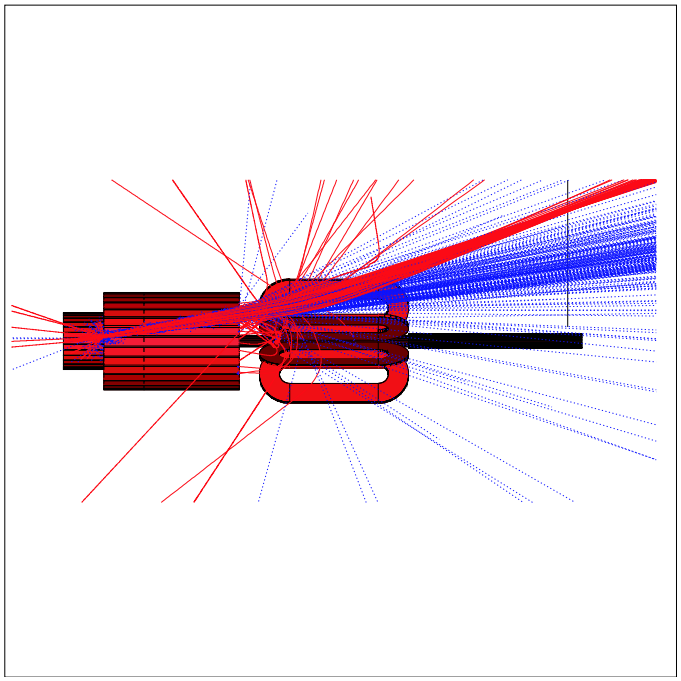

Figure 95: *The side view of the modeled setup with a sample of elastic trajectories restricted by the collimator to* $\theta_e = 9.0 \pm 2.0$ *deg and* $\phi_e = 0.0 \pm 14.0$ *deg. Also shown is the background caused by the reaction.*

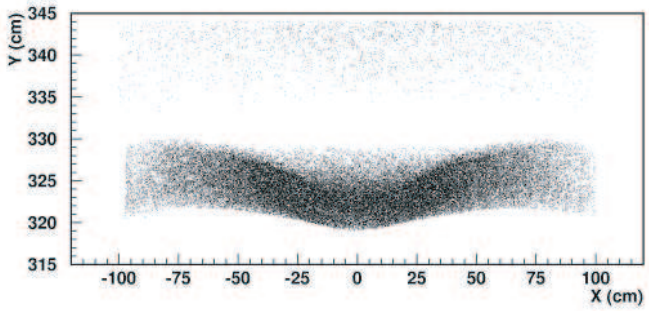

Figure 96: *Separation of elastically (lower distribution) and inelastically (upper distribution) scattered electrons on detector position. The kinematics is restricted to* $\theta_e = 9.0 \pm 2.0$ *deg and* $\phi_e = 0.0 \pm 14.0$ *deg. Only optical properties of the magnetic field are taken into account when creating this separation. No secondary electron reactions were allowed.*

The tight requirement of fitting the dimensions of the Čerenkov bar into the 5 inch diemeter phototube such that no special interface is needed is in conflict with the bar thickness defined by the requirement of the number of photoelectrons and will be studied in more detail throughout this report. It will be optimized considering the optical properties of quartz, the level of quality of surface polishing, and the detector orientation. A simple idea of the look of the Čerenkov quartz bar and the attached phototubes can be gathered from the sketch in Figure 97. The propagation of photons inside the bar is depicted with reduced reflectivity to create a clearer physical picture.

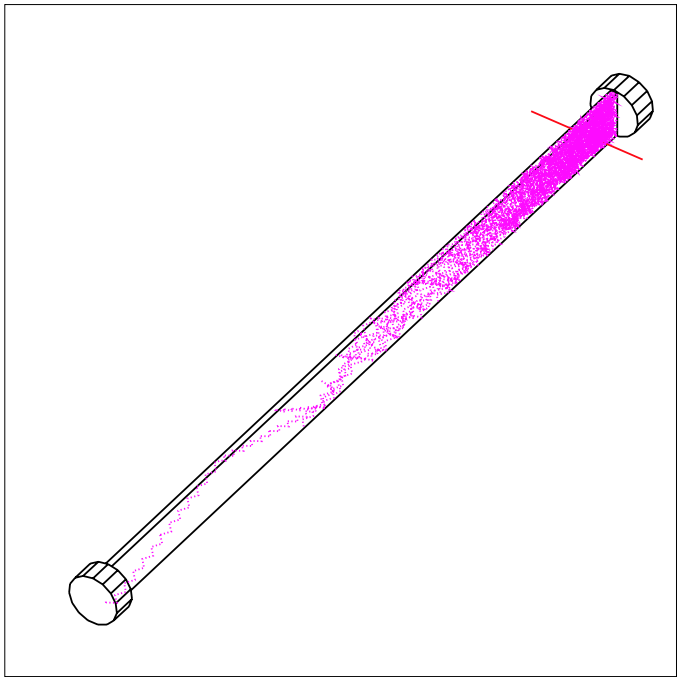

Figure 97: *The sketch of the Q^p_{Weak} 200 cm by 12 cm by 1.72 cm Čerenkov bar with two 5 inch phototubes attached on the sides. The reflectivity was reduced to show the propagation of photons generated by one electron.*

To satisfy the requirement of high quantum efficiency, the choice of photo cathode is the multialkali S20 cathode, whose response extends into the ultraviolet and red parts of the visible light spectrum. There is a slight variation of the quantum efficiency of this photocathode reported in the literature. A typical response, which will be used to estimate the number of photoelectrons in the design of the Q^p_{Weak} Čerenkov bar, is shown in Figure 98 [7].

The requirement of 50 or more photoelectrons per phototube and a small variance in the number of photoelectrons imposes a constraint on the coefficient of photon reflectivity of the quartz bar. The number of photoelectrons increases with the increase of reflectivity, but so does the cost of manufacturing the bar. An example of a Čerenkov detector bar comparable in size, shape and optical properties to the Q^p_{Weak} requirement is a fused silica bar used in the BaBar experiment [9]. The average index of reflectivity inside this bar can be as good as 0.9996 $\pm$

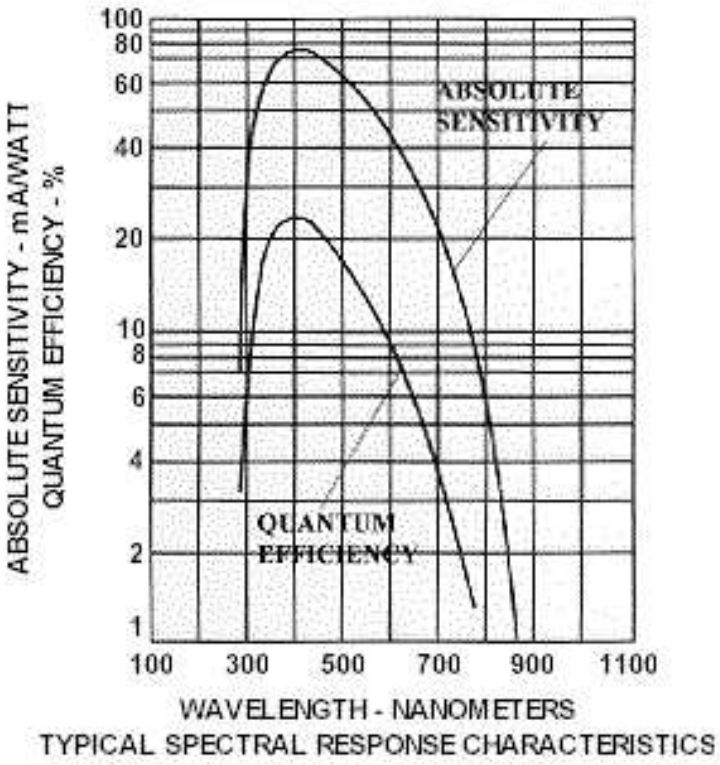

Figure 98: *Typical spectral response for the S20 photocathode.*

0.0001 [8].

The measurement of reflectivity shown on Figure 99 for DIRC (Detector of Internally Reflected Čerenkov light) bar implies 5-8 Å rms surface finish [10]. Such a finish requires state of the art in polishing technology and significantly increases the cost. For the design of the Q^p_{Weak} bar, the index of reflectivity is not as critical. In the first part of the Čerenkov detector study [6] the reflectivity requirement was reduced by a factor of 10 compared to the DIRC bar reflectivity to an average modest value of 0.997. In this report we will assume a "standard optical polish" of 25 Å rms and use an empirical formula to calculate reflectivity as a function of the wavelength, needed in the Q^p_{Weak} bar optical simulation:

$$R = 1. - 0.027\ e^{-0.004608\ \lambda}, \tag{9}$$

where R is coefficient of reflectivity and λ is the Čerenkov light wave length in nanometers.

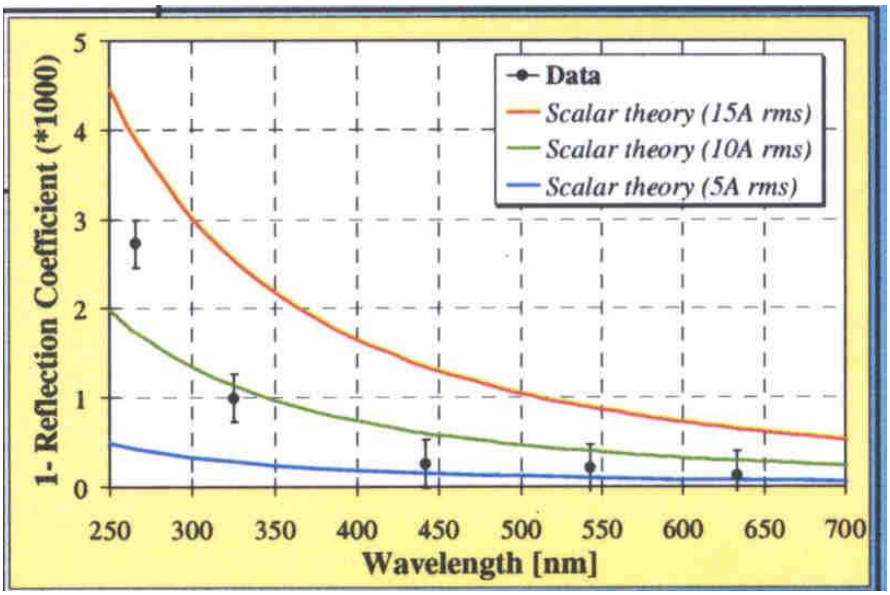

Figure 99: *A comparison of the internal reflection coefficient measured for the DIRC bar with the scalar scattering theory [10].*

The requirements for the Čerenkov counter design in this report go into more detail than the requirements in the first detector design report [6]. Consequently, not all the simulations from the first report will be repeated in this one.

In the previous study [6] we assumed the thickness of the bar to be 1.72 cm (the same as BaBar bar) and we required statistics of more then 100 photoelectrons per phototube. Assuming normal incidence of the elastically scattered electrons on the bar surface, it was shown that a sufficient number (100) of photoelectrons could not be produced. Therefore, the Čerenkov detector was modeled as a quartz and lead sandwich. The electrons proceeding through the lead created a shower of secondary electrons, positrons, and photons, and as a result the number of Čerenkov photons produced in quartz increased. A sandwich started with the lead converter to develop the shower, followed by one ore more layers of glass and lead, and always ending with lead. While the sandwiched Čerenkov counter satisfied the experimental requirement for the number of photoelectrons, it also increased the variance of the photoelectron distribution which was statistically dominated by the ionization process. The results from those studies are summarized in Figure 100 where the distribution of the number of photoelectrons on both sides, 20 cm and 180 cm from the incident electron trajectory are plotted.

While the previous report ended with a working solution for the Čerenkov counter the rest of this report will describe the improvement in the counter design, based on improved simulation codes and a better definition of experimental subsystems.

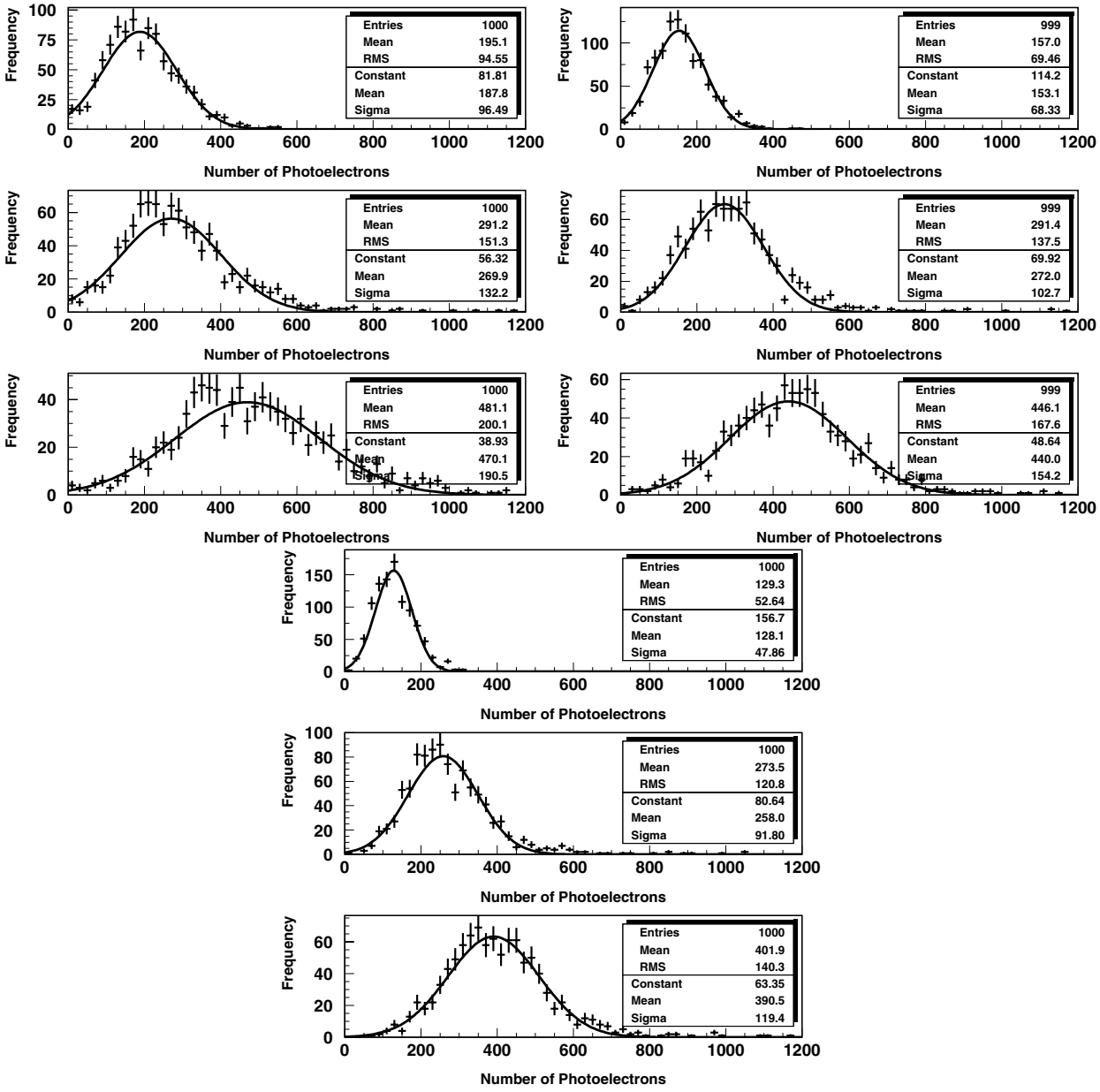

Figure 100: *The number of photoelectrons and its variance for one layered (top left), two layered (top right), and three layered (bottom) Čerenkov counters. Top distributions for each counter are for the phototube 180 cm from the electron trajectory, center for the phototube 20 cm from the electron trajectory, and the sums of both phototubes are the bottom distributions.*

14.2 Kinematical Considerations for the Čerenkov Counter Design

Simulations necessary for the Čerenkov counter design were performed in two steps. The first step produced the kinematical quantities at the position of the Čerenkov bar, and the second step exploited those quantities to study the optical properties of the bar.

The inputs into the first step were $Q^2 = .03$ GeV^2, an incident beam energy $E_0 = 1.165$ GeV, electron polar angle $\theta_e = 9.0 \pm 2.0$ deg, and azimuthal angle $\phi_e = 0.0 \pm 14.0$ deg. Using the GEANT simulation package [12] with this kinematical input, a proper magnetic field map, and selecting 35 cm for a liquid hydrogen target length, we found the optimal position of the center of the target at 650 cm upstream from the center of the magnet, and optimal position for the detector 580 cm downstream.

If sufficient number of scattered electrons' trajectories were restricted to initial polar and azimuthal angles generated at the detector position, their envelope provides not only the shape of the detector, as shown in Figure 96, but also all the kinematical quantities needed for a realistic simulation of the optical properties of the Čerenkov bar. The most important of those quantities are plotted in Figure 101 and Figure 102. They should be used as input to the simulation of the Čerenkov counter optical properties because, as one can see in Figure 103, the angle of impact on the detector depends on the position at the detector. The importance of using realistic kinematical quantities can be seen in Figure 104, which shows a nontrivial relation between the polar and azimuthal angles at the position of the detector.

The kinematical quantities produced in the first step of the simulations, defined in the coordinate system fixed to the magnet, were later transformed in the system fixed to the detector. The impact of the detector orientation on the detector optical properties could then be taken into account. Those studies are described in the next section.

14.3 Optics Simulation

The input to the simulations of the Čerenkov counter optical properties are the kinematical quantities described in the previous section, the quantum efficiency of the phototube (an example of which is shown in Figure 98, and the reflectivity of the quartz bar calculated as a function of the wavelength using Equation 1. Two more parameters needed for the simulation, the index of refraction and quartz light absorption coefficients, are presented in Table 14.3. as a function of the wavelength.

Wavelength $[nm]$	210	225	250	300	400	500	600	800
Absorption coeff. $[m^{-1}]$	100	8	1.35	0.062	0.0076	0.005	0.0044	
Index of refraction				1.487	1.470	1.464		1.454

Table 20: *Index of refraction and absorption coefficients [11] for the quartz Čerenkov bar.*

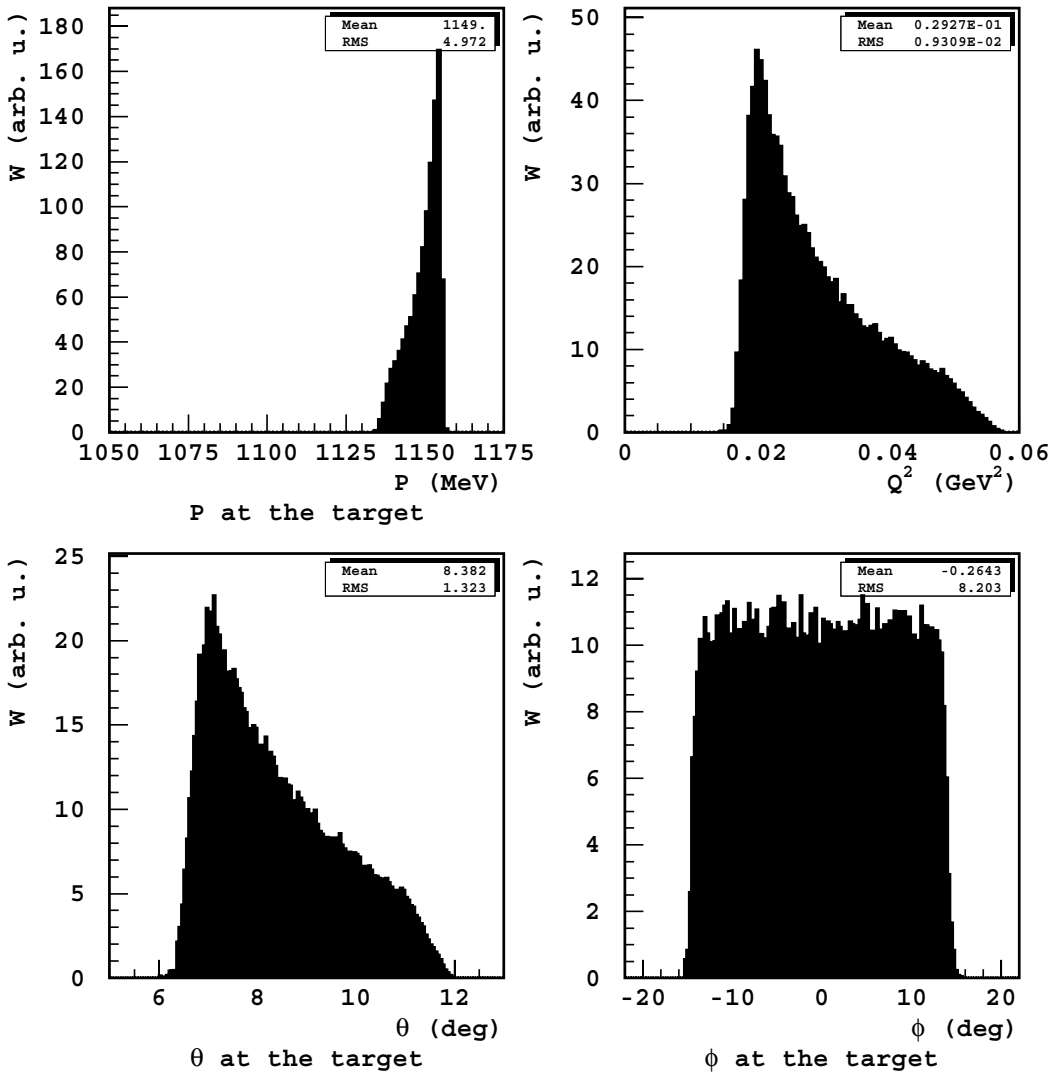

Figure 101: *The kinematical quantities needed for the Čerenkov detector simulation generated at the target. They include cross section weighted distributions of the momenta of the outgoing electrons, and their polar and azimuthal angles. The plot of Q^2 is for reference only.*

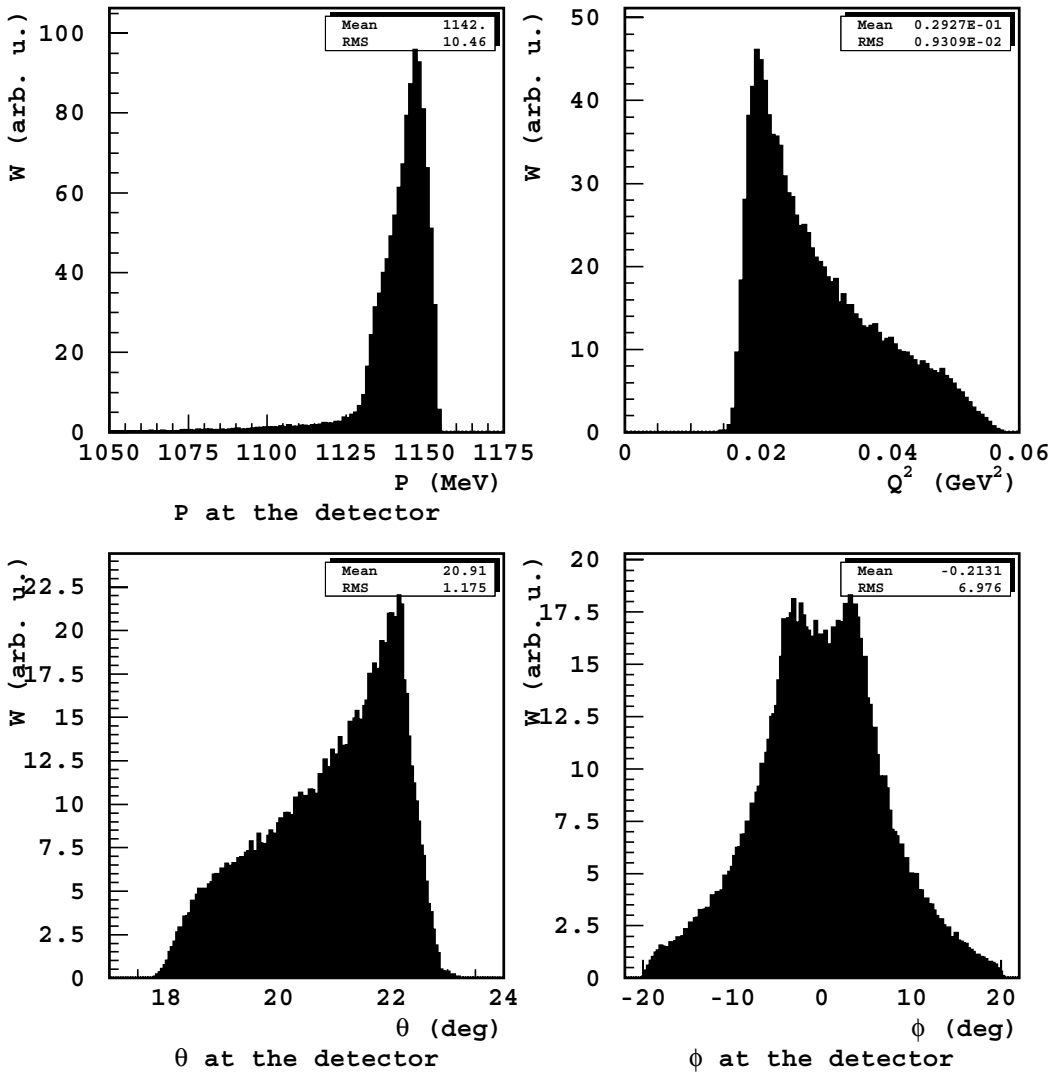

Figure 102: *The kinematical quantities needed for the Čerenkov detector simulation impacting the detector. They include cross section weighted distributions of the momenta of the incoming electrons, and their polar and azimuthal angles. The plot of Q^2 is for reference only.*

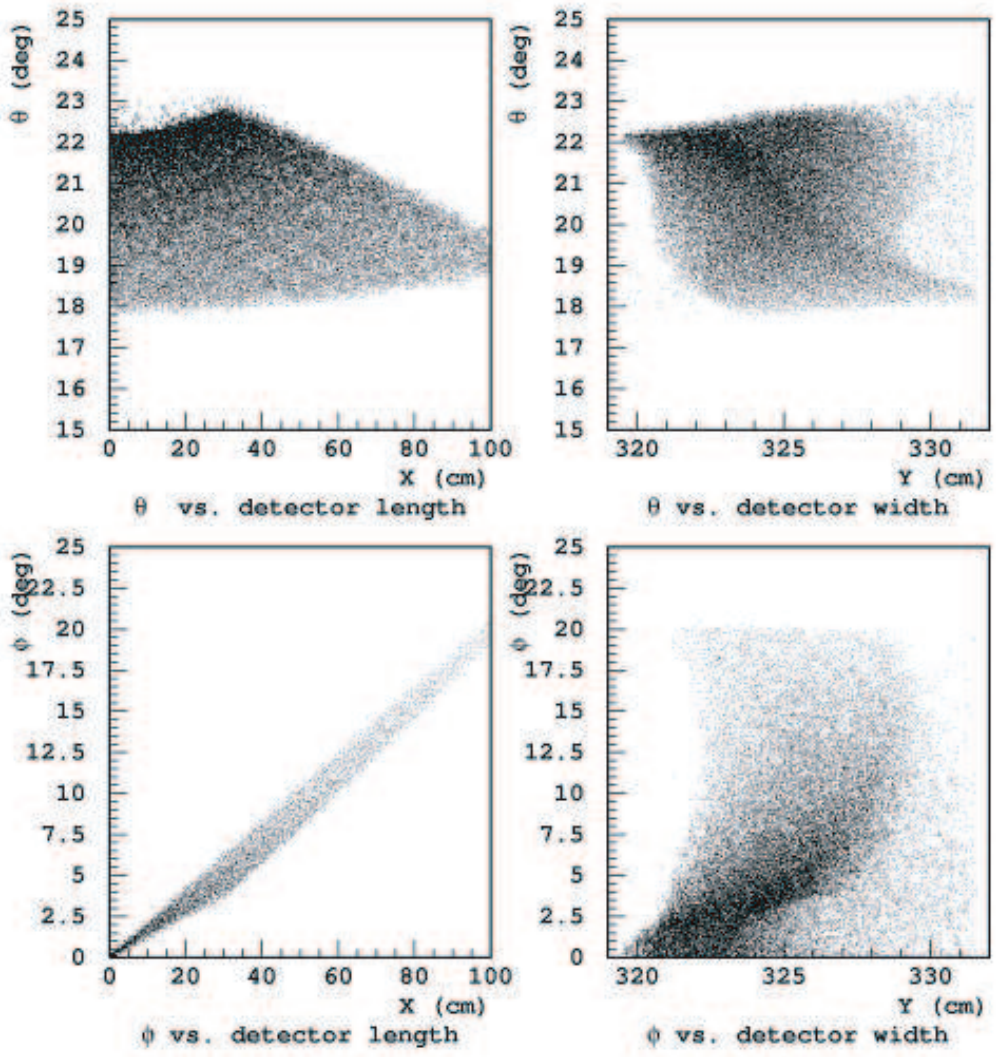

Figure 103: *The distribution of the polar and azimuthal electron angles along the length and the width of the Čerenkov counter. The distributions are weighted by the cross section.*

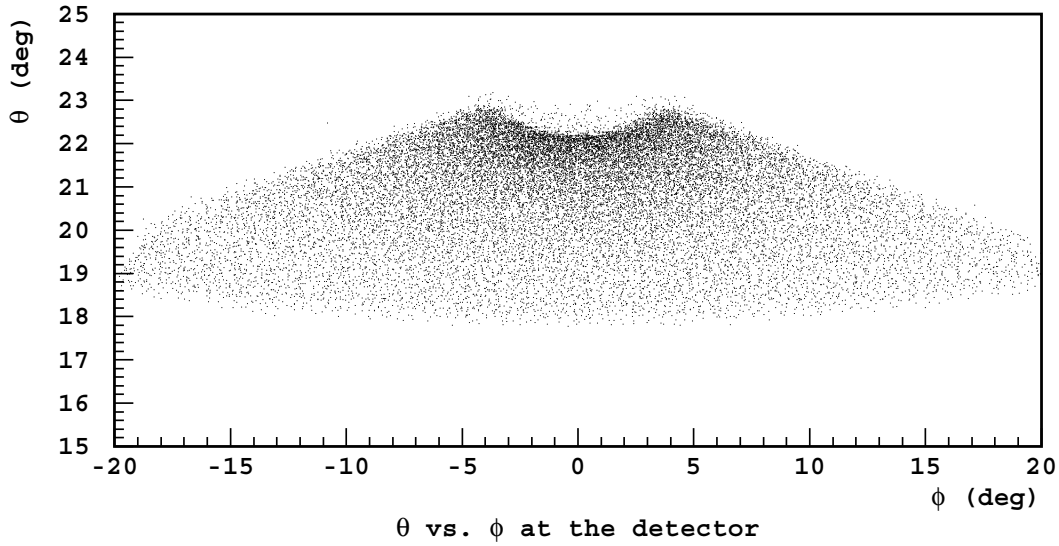

Figure 104: *The relation between the polar and azimuthal electron angles at the detector position. Distribution is weighted by the cross section.*

The following results were produced by slightly modified GEANT [12] Čerenkov photons tracking routines. The major difference between this version and the original GEANT program is that the reflectivity was incorporated into the photon tracking. The width of the Čerenkov bar was kept at 12 cm, the same as in the previous report [6], but the length was extended from 200 cm into 220 cm to reduce the number of photoelectrons produced by the electron impacting close to the phototube. The thickness of the bar and the rotation angle were the two parameters optimized in the following sets of simulations.

The first set of simulations studied the effect of the Čerenkov bar orientation. For this set of studies the thickness of the bar was fixed to 3.81 cm (1.5") and the bar was rotated relative to the axis fixed to the magnet from -10° to 15°. The results consisted of calculating the number of photoelectrons on each side, the total number of photoelectrons, and the position dependence of the number of photoelectrons along the length and the width of the Čerenkov bar, and are also shown. The distributions are all weighted by the cross section.

It is important to have a quantitative assessment of the importance of the number of photoelectrons, the variances, and the position dependence of the number of photoelectrons on the measured asymmetry, and define the criteria for optimization of the Čerenkov bar orientation. The asymmetry is calculated as a difference of the integrated detector signals for two helicity "pulse pairs" as

$$A = \frac{Y_+ - Y_-}{Y_+ + Y_-} \tag{10}$$

where Y is the total integrated detector signal normalized to incident beam charge for +(-) helicity. The statistical error in the determination of the asymmetry for each pulse pair arising

from counting statistics can be determined from

$$\Delta A_{count} = \frac{1}{\sqrt{2}} \frac{1}{\sqrt{N_{e-}}} \sqrt{1 + \left(\frac{\sigma_{N_{pe}}}{N_{pe}}\right)^2}, \tag{11}$$

where N_{e-} is the total number of scattered electrons detected per integration period, N_{pe} is the average number of photoelectrons generated in the Čerenkov detector per scattered electron, and $\sigma_{N_{pe}}$ is the standard deviation of the distribution of photoelectrons per event. Imposing a requirement for the statistical dilution to be

$$\sqrt{1 + \left(\frac{\sigma_{N_{pe}}}{N_{pe}}\right)^2} \leq 1.05 \tag{12}$$

implies

$$\left(\frac{\sigma_{N_{pe}}}{N_{pe}}\right) \leq 0.32 \tag{13}$$

This criterion, applied on each side, eliminates several possible orientations for the Čerenkov bar. For the 3.81 cm thick bar it eliminates the -10°, -5°, 0°, and 35° orientations, and for the 1.905 cm thick bar it eliminates the -10° orientations. For the remaining possibilities, the factor to be minimized is the variation in photon collection efficiency for events in different parts of the Čerenkov detector. Eliminating all the orientations with sharp changes along the X or Y axes restricts the rotational angles to the region between 15° and 25°.

Imposing that the overall helicity-correlated beam position is such that the correction to the asymmetry from that beam parameter is the same as the expected Q^p_{Weak} statistical error requires, using the run-averaged beam position at the target of $\sim .6\mu m$, and assuming a total of 100 photoelectrons per electron in the Čerenkov bar, the formula

$$\Delta A_{false} = \frac{1}{N_{pe}} \frac{\partial N_{pe}}{\partial x} \Delta x_{beam} \tag{14}$$

gives the limit for the position dependence of the number of photoelectrons

$$\frac{\partial N_{pe}}{\partial x} \leq 0.01 \;\; N_{pe}/cm. \tag{15}$$

The results show that this requirement is satisfied for the 1 inch thick Čerenkov bar rotated by 12.5° relative to the beam axis. The edge effects for the 3.81 cm thick bar are harder to eliminate. Even for the 12.5° rotation, the sharp changes in the numbers of photoelectrons close to the detector edge could not be eliminated relying only on internal reflection.

The entire study of the optical properties of the two Čerenkov bars and their orientations was based on the assumption of total internal reflection for the bar with regularly polished sides. While Figure **??** shows that the number of photoelectrons for the 1 inch thick bar is higher then

the minimum requirement of 20 photoelectrons, and $\sigma_{N_{pe}}/N_{pe} \simeq 0.2$, the study of the optical properties of the Čerenkov bar will be completed by exploring the effect of higher polishing requirements. Simulations were performed with the "standard optical polish" roughness of 25 Å rms decreased to 15 Å rms. No significant improvement in the total number of photoelectrons or in their position dependence were obtained. The total number of photoelectrons increased by $\simeq 17\%$ with the variance staying the same. The reflectivity for the surface roughness of 15 Å rms is close enough to the measured reflectivity of the DIRK Čerenkov bar that no stricter requirement could be imposed on the Q^p_{Weak} bar for the purpose of the optical properties simulation without a danger of producing nonrealistic results.

Using again the "standard optical polish" roughness of 25 Å rms we studied the effect of increase in thickness on the number of photoelectrons and their position dependence. The results for a 1 inch thick Čerenkov bar are show in Figure 113 and Figure 114. The total number of photoelectrons increased by more then 40% from 62 to 90, and $\sigma_{N_{pe}}/N_{pe}$ increased by 10% from 0.20 to 0.22. There was no significant change in the position dependence except for a little enhancement of the edge effect.

In estimating the number of photoelectrons, a typical spectral response for the S20 photocatode, as shown in Figure 98, was used. The effect of photocatode quantum efficiency on the number of photoelectrons can be estimated by selecting a different S20 photocatode. As an example, seen on Figure 115, the quantum efficiency of the Thorn 2.05 in S20(9658) photocatode is higher then the typical one used in the previous simulations. As expected, comparing Figure 113 and Figure 116 we find that using those quantum efficiency numbers, the number of photoelectrons increased by $\simeq 20\%$ with the variance staying the same.

The final simulation, the results of which are shown in Figure 118 and Figure 119, was performed after further reducing the thickness of the Čerenkov counter bar to 2 cm. The number of photoelectrons decreased by $\simeq 25\%$ with slightly decreasing variance.

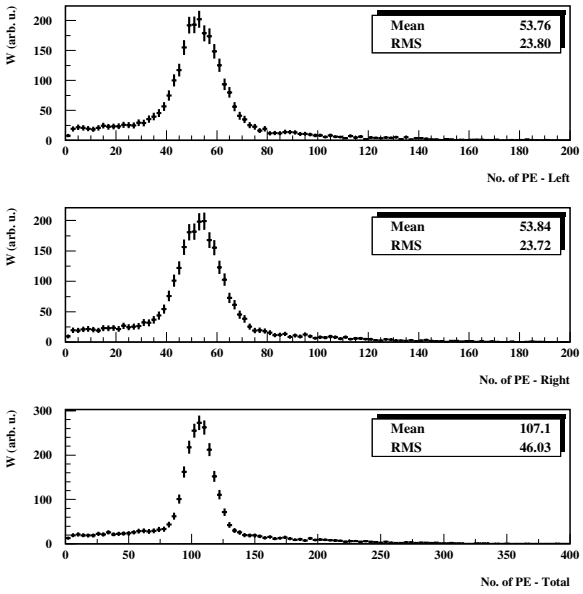

Figure 105: *The distribution of the number of photoelectrons on each of the phototubes, and the distribution of the total number of photoelectrons. The normal of the 1.5 inch Čerenkov bar is rotated by -10° relative to the beam axis.*

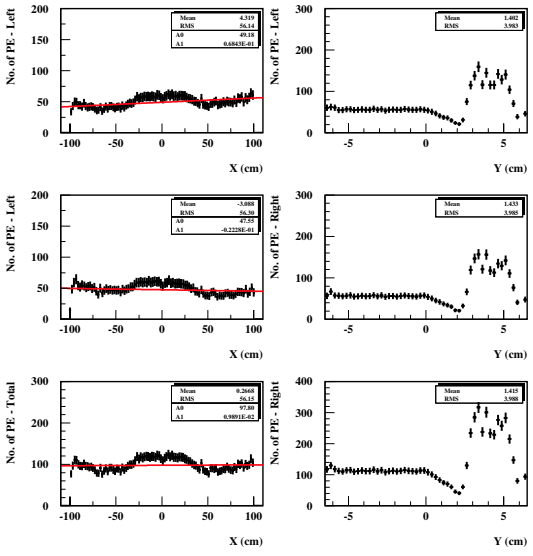

Figure 106: *The position dependence of the total number and number of photoelectrons on each of the phototubes along the length (left column) and the width (right column) of the 1.5 inch Čerenkov bar for the -10° rotated detector. The purpose of the fit is to quantitatively estimate the position dependence.*

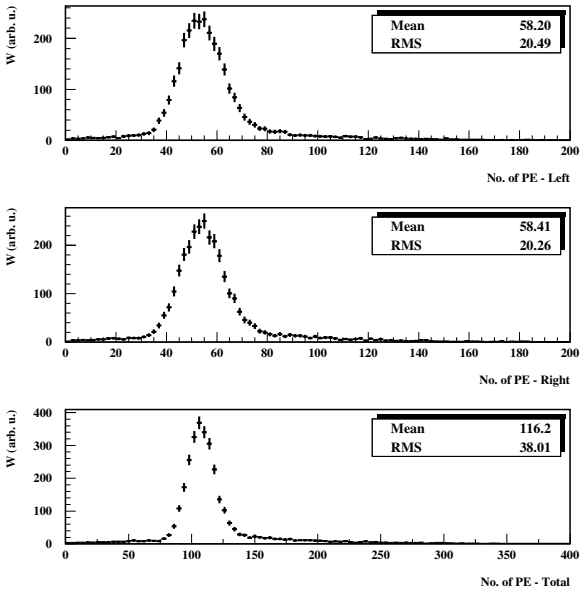

Figure 107: *The distribution of the number of photoelectrons on each of the phototubes, and the distribution of the total number of photoelectrons. The normal of the 1.5 inch Čerenkov bar surface is oriented along the beam axis.*

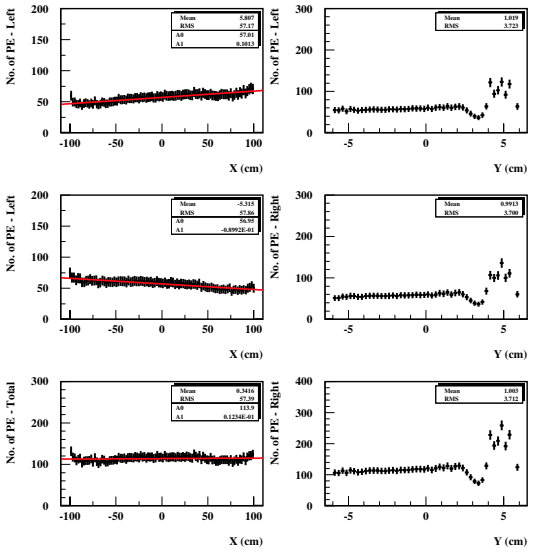

Figure 108: *The position dependence of the total number and number of photoelectrons on each of the phototubes along the length (left column) and the width (right column) of the 1.5 inch Čerenkov bar for the 0° rotated detector. The purpose of the fit is to quantitatively estimate the position dependence.*

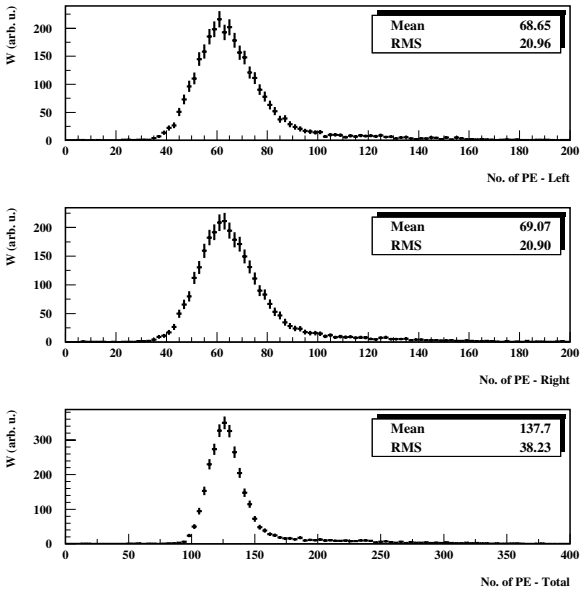

Figure 109: *The distribution of the number of photoelectrons on each of the phototubes, and the distribution of the total number of photoelectrons. The normal of the 1.5 inch Čerenkov bar is rotated by 10° relative to the beam axis.*

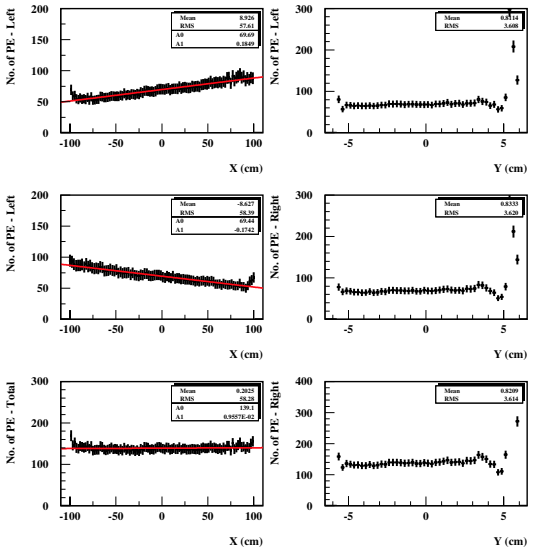

Figure 110: *The position dependence of the total number and number of photoelectrons on each of the phototubes along the length (left column) and the width (right column) of the 1.5 inch Čerenkov bar for the 10° rotated detector. The purpose of the fit is to quantitatively estimate the position dependence.*

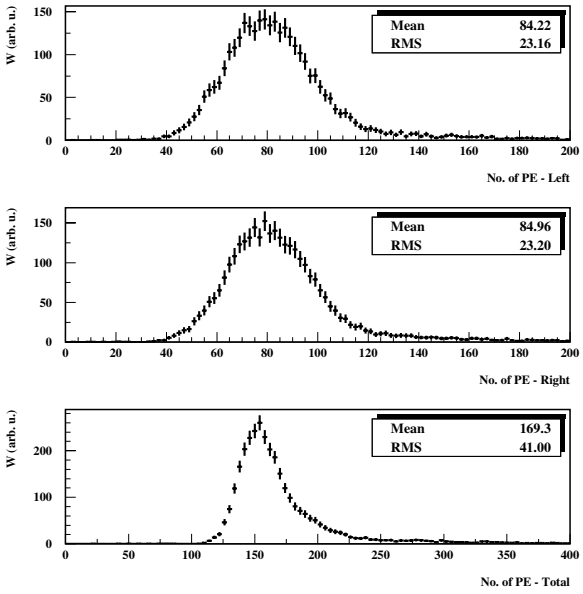

Figure 111: *The distribution of the number of photoelectrons on each of the phototubes, and the distribution of the total number of photoelectrons. The normal of the 1.5 inch Čerenkov bar is rotated by 15° relative to the beam axis.*

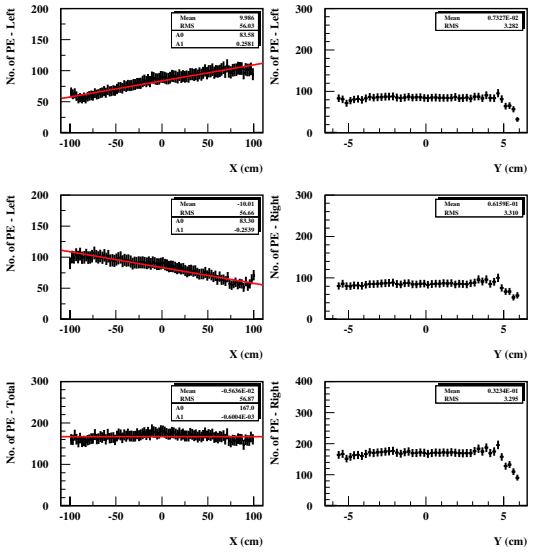

Figure 112: *The position dependence of the total number and number of photoelectrons on each of the phototubes along the length (left column) and the width (right column) of the 1.5 inch Čerenkov bar for the 15° rotated detector. The purpose of the fit is to quantitatively estimate the position dependence.*

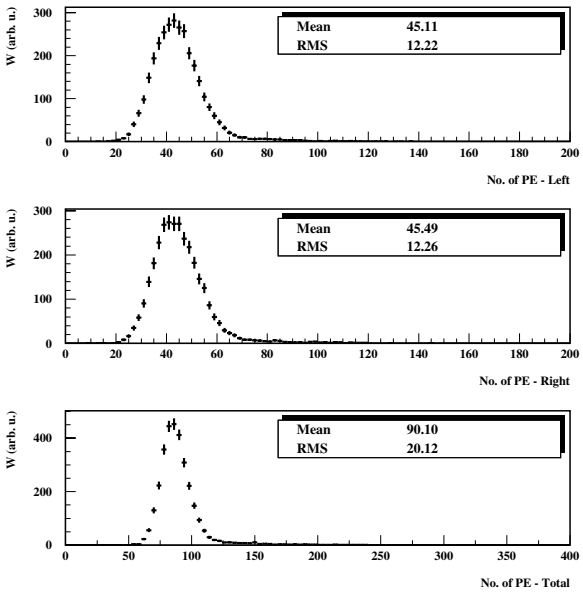

Figure 113: *The distribution of the number of photoelectrons on each of the phototubes, and the distribution of the total number of photoelectrons. The normal of this 1 inch thick Čerenkov bar is rotated by 12.5° relative to the beam axis.*

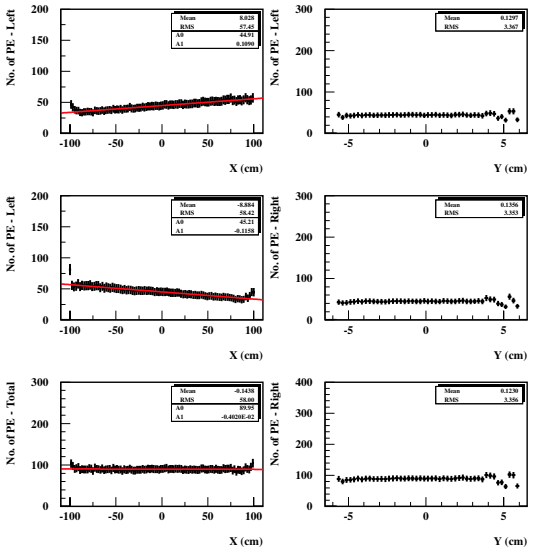

Figure 114: *The position dependence of the total number and number of photoelectrons on each of the phototubes along the length (left column) and the width (right column) of the 1 inch thick Čerenkov bar for the 12.5° rotation. The purpose of the fit is to quantitatively estimate the position dependence.*

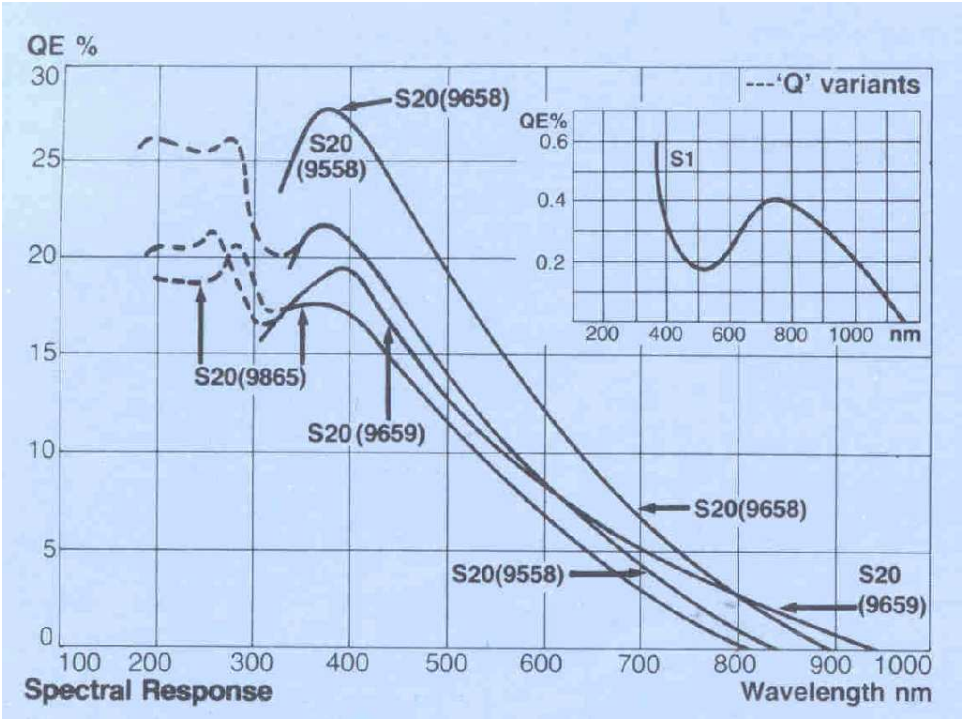

Figure 115: *Spectral response for the Thorn S20(9658) 2.05 in photocathode [13].*

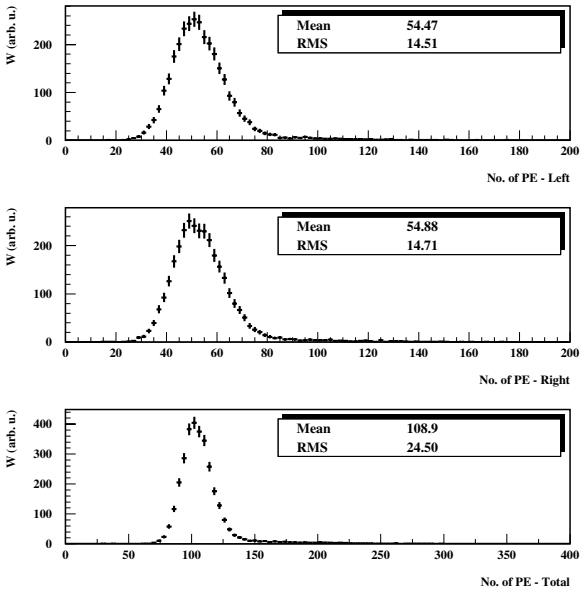

Figure 116: *The distribution of the number of photoelectrons on each of the phototubes, and the distribution of the total number of photoelectrons. The normal of the 1 inch thick Čerenkov bar is rotated by 12.5° relative to the beam axis.*

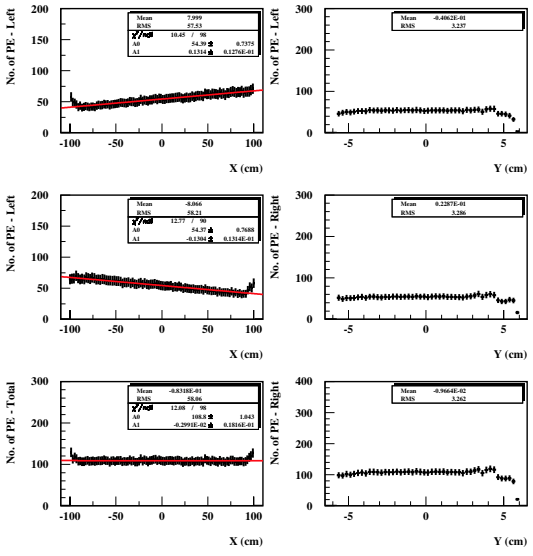

Figure 117: *The position dependence of the total number and number of photoelectrons on each of the phototubes along the length (left column) and the width (right column) of the 1 inch thick Čerenkov bar for the 12.5° rotated detector. The purpose of the fit is to quantitatively estimate the position dependence.*

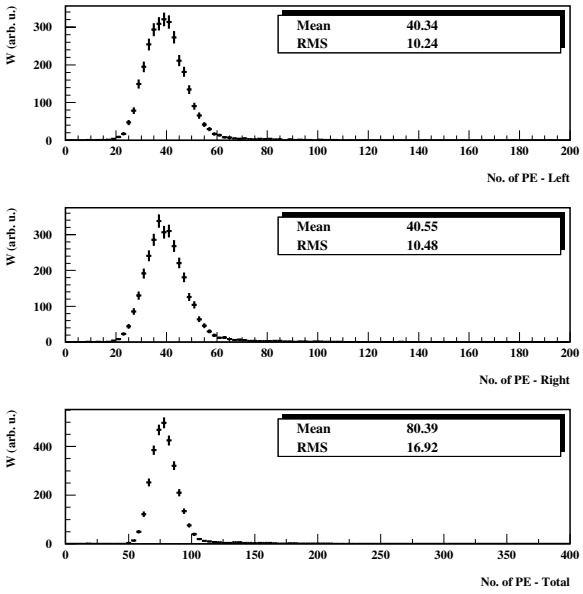

Figure 118: *The distribution of the number of photoelectrons on each of the phototubes, and the distribution of the total number of photoelectrons. The normal of the 2 cm thick Čerenkov bar is rotated by 12.5° relative to the beam axis.*

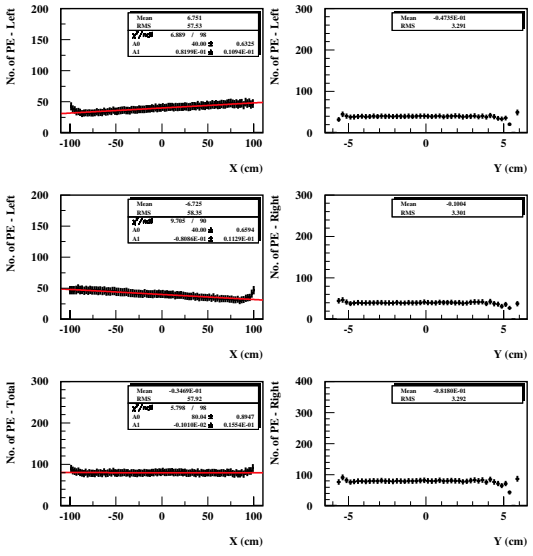

Figure 119: *The position dependence of the total number and number of photoelectrons on each of the phototubes along the length (left column) and the width (right column) of the 2 cm thick Čerenkov bar for the 12.5° rotated detector. The purpose of the fit is to quantitatively estimate the position dependence.*

14.4 Conclusion

This report finalizes the study of the design and properties of the Q^p_{Weak} Čerenkov detector. Detection of the elastically scattered electrons in the Q^p_{Weak} experiment will be performed in the integration mode using one quartz bar per magnet octant. The shape of such a counter is defined by the optical properties of the magnetic field, the target dimensions, and the distance from the magnet. It is generated by the elastically scattered electron envelope at a position close to the focal plane.

The entire set of mechanical and optical properties of the single quartz bar were also studied. This includes the effects of the bar dimensions and orientations, the effects of the thickness, the quality of surface polishing, and the effects of the photocathode quantum efficiency. The results of the previous report [6], where the effects of detector segmentation were studied, should be considered as a part of an overall assessment of the detector properties.

The conclusion is that there is a working solution for the Čerenkov counter. Recommended relevant parameters for this solution are summarized in Table 21. There is still a possibility for an improvement in the counter design, but this should be based on prototype testing rather than relying exclusively on simulations.

Table 21: *Selected parameters of the Q^p_{Weak} Čerenkov detector.*

Parameter	Value
Detector Position	580 cm from the magnet center
Detector Height	319.5-331.5 cm from the beam axis
Bar Length	200-210 cm
Bar Width	11-12 cm
Bar Thickens	1.905-2.54 cm
Rotation Around Beam Axis	$12.5° \pm 2.5°$
Polishing Quality	Normal Polishing (25 Årms roughness)
Material	Quartz (Fused Silica)
Photocathode	S20 (high Q.E.)

References

[1] Jlab Proposal E02-020, "The Q_weak Experiment: "A Search for Physics at the TeV Scale Via a Measurement of the Proton's Weak Charge", D. Armstrong et al., 2002

[2] G0 Technical Design Report, Nuclear Physics Laboratory, University of Illinois at Urbana-Champaign, 1993.

[3] Letter of Intent to TJNAF, R. Carlini, J. M. Finn and M. J. Ramsey-Musolf, spokespersons.

[4] N. Simicevic, LaTech Technical Report LATECH-CAPS-00-06a, G0-00-026, 2000. (at http://www.npl.uiuc.edu/exp/G0/docs/docs.html)

[5] N. Simicevic, LaTech Technical Report LATECH-CAPS-00-06b, G0-00-028, 2000. (at http://www.npl.uiuc.edu/exp/G0/docs/docs.html)

[6] N. Simicevic, LaTech Technical Report LATECH-CAPS-01-03a, G0-01-007, 2001. (at http://www.npl.uiuc.edu/exp/G0/docs/docs.html)

[7] ADIT at http://www.aditpmt.com

[8] I. Adam et al., SLAC-PUB-7707, November 1997

[9] BaBar Collaboration home page is at http://www.slac.stanford.edu/BFROOT/

[10] J. Cohen-Tanugi et al., ICFA Instrum.Bull.21:20-44,2001

[11] M. Smy and R. Wilson, BaBar Note # 220, 1995

[12] GEANT Detector Description and Simulation Tool, *CERN Program Library Long Writeup W5013*, CERN, Geneva, 1993

[13] THORN EMI Electron Tubes, 1982